Observations of Arctic low-level mixed-phase clouds at Ny-Ålesund: Characterization and insights gained by high-resolution Doppler radar

INAUGURAL-DISSERTATION

zur
Erlangung des Doktorgrades
der Mathematisch-Naturwissenschaftlichen Fakultät
der Universität zu Köln

vorgelegt von

Rosa Tuulia Gierens
aus Turku, Finnland

Köln 2021

Berichterstatter:

Prof. Dr. Ulrich Löhnert
Prof. Dr. Roel Neggers

Tag der mündlichen Prüfung: 17 November 2020

Abstract

Low-level mixed-phase clouds (MPCs) play an important role in the Arctic climate system by contributing to the surface warming. The complexities of the mixed-phase microphysics combined with the multitude of ways the low-level MPCs interact with the surface and the boundary layer make these clouds difficult to represent in climate models, which contributes to the uncertainties in predicting future climate change in the Arctic. Observations are needed to provide constrains for model parameterizations on one hand, and to improve process understanding on the other hand. However, continuous observations in the high Arctic are sparse, particularly on the eastern hemisphere.

This dissertation presents the first work investigating a multi-year dataset of remote sensing observations of persistent low-level mixed-phase clouds (P-MPC) above Ny-Ålesund, Svalbard. A state-of-the-art Doppler cloud radar providing highly vertically and temporally resolved cloud measurements was utilized in combination with further remote sensing and standard meteorological observations. Two complimentary approaches for addressing the observational gaps in measuring Arctic low-level mixed-phase clouds have been considered.

The first study investigated the P-MPCs above Ny-Ålesund in the context of the complex fjord environment. The occurrence and properties of P-MPC in different seasons and under different regional free-tropospheric and surface wind conditions were analyzed. Furthermore, the influence of thermodynamical coupling with the surface was investigated considering both its effect on cloud properties and how coupling is related to the local wind in the fjord. P-MPCs were found to occur most commonly with westerly winds (from the direction of the sea), and these clouds had a lower liquid base height and higher mean liquid and ice water paths compared to the clouds associated with easterly winds (from the direction of the interior of the island). The increased height and rarity of P-MPCs with easterly free-tropospheric winds suggest the island and its orography have an influence on the studied clouds. Most P-MPCs were found at least partially decoupled from the surface, and the decoupled cases where found to have on average a lower liquid water path than the coupled P-MPCs. Decoupling was more common with surface wind directions associated with katabatic winds.

The second study explored the potential of the cloud radar Doppler spectrum skewness for gaining insights in the microphysical properties of the P-MPCs. Combining case studies and statistical analysis of a 3-year dataset, a conceptual model relating the reflectivities of supercooled liquid and ice to the skewness profile in the mixed-phase layer at P-MPC top was developed and tested. The change from liquid dominated reflectivity at cloud top to ice dominating below was found to be associated with a skewness profile turning from positive to negative (when defining positive Doppler velocity down towards the radar), thus skewness is providing a reflectivity weighted measure of phase-partitioning in the mixed-phase layer. Although the approach is limited to profiles where the amount of liquid is sufficient to produce a clear signal in the Doppler spectrum, a third of all radar profiles obtained from P-MPCs were found to exhibit the described skewness feature. The analysis indicated that the height where skewness changes sign is to a large extend defined by the reflectivity of the ice phase, and skewness could therefore be useful for studying the early stages of precipitation formation. The statistical analysis carried out further revealed steady relationships between skewness and other cloud parameters, that could provide observational constrain for the evaluation of microphysical parameterizations applied in numerical models.

They know how to plot five days of rain
in bar graphs and line charts

but what units should I give them
to explain the wrong kind of downpour

at the wrong time of year?

from Geography Lessons
by Mariah Whelan

Contents

List of Figures

List of Tables

I Introduction

1 Motivation

The Earth's climate is warming at an unprecedented rate due to anthropogenic greenhouse gas emissions (IPCC, 2018). The globally observed increase in tropospheric temperature is pronounced in the Arctic, where the near-surface air temperature has risen more than two times faster than the global mean since the mid-1990s (IPCC, 2018, Richter-Menge et al., 2019). This phenomena has been termed Arctic amplification, yet the mechanisms responsible for the accelerated warming are not well understood (Osborne et al., 2018, Wendisch et al., 2017). Currently, Arctic warming exceeds the temperature increase at mid-latitudes by 2 K (Wendisch et al., 2019a). Climate change has already led to dramatic environmental changes in the Arctic, such as the rapid decrease in sea-ice extent, thawing of permafrost, decline of snow cover, and changes in precipitation patterns (Meredith et al., 2019, Stroeve et al., 2012). Future predictions are uncertain because climate models exhibit large discrepancies in the Arctic (Block et al., 2020). The temperature is projected to keep rising throughout the 21st century, although the models disagree on the exact magnitude (IPCC, 2013).

The rapid climate change has significant impacts on Arctic communities and ecosystems (Andersen et al., 2017, IPCC, 2018, 2019, Larsen et al., 2014). Increasing temperature and changes in sea ice – together with ocean acidification – impact marine habitats, populations, and their viability. Land ecosystems are disturbed by changes in the hydrological cycle, decrease in snow cover, and increase in temperature, and globally unique biodiversity is threatened (IPCC, 2019). Nowadays, 4 million people live in the Arctic, approximately 10% of whom are Indigenous. Changes in the physical environment have led to negative impacts on food security, water quality, livelihoods, infrastructure, transportation, tourism, and recreation (Larsen et al., 2014, Richter-Menge et al., 2019), although it should be noted that for many Indigenous peoples these issues are not exclusively associated with climate change (Whyte, 2017). Permafrost thawing is damaging infrastructure and related services (Melvin et al., 2017, Walker and Pierce, 2015). Further hazards, such as wildfires, unreliable ice and snow conditions, and more frequent and stronger storms are also threatening human settlements and livelihoods (IPCC, 2019, Richter-Menge et al., 2019). Increase in food- and water-borne diseases, malnutrition, injuries, and mental health challenges have been reported (IPCC, 2019). The impacts of climate change on the health and well-being of Arctic residents are significant, especially for many Indigenous peoples, and projected to increase in the future (IPCC, 2019, Jaakkola et al., 2018). Arctic communities are diverse and will be impacted by climate change differently. In addition to changes in the physical and biological environment, societal consequences are also connected to demography, culture, economic development, exploitative industries, and neo-colonialism (AMAP, 2017, Larsen et al., 2014, Whyte, 2017). Therefore, the possibilities for adaptation vary. In the future, it is possible that the rate of climate change exceeds the rate at which some Arctic natural and societal systems are able to adapt (Larsen et al., 2014).

The impacts of climate change in the Arctic extend beyond the Arctic region. The decrease in sea-ice cover is opening new economic possibilities for shipping and the extraction of oil, gas, and minerals, thereby impacting global trade and economy (AMAP, 2017, Hillmer-Pegram, 2014, Smith and Stephenson, 2013). However, the thinner and more mobile sea ice is also creating more hazards for marine activities, and the increase in resource exploration might be more influenced by economical conditions than the environmental changes (AMAP, 2017). The last two decades have already seen an increase in Arctic shipping in the summer time (IPCC, 2019). Yumashev et al. (2017) estimate that by the end of the century up to 5% of worlds trade could be shipped through the Northern Sea Route, generating wealth especially in Europe and Asia. On the other hand, the increased industrial activities on the Arctic ocean pose a risk on marine ecosystems, and the burning of fossil fuels sourced from the Arctic further accelerates climate change globally (AMAP, 2017, IPCC, 2019). Changes in species distribution is posing an additional challenge for the international and national ocean and fisheries governance (IPCC, 2019). Arctic amplification might also affect weather in the mid-latitudes (Cohen et al., 2020) and beyond (Kim et al., 2020), radically increasing the number of people impacted by Arctic climate change. There is, therefore, a critical need for accurate and reliable predictions of future climate change in the Arctic.

The sensitivity of the Arctic climate system and the difficulty to predict it stem from the multitude of interconnected feedback processes (Russotto and Biasutti, 2020, Wendisch et al., 2017). The Arctic is characterized by heterogeneous surface conditions (open ocean, sea ice), large seasonal differences in solar radiation (polar day and night), low sun angle, high surface albedo, temperature inversions close to the surface, and frequent and persistent low-level clouds (Curry, 1995, Schweiger et al., 2008, Wendisch et al., 2017). These features give rise to feedback mechanisms that lead to Arctic amplification. Several physical feedback mechanisms are known, such as the surface albedo feedback (Hall, 2004, Winton, 2006), the Planck feedback (Bony et al., 2006), the lapse rate feedback (Lauer et al., 2020, Payne et al., 2015), the water vapor feedback (Ghatak and Miller, 2013, Gordon et al., 2013), and the cloud feedback (Colman et al., 2001, Zelinka et al., 2012). However, the relative importance and combined influence of and the interactions between different feedbacks are poorly understood (Goosse et al., 2018, Wendisch et al., 2017). Substantial uncertainty is associated with estimating the cloud feedback. Its role in Arctic amplification is unclear, and different climate models do not even agree on the sign of the total cloud feedback (Ceppi et al., 2017, Goosse et al., 2018, Zelinka et al., 2020, and references therein). In addition, clouds are not only relevant for the cloud feedback, but also modulate the surface albedo, lapse rate and water vapor feedbacks (Crook et al., 2011, Sledd and L'Ecuyer, 2019, Stapf et al., 2019). The local feedbacks mentioned above are also influenced by the meridional transport of heat and water vapor (Pithan et al., 2018) that also seem to be changing due to climate change (Armour et al., 2019, Mattingly et al., 2016, Mewes and Jacobi, 2019). Given the many processes and their interactions, as well as our limited understanding of them, it is not surprising that models fall short in many aspects in the Arctic region (De Boer et al., 2012, 2014, Karlsson and Svensson, 2013, Tjernström et al., 2008). Specifically, clouds and cloud related feedback processes have been identified as a major source of uncertainty (Goosse et al., 2018).

Clouds interact with the surrounding atmosphere and the surface in multiple ways. By modifying long- and shortwave radiative fluxes, clouds directly impact the surface energy budget (Miller et al., 2017, Shupe and Intrieri, 2004). Clouds may also generate turbulence, vertically redistribute heat and moisture, and form precipitation (Brooks et al., 2017, Morrison et al., 2012, Solomon et al., 2014). Simultaneously, cloud properties can rapidly change due to changes in forcing conditions (Kalesse et al., 2016b, Young et al., 2016). Particularly low-level liquid-containing clouds are important for the warming of near-surface air (Shupe and Intrieri, 2004). These low-level clouds are typically mixed-phase, containing both ice and supercooled liquid. Arctic mixed-phase clouds (MPC) have been observed to occur frequently and to persist for hours or even days (Morrison et al., 2012, Pinto, 1998, Shupe, 2011). Unfortunately, these clouds are difficult to represent in numerical models (Morrison et al., 2008, Pithan et al., 2014, Zelinka et al., 2017). Particularly an issue for estimating the cloud radiative effect and for studying feedback mechanisms, climate models underestimate the occurrence of low-level clouds in the Arctic (Vignesh et al., 2020) and struggle with the partitioning between supercooled liquid and ice (Cesana et al., 2015, Guo et al., 2020, McCoy et al., 2016). Detailed evaluations of specific climate models have revealed issues in the representation of the cloud life cycle due to limitations in the microphysical parameterizations (English et al., 2014, McIlhattan et al., 2017) and the clouds' interaction with the local boundary layer (Kretzschmar et al., 2019). Also a weak poleward heat and moisture transport has been linked to the underestimation of low cloud cover in climate models (Baek et al., 2020). The peculiar persistency of Arctic MPCs under different environmental conditions remains an open question, and improvements in the process-level understanding are still required (Morrison et al., 2012, Wendisch et al., 2017, 2019a).

The study of Arctic MPCs is challenged by the sparsity of observations. Only few permanent stations with vertically resolved cloud observations exist in the high Arctic (Fig. 1). Additionally, several ship-based and airborne campaigns have taken place in the recent decades (see for example Curry et al., 2000, McFarquhar et al., 2011, Tjernström et al., 2014, Uttal et al., 2002, Verlinde et al., 2007, Wendisch et al., 2019b). Measurement campaigns provide comprehensive and detailed measurements, but only for a limited number of cases. On the contrary, continuously operated stations provide long time series that allow the assessment of seasonality, inter-annual variability, trends, and further statistical analysis (e.g. De Boer et al., 2009, Maturilli et al., 2015, Norgren et al., 2018, Shupe, 2011). Remote sensing plays a central role in cloud research. Synergistic methods utilizing ground-based radar, lidar, and radiometers are well established for the study of Arctic MPCs, although challenges still remain (Korolev et al., 2017, Shupe et al., 2008c). While ground-based stations lack the spatial coverage of satellite observations, they provide a much higher vertical and temporal resolution that allows for the study of cloud processes (Acquistapace et al., 2017, Mioche et al., 2015). Continuously operated stations therefore have an important role in Arctic cloud research.

Until recently permanent sites for detailed cloud observations have been focused on the western high Arctic (Fig. 1). Within the *ArctiC Amplification: Climate Relevant Atmospheric and SurfaCe Processes and Feedback Mechanisms (AC)*^{3} -project the French-German research station AWIPEV in Ny-Ålesund, Svalbard, was extended with several instruments in 2016–2017. Most notable was the addition of a novel frequency modulated continuous wave (FMCW) 94 GHz cloud radar in June 2016 (Küchler et al., 2017, Nomokonova et al., 2019). Further remote sensing and surface precipitation devices were

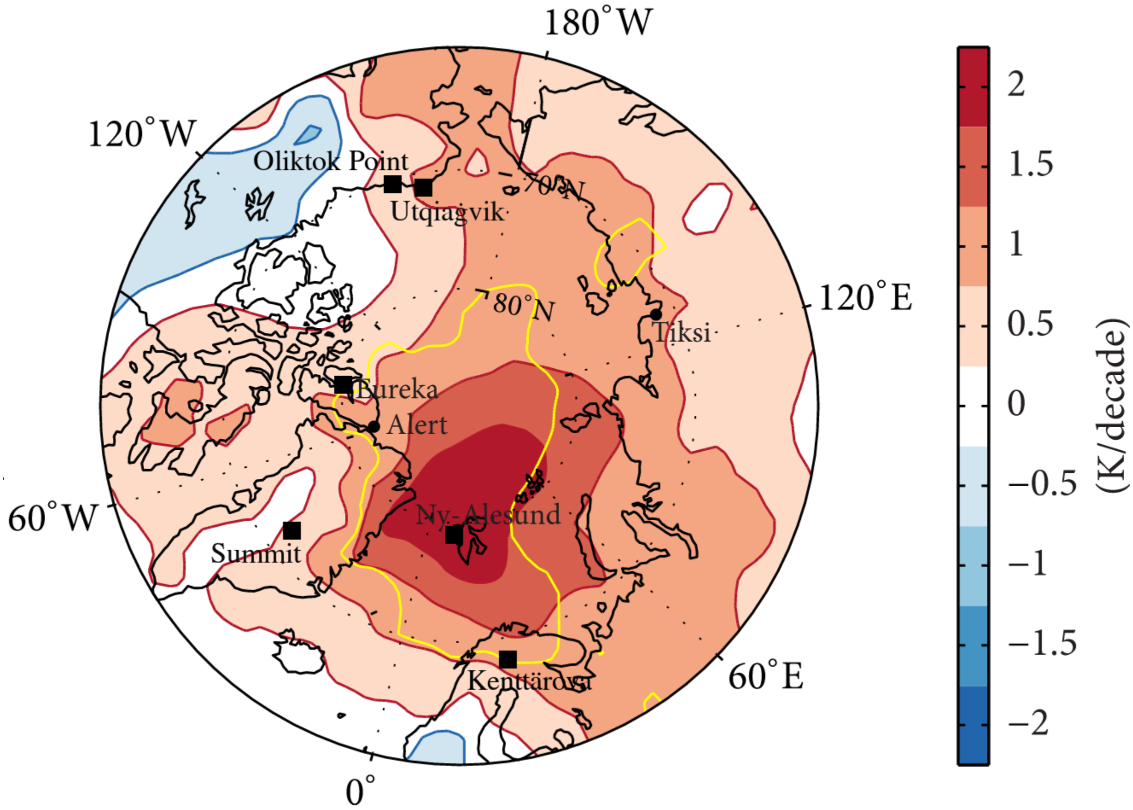

Figure 1: Atmospheric supersites in the Arctic. The black squares indicate sites with long term cloud radar observations. The color indicates the mean temperature trend at 850 hPa level in December-January-February based on Era-Interim reanalysis of the time period 1996–2016. The yellow lines encircle the areas with a significant trend on 95% confidence level. The figure is originally created by Dahlke and Maturilli (2017) and was published under the Creative Commons Attribution License (CC BY 4.0) by Hindawi, and has here been updated to include further measurement sites.

later included. Prior to the new installations the station already hosted various instruments for observing clouds, atmospheric radiation, thermodynamical properties, surface fluxes, and aerosols, as well as regular radiosoundings (Kulla and Ritter, 2019, Maturilli and Ebell, 2018, Maturilli et al., 2015, Maturilli and Kayser, 2017). The addition of a cloud radar made Ny-Ålesund a supersite for cloud research, an important extension to the sparse observational network. Especially interesting is the location of the station. Svalbard lies in the warmest part of the Arctic, in a region exhibiting the strongest surface warming (Dahlke and Maturilli, 2017). Intrusions of warm and moist air from lower latitudes and cold-air outbreaks are common (Pithan et al., 2018, Woods et al., 2013), which also has an influence on clouds in the Svalbard region (Mioche et al., 2017, Nomokonova et al., 2020). Locally, the archipelago exhibits large variations in surface properties (glaciers, seasonal sea ice, and snow cover) as well as orography. The new observations at the AWIPEV station provide exciting possibilities to study Arctic MPCs in a complex environment.

This thesis, carried out as part of the (AC)^3-project, utilizes the new cloud radar observations at AWIPEV. The studies presented are the first ones with a focus on low-level mixed-phase clouds above Ny-Ålesund that take advantage of the extended observational capabilities, analyzing the first 3-years of cloud radar measurements. Attention is given to the influence of synoptic and local-scale conditions, as well as the details of the mixed-phase layer revealed by high resolution Doppler radar observations. In the following, the current scientific understanding of Arctic MPCs is presented. First, processes and definitions relevant for all MPCs are described, after which Arctic low-level MPCs are considered in more detail. Furthermore, a brief introduction to the Ny-Ålesund site is given. The research questions and the contents of the dissertation are introduced in the last part of this chapter.

2 Scientific background

2.1 Mixed-phase clouds

A mixed-phase cloud (MPC) is a cloud that contains both supercooled liquid and ice (Andronache, 2017). This seemingly simple definition turns out to be ambiguous when inspected more closely. Real clouds in the atmosphere do not necessarily consist of homogeneously mixed droplets and ice particles (so called genuinely mixed-phase clouds), but often consist of inhomogeneously mixed hydrometeors and single-phase regions (so called conditionally mixed-phase clouds). Korolev et al. (2017) elaborate on the difficulty in defining mixed-phase: "should a cloud be defined as mixed phase if it has one ice particle per 10 or per 10^{12} liquid droplets? Should a cloud be considered glaciated if it contains one liquid droplet per 10^{12} ice particles, or is it still mixed phase?" No consensus of what defines a MPC has been established, and physically based definitions are challenging to use in studies utilizing imperfect measurement techniques. In situ and passive and active remote sensing instruments operate on significantly different spacial scales, and use different metrics to describe cloud structure (Korolev et al., 2017). Additionally, the heterogeneity in the cloud impacts microphysical processes and is an interesting question in itself (Zhang et al., 2019). In practice, the definition for a MPC varies based on the research focus and instrumentation used. Shupe (2011) defined MPCs as cloud systems "that contain liquid and ice water that are associated through microphysical processes within the same contiguous layer but must not necessarily contain both condensed phases in all cloud volumes." Although such cloud systems include volumes with single phase, these systems typically contain some genuinely mixed-phase volumes (Shupe et al., 2008c). Here, the definition given by Shupe (2011) is followed, within the sensitivity limits of the utilized instrumentation. In this section key concepts and processes relevant for MPCs in general are presented. Although references to Arctic conditions are provided, the description is in general not limited to MPCs in the Arctic. Arctic conditions and the cloud regime in the focus of this work are introduced in more detail in Sect. 2.2.

The mixture of water vapor, liquid droplets and ice crystals is thermodynamically unstable (Andronache, 2017). At sub-zero temperatures, the saturation vapor pressure over an ice surface is lower than over a liquid-water surface, causing ice crystals to grow at the expense of evaporating liquid droplets (Bergeron, 1935, Findeisen, 1938, Wegener, 1911). As a consequence, ice crystal growth is enhanced when liquid droplets are present, promoting the formation of precipitation and affecting cloud life time. This is known as the Wegener-Bergeron-Findeisen process (WBF), and is one of the major findings in cloud physics in the last century. Analysis of an array of climate models have found that the WBF plays a central role in determining the liquid fraction and life time of MPCs in the models (Cesana et al., 2015, Komurcu et al., 2014, Tan and Storelvmo, 2016). However, the WBF predicts that a mixed-phase cloud is fully glaciated within seconds to a few hours, depending on the number concentration of liquid and ice particles. This contradicts the observations of such clouds persisting for several days (Morrison et al., 2012, and references therein). The WBF only considers the conditions when the water vapor pressure exceeds the saturation vapor pressure of ice but is below the saturation vapor pressure over liquid, and is therefore a limited description of the possible range of water vapor pressure in a MPC (Korolev, 2007). Important for the persistency of MPCs, the vapor pressure often exceeds that of liquid saturation, in which case both droplets and ice particles grow simultaneously. Modeling studies have found that the WBF is active in MPCs only about half of the time (Fan et al., 2011, Lohmann and Hoose, 2009). That the vapor pressure can exceed the saturation vapor pressure over liquid makes it possible for supercooled liquid to form, slowing down the glaciation of the cloud and allowing mixed-phase conditions to persist.

Supercooled liquid has been found in the atmosphere at temperatures reaching down to $-40\,°\mathrm{C}$ (Korolev et al., 2017, and references therein). Cloud droplets form in the atmosphere when an air parcel reaches saturation through cooling or isobaric mixing (Yau and Rogers, 1996). Droplets are formed with the aid of sub-micron sized particles, i. e. aerosols. The aerosols that can act as centers for condensation are called cloud condensation nuclei (CCN). The efficiency of an aerosol particle to act as a CCN depends on its size and chemical composition (McFiggans et al., 2006). Although not every aerosol particle is as suitable as a CCN, there are enough CCN even in the more pristine areas for droplets to form when moderate supersaturation is reached (Pruppacher and Klett, 1997). In the Arctic, CCN concentrations vary from 100 to $1000\,\mathrm{cm}^{-3}$, but also values as low as $1\,\mathrm{cm}^{-3}$ have been reported (Mauritsen et al., 2011, Moore et al., 2011). Sources of CCN in the Arctic are long-range transport, anthropogenic pollution, and new particle formation (Gunsch et al., 2017, Herenz et al., 2018, Leaitch et al., 2016). After the activation of an aerosol to a cloud droplet, the droplet grows through vapor deposition as long as it resides in a supersaturated environment (Yau and Rogers, 1996). Initially, diffusional growth is very quick to increase the droplet size, but with increasing droplet radius the growth rate slows down. For cloud droplets larger than about $10\,\mathrm{\mu m}$ in radius, collision-coalescence becomes an important process to grow the droplets.

Supercooled droplets large enough to be considered drizzle droplets (droplets larger than $100\,\mathrm{\mu m}$) have been repeatedly observed (Cober et al., 2001, 1996, Isaac et al., 2005, Politovich, 1989, Singleton, 1960). Supercooled drizzle, or supercooled large droplets (SLD) as known in the literature, can form similarly as large droplets in warm clouds via collision-coalescence (the so called supercooled warm rain process, Huffman and Norman, 1988). Low ice particle concentrations, which indicate a limited loss of liquid to the ice phase via freezing or WBF, and low droplet number concentration and high liquid water content, which favor the warm rain process, have been associated with the formation of SLD (Lasher-Trapp et al., 2008, Rosenfeld et al., 2013, and references therein). Giant aerosol particles (radii greater than $1\,\mathrm{\mu m}$) have also been suggested to play a role in SLD formation (Beard and Ochs, 1993, Lasher-Trapp et al., 2008). Furthermore, certain mixing conditions at cloud top have been hypothesized to contribute to the development of SLD (Korolev and Isaac, 2000, Pobanz et al., 1994). Observations suggest that the occurrence of supercooled drizzle declines with decreasing temperature (Cortinas Jr. et al., 2004), although in situ observations of SLD below $-20\,°\mathrm{C}$ do exist (Cober et al., 2001). Particularly in Arctic MPCs, larger droplets are most often found close to cloud top (McFarquhar et al., 2007, Mioche et al., 2017), but have also been observed in liquid layers embedded in deeper MPC (Verlinde et al., 2013).

The process of phase transition towards increased molecular order (vapor $\rightarrow$ liquid $\rightarrow$ ice) requires overcoming the free energy barrier, and is generally called nucleation (Yau and Rogers, 1996). Unfortunately, there is no satisfactory overarching theory for the phenomena of nucleation, complicating the understanding of ice nucleation processes (Andronache, 2017). Ice particles form in atmospheric conditions through heterogeneous nucleation with the aid of ice nucleating particles (INP) or at temperatures below about -35°C via homogeneous nucleation. For mixed-phase clouds, heterogeneous nucleation is thought to be the main pathway of primary ice formation (Andronache, 2017). Heterogeneous ice nucleation can be divided into deposition nucleation and freezing nucleation (following the terminology by Vali et al., 2015). In deposition nucleation, ice is nucleated from supersaturated water vapor onto an INP without a prior formation of liquid. Freezing nucleation is ice nucleation within a body of supercooled liquid. Several freezing nucleation modes are known, most important being immersion freezing and contact freezing. The dominant mode of ice nucleation in Arctic MPCs is currently thought to be immersion freezing, where an INP is immersed in a liquid droplet (Cui et al., 2006, De Boer et al., 2011). However, contact nucleation, where freezing occurs when INP comes in contact with the surface of liquid particle, may also sometimes play a role (Ansmann et al., 2009). Ice nucleation depends strongly on the properties of the aerosol and environmental conditions (Kanji et al., 2017). Only a small fraction of aerosols are suitable INPs, and the particles ability to act as an INP is strongly temperature dependent. Substances known to act as INP in atmospheric conditions are mineral dust, bacteria, fungi, pollen, and plankton. Recently, the sea-surface micro-layer was found to contain ice nucleating entities, probably of biological origin. A lot is unknown about INP in the Arctic, particularly concerning spatial variability, temporal trends and the relative importance of different sources. INP concentrations in the Arctic vary from 10^{-5} to more than $10\,\mathrm{L}^{-1}$ (Wex et al., 2019, and references therein). INP from biological origin, both marine and terrestrial, have been identified (Conen et al., 2016, Irish et al., 2019). Wex et al. (2019) found INP concentrations to be higher in summer, from June to September, at all studied sites. Currently, the sea-surface micro-layer is being researched as a possible important source of Arctic INP (Chance et al., 2018, Irish et al., 2017, Wilson et al., 2015, Zeppenfeld et al., 2019). Although a lot of progress has been made, there are still many gaps in our understanding of the ice nucleation processes in the atmosphere, especially in the remote polar regions.

The growth processes of ice crystals are more complicated than that of liquid droplets, owing to the micro-structures of ice (Pruppacher and Klett, 1997). After nucleation, ice particles grow through vapor deposition. In a mixed-phase volume, ice particles are in a strongly super-saturated environment which promotes the diffusional growth. The diffusional growth rate depends on ambient temperature and pressure, and to a lesser extent on parameters such as super-saturation, ventilation and particle shape. At liquid saturation, the growth rate is at its highest around -14 to -16 °C. The environmental conditions do not only impact the growth rate, but also determine the habit of the growing ice crystal. Basic shapes include columns, plates, and dendrites. When the particle falls through different ambient conditions, it can experience various diffusional growth regimes leading to a large number of different kind of ice crystals (Magono and Lee, 1966). Ice particles may further grow through aggregation. Aggregation is most efficient at temperatures close to 0°C, because the sticking of ice crystals together after a collision has occurred is favored at warmer temperatures. Additionally, ice crystals with dendritic features may aggregate at colder temperatures. The process of a droplet colliding with an ice particle and subsequently freezing on it is called riming. For riming to play a significant role in increasing ice mass in the cloud, the droplets need to be large enough and their concentration needs to be high enough that the likelihood of collisions is sufficient (Lowenthal et al., 2011). All of these processes, namely diffusional growth, aggregation, and riming, may take place in the same cloud, leading to large variation in ice particle shape, size, density, and mass-area relation, which makes the study of ice microphysical processes via remote sensing challenging.

It is often observed that the number concentration of INPs is lower than the ice particle number concentration by an order of magnitude or more (Field et al., 2017). Mechanisms that lead to new ice particles in the presence of preexisting ice without the action of an INP or homogeneous nucleation are generally referred to as secondary ice production (SIP). The most well known secondary ice mechanism is rime-splintering, also known as the Hallett-Mossop process. In the right conditions, ice splinters are produced when droplets rime on a large ice particle. The process is effective in the temperature range from -3 to -8°C and in presence of droplets larger than 13 µm (Hallett and Mossop, 1974). Further known but less well quantified processes are collision-fragmentation (ice splinters produced by ice-ice collisions), droplet-shattering (ice splinters produced by freezing of large droplets), and sublimation fragmentation (ice particles separate when ice bridge sublimates). However, the physical basis of these processes are not well understood and the atmospheric and cloud conditions are poorly constrained. Because SIP can increase the ice concentration by orders of magnitude (Phillips et al., 2003), it is generally recognized as an important process for certain clouds.

Many different kind of MPCs are observed in the atmosphere (Andronache, 2017, Korolev et al., 2017). Stratiform low- and mid-level clouds and cumulus clouds may be mixed-phase. MPCs can be associated with frontal systems, orography and convection. After all, the only thing that is required for a cloud to be considered mixed-phase is the existence of both liquid droplets and ice particles. The temperature regime for mixed-phase clouds, defined by the melting and homogeneous freezing temperatures of water, is commonplace in the troposphere. A variety of dynamical conditions can lead to mixed-phase conditions, and the structure and life cycle of different types of MPCs vary considerably (Costa et al., 2017). A MPC is a complex system that emerges from the the microphysical processes in interaction with large- and cloud-scale dynamics, and is modified through internal processes as well as external forcings. To further understand the processes of a mixed-phase cloud system, it is necessary to set a more specific focus. This work focuses on the stratiform low-level mixed-phase clouds because of it their commonality, peculiar persistency and climatic relevance in the Arctic.

2.2 Mixed-phase clouds in the Arctic

The frequency of occurrence of clouds in the Arctic varies from 50% to nearly 100% depending on location, season and the criteria used to detect a cloud. Cloud climatologies based on satellite observations show highest cloudiness in autumn (Mioche et al., 2015, Zygmuntowska et al., 2012). Ground based observations agree with the high fraction of cloud cover in autumn, however, above Ny-Ålesund cloudiness seems to peak already at the end of summer (Maturilli and Ebell, 2018, Nomokonova et al., 2019) and in the western Arctic a second maximum in spring has been reported (Shupe et al., 2011). In general, the high cloud fraction is caused by the very frequent low-level clouds (Mioche et al., 2015, Nomokonova et al., 2019, Shupe et al., 2011). Fig. 2a shows the spatial variability in

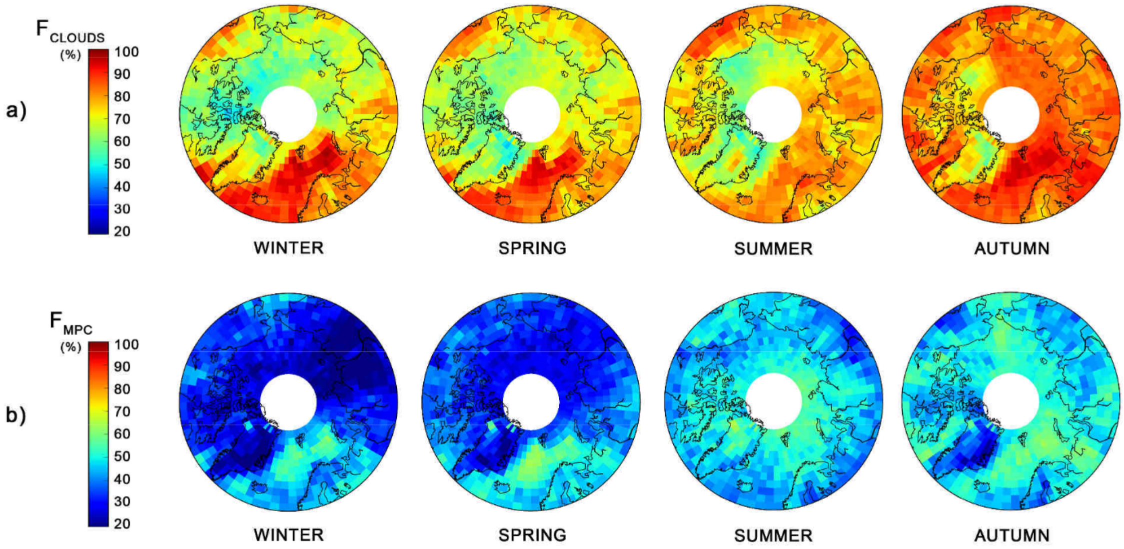

Figure 2: Seasonal cloud cover derived from a synergy of spaceborne radar and lidar (CALIPSO/CLOUDSAT) measurements taken from 2007 to 2010, covering altitude range 500–12 000 m. a) Occurrence of all clouds (relative to time), and b) fraction of MPCs (relative to all clouds). The figure is created by Mioche et al. (2015) and was published under the Creative Commons Attribution License (CC BY 3.0) by Copernicus Publications.

cloud cover across the Arctic in different seasons derived from satellite-based active remote sensing. Clouds occur particularly often on the Norwegian, Greenland, and Barents Seas. Not only are clouds more frequent in this region, a larger fraction of them is found to be mixed-phase (Fig. 2b). Furthermore, Mioche et al. (2015) analyzed clouds over the Svalbard region (defined as the area between 0°and 30°East and 75°and 80°North in their study) and found an average of 55% of observed clouds to be mixed-phase, most of them below 3 km, with the monthly MPC fraction varying between 45% and 60%. The commonality of MPCs in the Svalbard region makes Ny-Ålesund an attractive site for the study of MPCs.

Low-level mixed-phase clouds

Across different sites a typical structure of low-level MPCs is observed, characterized by one or more thin liquid layer(s) embedded in a deeper layer of ice, usually extending far below the liquid layer(s) (Hobbs and Rangno, 1998, Hobbs et al., 2001, Intrieri et al., 2002, McFarquhar et al., 2007, Morrison et al., 2012, Rangno and Hobbs, 2001, Shupe et al., 2001). A schematic picture of the main aspects of such stratiform clouds is presented in Fig. 3. A typical Arctic low-level MPC features a temperature inversion at cloud top, intensified by cloud liquid induced radiative cooling (Curry, 1986, Morrison et al., 2012). The cloud top cooling leads to negative buoyancy and top down driven turbulence (Pinto, 1998, Sedlar and Shupe, 2014). Supercooled liquid mainly forms in updrafts, where the rising air is adiabatically cooling (Harrington et al., 1999, Jiang et al., 2000, Morrison et al., 2005, Shupe et al., 2008a). Ice is nucleated in the liquid layer, mostly near the top of the cloud. Studies have shown an increase in cloud ice to coincide with increase in cloud liquid, suggesting that ice production is linked to cloud liquid water (Korolev and Isaac, 2003, Shupe et al., 2004, 2008a, 2006, Westbrook and Illingworth, 2011), and

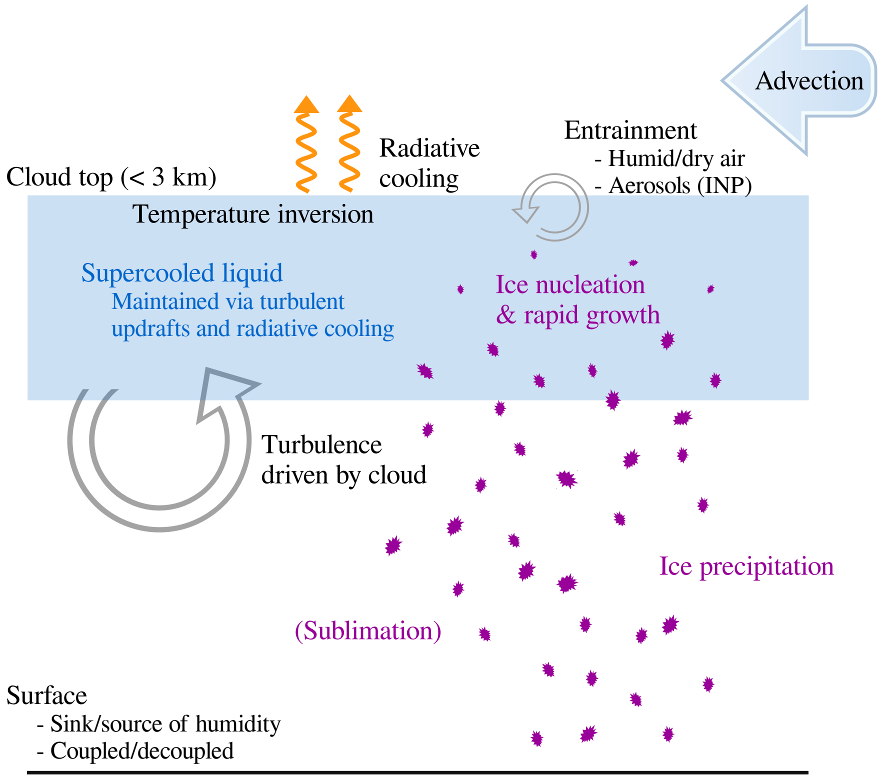

Figure 3: Simplified model of the persistent low-level MPC in the Arctic, adapted from Morrison et al. (2012). The blue shaded are indicates the liquid layer.

that the supercooled liquid precedes ice formation (Morrison et al., 2005, Westbrook and Illingworth, 2013). Once an ice crystal forms it grows very rapidly as it is in a strongly supersaturated environment (Sect. 2.1) and falls out of the liquid layer (Westbrook and Illingworth, 2013). There is therefore a constant sink of humidity, as well as INP, from the cloud via precipitation. Advection, surface fluxes and entrainment at cloud top can act as sources of humidity and INP for the cloud, depending on the environmental conditions where the cloud resides (Jackson et al., 2012, Morrison et al., 2012, Solomon et al., 2014). In some cases ice can sublimate before reaching the ground, and given the right mixing conditions the water vapor and INP can be recycled back to the cloud reducing the sink from the system (Solomon et al., 2011). In the following, aspects of the low-level MPC relevant for this work are introduced in more detail.

According to current understanding, supercooled liquid mainly forms in adiabatically cooling rising air and to a lesser extent due to radiative cooling at cloud top (Harrington et al., 1999, Jiang et al., 2000, Morrison et al., 2005, Rasmussen et al., 2002). Shupe et al. (2008a) analyzed a stratiform MPC case in detail and found an increase (decrease) in the amount of liquid in updrafts (downdrafts), which has later been reproduced in studies utilizing large eddy simulation (LES) (e.g. Solomon et al., 2011). Korolev and Field (2008) also showed theoretically that random turbulent motions lead to saturation with respect to liquid and can therefore create and maintain supercooled liquid in a cloud. The radiative cooling is localized to near cloud top (Egerer et al., 2019), and already very small amounts of liquid can effectively reduce the temperature of the cloud layer. However, the magnitude of radiative cooling does not only depend on the cloud but also the overlying atmosphere. Specifically, a second cloud layer above the low-level cloud can significantly reduce the cooling rate (Shupe et al., 2013). The radiative cooling acts as a positive feedback mechanism for the liquid layer to maintain itself, as radiative cooling drives turbulence that lead to vertical motions (Pinto, 1998, Shupe et al., 2008a). Given the right conditions, large scale subsidence can lead to the collapse of the cloud (Neggers et al., 2019).

In situ observations carried out by aircrafts have found that the liquid water content (LWC) and the size of cloud droplets is increasing with distance from cloud base, while the droplet number concentration (N_d) remains rather constant with height (Jackson et al., 2012, McFarquhar et al., 2007, 2011, Mioche et al., 2017). The LWC profile has often been found to be sub-adiabatic, which has been attributed to the WBF process and near cloud top to the entrainment of dry air (Jackson et al., 2012, Mioche et al., 2017, Shupe et al., 2008a). Mioche et al. (2017) analyzed cloud properties from four aircraft campaigns on the Greenland and Norwegian seas, and report a mean LWC of $0.1\,\mathrm{g\,m^{-3}}$ at the bottom of the liquid layer and almost $0.2\,\mathrm{g\,m^{-3}}$ near the cloud top, and a mean N_d of about $120\,\mathrm{cm^{-3}}$. Supercooled drizzle droplets are also occasionally observed, usually in the upper parts of the cloud (Jackson et al., 2012, McFarquhar et al., 2007, Mioche et al., 2017).

Across different measurement campaigns, ice particle number concentration (N_i) have been found to range from 0.1 to $10\,\mathrm{L^{-1}}$ (Andronache, 2017). Although the N_i concentration vary greatly, the N_i is usually orders of magnitudes lower than the N_d in the same MPC. In different studies the mean ice water content (IWC) have been found to vary from 0.01 to $0.035\,\mathrm{g\,m^{-3}}$ and IWC is either reported to increase from cloud top downwards or no clear trend is found (Jackson et al., 2012, McFarquhar et al., 2011, Mioche et al., 2017). Mioche et al. (2017) found the majority of ($> 100\,\mu\mathrm{m}$) particles to be rimed or irregulars, with some plates and stellars. Also McFarquhar et al. (2007) report a large fraction of irregular particles, in addition to the considerable portions of rosettes, needles, and columns. The in situ observations show a large variability of the properties of the precipitating ice (see also Korolev et al., 1999, Wendisch et al., 2019b) hinting towards multiple processes impacting the ice particle habit, N_i and IWC. However, the different studies agree that cloud top is dominated by liquid droplets, and in the lower part of the cloud and below the liquid base large ice particles are present.

The MPC can reside in a throughout mixed boundary layer, but also commonly observed is a structure with a cloud driven mixing layer over a surface based stable layer (Morrison et al., 2012, Pinto, 1998). In the Arctic, strong surface inversions and stable stratification in the lower troposphere are common, particularly in winter. When the entire layer from surface to the cloud is turbulent, the cloud is said to be thermodynamically coupled with the surface. Coupling has been found to be more likely if the cloud is low and thereby closer to the surface (Brooks et al., 2017, Shupe et al., 2013). The turbulence driven by the cooling at cloud top is characterized by narrow strong downdrafts and weak broad updrafts. This kind of vertical wind structure has been observed for both coupled and decoupled cases (Sedlar and Shupe, 2014, Shupe et al., 2013) indicating that surface driven turbulence is not necessary for the cloud to become coupled. Within the cloud, the liquid layer may extend into the cloud top inversion so that in the upper part a stable layer is present (Sedlar et al., 2012). This can take place to the extent that the entire liquid layer is stably stratified, for example Silber et al. (2020) found 25% of liquid bearing clouds at Utqiaġvik, Alaska, to be stable. Some studies have also considered the stability of the cloud and associated boundary layer in the context of the cloud life cycle. Sotiropoulou et al. (2014) suggest that clouds may start low and coupled to the surface. Over time the cloud base lifts and the cloud driven mixing layer disconnects from the surface causing the cloud to become decoupled. Stabilization of the cloud layer increases with decreasing liquid as the cloud develops towards glaciation. Finally, the entire cloud layer is stably stratified. Contrarily, Silber et al. (2020) claim that stable stratification is more common at the early stages of the cloud life cycle.

Whether the cloud is (de-)coupled with the surface regulates the interaction between the surface and the cloud, as the surface can only act as a source of humidity, aerosols, or precursors for CCN and INP, when there is vertical transport from the surface to the cloud layer. Only few studies have explicitly considered the impact of coupling on cloud properties. For example, Sotiropoulou et al. (2014) did not find a difference in liquid or ice water path between the coupled and decoupled clouds. Taking another point of view, Li et al. (2017) used LES to test how changes in sea ice cover lead to changes in the thermodynamic structure of the atmospheric boundary layer, and also found a change in the total condensed water of the associated low-level MPC. Further modeling (Eirund et al., 2019) and observational (Young et al., 2016) studies have found a change in cloud properties when moving from over sea ice to open sea or vice versa. Thus, evidence on the influence of surface conditions on the low-level MPC do exist, but the mechanisms are unclear owing to the complex nature of the interactions between the surface and low-level clouds.

To maintain the liquid layer(s), the production of liquid needs to balance the sink on the ice particles. To maintain cloud ice, new ice particles need to be continuously initiated, either by ice nucleation or secondary processes. The turbulence, that is caused by cloud liquid and acts to maintain the liquid layer in the presence of a constant sink, is considered a key internal feedback mechanism leading to the long life time of the Arctic MPCs (Morrison et al., 2012). Another necessary condition for MPCs to occur and to persist is that CCN are more abundant than INP, and thereby the cloud droplet number concentration is much larger than the ice particle number concentration, limiting the effectiveness of WBF to remove liquid from the MPC. Modeling studies have shown that high INP concentrations lead to a rapid glaciation of the cloud (e.g. Morrison et al., 2011). Furthermore, investigations of the INP budget found that the INP in the boundary layer deplete rapidly, after which the entrainment rate of INP at cloud top controls the ice number concentration to a large degree (Fridlind et al., 2012, Fu et al., 2019). The modeling study by Avramov and Harrington (2010) also indicated that the ice particle growth rate and fall velocity can impact the phase-partitioning and evolution of the stratiform MPC. Additionally, also the constant sink of humidity via precipitation needs to be balanced for the cloud to maintain itself (Savre et al., 2015, Solomon et al., 2014). In the right conditions, as already discussed, the surface can act as a source of humidity. Several modeling studies have shown the importance of humidity advection and the entrainment of humidity from above the cloud, particularly in the absence of surface sources (Jiang et al., 2000, Savre et al., 2015, Solomon et al., 2014, 2011, Sotiropoulou et al., 2018). Sedlar et al. (2012) report that a specific humidity inversion is observed near cloud top more often than not. Furthermore, a dry layer below the cloud can lead to the sublimation of precipitating ice particles, and the INP of the sublimated precipitation may be transported back to the cloud (Savre et al., 2015, Solomon et al., 2015, 2014). The large scale advection is not only relevant for providing the cloud with a source of humidity, but the synoptic situation can also alter the thermodynamic conditions (e.g. Kalesse et al., 2016b, Shupe et al., 2013). However, although the phase-partitioning of the cloud can shift due to forcings, the remarkable resilience is a characteristic feature of the low-level clouds in the Arctic. Eventually, the MPC might fully glaciate and dissipate, as the ice production ceases in the absence of supercooled liquid. The MPC might also turn into a single phase liquid or ice cloud.

The central role of low-level MPCs in the Arctic climate system stems from the multiple ways the clouds interact with their environment. The cloud modifies the boundary layer where it resides by modifying radiative fluxes, generating turbulence, and vertically redistributing moisture. Furthermore, clouds control precipitation, and thereby indirectly influence further properties of the climate system such as snow cover and surface albedo. Hence, clouds are not relevant only for the cloud feedback, but also modulate the surface albedo, lapse rate and water vapor feedbacks (Crook et al., 2011, Sledd and L'Ecuyer, 2019, Stapf et al., 2019). Understanding the emerging properties of the coupled cloud-atmosphere-sea/land surface system is challenging. For example, decrease in sea-ice has been linked to anomalously low cloud cover (Kay et al., 2008), while on the other hand reduced sea-ice is thought to increase cloud fraction (Kay and Gettelman, 2009, Liu et al., 2012), at least in some seasons (Morrison, 2019).

Despite the progress made in the last decade (Zelinka et al., 2017), state of the art climate models underestimate the occurrence of Arctic low-level clouds (Vignesh et al., 2020). Particularly an issue for estimating the cloud radiative effect and the study of feedback processes, climate models struggle with the partitioning between supercooled liquid and ice (Cesana et al., 2015, McCoy et al., 2016). These issues, however, might be related. Engström et al. (2014) report an improvement in model performance after modifying the speed of glaciation, e.g. the rate at which supercooled liquid is converted to ice. English et al. (2014) reduced the cloud cover and cloud liquid bias by modifying the ice nucleation scheme. McIlhattan et al. (2017) found an overestimation of precipitation in climate models, which was attributed to microphysical processes controlling the liquid-to-ice formation in MPC. These studies suggest that too rapid glaciation, leading to the removal of the cloud through precipitation, might be responsible for the underestimated low-cloud fraction in climate models. However, Kretzschmar et al. (2019) report that changing the glaciation speed alone was not sufficient to remove bias in low cloud fraction or cloud phase in the climate model in question, but room for improvement is left in the interaction between clouds and the local boundary layer. Specifically, Taylor et al. (2019) compared a range of climate models and found a large disagreement in cloud amount under stable conditions in the lower troposphere. Studies applying highly resolved models by Loewe et al. (2017), Ovchinnikov et al. (2014), and others, further confirm the impact of microphysical processes on the life cycle of low-level mixed-phase clouds. Recent studies also highlight the sensitivity of cloud radiative forcing and cloud feedback to mixed-phase microphysics (Bodas-Salcedo et al., 2019, Tan and Storelvmo, 2019). Improvements in the process-level understanding of microphysical processes and their implications to the MPC lifecycle are needed to improve the description of low-level mixed-phase clouds in climate models (Kay et al., 2016, Klein et al., 2009, McCoy et al., 2016).

2.3 Ny-Ålesund and the Svalbard region

The Svalbard archipelago, where the observations utilized in this work were carried out, lies in the warmest part of the Arctic. Furthermore, the region is experiencing some of the most rapid seasonal warming on the globe (Fig. 1, Dahlke and Maturilli, 2017). Across the Arctic, the strongest increase in surface air temperature is found in winter, when depending on the data set and time period evaluated the strongest increase in temperature are found on the eastern Arctic Ocean, northern Atlantic, the Greenland, Barents or Kara seas (Hansen et al., 2010, Serreze and Barry, 2011). The North Atlantic is also a region with large mean poleward heat and moisture transport, and a large variation in this transport (Oshima et al., 2004, Woods et al., 2013). Intrusions of warm and moist air from lower latitudes and the transport of cold dry Arctic airmasses southwards are associated with air mass transformations where boundary layer clouds also play a role (Pithan et al., 2018). The increasing temperature at Svalbard has been linked with increased heat transport from mid-latitudes and increasing downwelling longwave radiation (Dahlke and Maturilli, 2017, Maturilli et al., 2015). Rinke et al. (2019) and Maturilli and Kayser (2017) report also an increase in humidity over Svalbard in the recent decades. Ny-Ålesund is therefore well situated for observing the changing climate in the Arctic, and a necessary addition to the sparse cloud radar network (Fig. 1).

Locally, Svalbard exhibits large variations in surface properties (glaciers, seasonal sea-ice and snow cover) as well as orography. Ny-Ålesund is located on the south side of Kongsfjorden on the west coast of Spitzbergen, the largest island on the Svalbard archipelago. In the recent years, including the entire time period considered in this work, the sea has remained ice-free at the west coast of Svalbard throughout the year. The area around Ny–Ålesund exhibits a typical tundra system, and the highest mountains around Kongsfjorden reach to 800 m. Above the mountaintops in the free-troposphere westerly winds prevail, but near the surface the wind is channeled along the fjord and the predominant wind direction is from southeast (Beine et al., 2001, Jocher et al., 2012, Maturilli and Kayser, 2017). Previous studies have found the local boundary layer to be shallow and strongly affected by the orography (Beine et al., 2001, Chang et al., 2017, Dekhtyareva et al., 2018, Kayser et al., 2017). Mioche et al. (2015) find less MPCs over the islands than over the surrounding sea during winter and spring, while during summer and autumn the differences are small, indicating that the islands modify the local boundary layer and the associated clouds. Over Antarctica, Scott and Lubin (2016) found that orographic lifting of marine air is likely causing thick MPCs with high ice water content and Grazioli et al. (2017) showed reduction in snowfall due to katabatic winds, hinting at possible mechanisms that might also occur at Ny-Ålesund.

Prior to the installation of the cloud radar, ceilometers were already operated at AWIPEV (Maturilli and Ebell, 2018). The analysis of ceilometer observations by Shupe et al. (2011) and Maturilli and Ebell (2018) showed that monthly cloud occurrence fraction varied between 50% and 80% being highest in summer and early autumn. The monthly median of the lowest cloud base height was found to vary between 500 and 1400 m, and the cloud base height is on average lower in summer than in winter. The studies also agree on a large inter-annual variability. In addition, ship-based and aircraft campaigns have taken place in the region. Recently, Mioche et al. (2017) combined observations from four different aircraft campaigns over the Greenland and Norwegian seas and evaluated the differences in microphysical properties of MPCs associated with different airmass characteristics. They found that warm southerly airmasses had a higher LWC and N_d compared to the warm northerly airmasses that had the smallest N_d and the cold airmasses with the lowest LWC. For the ice phase, the cold airmasses were found to have the highest N_i and IWC. Although the statistics presented by Mioche et al. (2017) only cover a handful of cloud cases (the analyzed data was collected on 18 days, to be precise), their study points towards the need to consider the influence of airmass properties and large scale advection on MPCs in the Svalbard region.

Following the installation of the cloud radar at AWIPEV in 2016, a more detailed view of clouds above Ny-Ålesund became available. Nomokonova et al. (2019) report the first year of these observations, during which clouds were present over 80% of the observed time. They found low clouds to dominate, in agreement with previous studies and observations reported from other sites (Shupe, 2011). Hydrometeors occurred most frequently in the first 2 km, with a maximum frequency of occurrence at 660 m. Liquid was detected in all seasons, with the monthly frequency of occurrence ranging from 70–80% in summer and autumn to the minimum of 36% in winter. From single cloud layers, mixed-phase clouds (defined as clouds with ice and liquid occurring at any height of the cloud) were most common. The MPCs were also found to have a higher LWP than liquid-only clouds. Following the availability of the cloud radar data and products derived from it, the radar measurements have since been used for the study of cloud radiative effects (Ebell et al., 2020), the impact on water vapor anomalies on cloud properties (Nomokonova et al., 2020), ice crystal seeding (Vassel et al., 2019), and for evaluating high-resolution model performance (Schemann and Ebell, 2020). This thesis, as mentioned in Sect. 1, presents the first work dedicated on low-level MPCs utilizing the long-term measurements provided by the comprehensive set of remote sensing instrumentation operated at AWIPEV.

3 Objectives

This dissertation addresses observational gaps in measuring Arctic low-level mixed-phase clouds in two ways. First, observations of low-level MPCs in a fjord environment in the warmest region of the Arctic are presented, and the influence of large scale and local forcings on cloud properties is analyzed. Second, the potential of cloud radar Doppler spectrum skewness for providing insights to microphysical processes in mixed-phase cloud volumes is investigated. The two topics are tackled in the two scientific studies of the thesis, introduced below.

Scientific Study I. Characterization of low-level mixed-phase clouds at Ny-Ålesund

Previous studies have shown that both the large scale advection of airmasses and the interaction with the local boundary layer and underlying surface can modify the low-level MPCs. The first study focuses on the characterization of persistent low-level MPCs (P-MPC) in the context of the complex features of the measurement site. The specific questions addressed are:

- What is the frequency of occurrence of P-MPCs above Ny-Ålesund, and what are their typical properties (altitude, liquid and ice water path)? Do these parameters exhibit seasonal variation?

- How can the thermodynamical coupling of the P-MPC with the surface be evaluated from the continuous observations? How often are P-MPCs above Ny-Ålesund found to be coupled, and does thermodynamical coupling of the cloud with the surface influence the amount of liquid and ice in the cloud?
- How are the large-scale and local wind conditions in the fjord influencing the occurrence and properties of P-MPCs? How does the location of the measurement site on a mountainous coastline impact the observed P-MPCs?

The objective is to provide a foundation for the investigation of P-MPCs at the AWIPEV site. Based on the characterization it is possible to draw first conclusions of the differences and similarities of the P-MPC observed at Ny-Ålesund and elsewhere in the Arctic, and the representativeness of the observations carried out at AWIPEV. Furthermore, the analysis provides insights to the relative importance of local scale phenomena and large scale forcing on the low-level MPCs above Ny-Ålesund.

Scientific Study II. Observational signatures of mixed-phase cloud structures revealed by radar Doppler spectrum skewness

While the large scale advection and local boundary layer processes are important, the microphysical processes also play an essential role in determining the evolution of low-level MPCs. However, evaluating microphysical parameterizations in numerical models is challenging when only limited observational constrains are available. Cloud radars are one of the few techniques providing vertically resolved measurements of both supercooled liquid and ice. The skewness of the Doppler spectrum has been successfully used to study processes in warm clouds and to retrieve microphysical properties of ice clouds (Kollias et al., 2011b, Maahn and Löhnert, 2017), but in the mixed-phase regime Doppler spectrum skewness has barely been utilized. The second study investigates the potential of the Doppler spectrum skewness for gaining insights in the P-MPC, and specifically considers:

- In which conditions can skewness provide additional information about the microphysical properties in a mixed-phase volume?
- What defines the skewness of the Doppler spectrum of a vertically pointing cloud radar in a mixed-phase cloud?
- Which microphysical processes leave hints in the Doppler spectra that could be studied with the help of the skewness of the spectrum?

The objective is to identify features in the observed skewness profiles that can be related to the microphysical properties of a mixed-phase cloud volume. Such features could be used in the future for studying microphysical processes in the MPCs, for developing observational constrains for model parameterizations, or as part of a retrieval for microphysical properties. However, a prerequisite for any of this is an understanding of the parameters that define the skewness profile.

The thesis is organized as follows. Chapter II introduces the observations and auxiliary data utilized in both scientific studies. Chapters III and IV comprise the Scientific Study I and

II, respectively. These chapters also include more specific background information relevant for each study, such as the description of the local wind climatology in Kongsfjorden in Study I, and method development required for the specific analysis carried out, such as the noise reduction in the skewness data in Study II. The outcome of the first study has been published by Gierens et al. (2020), and the publication is included here as part of the thesis. In the end, Chapter V provides a summary of the main findings and draws conclusions from the scientific studies, and gives an outlook.

II Tools and Data

This chapter introduces the data that forms the basis of the scientific work carried out in the thesis. First, the instruments and measured parameters are presented in Sect. 4. Because of the central role of the cloud radar, also the main aspects of the governing theory and operating principles, as well as the data processing carried out, are shortly presented. For the other instrumentation, only a brief description focusing on the main aspects and measurement details relevant for this work is given. Following the introduction of the measurements, the synergistic approach used for combining the different remote sensing observations, i.e. the Cloudnet algorithm, is presented in Sect. 5. The microphysical and thermodynamical retrievals used are covered in Sect. 6, and lastly, the auxiliary data product derived from reanalysis in Sect. 7.

4 Measurements

All observations utilized are collected at the French-German Arctic Research Base AWIPEV, operated in collaboration by the German Alfred Wegener Institute for Polar and Marine Research (AWI) and the French Polar Institute Paul Emile Victor (IPEV). AWIPEV is located in the Ny-Ålesund research village (78.9°N, 11.9°E), on the west coast of Spitzbergen. The station operates a wide range of instruments for disciplines ranging from biology to astronomy. The measurements utilized in this work are shown in Fig. 4, and include: two 94 GHz cloud radars (Sect. 4.1), a microwave radiometer (Sect. 4.2), a ceilometer (Sect. 4.3), and surface meteorological measurements and radiosondes (Sect. 4.4).

4.1 Cloud radars

The cornerstone of the thesis is the frequency modulated continuous wave (FMCW) 94 GHz Doppler cloud radar. Two different cloud radars of the University of Cologne have been deployed at AWIPEV since 2016. First, the Jülich Observatory for Cloud Evolution (JOYCE) Radar-94 GHz (JOYRAD-94) was installed at the AWIPEV station from 8 June 2016 to 26 July 2017, and again from 12 June 2019 onwards. In between, the Microwave Radar/Radiometer for Arctic Clouds (MiRAC) was measuring at AWIPEV from 27 July 2017 to 8 October 2018. Only the active component of MiRAC, e.g. the cloud radar referred to as MiRAC-A, is used in this work. Fig. 4a and b show JOYRAD-94 and MiRAC-A installed at the roof of the AWIPEV observatory, where they were operated in a zenith pointing mode. Both instruments are a RPG-FMCW-94-SP -type radar, described in detail by Küchler et al. (2017). Key technical specifications are given in Table 1. MiRAC-A was constructed so that it can be mounted on an aircraft and it therefore has smaller antennas (Mech et al., 2019). Consequently, the sensitivity of the radar is reduced by 6 dB compared to JOYRAD-94. The instruments also include a 89 GHz passive channel, but

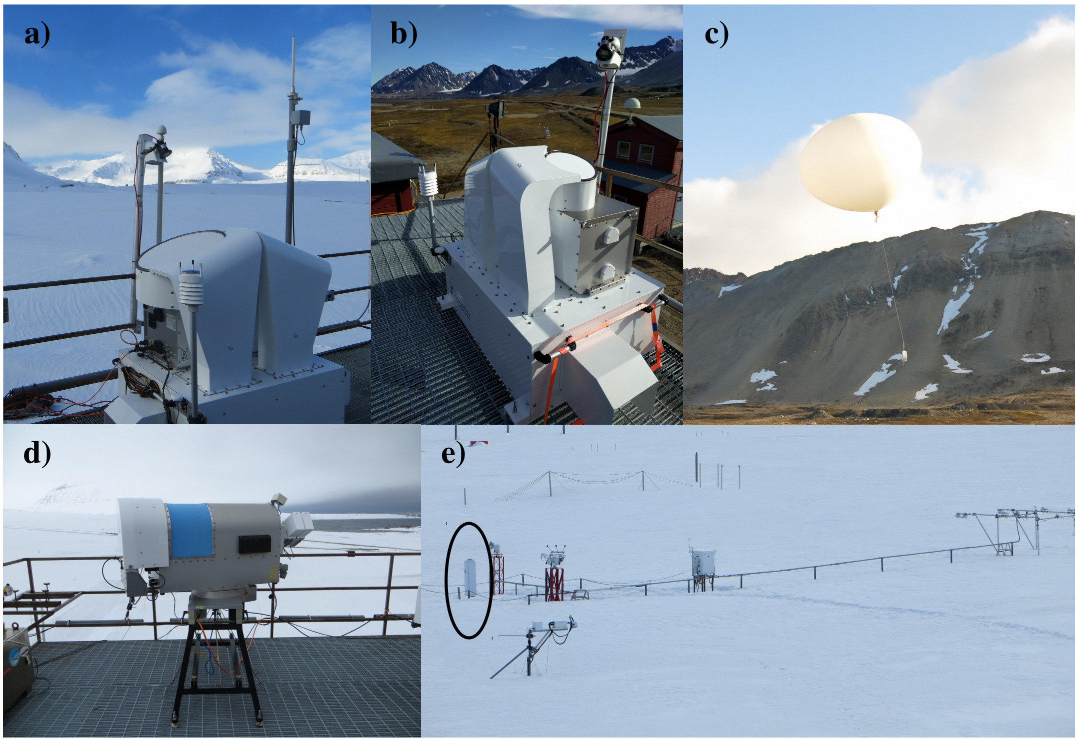

Figure 4: Instruments used (see text for details): a) JOYRAD-94, b) MiRAC-A, c) radiosounding, d) microwave radiometer HATPRO, e) BSRN measurement field with the ceilometer indicated by the black ellipse. Photos provided by T. Nomokonova (b), B. Pospichal (d), and K. Ebell (a,c,e).

Table 1: Technical details of the two cloud radars utilized, JOYRAD-94 and MiRAC-A.

	JOYRAD-94	MiRAC-A
Center Frequency (wavelength)	94 GHz (3.2 mm)	94 GHz (3.2 mm)
Transmitted power	1.5 W	1.2 W
Antenna type	Two antennas with 500 mm aperture	Two antennas with 250 mm aperture
Antenna separation	568 mm	298 mm
Half power beam width	0.53°	0.85°
Antenna Gain	51.5 dB	47 dB
Reference	Küchler et al. (2017)	Mech et al. (2019)
Installation at AWIPEV	8 June 2016 – 26 July 2017 12 June 2019 – ongoing	7 July 2017 – 8 October 2018

due to technical issues degrading the quality of the measurement this data was not utilized in this work. Here, the radar theory and operating principle of the FMCW radar are briefly introduced. After that, the specific measurement configurations used at AWIPEV are presented, followed by a description of the data processing steps which have been also carried out within this thesis.

Radar theory

A radar is a system that transmits a radio wave and measures the signal that is returned to its antenna due to scattering by objects in the atmosphere. The radar equation gives the power returning to the receiving antenna (P_R) depending on the range (r), scattering properties of the target, and the transmitted power (P_T) (Doviak and Zrnić, 2006). Assuming that the electromagnetic wave with the wavelength λ propagates without loss due to hydrometeors or atmospheric gases, the general form of the radar equation for a point target is

$$\frac{P_R}{P_T} = \frac{G_T^2 \lambda^2 f^4}{(4\pi)^3 r^4} \sigma_B \quad . \tag{1}$$

Here σ_B is the backscattering cross section and contains all details of the scattering process. f^2 is the normalized power density pattern that describes the power density at a given distance from the beam axis. It is also assumed that the transmitter's antenna gain (G_T) equals the receiver's antenna gain. For a volume scattering target, such as a cloud, the power scattered back towards the radar depends on the scattering cross sections of all hydrometeors in the volume, given by

$$\eta = \int_0^\infty N(D) \sigma_B(D) dD \tag{2}$$

where η is called the radar reflectivity, $N(D)$ is the particle size distribution and D stands for diameter. The backscattering cross section for liquid droplets much smaller than the wavelength (i.e. scattering in the Rayleigh regime) is

$$\sigma_B(D) = \frac{\pi^5 |\kappa_w|^2}{\lambda^4} D^6 \tag{3}$$

where κ_w is the dielectric factor for water. σ_B depends not only on the particle diameter and phase, but also on the shape and density, and is therefore difficult to estimate for ice particles (DeVoe, 1964, 1965). Using the soft sphere approach the backscattering cross section for ice particles have been found to be proportional to D^4 (Field et al., 2005). Inserting Eq. 3 into Eq. 2 results in

$$\eta = \frac{\pi^5 |\kappa_w|^2}{\lambda^4} Z \tag{4}$$

where Z is the radar reflectivity factor defined as

$$Z \equiv \int_0^\infty N(D) D^6 dD \quad . \tag{5}$$

As Eq. 4 is based on Rayleigh scattering off liquid droplets it is not as such applicable to all hydrometeors. Hence, in radar meteorology the equivalent radar reflectivity factor (Z_e)

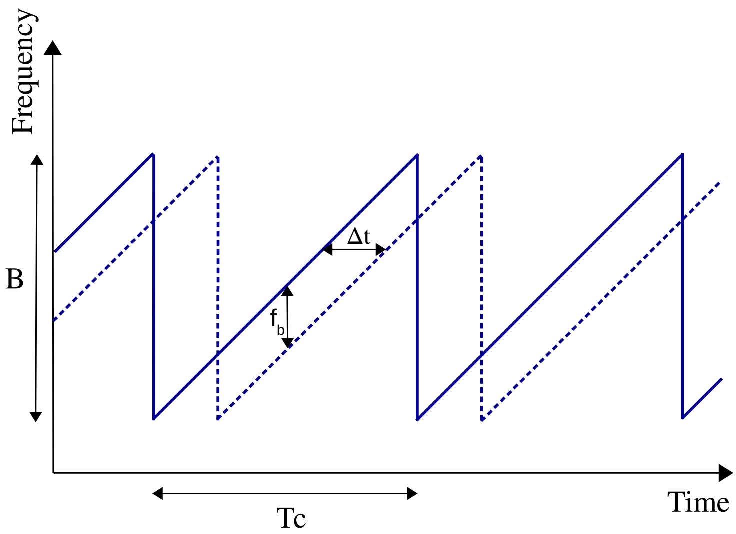

Figure 5: The sawtooth chirp. The solid line illustrates the transmitted signal, and the dashed line the returned signal which is a delayed version of the transmitted signal. See text for explanation of symbols.

is used instead, defined as

$$Z_e = \frac{\lambda^4}{\pi^5 |\kappa_w|^2}\eta \quad . \tag{6}$$

Z_e is defined so that for rain in the Rayleigh scattering regime $Z_e = Z$. Z_e has units of $\mathrm{mm^6 m^{-3}}$, but is usually given as dBz defined as decibels relative to the $1\,\mathrm{mm^6 m^{-3}}$ reference level (Smith, 2010). For simplicity, Z_e is often referred to as simply 'reflectivity'. Using the definition of Z_e for a Gaussian beam results in the radar equation for a cloud volume:

$$\frac{P_R}{P_T} = \frac{G_T^2 \theta^2 \pi^3 |\kappa_w|^2}{2^9 \lambda^2} \frac{\delta r}{r^2} Z_e = C_R \frac{\delta r}{r^2} Z_e \tag{7}$$

where δr is the range resolution and θ is the antenna's half power beam width. C_R is the radar constant summarizing all the radar specific parameters and the dielectric properties of the medium which are assumed to be constant. Radiometer Physics GmbH, the manufacturer of JOYRAD-94 and MiRAC-A, reports that the beam pattern of the radars overlaps with a Gaussian pattern to 95% (Rose, 2015). For $|\kappa_w|$ the value of 0.86 is used, which corresponds to the $|\kappa_w|$ of pure liquid water at 90 GHz. An important simplification in Eq. 7 is the omission of the attenuation due to hydrometeors and atmospheric gases. At 94 GHz the attenuation due to dry gases, water vapor, and liquid hydrometeors is not negligible (Lhermitte, 1990). Furthermore, the D^6 (D^4) dependency of Z_e for droplets (ice particles) is only valid for the Rayleigh scattering regime, i.e. when $D << \lambda$. The radars used in this study are measuring at a wavelength of 3.19 mm, so that for larger ice particles Mie scattering becomes relevant. However, for cloud droplets, drizzle, and small ice particles Rayleigh scattering can be assumed.

Operating principle of the FMCW Doppler radar

As suggested by its name, a FMCW radar transmits a continuous wave whose frequency is modulated (Ulaby and Long, 2014). The RPG-FMCW-94-SP radars used in this study are linear FMCW radars that use a sawtooth frequency pattern, referred to as a chirp.

Fig. 5 illustrates a transmitted chirp and the returned signal for a stationary point target. The time (t) for the signal to travel to the target and back is

$$\Delta t = \frac{2r}{c} \tag{8}$$

where c is the speed of light. In the radar the transmitted and received signal are mixed, which generates the intermediate frequency signal, also referred to as the beat signal (Meta, 2006). The frequency difference between the transmitted and received signal f_B is given by the frequency of the beat signal. From Fig. 5 it can be seen that f_B is related to Δt by

$$f_B = \frac{B}{T_c} \Delta t \tag{9}$$

where B is the chirp bandwidth and T_c is the chirp duration. Thus, by measuring f_B the range of the target can be obtained by combining Eqs. 8 and 9. Without going into detail, it is noted that f_B can only be obtained with a finite resolution of δf, and the range resolution δr is directly proportional to δf.

When the target is moving, the frequency is shifted due to the Doppler effect by

$$f_D = \frac{2V_D}{\lambda} \tag{10}$$

where V_D is the velocity component in the direction of the beam (i.e. Doppler velocity) and λ is the wavelength of the transmitted signal. Repeating the chirp N_{chirp} times, a time series of the beat signal is obtained. Applying a Fourier transform to this time series provides the frequency shifts due to the moving targets. The discrimination of frequency shifts due to range and Doppler velocity is based on the assumption that the latter is smaller. Thus, the returned power can be mapped to a (discrete) range and Doppler velocity space. Further making use of Eq. 7 results in the equivalent radar reflectivity factor at each range gate as a function of Doppler velocity, i.e. the radar Doppler spectrum. The largest f_D that can be detected is restricted by the chirp repetition time (e.g. T_c), which in turn is related to the bandwidth and the discrete frequency steps that form the chirp. The maximum unambiguous Doppler velocity (i.e. Nyquist velocity V_{nyq}) which can be obtained is therefore dictated by the chosen sampling strategy. If the Doppler velocity of the target exceeds V_{nyq} the signal appears in the wrong range-Doppler velocity-bin, which is referred to as aliasing.

The main advantages of the FMCW radars compared to traditional pulsed radars is the higher range resolution that can be obtained and the lower transmission power that is required to achieve similar sensitivities. The higher range resolution allows for more detailed information to be gained about the hydrometeor populations, especially in regions of strong vertical gradients. The lower transmission power means that no high-voltage components are required in the radar apparatus, leading to lower production costs and power consumption. On the other hand, the signal attenuates quicker, which however is not a serious issue for the low-level MPCs investigated in this study.

Measurements carried out at AWIPEV

As can be seen from Eq. 1, the power of the returned signal is decreasing with range proportional to r^4. To compensate for the sensitivity loss at higher altitudes while still

Table 2: Key parameters of the sampling strategy used for the first JOYRAD-94 installation (June 2016 – July 2017). δr = range resolution, δV_D = Doppler velocity resolution, V_{nyq} = Nyquist velocity. 'Total time' gives the time required to carry out the sampling, and the time needed for measuring a complete profile is the sum of the column, i.e. 2.4 s.

Range	δr (m)	δV_D ($\mathrm{m\,s^{-1}}$)	V_{nyq} ($\mathrm{m\,s^{-1}}$)	Total time (s)
100–400 m	4.0	0.025	6.2	0.53
400–1200 m	5.3	0.017	4.2	0.59
1200–3000 m	6.7	0.021	2.5	0.731
3000–12 000 m	17	0.021	2.5	0.568

Table 3: As Table 2, but for MiRAC-A (July 2017 – October 2018) and the second JOYRAD-94 installation (June 2019 onwards). Time required for measuring the complete profile was 2.0 s.

Range	δr (m)	δV_D ($\mathrm{m\,s^{-1}}$)	V_{nyq} ($\mathrm{m\,s^{-1}}$)	Total time (s)
100–400 m	3.2	0.02	5.1	0.64
400–1200 m	7.5	0.02	5.1	0.48
1200–3000 m	9.7	0.013	3.2	0.503
3000–12 000 m	23.8	0.025	3.2	0.377

making use of the instruments capability to provide a high vertical resolution, the RPG-FMCW-94-SP gives the possibility to measure different atmospheric layers using different chirps executed consecutively (Küchler et al., 2017). For the measurements carried out at AWIPEV four chirps where used, three for the lowest 3 km and one for the range from 3 to 10 km. Key parameters for the sampling strategies chosen for the first JOYRAD-94 installation (June 2016 – July 2017), the MiRAC-A installation (July 2017 – October 2018) and the second JOYRAD-94 installation (June 2019 onwards) are given in Tables 2 and 3. The radars were continuously operated with the given specifications except for short periods used for testing different settings. Furthermore, to limit the amount of data collected, data logging only took place when high enough signal-to-noise ratio was obtained.

Data processing

Following the principles described above, the radars provide the spectral Z_e, i.e. Z_e as a function of Doppler velocity ($Z_e(V_D)$). To assure the quality of the data, further data processing was carried out on routine basis. Known artifacts were removed or corrected for. The most substantial part of the processing of the data is the dealiasing algorithm applied. Küchler et al. (2017) introduced a dealiasing procedure for the JOYRAD-94 that made use of a co-located radar whose Doppler spectra was assumed non-aliased. The algorithm was further extended to a stand-alone version in Küchler (2019). As part of this work, the data processing program was applied to the JOYRAD-94 and MiRAC-A data collected at AWIPEV and the development of the software was continued to follow the progress of the instruments software development and to allow processing data from new radars with additional capabilities (specifically the polarimetric RPG-FMCW-94-DP). The resulting dataset, as well as the raw binary data logged by the instrument, are stored at the computing center of the University of Cologne for 10 years. Study II focuses on the analysis of the Doppler spectrum, and the quality of the spectral data is therefore of great importance.

When the Doppler velocity of the target exceeds the Nyquist velocity, in a FMCW radar the signal appears in the adjacent range gate (Maahn and Kollias, 2012). The spectra can be restored by concatenating the spectral data with that of the adjacent range gate, but additional criteria are now required to determine the correct ranging of the spectra. In the algorithm applied here, first the occurrence of aliasing is detected by evaluating if a significant signal above the noise floor is found in the first and last 5% of the Doppler spectral bins. If any aliasing is identified, the entire cloud layer is dealiased. First, the spectra from two range gates below and above are concatenated. At cloud top, it is assumed that the measured mean Doppler velocity is non-aliased, and moving step-wise down from cloud top the spectra are assigned to (presumably correct) range gates. This method fails when strong up- or downdrafts are present at cloud top, or if too strong vertical gradients are present in the cloud layer. To mitigate these issues, the time series of the dealiased mean Doppler velocity is checked to find and correct profiles that differ too much from the neighboring profiles.

The spectral moments of $Z_e(V_D)$ were obtained as follows. The mean and peak noise levels of the Doppler spectra were determined following Hildebrand and Sekhon (1974). A minimum of three consecutive bins above peak noise level were required for the signal to be considered significant, but no limitations on how many significant peaks could be detected within one spectra was applied. The zeroth moment gives the reflectivity, and is simply the integral of $Z_e(V_D)$:

$$Z_e = \sum Z_e(V_D)\delta V_D \quad . \tag{11}$$

The first moment, i.e. the mean Doppler velocity (V_m),

$$V_m = \frac{\sum Z_e(V_D)V_D}{Z_e} \tag{12}$$

represents the reflectivity weighted mean Doppler velocity of the scatterers in the radar volume. The second moment is the Doppler spectrum width σ

$$\sigma = \sqrt{\frac{\sum Z_e(V_D)(V_D - V_m)^2}{Z_e}} \quad , \tag{13}$$

which is related to the variance of the Doppler velocity of the scatters. Different fall velocities of co-existing hydrometeors, turbulence, and wind shear contribute to the broadening of the Doppler spectra (Doviak and Zrnić, 2006). The third moment, i.e. the skewness of the Doppler spectrum (S_k),

$$S_k = \frac{\sum Z_e(V_D)(V_D - V_m)^3}{Z_e\sigma^3} \tag{14}$$

describes the symmetry of the Doppler spectrum compared to a Gaussian shape. How S_k can be related to the microphysical parameters in a mixed-phase cloud is the topic of Study II.

4.2 Microwave radiometer

The humidity and temperature profiler HATPRO (Rose et al., 2005) is a microwave radiometer (MWR) used to retrieve column integrals of liquid and water vapor and coarse temperature and humidity profiles. HATPRO measures the atmospheric brightness temperature (T_B) at 14 channels in the K-band (22.24–31.40 GHz) and V-band (51.26–58 GHz) with a temporal resolution of 1–2 s. HATPRO has been measuring at AWIPEV since March 2011 (Nomokonova et al., 2019). Since October 2016 a scanning strategy is applied that interrupts the mainly zenith pointing measurement at regular intervals. Every half an hour a 360° azimuth scan is performed at an elevation angle of 30°, followed by an elevation scan consisting of six elevation angles (5.4°, 10.2°, 19.2°, 30°, 42°, and 90°) which is repeated after 15 min. To provide accurate measurements of brightness temperatures, an absolute calibration is carried out approximately biannually. The measurement suffers from wetness on the radome, and instances with liquid precipitation are therefore flagged and removed from the analysis. This work makes use of the liquid water path and integrated water vapor as well as the temperature profile in the lower troposphere, obtained by the retrievals introduced in Sections 6.1 and 6.3, respectively.

4.3 Ceilometer

A ceilometer is an active remote sensing instrument using lidar technology, emitting a short laser pulse and detecting the returning signal (Emeis, 2011). Cloud and rain droplets scatter the emitted beam efficiently, which provides a strong signal but also causes a rapid attenuation in the liquid layer. Since August 2011 a Vaisala CL51 ceilometer is operated at AWIPEV (Maturilli and Ebell, 2018). The instrument measures at 905 nm and provides backscatter profiles with a temporal resolution of 12–20 s and vertical resolution of 10 m for a range up to 13 km. The Vaisala CL51 uses a rather strong pulse for being a ceilometer, which allows for a larger range and makes it more sensitive to high cirrus clouds but also means it is not eye-safe like most other ceilometers (Vaisala, 2010). The measured backscatter is calibrated following O'Connor et al. (2004). In this work the attenuated backscatter (β') profiles are used as part of the Cloudnet algorithm (Sect. 5) and for introducing case studies analyzed in Study II.

4.4 Auxiliary measurements

Standard surface meteorological observations are carried out as part of the Baseline Surface Radiation Network (BSRN). Surface pressure is measured with a Paroscientific, Inc. 6000-16B and the 10 m wind speed and direction with a Thies Clima Combined Wind Sensor Classic. Ambient temperature at 2 and 10 m are measured with Thies Clima PT100. The obtained data are quality controlled (Maturilli et al., 2013) and provided with 1 min temporal resolution (Maturilli, 2020).

Radiosondes are launched routinely at AWIPEV every day at 11:00 UTC, with additional launches carried out during campaigns (Maturilli and Kayser, 2017). From the beginning of the time period covered in this work (June 2016) until 2 May 2017 all sondes were of the type Vaisala RS92, and the data was processed using the GRUAN version 2 data processing (Maturilli and Kayser, 2016, Sommer et al., 2016). Since 2 May 2017 the sondes where of type Vaisala RS41.

5 Instrument synergy: Cloudnet

The Cloudnet algorithm combines reflectivity (Z_e) and mean Doppler velocity (V_m) from the cloud radar, LWP from the HATPRO, and attenuated backscatter (β') from the ceilometer, with thermodynamical profiles from a numerical weather prediction (NWP) model to provide best estimates of cloud properties in an unified framework (Illingworth et al., 2007). The NWP models used for the Cloudnet application at Ny-Ålesund are the Global Data Assimilation System 1 (GDAS1, Kanamitsu, 1989) used until the end of January 2017, and the operational version of the ICON (ICOsahedral Non-hydrostatic) NWP model (Zängl et al., 2015) used from February 2018 onwards. In the Cloudnet program the observations are averaged to a common 20 m vertical and 30 s temporal resolution, known instrumental artifacts are removed, correction procedures are carried out and suspicious data is flagged. Specifically, for Z_e a correction for liquid attenuation is applied. Cloudnet aims to provide best estimates of the measured parameters, and also provides estimates of the associated uncertainties.

Cloudnet performs a classification of the lidar and radar echoes following Hogan and O'Connor (2004). In this work the target classification is of key importance, as the identification and sampling of the persistent low-level MPCs analyzed in both scientific studies is based on the classification. Each pixel is classified as either containing hydrometeors, aerosols, insects, or clear sky. An example of the Cloudnet target classification product is given in Fig. 2 of the publication included in Sect. 8. The base of a liquid layer is determined from the β'-profile. First, the presence of a liquid layer is identified based on β' exceeding a set threshold, which is followed by a relatively rapid decrease in β'. Second, the precise altitude of the liquid base is determined based on the β'-gradient. The top of the liquid layer is defined as the last bin with non-zero β' in the case that this is found within few hundred meters above the liquid base, otherwise the β'-gradient is used again. If radar signal is found above the β'-defined liquid top, the liquid top is moved upwards to the radar defined cloud top. However, at sub-zero temperatures the radar signal is only considered up to 300 m above the β'-defined cloud top in order to avoid misclassifying ice falling from above as liquid. Furthermore, no liquid at temperatures below -40 °C is allowed. The identification of ice is somewhat simpler. All pixels with measured radar Z_e and wet-bulb temperature below zero are assumed to be ice, unless the radar echo is identified within a liquid layer where the reflectivity is higher at 20% below cloud top than at 20% above cloud base, in which case the cloud is considered liquid-only. Furthermore, ceilometer echo above 6 km is also classified as ice. Note that all precipitation at sub-zero temperatures is assumed to be ice.

The temperature information required in the classification outlined above is provided by the NWP data. Nomokonova et al. (2019) evaluated the temperature output of the NWP models used in Cloudnet by comparison with radiosonde profiles, and found the standard deviation between the model and measured temperature not to exceed 1.7 K. Hence, there might be uncertainties in the identification of ice at temperatures close to zero. However, the main limitations of the Cloudnet target classification in the context of this work are 1) the limited possibility to detect several liquid layers in an atmospheric column due to the attenuation of the ceilometer signal, and 2) the lack of a detection scheme for drizzle or rain at temperatures below zero.

In addition to the target classification informing the selection of clouds for the scientific studies, the classification is also used to determine when the ice water content retrieval

(Sect. 6.2) is to be applied. Furthermore, the liquid base height identified by Cloudnet is used instead of the product provided by the instrument manufacturer. Also the cloud top height required in Study II is given by Cloudnet.

6 Microphysical and thermodynamical retrievals

6.1 Liquid water path and integrated water vapor

The liquid water path (LWP) and integrated water vapor (IWV) were retrieved from the T_B of the K-band channels of the HATPRO (Sect. 4.2) following the multivariate linear regression approach (Crewell and Löhnert, 2003, Löhnert and Crewell, 2003). A detailed description of the procedure to obtain site-specific regression coefficients and the offset correction applied is provided by Nomokonova et al. (2019) and Nomokonova (2020). Nomokonova (2020) also evaluated the performance of the IWV retrieval specifically at Ny-Ålesund, and found a root mean square error (RMSE) of $0.56\,\mathrm{kg\,m^{-2}}$ between the IWV obtained from radiosondes and HATPRO. In previous studies, the uncertainty of the LWP retrieval has been estimated to be 20–25 $\mathrm{g\,m^{-2}}$ (Löhnert and Crewell, 2003).

LWP is used in this work to characterize the amount of supercooled liquid in the low-level MPC, and is therefore one of the key parameters analyzed. Because no information about the vertical distribution of liquid is available (beyond the liquid layers detected by Cloudnet, see Sect. 5), the LWP values are only used when no further cloud layer above the low-level cloud is detected to avoid attributing liquid of a mid-level cloud to the low-level cloud. Additionally, the IWV is used in Study I to provide context for the atmospheric conditions associated with different seasons and wind regimes. The retrievals are only applied on vertically pointing measurements, so that periodic gaps in the data occur during scanning (Sect. 4.2).

6.2 Ice and liquid water content

For estimating the ice water content (IWC), the retrieval developed by Hogan et al. (2006) was used. The IWC is related to the Z_e and temperature (T) at 94 GHz by

$$\log_{10}(IWC) = 0.000580 Z_e T + 0.0923 Z_e - 0.00706 T - 0.992 \quad . \tag{15}$$

The uncertainty in the retrieved IWC has been estimated to range from -50% to 100% (Heymsfield et al., 2008, Hogan et al., 2006). Nomokonova and Ebell (2019) provide an IWC dataset for Ny-Ålesund, where the IWC was calculated using the Z_e and T provided by Cloudnet. The retrieval is applied to all bins where Cloudnet identifies ice, and it is assumed that in mixed-phase bins the contribution of liquid to the reflectivity is negligible. These IWC data were used in this work to calculate the ice water path (IWP, i.e. the column integral of IWC) in Study I. Furthermore, the IWC retrieval is used in Study II to estimate the IWC related to specific Z_e.

For retrieving the liquid water content (LWC), the algorithm by Frisch et al. (1998) was used. The retrieval scales the measured LWP to the liquid layer using

$$LWC_i = \frac{LWP(Z_{e,i})^{1/2}}{\sum_{n=1}^{N_l} \delta r_n (Z_{e,n})^{1/2}} \tag{16}$$

where δr_i and $Z_{e,i}$ are the range resolution and reflectivity at range gate i and N_l is the total number of range gates in the cloud. The uncertainty of the LWP translate to uncertainties in the retrieved LWC. However, the main challenge in the context of this work is that the Z_e in a mixed-phase cloud is not exclusively associated with liquid, invalidating the assumptions of the retrieval. The LWC retrieval is therefore only used for a specific mixed-phase profile in Study II, for which the Z_e could be decomposed to the Z_e from supercooled liquid (Z_{liquid}) and ice (Z_{ice}).

6.3 Temperature profiling

The T_B measured by the V-band channels of the HATPRO (Sect. 4.2) were used for temperature profiling following the multivariate linear regression retrieval analogously to the LWP and IWV retrievals (Sect. 6.1, Löhnert and Crewell, 2003, Nomokonova et al., 2019). Crewell and Löhnert (2007) showed that combining brightness temperatures measured at varying elevation angles provides an increased accuracy in the temperature profile retrieved in the lower troposphere compared to zenith-only measurements. The temperature profiles used in this study were retrieved from the elevation scans performed 3–4 times per hour (Sect. 4.2). The retrieval was applied on a vertical grid with a resolution of 50 m near ground and decreasing with height (Crewell and Löhnert, 2007). Note, that this is not the vertical resolution of the measurement itself but the height levels for which the retrieval was applied. Nomokonova et al. (2019) showed that the uncertainties in the temperatures from the NWP models were larger in the lowest 2 km, which is the reason for using the temperature profiles retrieved from the HATPRO elevation scans in this work. However, the retrieval is not able to resolve the strong temperature gradient present at the top of most low-level MPCs. A comparison of temperature profiles retrieved from the HATPRO elevation scans and radiosondes including only profiles obtained when a persistent low-level MPC was identified above Ny-Ålesund revealed an RMSE up to 1.7 K in the lowest 2.5 km (not shown), which is comparable to the RMSE of the NWP models for all scenes in the same height region (Nomokonova et al., 2019). The temperature profiles obtained are used in Study I for detecting the thermodynamical coupling of the cloud with the surface and to provide context for the atmospheric conditions associated with different seasons and wind regimes.

Cloud top temperature

In both scientific studies the cloud top temperature is analyzed. Cloud top temperature was obtained by linearly interpolating the temperature profile from nearest vertical grid points and between adjacent profiles given that the time difference between the profiles did not exceed half an hour. In Study II, the temperature from the NWP model in the Cloudnet dataset is used to fill in for the HATPRO data for the cases when HATPRO data was not available.

7 Other data products

7.1 Circulation weather type

In order to evaluate the low-level MPCs in the context of the synoptic wind conditions in Study I, a circulation weather type (CWT) classification is used. The CWT following

Jenkinson and Collison (1977) was obtained from the ERA-Interim (Dee et al., 2011) reanalysis data using the cost733class software package (Philipp et al., 2014). 16 grid points centered around Ny-Ålesund are used, covering an area from 77.5° N to 80.5° N, and 9.75° E to 14.25° E (indicated in Fig. 1a of the publication included in Sect. 8). As a result, the flow on the 850 hPa level is classified as either W, NW, N, NE, E, SE, S, SW, cyclonic, or anticyclonic.

III | Characterization of low-level mixed-phase clouds at Ny-Ålesund

8 Low-level mixed-phase clouds in a complex Arctic environment

In this study, the persistent low-level mixed-phase clouds (P-MPC) observed above Ny-Ålesund are investigated in the context of the fjord environment. Long-term cloud radar observations in the high-Arctic are sparse (Fig. 1), and the measurements carried out at AWIPEV are a necessary addition to this network. However, analyzing cloud observations obtained at AWIPEV is challenged by the complexities associated with the measurement site, namely the orography and coastal location that give rise to meso-scale phenomena such as sea breeze and katabatic winds (Esau and Repina, 2012), large heterogeneities in surface properties, and the location of Svalbard on the North-Atlantic, which is one of the main pathways of heat and humidity from lower latitudes into the Arctic (Jakobson and Vihma, 2010). In this study, the occurrence and properties of P-MPC in different seasons and under different surface and regional free-tropospheric wind (represented by the CWT, Sect. 7.1) conditions are analyzed. Furthermore, the influence of the thermodynamical coupling state on cloud properties, and how coupling is related to the local wind in the fjord, are investigated. The parameters analyzed are the frequency of occurrence of the P-MPC, the height of the liquid layer, the liquid and ice water paths, and cloud top temperature. To carry out the analysis, first a criteria for the detection of P-MPC based on the Cloudnet target classification (Sect. 5) is developed. This P-MPC sampling criteria is further used in Study II. A new method to evaluate the thermodynamical coupling of the liquid layer with the surface was developed and evaluated using radiosonde profiles. The presented study is the first investigation focusing on low-level MPCs utilizing the extended remote sensing suite at AWIPEV, and provides a characterization of the P-MPCs in the complex fjord environment based on 2.5 years of observations. The insights gained provide a foundation for considering the local influences on low-level clouds in any future studies, and are a prerequisite for designing future research on interactions between the low-level MPC and the surface in the Kongsfjorden valley. The results also provide guidance to assess the representativeness of the low-level observations carried out at Ny-Ålesund.

The study has been published in

Gierens, R., Kneifel, S., Shupe, M. D., Ebell, K., Maturilli, M., and Löhnert, U. (2020). Low-level mixed-phase clouds in a complex Arctic environment. *Atmos. Chem. Phys.* 20 (6), 3459–3481. https://doi.org/10.5194/acp-20-3459-2020

The article was published by Copernicus Publications and is here reproduced under the Creative Commons Attribution License (CC BY 4.0). The first author carried out the analysis and writing for the manuscript in its entirety, and prepared all figures with the exception of Fig. 1b. For the contributions of other authors, see 'Author contributions' in the manuscript.

Atmos. Chem. Phys., 20, 3459–3481, 2020
https://doi.org/10.5194/acp-20-3459-2020

Atmospheric Chemistry and Physics
Open Access

Low-level mixed-phase clouds in a complex Arctic environment

Rosa Gierens[1], Stefan Kneifel[1], Matthew D. Shupe[2,3], Kerstin Ebell[1], Marion Maturilli[4], and Ulrich Löhnert[1]

[1]Institute for Geophysics and Meteorology, University of Cologne, Cologne, Germany
[2]Cooperative Institute for the Research in Environmental Sciences, University of Colorado Boulder, Boulder, Colorado, USA
[3]Earth System Research Laboratory, National Oceanic and Atmospheric Administration, Boulder, Colorado, USA
[4]Alfred Wegener Institute Helmholtz Centre for Polar and Marine Research, Potsdam, Germany

Correspondence: Rosa Gierens (rgierens@uni-koeln.de)

Received: 27 June 2019 – Discussion started: 8 July 2019
Revised: 2 January 2020 – Accepted: 10 February 2020 – Published: 24 March 2020

Abstract. Low-level mixed-phase clouds (MPCs) are common in the Arctic. Both local and large-scale phenomena influence the properties and lifetime of MPCs. Arctic fjords are characterized by complex terrain and large variations in surface properties. Yet, not many studies have investigated the impact of local boundary layer dynamics and their relative importance on MPCs in the fjord environment. In this work, we used a combination of ground-based remote sensing instruments, surface meteorological observations, radiosoundings, and reanalysis data to study persistent low-level MPCs at Ny-Ålesund, Svalbard, for a 2.5-year period. Methods to identify the cloud regime, surface coupling, and regional and local wind patterns were developed. We found that persistent low-level MPCs were most common with westerly winds, and the westerly clouds had a higher mean liquid ($42\,\mathrm{g\,m^{-2}}$) and ice water path ($16\,\mathrm{g\,m^{-2}}$) compared to those with easterly winds. The increased height and rarity of persistent MPCs with easterly free-tropospheric winds suggest the island and its orography have an influence on the studied clouds. Seasonal variation in the liquid water path was found to be minimal, although the occurrence of persistent MPCs, their height, and their ice water path all showed notable seasonal dependency. Most of the studied MPCs were decoupled from the surface (63 %–82 % of the time). The coupled clouds had 41 % higher liquid water path than the fully decoupled ones. Local winds in the fjord were related to the frequency of surface coupling, and we propose that katabatic winds from the glaciers in the vicinity of the station may cause clouds to decouple. We concluded that while the regional to large-scale wind direction was important for the persistent MPC occurrence and properties, the local-scale phenomena (local wind patterns in the fjord and surface coupling) also had an influence. Moreover, this suggests that local boundary layer processes should be described in models in order to present low-level MPC properties accurately.

1 Introduction

The Arctic is warming more rapidly than any other area on Earth due to climate change (Serreze et al., 2009; Solomon et al., 2007; Wendish et al., 2017). It is well established that clouds strongly impact the surface energy budget in the Arctic (Dong et al., 2010; Shupe and Intrieri, 2004), but feedback processes that include clouds are not well characterized (Choi et al., 2014; Kay and Gettelman, 2009; Serreze and Barry, 2011). Particularly low-level mixed-phase clouds are important for the warming of near-surface air (Shupe and Intrieri, 2004; Intrieri et al., 2002; Zuidema et al., 2005). The multitude of microphysical and dynamical processes within the cloud and the interactions with local and large-scale processes make these mixed-phase clouds difficult to represent in numerical models (Morrison et al., 2008, 2012; Komurcu et al., 2014). Improvements in the process-level understanding are still required to improve the description of low-level mixed-phase clouds in climate models (McCoy et al., 2016; Kay et al., 2016; Klein et al., 2009).

Previous studies have shown the prevalence of mixed-phase clouds (MPCs) across the Arctic (Shupe, 2011; Mioche et al., 2015). MPCs occur in every season, with the highest occurrence in autumn and in the lowest 1 km above the surface, and they can persist from hours to days (Shupe et al., 2006; Shupe, 2011; De Boer et al., 2009). The persistent low-level MPCs have a typical structure that consists of

Published by Copernicus Publications on behalf of the European Geosciences Union.

one or more supercooled liquid layers embedded in a deeper layer of ice, where liquid is usually found at cloud top, and the ice precipitating from the cloud may sublimate before reaching the ground (Morrison et al., 2012, and references therein). Several studies have shown an increase in cloud ice to coincide with increase in cloud liquid, suggesting that ice production is linked to the liquid water in the cloud (Korolev and Isaac, 2003; Shupe et al., 2004, 2008, 2006; Westbrook and Illingworth, 2011; Morrison et al., 2005). The amount of liquid and ice and the partitioning between the condensed phases (i.e., phase partitioning) are important parameters due to their key role in determining the clouds' radiative effect (Shupe and Intrieri, 2004).

A variety of environmental conditions can effect cloud micro- and macro-physical properties. According to simulations over different surface types, changes in surface properties lead to changes in the thermodynamic structure of the atmospheric boundary layer, the extent of dynamical coupling of the cloud to the surface, and the microphysical properties of the MPC (Morrison et al., 2008; Li et al., 2017; Savre et al., 2015; Eirund et al., 2019). Also, observational evidence on the connection between changes in surface conditions and MPC occurrence (Morrison et al., 2018) as well as thermodynamic structure and droplet number concentration (Young et al., 2016) has been found. Kalesse et al. (2016) discovered in a detailed case study that for the MPC in question phase partitioning was affected by the coupling of the cloud to the surface, large-scale advection of different air masses as well as local-scale dynamics. Conversely, Sotiropoulou et al. (2014) did not find differences in cloud water properties between coupled and decoupled clouds. Scott and Lubin (2016) show that at Ross Island, Antarctica, orographic lifting of marine air is likely causing thick MPCs with high ice water content. Changes in aerosol population, especially ice-nucleating particles (INPs), have been found to modulate the ice formation rate (Jackson et al., 2012; Morrison et al., 2008; Norgren et al., 2018; Solomon et al., 2018). To complicate matters further, the cloud also modifies the boundary layer where it resides by modifying radiative fluxes, generating turbulence (due to cloud-top cooling), and vertically redistributing moisture (Morrison et al., 2012; Solomon et al., 2014; Brooks et al., 2017).

While being common in the entire Arctic, MPCs are most frequently observed in the area around Svalbard and the Norwegian and Greenland seas (Mioche et al., 2015). Nomokonova et al. (2019b) report 1 year of ground-based remote sensing observations of clouds at Ny-Ålesund, Svalbard, and find that 20 % of the time single-layer MPCs (defined as single-layer clouds with ice and liquid occurring at any height of the cloud) were present, with the highest frequency in autumn and in late spring–early summer. Svalbard lies in a region where intrusions of warm and moist air from lower latitudes are common (Woods et al., 2013; Pithan et al., 2018), and differences in air mass properties have been associated with differences in ice and liquid water content and particle number concentration in MPCs (Mioche et al., 2017). Locally, the archipelago exhibits large variations in surface properties (glaciers, seasonal sea ice, and snow cover) as well as orography. There are fewer MPCs over the islands than over the surrounding sea during winter and spring, while during summer and autumn the differences are small (Mioche et al., 2015), indicating that the islands modify the local boundary layer and the associated clouds. How the orography influences the low MPCs in more detail is difficult to study using spaceborne radars due to the rather big blind zone and considerably large footprint. Aircraft and ground-based remote sensing, together with modeling studies, are better suited for answering this question.

In this paper we investigate persistent low-level mixed-phase clouds (P-MPCs) observed above Ny-Ålesund on the west coast of Svalbard. Mountainous coastlines are common at Svalbard, Greenland, and elsewhere in the Arctic (Esau and Repina, 2012). Ny-Ålesund is an excellent site to study low-level MPCs in such complex environments. The time period considered is June 2016–October 2018, when a cloud radar of the University of Cologne was operating at the French–German Arctic Research Base AWIPEV as part of the project Arctic Amplification: Climate Relevant Atmospheric and Surface Processes, and Feedback Mechanisms $(AC)^3$. A combination of ground-based remote sensing instruments, surface meteorological observations, radiosoundings, and reanalysis data was used to identify and characterize the P-MPCs, to describe the extent of surface coupling, and to evaluate these in the context of wind direction in the area around the station. In addition to providing a description of micro- and macro-physical properties of P-MPCs and their seasonal variation, we aim to identify some of the impacts the coastal location and the mountains have on the observed P-MPCs as well as determine the relevance of surface coupling for cloud properties at the site. In Sect. 2 the measurement site, the instrumentation, and the data products used are introduced, followed by the description of the methodology developed to identify persistent low-level MPCs (Sect. 3.1), coupling of the cloud to the surface (Sect. 3.2), and the approach to describing regional and local wind conditions (Sect. 3.3 and 3.4). The Results and discussion section describes the occurrence of P-MPCs (Sect. 4.1) and their average properties as well as variation under different seasons and dynamical conditions. The relationship between P-MPC and the regional wind direction (Sect. 4.2), different seasons (Sect. 4.3), surface coupling (Sect. 4.4), and local wind conditions (Sect. 4.5) are considered. The results are discussed in the context of atmospheric temperature and humidity and considering previous studies at Ny-Ålesund and other Arctic sites. In the end the main aspects are summarized followed by conclusions in Sect. 5.

2 Observations

2.1 Measurement site

The measurements were carried out at the French–German Arctic Research Base AWIPEV in Ny-Ålesund (78.9° N, 11.9° E), located on the west coast of Svalbard, on the south side of Kongsfjorden (Fig. 1). The area is mountainous, featuring seasonal snow cover, a typical tundra system, and glaciers. In the period investigated the sea remained ice-free throughout the year. The local boundary layer is known to be strongly affected by the orography (Kayser et al., 2017; Beine et al., 2001) and is often quite shallow with an average mixing layer height below 700 m (Dekhtyareva et al., 2018; Chang et al., 2017). Surface layer temperature inversions are common, especially in winter (Maturilli and Kayser, 2017a). The mountains reach up to 800 m and strongly influence the wind around Ny-Ålesund. In the free troposphere westerly winds prevail. The wind conditions are described more in detail in Sect. 3.4. Clouds have been found to occur above Ny-Ålesund 60 %–80 % of the time (Nomokonova et al., 2019b; Maturilli and Ebell, 2018; Shupe et al., 2011). Clouds generally occur more frequently in summer and autumn and are less common in spring, although the inter-annual variability is large.

2.2 Measurements and data products

Most of the measurements and cloud and thermodynamic parameter retrievals utilized were described in detail by Nomokonova et al. (2019b) and references therein. Here, the most important aspects are summarized, together with additional data products used. A summary of the instrumentation, their specifications, and derived parameters is given in Table 1.

2.2.1 Instrumentation

We employ a suite of remote sensing instruments: radar, microwave radiometer, and ceilometer. Within the frame of the (AC)[3] project the JOYRAD-94 cloud radar was installed at AWIPEV on June 2016. In July 2017 it was replaced by the MIRAC-A cloud radar, which operated until October 2018. Both instruments are frequency-modulated continuous-wave cloud radars measuring at 94 GHz, described in detail by Küchler et al. (2017). The main difference between the two radars is the size of the antenna, which for MIRAC-A is only half of that of the JOYRAD-94. The smaller antenna leads to a sensitivity loss of about 6 dB and an increase in the beam width from 0.53 to 0.85° (Mech et al., 2019). A Humidity and Temperature PROfiler (HATPRO) passive microwave radiometer (MWR) has been operated continuously at AWIPEV since 2011. The instrument has 14 channels in the K- and V-bands to retrieve liquid water path (LWP), integrated water vapor (IWV), and temperature and humidity profiles (Rose et al., 2005). In addition to the zenith pointing measurements, an elevation scan is performed every 15–20 min to obtain more accurate temperature measurements in the boundary layer (Crewell and Löhnert, 2007). Finally, the Vaisala CL51 ceilometer measures at 905 nm, providing attenuated backscatter coefficient (β) profiles (Maturilli and Ebell, 2018).

To complement the remote sensing observations, we make use of soundings and standard meteorological parameters measured at the surface. In Ny-Ålesund radiosondes are launched routinely every day at 11:00 UTC, and more often during campaigns (Maturilli and Kayser, 2017a; Dahlke and Maturilli, 2017). From the surface measurements we utilized temperature, pressure, and wind speed and direction data (technical details in Table 1). The instruments for surface meteorology are continuously maintained by the AWIPEV staff, and all data are quality controlled (Maturilli et al., 2013).

2.2.2 Cloudnet

The Cloudnet algorithm combines radar, radiometer, and ceilometer measurements with thermodynamic profiles from a numerical weather prediction (NWP) model to provide the best estimates of cloud properties (Illingworth et al., 2007). The observational data, described in the previous section, are homogenized to a common resolution of 30 s in time and 20 m in the vertical. In the Ny-Ålesund data set, the Global Data Assimilation System 1 (GDAS1, more info at https://www.ready.noaa.gov/gdas1.php, last access: 28 February 2019) was used as the NWP model until the end of January 2017, after which it was replaced by the operational version of the ICON (ICOsahedral Non-hydrostatic) NWP model (Zängl et al., 2015).

In our work we rely on the target classification product (Hogan and O'Connor, 2004) that classifies objects detected in the atmosphere as aerosols, insects, or different types of hydrometeors (cloud droplets, drizzle, rain, ice, melting ice; see Fig. 2 for an example). Radar reflectivity (Z_e) and ceilometer β-profiles are used to detect the presence and boundaries of clouds. Cloud phase is distinguished on the basis of Z_e, β, temperature (T), and wet bulb temperature; in addition, Doppler velocity from radar is used to position the melting layer. No differentiation is made between ice in a cloud and precipitating ice. While applying this widely accepted methodology, for our study there are two important limitations. Firstly, the detection of liquid within a MPC is based on β, such that if cloud top is not found within 300 m from the height where the ceilometer signal is extinguished, all cloudy bins above this height are classified as ice. Secondly, no method to distinguish supercooled drizzle from ice is available yet (Hogan et al., 2001; Hogan and O'Connor, 2004).

Table 1. The instruments used, the most relevant specifications of each measurement, and overview of derived parameters are shown. If the vertical (Δz) or temporal resolution (Δt) is changed from that measured by the instrument, the resolution used in the analysis is given in the last column.

	Instrument	Temporal resolution	Vertical resolution	Parameters measured	Derived parameters
JOYRAD-94	RPG-FMWC94-SP	2–3 s	100–400 m: 4 m 400–1200 m: 5.3 m 1.2–3 km: 6.7 m	Radar reflectivity (Z_e), Doppler velocity (V_m)	Cloud presence, cloud boundaries (by Cloudnet; $\Delta z = 20$ m, $\Delta t = 30$ s)
MIRAC-A		2–3 s	100–400 m: 3.2 m 400–1200 m: 7.5 m 1.2–3 km: 9.7 m		Ice water content (IWC) $\Delta z = 20$ m, $\Delta t = 30$ s
Microwave radiometer	HATPRO	1 s	–	Brightness temperatures at 22.24–31.40 GHz	Liquid water path (LWP)
		15–20 min	–	Brightness temperatures at 51.26–58 GHz	Potential temperature (θ)-profiles, $\Delta z = 50$–250 m in the lowest 2.5 km
Ceilometer	Vaisala CL51	12–20 s	10 m	Attenuated backscatter (β) at 905 nm	Cloud base, liquid presence (by Cloudnet; $\Delta z = 20$ m, $\Delta t = 30$ s)
Surface meteorology	Thies Clima PT100	1 min	Measurement at 2 and 10 m	Temperature	Potential temperature (θ)
	Paroscientific, Inc. 6000-16B		–	Pressure	
	Combined Wind Sensor Classic, Thies Clima		Measurement at 10 m	Wind speed and direction	30 min mean wind speed and direction
Radiosonde	RS92, RS41		5–7 m	Temperature, pressure	Potential temperature (θ)
				Wind direction	Wind direction

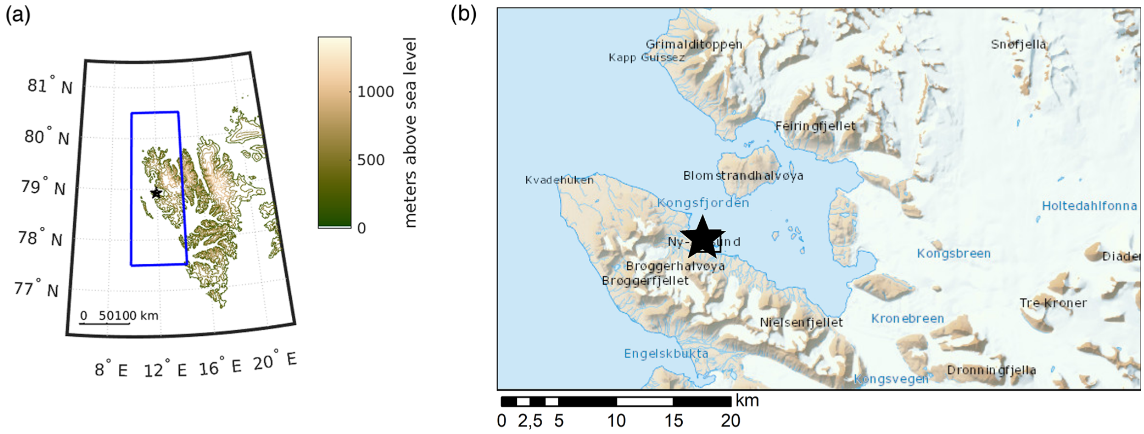

Figure 1. Topography map for Svalbard **(a)** and a detailed illustration of the Kongsfjorden area **(b)**. The black star indicates the location of Ny-Ålesund, where the measurements are taken. The domain covered by the circulation weather type (see Sect. 3.3) is shown by the blue rectangle. Topography data by Amante and Eakins (2009) **(a)** and the Norwegian Polar Institute (2014) **(b)**.

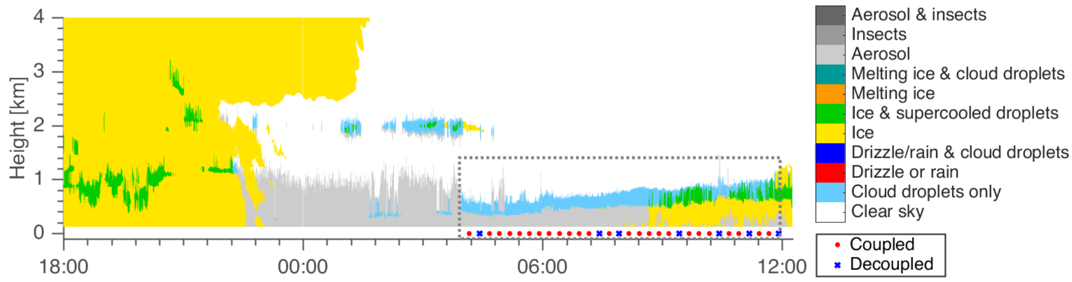

Figure 2. Example of the Cloudnet target classification product from 29 May, 18:00 UTC to 30 May 2018, 12:00 UTC. For the P-MPC, indicated by the gray dashed box, the time series of coupling is also shown. This case was classified as coupled.

2.2.3 Derived properties

The amount of liquid and ice in the cloud, and their ratio, is one of the most important properties of MPCs. In addition, humidity supply is a key requirement for cloud formation and continuation. Liquid water path (LWP) and integrated water vapor (IWV) were retrieved from the zenith-pointing observations of the MWR using statistical multivariate linear regression (Löhnert and Crewell, 2003). Coefficients for the retrieval were based on sounding data; more details about the retrieval and corrections applied are given by Nomokonova et al. (2019b). Previous studies have found the accuracy of the method to be 20–25 $\mathrm{g\,m^{-2}}$ (Löhnert and Crewell, 2003).

Ice water content (IWC) was calculated using the Z_e–T relationship from Hogan et al. (2006), where temperature was taken from the same model as used for Cloudnet. The uncertainty of the retrieval is estimated to be $-33\,\%$ to $+50\,\%$ for temperatures above $-20\,°\mathrm{C}$. Ice water path (IWP) for P-MPCs was calculated by integrating IWC from the surface to cloud top. Furthermore, the LWP was averaged to 30 s to match the temporal resolution of IWP.

In order to calculate the potential temperature (θ) profile based on the temperature profile retrieved from the MWR elevation scans, an estimate of the pressure profile is required. For this we took the measured surface pressure and used the barometric height formula to estimate pressure at each height. The resulting θ-profiles were compared with the profiles from radiosondes in the period June 2016–October 2018 (not shown). A slight cold bias is present (< 0.4 K). The RMSE increases with altitude, but in the lowest 2.5 km the RMSE is still below 1.8 K. For cloud-top temperature, the temperature retrieved from the MWR elevation scan was linearly interpolated between the retrieval levels to cloud-top height.

3 Methods

3.1 Identification of persistent low-level mixed-phase clouds

To identify P-MPCs, each profile was evaluated individually to detect low pure-liquid and liquid-topped mixed-phase cloud layers, after which the persistency of the liquid layer was considered. Using Cloudnet target classification, the first step was to identify different cloud layers in each profile. Here a cloud layer refers to a continuous (gaps of fewer than four height bins, corresponding to 80 m, were omitted) layer of cloud droplets and/or ice. Each layer in the profile was classified as ice only, liquid only, or mixed phase. To distinguish between low stratiform and deep multilayered mixed-phase clouds, only profiles with a single liquid layer and the liquid layer being close to cloud top were considered. In practice, the detected upper boundary of the liquid layer was required to be in the uppermost 20 % of the cloud layer. The requirement for liquid being exactly at cloud top was relaxed since the ceilometer signal cannot necessarily penetrate the entire depth of the liquid layer. These criteria (single liquid layer, liquid close to cloud top) were very effective in selecting the desired low-level mixed-phase cloud regime. However, some mid-level clouds also fulfilled the criteria, and therefore we limited cloud-top height to be below 2.5 km. For the remaining profiles, which all contain either liquid-only or liquid-topped mixed-phase clouds, the persistence of the liquid layer was evaluated. We only included clouds where the liquid layer existed for a minimum of 1 h, with gaps ≤ 5 min. Since the focus of this study is on mixed-phase clouds, we further excluded clouds where no ice was detected. Note that continuous presence of ice was not required; only the cloud liquid had to persist in time. The result is a data set with clouds below 2.5 km where liquid is located at cloud top and persists at least 1 h, and at some point in time ice is associated with the liquid layer. Note that time periods where another cloud layer is found above the P-MPC are not excluded. Figure 2 shows an example of the identified persistent MPC as well as another mixed-phase cloud. Despite the strict criteria, such clouds were present 23 % of the observational time.

In addition to identifying the time periods with P-MPCs present, the Cloudnet data were used to determine the base of the liquid layer and the cloud-top height. A P-MPC case was defined as the time from the beginning to the end of the identified persistent liquid layer. Furthermore, we consider the layer from liquid base to cloud top as the cloud and everything below liquid base to be precipitation. This definition was chosen because the liquid base is well defined from the ceilometer observations. Considering the focus on a persistent liquid layer identified by vertically pointing measurements, the cases included implicitly require either very low wind speeds or a larger cloud field being advected over the site. When another cloud is detected above the P-MPC, the possibility that it contains undetected liquid cannot be excluded, and in these cases the measured LWP cannot be unambiguously attributed to the liquid layer of the P-MPC. Hence, those time periods were flagged to be removed in any analysis of the cloud's liquid content. Unfortunately, we cannot make the assumption that upper cloud layers would not impact the liquid content of a P-MPC (Shupe et al., 2013). The presented LWP distributions are therefore only representative for single-layer cases. Furthermore, all columns with liquid precipitation or drizzle were excluded, leading to a loss of data mainly in the summer months. While this is somewhat unavoidable (e.g., when the MWR measurements suffer from a wet radome), it leads to the exclusion of rather warm precipitating P-MPCs from the analysis.

3.2 Detecting surface coupling

3.2.1 Defining coupling with radiosonde profiles

The thermodynamic coupling of the P-MPC to the surface was determined based on the θ-profile. A quasi-constant profile was taken to indicate a well-mixed layer, while an inversion denotes decoupling between different layers. For the sounding profiles, we simplified the methodology of Sotiropoulou et al. (2014). The cumulative mean of θ from the liquid layer base height downward is compared to θ at each level below the cloud. If this difference exceeds 0.5 K, the cloud is considered decoupled. Figure 3a and b show two example cases, one for a coupled and one for a decoupled cloud, respectively. Both profiles demonstrate a structure typical for stratiform Arctic MPC: a temperature inversion at cloud top, below which a well-mixed layer is identifiable. In the case of the coupled P-MPC (Fig. 3a), the well-mixed layer extends to the surface. For the decoupled P-MPC (Fig. 3b) the well-mixed layer extends 200 m below the liquid layer base, below which several weaker temperature inversions and a generally stable stratification can be identified.

3.2.2 New continuous method

To continuously evaluate the coupling of the P-MPC to the surface, we developed a new method based on surface observations and the potential temperature profiles retrieved from the MWR, which are available more frequently, i.e., every 15–20 min, compared to radiosonde data (Sect. 2.2.3). At each time when a MWR θ-profile was available, the cloud was classified as either coupled or decoupled based on a two-step algorithm. First, the stability of the surface layer was evaluated using the measurements of the meteorological station. The premise of this criteria is that if the surface layer is stably stratified, the cloud must be decoupled from the surface as there exists a stable layer between the surface and cloud base. The θ-profile is used as a proxy for stability. If the gradient of the 30 min mean θ between 2 and 10 m was positive (e.g., an inversion was present between 2 and 10 m), the surface layer was considered stably stratified, and therefore the cloud was decoupled. If this was not the case, the second criteria based on the MWR θ-profile was used. We calculate the difference in potential temperature ($\Delta\theta$) between the surface level and at the height halfway to the liquid base height. If $\Delta\theta$ is below the threshold of 0.5 K, the cloud at this instance was considered coupled, and otherwise it was considered decoupled. The reason for using the height equaling half of the liquid layer base height can be understood by comparing the θ-profiles from sounding and MWR in Fig. 3a and b. While the general shape of the profile can be retrieved from the MWR measurements, it is not possible to resolve sharp

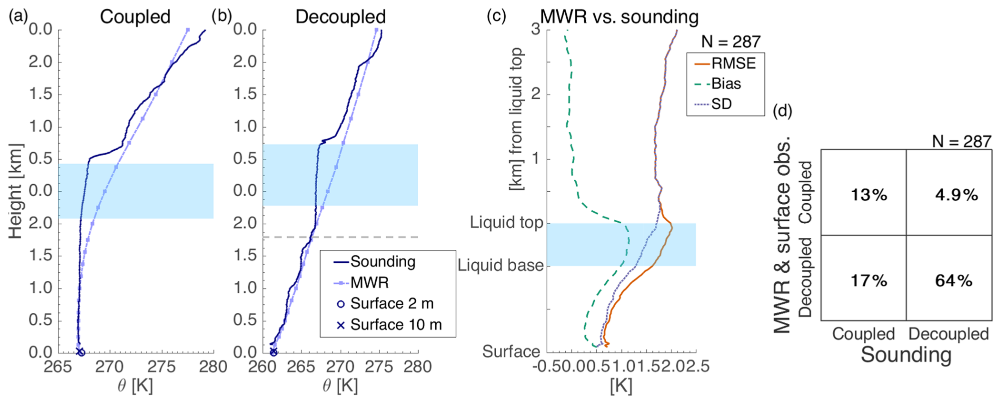

Figure 3. Examples of θ-profiles from sounding and MWR, as well as surface observations: a coupled cloud on 24 October 2017 11:55–12:05 UTC **(a)** and a decoupled cloud on 1 February 2018 16:47–16:56 UTC **(b)**. The blue shaded area indicates the cloud layer, where cloud base and top are determined as the median values of the Cloudnet-based cloud base and top for the duration of the sounding. The gray dashed line indicates the decoupling height defined from the sounding θ-profile. Comparison of potential temperature profiles from sounding and retrieved from MWR measurements when P-MPCs were present, with height normalized with respect to the liquid layer **(c)**. Comparison of the diagnosed coupling with the new method based on MWR and surface observations and based on sounding profiles **(d)**.

inversions or detailed structures of the profile. Yet temperature inversions are very common at the top of P-MPCs. The comparison of MWR profiles with all available soundings when a P-MPC was present (Fig. 3c) shows that the accuracy of the retrieved potential temperature is reduced in the vicinity of the liquid layer top and that the influence extends to below the liquid layer base. At 0.5× liquid base height the impact of cloud-top inversion is smaller than at liquid base and the RMSE is below 1 K, which is why we chose this height to determine the stability of the subcloud layer. Note that it should not be inferred that the method can only detect decoupling occurring in the lowest half of the subcloud layer. When decoupling occurs above the layer explicitly included, it is common that the lower half of the subcloud layer is at least partly stably stratified, as can also be seen in the example of Fig. 3b, prompting a correct decoupling classification.

As the final step, the individual profiles were considered together to define the degree of coupling of each observed P-MPC case. For each detected cloud event, the number of coupled and decoupled profiles were counted. If all profiles were decoupled, the P-MPC was considered fully decoupled. When more than 50 % of the profiles were found to be decoupled, the P-MPC was defined as predominantly decoupled. The rest were considered coupled.

3.2.3 Comparison of methods

The performance of the new method for estimating the coupling for each individual profile was evaluated using the soundings as a reference. We restricted the soundings to cases for which the cloud was present from the launch time until the sonde passed a height of 2.5 km (maximum cloud-top height considered). Those soundings were compared to the MWR profile closest (but not more than 20 min away) to the radiosonde launch time. The sounding-based diagnosis found 31 % of the evaluated P-MPCs to be coupled and 69 % to be decoupled, compared to 18 % and 82 %, respectively, for the newly developed method for the corresponding clouds (Fig. 3d). This suggests a tendency in our method towards decoupling. However, the sounding profiles may miss very shallow surface-based inversions. For 24 % of the profiles considered to be coupled based on the radiosondes, the 2 and 10 m temperatures indicate a surface inversion. Classifying these clouds as decoupled instead changes the ratio of coupled and decoupled P-MPCs from the sounding data set to 23 % and 77 %, which is closer to that found with the new method. The main disadvantage of our method is that the temperature profiles retrieved from the MWR measurements do not provide a detailed profile, but rather the general shape of the profile, and so the developed method occasionally fails. Furthermore, the 10 m layer considered for surface stability is rather shallow, and intermittent coupling could occur regardless of the thermodynamic profile structure.

3.3 Circulation weather type

Since the local wind direction in the lower troposphere above Ny-Ålesund is heavily influenced by the orography (Maturilli and Kayser, 2017a), the circulation weather type based on Jenkinson and Collison (1977) was applied in order to evaluate cloud properties in the context of the regional wind field. Using 850 hPa geopotential height and shear vorticity from ERA-Interim, the flow at each time (00:00, 06:00, 12:00, and 18:00 UTC) was classified as either W, NW, N, NE, E, SE, S, SW, cyclonic, or anticyclonic. A total of 16 grid points centered around Ny-Ålesund were used, so that the area covered is approximately 300 km in the meridional and 100 km in the zonal direction (77.5–80.5° N, 9.75–14.25° E;

see Fig. 1a). The approach aids in assessing whether the observed clouds were advected to the site from the open sea or over the island as well as the proximity of high- and low-pressure systems.

3.4 Local wind conditions

The channeling of the free-tropospheric wind along the fjord axis is a typical feature of an Arctic fjord (Svendsen et al., 2002; Esau and Repina, 2012, and references therein). Previous work has found the feature to also be prominent at Kongsfjorden (Maturilli and Kayser, 2017a). It is well documented that despite the dominating westerly free-tropospheric wind direction, in Kongsfjorden the near-surface wind tends to blow southeasterly along the fjord axis (Maturilli and Kayser, 2017a; Beine et al., 2001; Jocher et al., 2012). This is usually attributed to katabatic forcing of the Kongsvegen glacier about 15 km east-southeast from Ny-Ålesund (Fig. 1), although Esau and Repina (2012) argued that for typical synoptic conditions the land–sea breeze circulation would be the dominant driver. The secondary mode in surface wind is from the northwest, from the sea towards the island's interior. According to Jocher et al. (2012), the northwesterly surface winds are associated with cold air advection that is related to passing low-pressure systems. Beine et al. (2001) find this wind direction to be pronounced in June and July, which they associate with sea breeze and the melting of sea ice. In addition, at Ny-Ålesund weak southwesterly surface winds are observed, caused by katabatic flow from Zeppelin mountain range and the Brøggerbreen glacier south of Ny-Ålesund (Jocher et al., 2012; Beine et al., 2001) under specific synoptic conditions (Jocher et al., 2012; Argentini et al., 2003). The local wind conditions impact the stratification of the local boundary layer (Argentini et al., 2003; Svendsen et al., 2002). Argentini et al. (2003) show that during the ARTIST campaign (15 March–16 April 1998 at Ny-Ålesund) stable conditions were mainly observed with southeast wind and hardly ever with northwest wind. Unstable conditions occurred from 90 to 270° and under light wind conditions. Furthermore, large wind shear was observed to generate turbulence and lead to neutral stratification. This brief summary of previous studies demonstrates the complexities of the local wind conditions present at the AWIPEV station.

We cannot properly describe the circulation in Kongsfjorden from our point measurements at Ny-Ålesund or evaluate the drivers behind the local wind, nor are these processes within the scope of our study. However, it is possible that certain wind patterns are associated with phenomena (shear-induced turbulence, drainage flows from mountains and glaciers transporting cold air into the sub-cloud layer) that modify the P-MPC studied. To evaluate whether the local wind patterns modify the P-MPC, we identified the main modes in the 10 m wind direction and combined them with the circulation weather type to create a proxy for different wind regimes. As expected, three modes can be identified in the surface wind (Fig. 4a). The dominating wind direction (85–165°) corresponds to the direction out of the fjord to the open sea. Less pronounced but clearly identifiable are the two other modes that indicate flow from the sea into the fjord (270–345°) and the katabatic flow from the glaciers south of the station (200–270°). Wind speed above 12 $\mathrm{m\,s^{-1}}$ was only observed between 90 and 120°. Seasonal wind roses are provided in Appendix A2. The frequency with which each surface wind mode was associated with the different weather types during the cloud observation period (June 2016–October 2018) is illustrated in Fig. 4b. For most circulation weather types, the southeasterly surface wind dominated and the northwesterly wind was rare. An exception were the weather types N and NW, for which the northwesterly direction was most common.

To illustrate how the weather type and surface wind direction modes correspond to different wind profiles, the average wind direction profiles based on radiosonde data from June 2016 to October 2018 are shown for weather type W (Fig. 4c). When the surface wind direction was northwesterly, the average direction changed only slightly from 280° in the free troposphere to align with the fjord axis at about 310°. The largest variation in the lowest 200 m was exhibited by the southwesterly surface wind direction. The most common regime (surface wind from southeast) had an average profile with free-tropospheric wind from the west, turning south and all the way to the southeast (120°) in the lowest 300 m. Figure 4c illustrates why a combination of surface and free-tropospheric wind direction is needed to isolate different patterns. Considering the moderate standard deviation in the wind direction profiles shown in Fig. 4c, it is reasonable to assume that each surface wind direction mode together with the weather type, which describes the mean regional wind direction at 850 hPa, describes a certain wind pattern and thus gives a first estimate of the wind conditions around Ny-Ålesund.

3.5 Statistical tools

To test the statistical significance of differences between two or more distributions, the Mood's median test to compare the medians in different populations was used (Sheskin, 2000). This test was chosen because it does not require normally distributed data and the compared samples can be of different sizes. The median of each population is compared to the median of the distribution including all data, and the Pearson's χ^2 test is used to test the null hypothesis that medians from different populations are identical. To reject the null hypothesis thus leads to the conclusion that the different populations have different medians.

The data points in the time series of the variables tested (LWP, IWP, cloud-top temperature, and cloud-base height) are correlated with each other and can not as such be used in the statistical test. We assume that each P-MPC case is independent of the others, and for cloud-top temperature and cloud-base height we use the medians for each case for testing. LWP and IWP were found to vary more within each case, and therefore several data points from every P-MPC case were sampled. For this, we estimated the de-correlation timescale as the time where the autocorrelation function, computed for each P-MPC case individually, reaches zero. For the majority of P-MPC cases there were too many gaps in the data to reliably compute the autocorrelation function, and hence no de-correlation timescale could be estimated. From the values available, the median was calculated and then double the median was used as the de-correlation timescale Δt_{dcr} for all cases. For testing, the data were sampled randomly, with a minimum gap of Δt_{dcr} between the sampled data points.

4 Results and discussion

4.1 Occurrence of persistent MPC and other clouds

We first examine the frequency of occurrence of different types of clouds in the observation period of the cloud radar (10 June 2016–8 October 2018) considering the 30 s averaged columns of the Cloudnet product. A cloud was found above Ny-Ålesund 76 % of the time measurements were running. The month-to-month variation was considerable, varying from 40 % to over 90 % (Fig. 5). Averaging for all years, cloudiness was slightly higher in summer (June–August; 80 %) and autumn (September–October; 77 %) and lower in spring (March–May; 69 %) and winter (December–February; 74 %). Intra-annual variation is pronounced in autumn, when cloud occurrence frequency varied from 69 % to 84 %. MPCs (defined here as any profile where co-located cloud liquid and ice are found) were present 41 % of the time, with a somewhat higher frequency in autumn. Liquid-only clouds (profiles with cloud droplets without co-located ice) had an overall occurrence frequency of 14 % and a clear seasonal cycle with most liquid-only clouds occurring in summer and hardly any in winter or spring. Thus, the radiatively important cloud liquid was more often found in mixed-phase clouds, although the contribution of liquid-only clouds was notable in summer. All of the presented figures are given relative to the amount of data available. Figure 5a shows the high data coverage obtained, implying that – with the exception of the first and last months – we can give a reliable estimate of the frequency of cloud occurrence within the detection limits of the instruments.

The persistent low-level mixed-phase clouds (P-MPCs; see Sect. 3.1 for definition) cover 23 % of the data set, highlighting the relevance of this cloud regime. In total 1412 cases of P-MPC were identified. The “all MPC” and the P-MPC occurrences in Fig. 5 are not directly comparable, since the first one refers to individual profiles and the latter is to a large extent defined by a temporally continuous liquid layer and also includes profiles without a mixed-phase layer detected. P-MPCs were most common in summer (32 %) and occurred less often in winter (15 %) and spring (16 %), with autumn being the intermediate season (24 %). The P-MPC occurrence thus follows the seasonal cycle of cloud liquid occurrence (Nomokonova et al., 2019b).

For defining the persistence of the liquid layer some thresholds needed to be set, including how long gaps were allowed and the minimum duration required. The choices made (5 min and 1 h) were motivated by the aim for a certain cloud regime, namely a stratiform mixed-phase cloud in the boundary layer. A sensitivity test allowing only 2 min gaps in the liquid layer showed the only major difference to be in the occurrence frequency of P-MPCs, while the properties of the clouds or the seasonal cycle of P-MPC occurrence did not differ substantially.

4.2 P-MPC properties and regional wind direction

Figure 6 shows the occurrence of each weather type (used to determine the regional free-tropospheric wind direction; see Sect. 3.3) in our period of study, and the fraction of those times when a P-MPC was identified. In general, NE, SE, and NW were less common than the other wind directions. For a given weather type, the fraction of P-MPC occurrence varied considerably. Almost a third of the time when winds were from the west (W), a P-MPC was found at Ny-Ålesund. Weather types S, SW, NW, and anticyclonic were also favorable for P-MPC. Based on an evaluation of sounding profiles, the most common free-tropospheric wind direction for the weather type anticyclonic was west (not shown). On the other hand, winds from north and east (weather types N, NE, and E) brought P-MPCs to the site less often. The weather types which are most commonly associated with P-MPCs can be determined by combining the occurrence frequency of each weather type and its P-MPC fraction (Fig. 6). Consequently, P-MPCs were most often associated with the weather types W, SW, and anticyclonic, which include almost half (48 %) of all profiles.

The distributions of liquid layer base height, LWP, and IWP and their dependence on wind direction are presented in Fig. 7. The base of the liquid layer was usually between 540 and 1020 m above the surface, with mean and median liquid base height of 860 and 760 m, respectively. The typical P-MPC thus lies above the fjord at a height fairly close to the mountaintops. Fewer P-MPCs were associated with weather types NE, E, and SE, and with mean liquid base heights well above 1 km these were found at larger altitudes than most of the P-MPCs. The mean LWP for P-MPCs was $35\,\mathrm{g\,m^{-2}}$ with a standard deviation of $45\,\mathrm{g\,m^{-2}}$. On average most liquid was found in the P-MPC in weather type SW ($49\,\mathrm{g\,m^{-2}}$), and the least was found in weather type NE ($12\,\mathrm{g\,m^{-2}}$). However, the variability within each weather type was larger than the differences between the weather types. The IWP distributions are strongly skewed (Fig. 7c) towards low values. Zeros

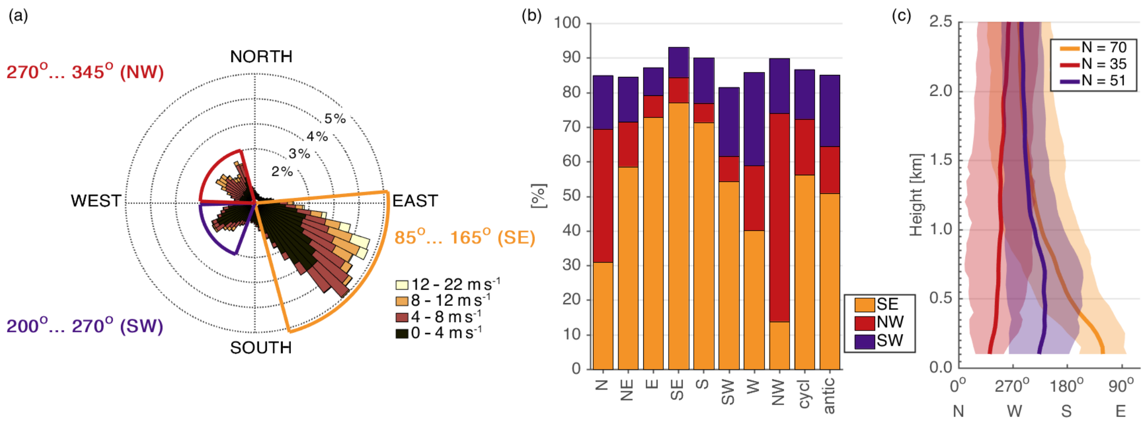

Figure 4. Wind rose for 30 min mean 10 m wind for the cloud observation period (June 2016–October 2018) with the three main modes identified **(a)** and the relative frequency of occurrence for each weather type **(b)**. Wind direction profiles corresponding to each identified near-surface wind direction mode for weather type W based on radiosoundings from June 2016 to October 2018 **(c)**. The line shows the mean wind direction, and the shaded area shows the mean ± standard deviation at each height, estimated using the method by Yamartino (1984). Data points with wind speed below 0.5 m s^{-1} were omitted. N gives the number of soundings available for each mean profile.

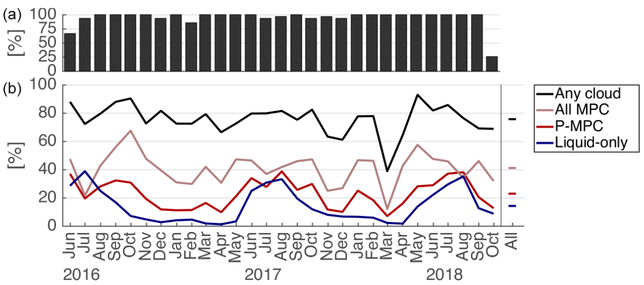

Figure 5. Monthly and total occurrence frequency of clouds in general and selected specific cloud types (see text for definitions) **(b)** and coverage of Cloudnet data **(a)**.

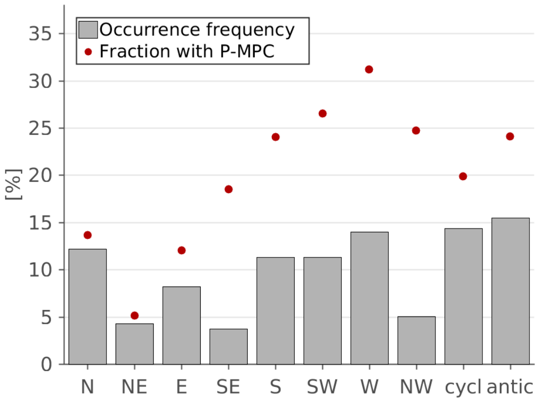

Figure 6. The frequency of occurrence of each weather type and the fraction with P-MPC presence.

were ignored, but all nonzero values were included. For all P-MPCs, the mean and median IWPs were 12 and 2.1 g m^{-2}, respectively. Between the different weather types, the mean (median) varied from the 5.6 (1.1) g m^{-2} of weather type SE to 17 (6.2) g m^{-2} of weather type NW. The weather types NW, W, and SW stand out in terms of high IWP and have a mean IWP of 16 g m^{-2}. Overall, the westerly weather types (SW, W, and NW) were associated with lower P-MPCs and with more liquid and ice (mean LWP 42 g m^{-2}), while the easterly weather types (SE, E, and NE) were less common, distinctly higher, and connected to the lowest average LWP and IWP.

Large-scale advection and air mass properties are known to influence MPC properties (Mioche et al., 2017; Qiu et al., 2018, amongst others). Previous studies suggest that at Svalbard northerly flow is often associated with cold air masses originating from the central Arctic and that southerly flows bring warmer and more humid air from lower latitudes (Dahlke and Maturilli, 2017; Knudsen et al., 2018; Kim et al., 2017; Mioche et al., 2017). Furthermore, the open sea west of the Svalbard archipelago might act as a local source of humidity and heat. Here we use temperature at 1.5 km (corresponding to the 850 hPa level) and integrated water vapor (IWV) from the MWR to represent the atmospheric temperature and humidity conditions under which the P-MPCs were occurring. In agreement with previous studies, Fig. 8 shows that the highest average IWV and warmest temperatures were associated with southerly winds, while the lowest average IWV and coldest temperatures were associated with northerly winds. The domain considered for the weather type (Fig. 1a) is too small to describe large-scale advection or air mass origin, but Fig. 8 suggests the weather type is nonetheless a useful proxy for air mass properties. The average IWV and 1.5 km temperature can explain the first-order variation in P-MPC occurrence and LWP between weather types. The south-southwesterly winds are warm and humid and are associated with frequent occurrence of P-MPC with relatively

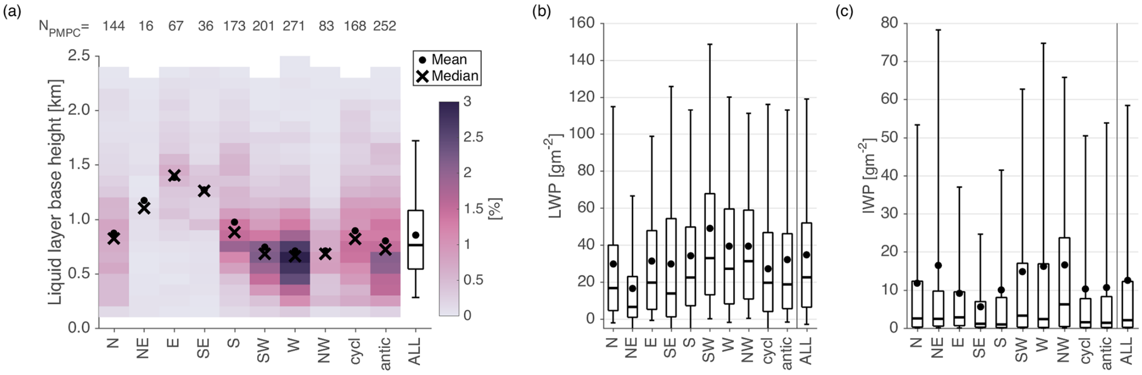

Figure 7. Height of the P-MPC liquid layer base **(a)**, the LWP **(b)** and IWP **(c)** distributions for each weather type, and all P-MPCs. The number of P-MPC cases for each weather type is given in **(a)**. The box shows the 25th, 50th, and 75th percentiles, the dot the mean, and the whiskers the 5th and 95th percentiles. The medians for different weather types were found to differ on a 95 % confident level.

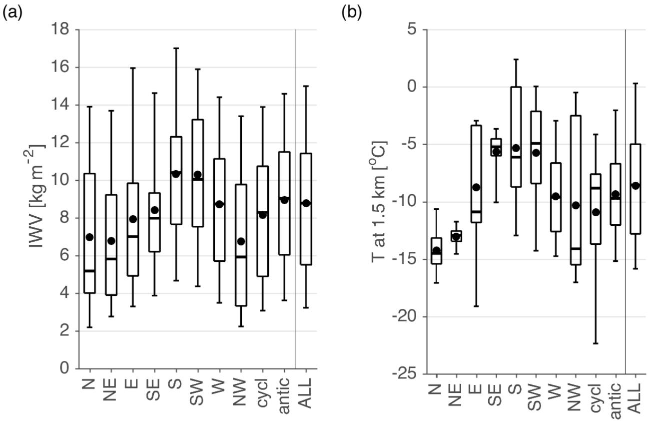

Figure 8. IWV **(a)** and 1.5 km temperature **(b)** for time periods with P-MPC present for each weather type. Boxes and whiskers as in Fig. 7. The medians were found to differ on a 95 % confidence level.

high amounts of liquid, compared to the north-northeasterly winds, which are drier and colder and are associated with less frequent P-MPC occurrence and lower LWP (Figs. 6, 7b, and 8a). Owing to the complexity of ice microphysical processes, such a direct relationship cannot be found between atmospheric humidity and temperature (Fig. 8) and IWP (Fig. 7c). On the other hand, as already noted above, Fig. 7 shows a clear contrast between the properties of easterly and westerly P-MPCs. These differences cannot be explained by the IWV and 1.5 km temperature distributions, which are rather similar for weather types W and E. Hence, atmospheric temperature and humidity are important but not the only relevant forcing for P-MPC at Ny-Ålesund.

The influence of the island and its orography clearly affects the height of the liquid layer (Fig. 7a). The median altitude of the P-MPC base with easterly winds (weather types NE, E, and SE) was above the height of the mountaintops, suggesting that the clouds were usually advected to the site above the mountains rather than forming locally in the fjord. The P-MPCs associated with easterly winds were also less frequent (Figs. 6 and 7a). If we assume the majority of observed P-MPC being of an advective nature, the low occurrence frequency with winds from the east would imply less cloud formation over the island compared to over the sea or dissipation of cloud fields while being advected over the island. Mioche et al. (2015) found less low (below 3 km) MPC over land than over sea in the Svalbard region in spring and winter, while in summer and autumn the differences were small. Cesana et al. (2012) studied liquid-containing clouds in the Arctic and found fewer low (below 3.36 km) liquid-containing clouds above Svalbard than over the surrounding sea in all seasons. Although direct comparison is not possible due to inconsistencies in the observation techniques, cloud sampling, and the considered area, the mentioned studies all indicate that the influence of the Svalbard archipelago decreases the amount of low liquid-bearing clouds.

The combination of the effects of large-scale advection and air mass properties, as well as the influence of the Svalbard archipelago, can provide an explanation for the dependence of the P-MPC properties on weather type presented in Figs. 6 and 7. Southwesterly and westerly free-tropospheric winds were associated with most P-MPCs and the highest average LWP and IWP, likely due to higher amounts of humidity available from lower latitudes. The southeasterly to northeasterly winds had the least P-MPCs and comprise the lowest average LWP and IWP, related to the drier air masses from the north and less favorable conditions for cloud formation over the island. Other mechanisms can be considered to further explain the observed IWP variation. Ice formation could be enhanced in the cold temperatures for weather types N and NE (Fig. 8), whereas the higher IWP for weather types SW, W, and NW might be related to larger amounts of supercooled liquid available in the P-MPCs (Fig. 7b, c) or higher aerosol concentration in air masses advected from lower latitudes.

4.3 Seasonality

The seasonal variation in the studied P-MPC properties and atmospheric conditions at Ny-Ålesund are presented in Fig. 9. In agreement with previous studies (Nomokonova et al., 2019b; Maturilli and Kayser, 2017a), the highest average temperature and humidity are found in summer and the lowest in winter and spring (Fig. 9a, b). The height of the P-MPC shows a clear seasonality, with lower liquid base height in summer and higher in winter (Fig. 9c). Zhao and Wang (2010) evaluated 5 years of low-level clouds (cloud base below 2 km) observed at Utqiaġvik (previously known as Barrow), Alaska, and also found a seasonality in cloud height with a minimum in summer. Furthermore, these results are in agreement with the seasonality in cloud height at Ny-Ålesund reported by Shupe et al. (2011). The IWP distributions show a clear seasonality, with low values in summer and autumn and a clear maximum in spring (Fig. 9e). The low IWP in summer and autumn (median 0.2 and 1.0 $\mathrm{g\,m^{-2}}$, respectively) can be attributed to relatively warm temperatures close to 0 °C. The median IWP in spring (7.5 $\mathrm{g\,m^{-2}}$) is almost 2-fold of the median IWP in the winter (4.0 $\mathrm{g\,m^{-2}}$), which can hardly be attributed to the different temperature conditions (Fig. 9b). The higher IWV in spring compared to winter (Fig. 9a), however, can play a role. Furthermore, the high IWP in spring could be related to the generally higher aerosol loading in the Arctic atmosphere in the late winter and spring, a time period also known as the Arctic haze season (Quinn et al., 2007).

Conversely, the LWP distributions show a minimal seasonality despite the seasonal variation in IWV and 1.5 km temperature related to the P-MPC (Fig. 9a, b, d). The highest (lowest) median LWP in summer and spring (winter) was 24 $\mathrm{g\,m^{-2}}$ (18 $\mathrm{g\,m^{-2}}$), and the seasonal mean values varied from 33 to 36 $\mathrm{g\,m^{-2}}$. Note that this result does not imply a lack of seasonal variability in overall cloud LWP (see Fig. 5 in Nomokonova et al., 2019a), only in the specific cloud regime evaluated. One challenge of the algorithm to identify the P-MPC are thick liquid layers where Cloudnet only identifies the lowest parts of the layer as containing liquid. The problem was partly mitigated by relaxing the criteria for liquid presence at cloud top; nonetheless we find cases with a thick liquid layer that do not fulfill the criteria of a liquid-topped mixed-phase layer and the rest of the cloud gets cut off (see Fig. 2 at 12:00 UTC on 30 May 2018). This artificially limits our data set to clouds where the liquid layer is thin enough, and there might be some clouds with more liquid that are not included in our analysis. Considering the LWP distributions were skewed towards lower values (Fig. 7b), these cases are likely to be a minority for the cloud regime considered. However, it is possible that the average LWP is somewhat underestimated. In addition, it could be that the cloud detection algorithm limits the considered cases to a specific LWP regime, which results in the lack of seasonality in the LWP of the P-MPC.

Since P-MPC properties (excluding LWP) as well as atmospheric temperature and humidity vary seasonally, a seasonal dependency in wind direction could explain the weather-type-dependent variations in P-MPC properties found in Sect. 4.2. To examine this possibility, Fig. 10 shows the proportion of P-MPC observations in each season for every weather type. The observation period of 2.5 years from June 2016 to October 2018 together with the seasonal variation in P-MPC occurrence (Fig. 5) lead to the uneven distribution of data between seasons. Overall, the summer months contribute most to the data set. However, there are no extensive differences found between the weather types. Most noteworthy is the high spring and low autumn occurrence of NW, which might contribute to the high IWP for this weather type (Fig. 7c). Furthermore, N and E were relatively more common in winter, N and SE more common in spring, and N less common in autumn. Given the lack of a distinct signal, we believe the seasonal variation in wind direction plays a minor role in the weather-type-dependent differences in P-MPC occurrence and properties described in the previous section.

We further compare properties of the P-MPCs at Ny-Ålesund and their seasonal variation to observations of similar cloud regimes at other Arctic sites. Only studies that comprise at least 1 year of observations were considered. Shupe et al. (2006) evaluated MPCs observed at the 1-year-long Surface Heat Budget of the Arctic Ocean (SHEBA) campaign and found an annual average LWP and IWP of 61 and 42 $\mathrm{g\,m^{-2}}$, respectively. Both IWP and LWP were found to have a maximum in late summer and autumn. The study did not explicitly focus on low-level clouds but found that 90 % of the observed MPCs had a cloud base below 2 km. De Boer et al. (2009) focused on single-layer mixed-phase stratus at Eureka, Canada, and reported seasonal mean LWP to vary between 10 and 50 $\mathrm{g\,m^{-2}}$. Zhao and Wang (2010) show monthly mean values for LWP at Utqiaġvik to vary from 10 to 100 $\mathrm{g\,m^{-2}}$ and for IWP from 10 to 25 $\mathrm{g\,m^{-2}}$. Similarly to SHEBA, at both Eureka and Utqiaġvik the maximum LWP was found in autumn. However, at Eureka as well as Utqiaġvik a maximum in the amount of ice in MPCs was found in spring as well as autumn. The differences in seasonal cycles of LWP and IWP at different sites could be due to different forcing conditions, in addition to the choice of the cloud regime that might also play a role. Sedlar et al. (2012) included all single-layer clouds below 3 km and found that most of the LWP distribution was within 0 to 100 $\mathrm{g\,m^{-2}}$, with slightly higher values in the data set from SHEBA than Utqiaġvik. The average figures are comparable to those observed for P-MPC at Ny-Ålesund, although the mean values in our study are at the lower end of the range reported at Utqiaġvik and SHEBA.

Finally, the seasonal variation in P-MPC occurrence is compared with previous studies in the Svalbard region. Shupe et al. (2011) as well as Maturilli and Ebell (2018) report most clouds in summer and early autumn above Ny-Ålesund, agreeing with our findings. Conversely, Mioche

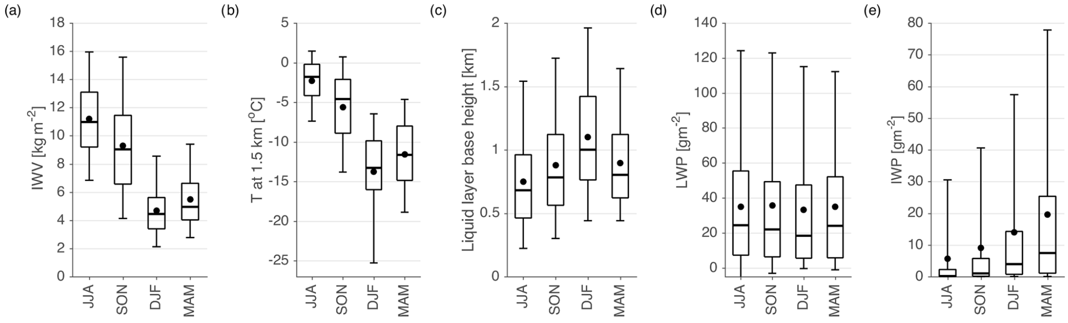

Figure 9. IWV **(a)**, 1.5 km temperature **(b)**, liquid base height **(c)**, LWP **(d)**, and IWP (e) distributions for each season. Only time periods with P-MPCs present are included. Boxes and whiskers as in Fig. 7; the medians were found to differ on a 95 % confident level.

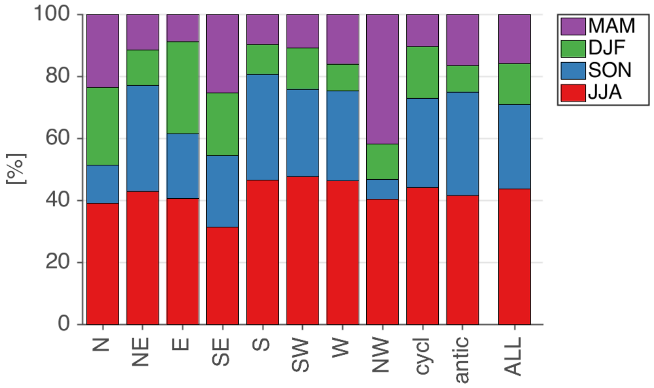

Figure 10. Distribution of seasons in the studied data set for each weather type. Only time periods when a P-MPC was present are included to evaluate the possible impact of wind direction seasonality on cloud properties and occurrence.

et al. (2015) identified most low-level (below 3 km) MPCs in the Svalbard region in autumn and a minimum in occurrence in summer based on the synergy of the measurements from CloudSat and CALIPSO. P-MPCs commonly contain very low amounts of ice, which might be below the sensitivity limit of the satellite observations, explaining some of the disagreement. Furthermore, Mioche et al. (2015) were missing clouds below 500 m due to the blind zone of CloudSat, and since clouds generally are lower in summer this would lead to a higher fraction of missed clouds in this season. In any case, considering the large month to month variation in cloud occurrence (also shown by Shupe et al., 2011), different results when considering different time periods can be expected. Our time series might still not be long enough to give a precise estimate of the seasonal variation in cloud occurrence frequency.

4.4 Surface coupling

Figure 11a shows the fraction of observed P-MPCs classified as coupled, predominantly decoupled and fully decoupled in each season. A total of 63 % of all observed P-MPC cases were found to be fully decoupled, and only 15 % were coupled. The degree of coupling had a clear seasonal cycle, with decoupling being the dominant mode in autumn and winter and most coupled P-MPCs occurring in summer. The observed seasonality in the surface coupling of P-MPC could be related to the overall higher lower-tropospheric stability in winter, which could limit the coupling of the cloud. Previous studies have found that the coupling of low Arctic MPCs depends on the proximity of the cloud to the surface since the cloud-driven mixing layer is more likely to reach the surface if the cloud is low (Shupe et al., 2013; Brooks et al., 2017). Also, in our data set the median cloud-base height for decoupled P-MPCs (1010 m) is considerably larger than the median cloud-base height of the coupled P-MPCs (620 m) (Fig. 11b). For P-MPC with liquid base heights of more than 1.5 km, coupling to the surface was not observed. P-MPCs were on average higher in winter and lower in summer (Fig. 9c), which could partly explain the seasonal variation in the frequency of surface coupling.

To evaluate the effect surface coupling has on cloud properties, we only considered P-MPC in weather types SW and W in order to limit the different factors in play. These clouds include the full range of coupling states and cover one-third of the data set (Fig. 7a). The coupled P-MPCs had more liquid than the fully and predominantly decoupled P-MPCs (Fig. 12a). The median LWP did not differ significantly between the predominantly and fully decoupled P-MPCs (25 and 28 g m^{-2}, respectively), while the median LWP for coupled cases was clearly larger (47 g m^{-2}). Differences in IWP between the coupling states were small (Fig. 12b). The medians did not vary significantly (from 11 to 12 g m^{-2}), but the larger IWP values (between 30 and 100 g m^{-2}) were less likely for the coupled P-MPC. From the LWP and IWP distributions it follows that the total amount of condensed water (LWP + IWP) was higher for coupled than predominantly or fully decoupled P-MPC. This suggests either a source of humidity from the surface that is not available for the decoupled P-MPC or a smaller sink.

Many ice microphysical processes have a temperature dependency (Lamb and Verlinde, 2011), and the observed dif-

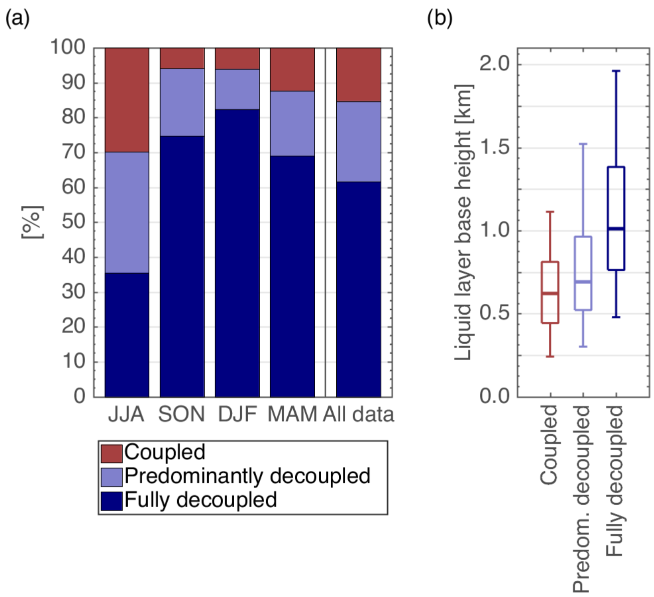

Figure 11. The fraction of P-MPC cases classified as coupled, predominantly decoupled, and fully decoupled in each season and for the entire data set **(a)**, and the distribution of the liquid layer base height in the coupling classes **(b)**. Boxes and whiskers as in Fig. 7; the medians were found to differ on a 95 % confident level.

ferences in LWP and IWP distributions between coupled and decoupled P-MPCs could be caused by different sampling across the temperature range. Observed cloud-top temperatures ranged from −28 to +5 °C, with most P-MPCs occurring at the warm end of this range (Fig. 12c). As the persistent liquid layer is the defining feature of the P-MPCs, it is not surprising that they occurred more often at warmer temperatures where liquid is generally more abundant. The coldest P-MPCs (cloud-top temperatures below −18 °C) were always decoupled and occurred in winter and early spring. The cloud-top temperature distributions were very similar for the coupled and predominantly decoupled P-MPCs, suggesting that the differences in IWP and LWP distributions between these two groups can not be explained by a varying frequency of different temperature regimes. The cloud-top temperature distribution of fully decoupled P-MPC differs from that of the predominantly decoupled and coupled clouds by having a larger number of cold cloud tops and a smaller peak at the warm end of the distribution. Yet the IWP and LWP distributions do not differ substantially between fully and predominantly decoupled P-MPCs. Although the observed differences in LWP and IWP between coupled and fully decoupled P-MPCs could be caused by differences in temperature, we cannot explain the differences between predominantly decoupled and coupled clouds or the similarity of the predominantly and fully decoupled P-MPCs simply from the cloud-top temperature distributions.

The analysis presented only included weather types SW and W. These weather types are amongst the weather types with the largest average LWP and IWP. The variation in LWP and IWP between coupled and decoupled P-MPCs for the other weather types would therefore be smaller in absolute numbers. Including all weather types, the medians for LWP for coupled and predominantly and fully decoupled were 34, 22, and 20 $\mathrm{g\,m^{-2}}$, and the medians for IWP were 7.5, 9.4, and 9.4 $\mathrm{g\,m^{-2}}$, respectively. The outcome that coupled P-MPC had more liquid and that differences in IWP were small is the same. One needs to keep in mind that these numbers are dominated by the westerly weather types which cover the bulk of the data. It is possible that different relationships between cloud properties of coupled and decoupled clouds would be found for weather types which have distinctly different mean wind conditions. While we cannot conclude that the presented results hold for all situations occurring at Ny-Ålesund, they describe the most common conditions.

The comparison between the coupling detection from sounding and the new method based on MWR and surface observations implied that the new method is more inclined to consider a profile decoupled (Sect. 3.2.3). Yet, the similarity of the LWP and IWP distributions for predominantly and fully decoupled P-MPCs suggests that these groups were very similar. Considering cloud properties, it does not seem that the predominantly decoupled clouds would be mistakenly considered more decoupled than they are. It is possible that our method erroneously classifies weakly coupled P-MPC as predominantly decoupled and that in these cases the interaction with the surface is limited and does not modify the cloud properties, considerably leading to similar LWP and IWP distributions for these clouds and the actually decoupled P-MPC. Accordingly, we conclude that decoupling might be overestimated, but this does not have serious consequences on the results on cloud properties. Considering the different estimates (Figs. 3d and 11a), we can regard 63 %–82 % of the P-MPCs to be decoupled and 15 %–33 % to be coupled. Moreover, intermittent turbulence and the coupling it may lead to are rather challenging for our approach, as the thermodynamic profile takes time to adjust. However, the turbulent transport of heat can be assumed to be similar to the transport of any other scalar. If the turbulence that occurred was too short-lived to modify the temperature profile distinctly, it would also be unlikely to transport great amounts of water vapor or aerosols to the cloud layer.

Shupe et al. (2013), Sotiropoulou et al. (2014), and Brooks et al. (2017) have evaluated the coupling of low clouds during the ASCOS campaign (August–September 2008) using different methods and slightly different time periods and observed decoupling from the surface 75 %, 72 %, and 76 % of the time, respectively. Their measurements were mostly of clouds above sea ice, and for a shorter time period. The results are therefore not directly comparable with the multiyear statistic presented here. Moreover, the mechanisms that lead to decoupling at ASCOS were likely different than at Ny-Ålesund. Like Shupe et al. (2013), but unlike Sotiropoulou et al. (2014), we found a difference in LWP between cou-

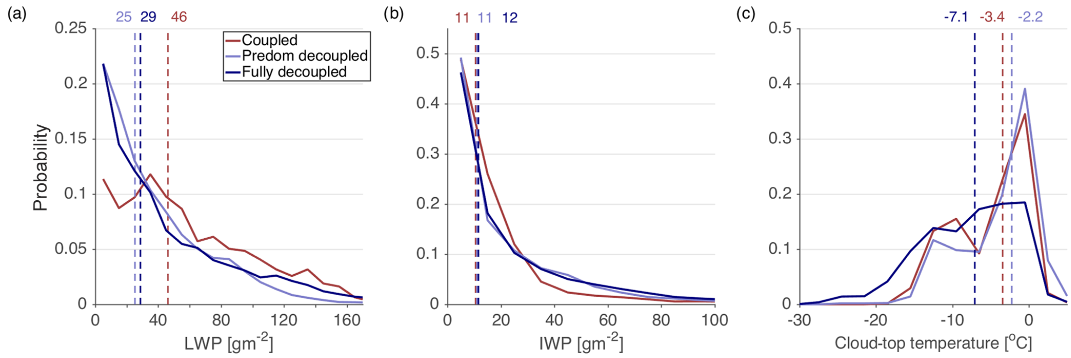

Figure 12. Comparison of LWP **(a)**, IWP **(b)**, and cloud-top temperature **(c)** distributions between P-MPC in weather types W and SE with different degrees of surface coupling. The dashed line and the numbers on top show the median value of each distribution. The bin size for LWP and IWP is $10\,\mathrm{g\,m^{-2}}$ and for cloud-top temperature 3 °C. The medians were found to differ on a 95 % confident level for LWP and cloud-top temperature.

pled and decoupled clouds (Fig. 12a). If we assume that the (sea) surface can provide a source of moisture for the P-MPC, coupling could add moisture to the cloud layer and lead to a higher total water path. Considering the small differences in IWP (Fig. 12b), it does not seem that the surface would be an important source for INPs, or there are some other mechanisms that limit ice formation in coupled clouds where more liquid water is present. The observed seasonality in the surface coupling of P-MPC (Fig. 11a) could be related to the overall higher lower-tropospheric stability in winter, which could limit the coupling of the cloud as well as to the lower cloud-base height in summer (Fig. 9c) that makes it easier for the cloud to couple to the surface due to its proximity.

4.5 Local wind patterns around Ny-Ålesund

The effects local winds have on the P-MPC were evaluated using the weather type together with the surface wind direction as a proxy for the wind conditions at Ny-Ålesund (Sect. 3.4). The most common wind situation for the P-MPC at Ny-Ålesund is a southeasterly surface wind underlying westerly and southwesterly upper winds (Figs. 4, 6). Hence, the wind turns from the surface upwards to the almost opposing direction by 1.5 km height (Fig. 4c). Directional wind shear is therefore commonplace for P-MPC at Ny-Ålesund (Fig. 4b), either in or below the cloud layer. The magnitude of the wind direction change varies with the free-tropospheric wind. The only exception are weather types N and NW, for which the most common surface wind is northwesterly, and the wind does not turn, or only turns slightly, with increasing altitude. A further consideration related to the surface wind direction is the history of the boundary layer. The air has experienced very different surface properties when moving from open sea to land with northwesterly surface wind or from mountainous, often snow- and ice-covered terrain to a flat sea surface with southeasterly surface wind.

The influence of local winds on the P-MPC was found to be limited. Figure 13a shows the fraction of time with P-MPC occurring (similarly to Fig. 6) for each weather type and surface wind direction combination. Weather types cyclonic and anticyclonic are somewhat hard to interpret, as these are associated with varying free-tropospheric wind directions above the site and were therefore not included. The low number of cases with southwest and northwest surface wind limits the possibilities to compare different surface wind regimes for most of the weather types. For weather types SW and W the southwest surface wind was associated with higher frequency of cloud occurrence compared to the southeast surface wind. In contrast, for weather type N northwest surface wind had P-MPCs most often and southwest the least. Based on this analysis no overall tendency for a certain surface wind direction or the amount of directional shear between the surface and the free-tropospheric wind to increase or decrease P-MPC occurrence was found.

Regarding P-MPC properties, no strong relationships with surface wind direction were identified. Only the main findings are summarized here and further details are provided in Appendix A1. Considering weather types N, W, and SW, which have the most cases across different surface wind directions, no statistically significant differences were found in the median liquid base height or cloud-top temperature. The northwest surface wind was associated with the highest median LWP, possibly due to the higher level of humidity available over the open sea. The southwest surface wind was associated with a significantly higher IWP for weather types W and SW (median IWP 16 and $18\,\mathrm{g\,m^{-2}}$, respectively). However, these variations in LWP and IWP were not found for all three weather types analyzed.

Local winds in Kongsfjorden were quite apparently connected to the coupling of the P-MPC (Fig. 13b). Coupling was most common with northwest surface wind (from the sea) and least common with the southeast surface wind (towards the sea), and the same behavior was found for every

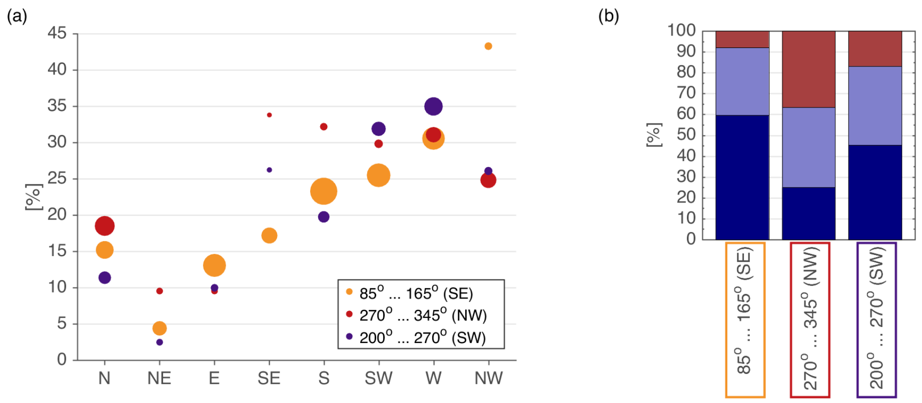

Figure 13. Fraction of time with P-MPC occurring for each surface wind direction and weather type regime **(a)**. The size of the dots represents the amount of data available to compute the value. The fraction of P-MPC cases classified as coupled, predominantly decoupled, and fully decoupled for each surface wind direction mode **(b)**.

season despite the seasonality of both surface wind direction and cloud coupling (see Appendix A2). For the P-MPC to be thermodynamically decoupled from the surface, a stably stratified layer needs to exist between the surface and the cloud base. Argentini et al. report a dependence of surface layer stratification on wind direction (Argentini et al., 2003, Fig. 5). Stable conditions were most often found with southeast surface wind, for which only 8 % of the P-MPCs were considered coupled. On the other hand, stable conditions were rare with northwest surface wind, for which 37 % of the P-MPCs were coupled. The near-surface wind from the southwest and southeast is often related to flows from the glaciers (Jocher et al., 2012; Beine et al., 2001; Sect. 3.4) that bring cold air down to the valley in a shallow layer close to the surface. Such a cold surface layer is very efficient in decoupling the cloud and acts against the cloud-driven turbulence that could otherwise couple the P-MPC to the surface. This effect might be stronger with southeast than southwest surface wind, since the katabatic winds from the southwest are weaker (Fig. 4a). The differences in the coupling of the P-MPC with varying wind conditions can be explained by the differences in stratification of the lower boundary layer under different surface wind conditions. We conclude that the surface wind has the potential to modify the conditions in the boundary layer, which in turn can act to suppress coupling.

The local influence on coupling makes assessing the connection between coupling and cloud properties more challenging. The cloud might have been coupled to the surface while over the sea, and when it was advected into the Kongsfjorden valley the local wind changed in the sub-cloud layer, leading to decoupling. It is also difficult to evaluate coupling and local winds separately, because most coupled clouds were associated with northwest surface wind (Fig. 13b). Coupled P-MPCs had higher LWP than decoupled P-MPCs (Fig. 12a), and P-MPCs associated with northwest surface wind had higher LWP than those occurring with other surface wind directions (Fig. A1b). Perhaps the higher LWP is related to the combined effect of the two: more humidity is available from the open sea than over land and coupling is required for the water vapor to be transported from the surface to the cloud layer. There is a relationship between surface coupling and the local wind conditions at Ny-Ålesund, but to understand the impact of the combined effects on P-MPC properties would require further studies.

5 Conclusions

We present 2.5 years of vertically resolved cloud observations carried out at the AWIPEV station at Ny-Ålesund. Methods to identify persistent low-level mixed-phase clouds (P-MPCs), their coupling to the surface, and the regional and local wind conditions were developed. We found P-MPC to occur 23 % of the time, most often in summer and least often in winter. The cloud base was typically 0.54–1.0 km high, LWP was 6–52 $g\,m^{-2}$, and IWP was 0.2–12 $g\,m^{-2}$. P-MPCs were found to occur at higher altitudes in winter and lower altitudes in summer. LWP presented a lack of seasonal variation, possibly due to the selection of the cloud regime in this study. On the other hand, IWP had a clear seasonal dependence. IWP was low in the relatively warm months of summer and autumn and had a clear maximum in spring. The frequency of occurrence was found to depend on free-tropospheric wind direction, and most P-MPCs were associated with westerly winds. The height of the cloud was strongly influenced by orography. Less frequent P-MPCs and with higher cloud-base height were found with easterly winds compared to westerly winds, and these clouds had lower LWP and IWP. The most common surface wind direction in Kongsfjorden is from the southeast, but this is typically underlying synoptic winds from westerly directions. Local winds were not found to impact the occurrence or the height of the P-MPCs, but for some free-tropospheric wind directions the surface wind direction was related to variations in LWP and IWP. P-MPCs were mostly decoupled (63 %–82 % of the time), and coupling occurred most often in summer and for clouds close to the surface. Coupled P-MPC had a higher LWP than decoupled P-MPC, but no differences in IWP were found. Furthermore, the local wind patterns appeared to be related to surface coupling; specifically, the P-MPCs with surface wind directions associated with glacier outflows were more commonly decoupled. The variation in median LWP between different wind directions at 850 hPa was larger than the variation found between different surface wind regimes or coupling states. On the other hand, IWP was found to vary with regional and local wind direction as well as season, but no dependency with coupling to the surface was found. We conclude that while the regional to large-scale wind direction was important for P-MPC occurrence and their properties, the local-scale phenomena such as surface coupling and the local flow in the fjord also had an influence.

Our results suggest that the P-MPC water properties can be influenced by the processes in the local boundary layer. The observed LWP values are in the range where the clouds are not yet fully opaque, and changes in LWP will have an impact on the radiative forcing of clouds at Ny-Ålesund (Ebell et al., 2019). For numerical models to correctly describe low-level MPCs' ice and liquid water content, and hence the radiative effect, the boundary layer dynamics need to be accurately described. In Ny-Ålesund, and in other Arctic fjords, this requires that local wind in the fjord is represented, and thus a description of the orography and key surface properties (temperature, snow cover, etc.) needs to be accounted for in the model.

Long-term data sets are valuable for evaluating models since the evaluation can be carried out in a statistical manner instead of case-by-case basis. The data set presented in this paper can be used for model comparison, to provide insight into model performance regarding low-level MPCs in the complex Arctic fjord environment. In addition, the results presented here provide background information that aids the interpretation of case studies underway from recent measurement campaigns (Wendisch et al., 2019). In this study, the effects of aerosols acting as ice-nucleating particles or cloud condensation nuclei have not been evaluated. Also, the cloud microphysical processes taking place should be considered in more detail. Further work is thus needed to understand the relationships between various processes controlling the properties and development of low-level MPCs at Ny-Ålesund.

Appendix A: Details on the relationship between local wind conditions and P-MPC

A1 P-MPC properties

The results of the analysis on P-MPC properties for different wind regimes is provided here, and some possible mechanisms are contemplated. The cloud properties associated with different surface wind directions were compared separately for each weather type. Only weather types N, W, and SW were considered (Fig. A1) in order to have a sufficient amount of data (at least 30 cases) in each group being compared (Fig. 13a). The median liquid base height did not differ significantly (on a 95 % confidence level) for any of the three weather types evaluated. The northwest surface wind was associated with the highest median LWP; however, for weather type SW the differences were not statistically significant. For weather type N the median LWP for northwest surface wind was $22\,\mathrm{g\,m^{-2}}$ compared to 12 and $7.8\,\mathrm{g\,m^{-2}}$ of southeast and southwest surface winds, respectively. Also, for weather type W the northwest surface wind was associated with the highest median LWP ($39\,\mathrm{g\,m^{-2}}$), however the lowest median LWP was with southeast surface wind ($18\,\mathrm{g\,m^{-2}}$). The median IWP varied insignificantly (from 7.8 to $9.7\,\mathrm{g\,m^{-2}}$) for weather type N. For weather type SW, the southwest surface wind had the highest median IWP at $18\,\mathrm{g\,m^{-2}}$, almost double that of the median of southeast ($10\,\mathrm{g\,m^{-2}}$) and northwest ($9.1\,\mathrm{g\,m^{-2}}$) surface winds. Similarly, for weather type W the median IWP for the southwest was $16\,\mathrm{g\,m^{-2}}$ and only 11 and $9.6\,\mathrm{g\,m^{-2}}$ for southeast and northwest surface winds. Because of the temperature dependence of many microphysical processes, it would be possible that the observed differences were a result of different temperature regimes dominating in the compared groups. However, no statistically significant difference in the cloud-top temperature distributions was found (Fig. A1d).

Local conditions evidently modify the wind field in the fjord (Sect. 3.4), but whether this affects the P-MPC is not as easily determined. Although we find some differences in the P-MPC occurrence and properties with different local low-level wind patterns (Figs. 13 and A1), these could also be due to the large-scale conditions related to different local circulation patterns. We here consider some phenomena that might be taking place. The near-surface wind from the southeast could hinder the low P-MPC residing over the sea from advecting into the fjord where the observations were taking place. This would lead to higher cloud-base height for the southeast surface wind regime, or a lower frequency of occurrence, as the lowest P-MPC would be limited. For both weather types N and W the northwest surface wind had the lowest 25 percentiles of the liquid layer base height (lower edge of the boxes in Fig. A1a). Figure 13a gives no indication that the southeast surface wind would have been related to an overall lower frequency of occurrence. Although the lowest P-MPCs were more often associated with northwest surface wind, liquid base height below 400 m was also not that common for this wind regime. Hence, it seems that the southeast surface wind did not substantially prevent the P-MPC on the sea from advecting into the fjord. Considering Figs. 4c and A1a together, the depth of the layer where wind is found to deviate the strongest from the free-tropospheric wind direction is below the median P-MPC base height, and the 25th percentile is above the depth of the layer where on average the wind is in alignment with the surface wind direction. Hence, many of the P-MPCs reside in a layer where the wind direction is changing with altitude, or just above it. The wind shear could induce turbulence, which in turn could affect the properties of P-MPCs, and it might be influencing vertical fluxes of heat, moisture, and aerosols. These kind of processes could explain the differences found in IWP and LWP between different wind regimes. However, to examine these processes would require a more sophisticated description of the local circulation and turbulence in the boundary layer than was used here.

A2 Seasonality of surface wind direction and P-MPC coupling

Seasonality in near-surface wind and the degree of P-MPC coupling with different surface wind directions are presented. Figure A2 shows the wind rose for each season for 10 m wind in the studied period, June 2016–October 2018. Differences between the seasons are present in the relative importance of the three surface wind modes, in agreement with Beine et al. (2001) and Maturilli and Kayser (2017a). The summer months stand out with more common northwesterly winds, which has previously been attributed to sea breeze (Beine et al., 2001). Subsequently, the other directions are less frequent. In autumn and winter the northwesterly winds almost completely disappear. The seasonal variation is likely due to the different degree at which the drivers (e.g., sea breeze circulation, katabatic flow, channeling of free-tropospheric wind along the fjord) act in different seasons.

The relationship between surface wind and P-MPC coupling is similar in all seasons except summer (Fig. A2e–h). In winter, autumn, and spring coupling with southeast surface wind was rare or nonexistent. Coupling mostly occurred with northwest surface wind. The reasons follow those given in Sect. 4.5: the more (less) stable stratification of the lower boundary layer associated with the southwest (northwest) wind, probably related to the cold outflow from the glaciers that increase the stability of the sub-cloud layer promoting decoupling. In summer the situation is somewhat different from the other seasons. Southeast wind was still related to the fewest coupled P-MPCs, but the differences between different wind directions were smaller. Furthermore, the coupling frequency with southwest wind was very similar to that of northwest wind. The wind roses for each season (Fig. A2a–d) suggest a variation in boundary layer dynamics in summer, which could be contributing to the altered rela-

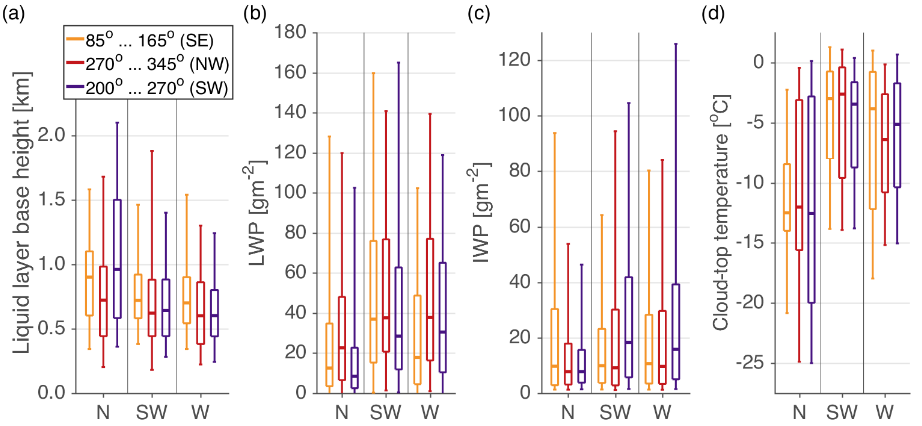

Figure A1. P-MPC liquid layer base height **(a)**, LWP **(b)**, IWP **(c)**, and cloud-top temperature **(d)** distributions for selected weather types and surface wind directions. Boxes and whiskers as in Fig. 7. The medians were found to differ (on a 95 % confidence level) in LWP for N and W and IWP for SW and W.

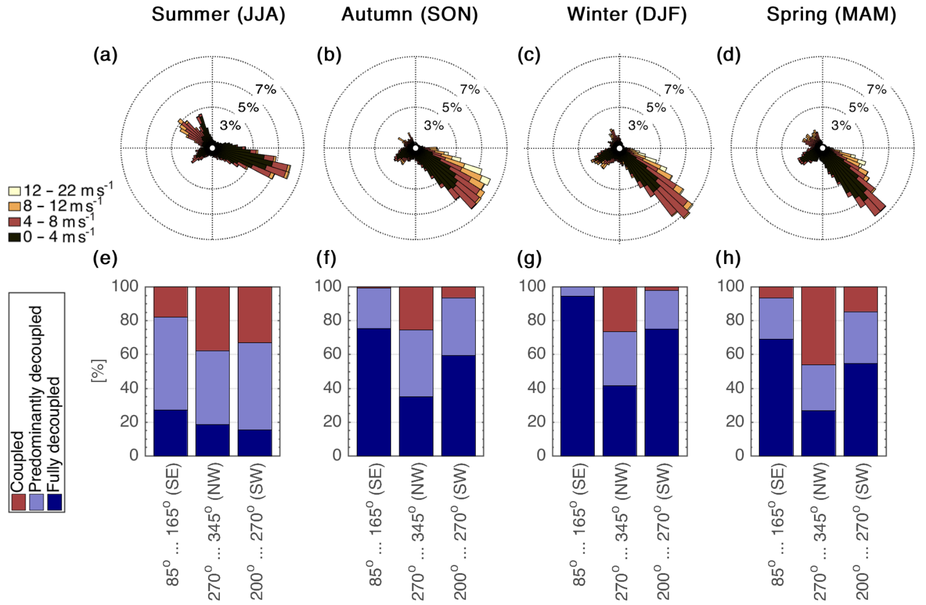

Figure A2. Wind rose for 30 min mean 10 m wind for each season **(a–d)** in the cloud observation period (June 2016–October 2018). The fraction of P-MPC cases classified as coupled, predominantly decoupled, and fully decoupled for each surface wind direction mode in each season **(e–f)**.

tionship between surface wind direction and the frequency of P-MPC coupling. Moreover, as discussed in Sect. 4.4, the overall lower stability in the boundary layer as well as the lower cloud-base height in summer enhance surface coupling compared to the other seasons. Hence, local wind conditions seem to have less importance in summer, although the interaction with the local boundary layer is present in all seasons.

Code and data availability. The Cloudnet data are available at the Cloudnet website (http://devcloudnet.fmi.fi/, last access: 25 June 2019). The radiosonde data are available in PANGAEA (https://doi.org/10.1594/PANGAEA.845373, Maturilli and Kayser (2016) for 1993–2014; https://doi.org/10.1594/PANGAEA.875196, Maturilli and Kayser (2017b) for 2015–2016; search term "project:label:AC3 ny-alesund radiosonde" afterwards). The meteorological surface observations are available in PANGAEA under the search term "Continuous meteorological observations at station Ny-Ålesund". The MWR data are also available in PANGAEA (https://doi.org/10.1594/PANGAEA.902183, Nomokonova et al., 2019c). The software used for the median test was available courtesy of Keine (2019). The cloud microphysical data set is currently under review for PANGAEA (https://doi.org/10.1594/PANGAEA.898556, Nomokonova and Ebell, 2019). Topography data in Fig. 1 are provided by Amante and Eakins (2009) (panel a) and the Norwegian Polar Institute (2014) (panel b). Color maps used in Figs. 1a, 4a, 7a, and A2a–d are provided by Crameri (2018).

Author contributions. RG carried out the method development, statistical analysis, and visualization of the results and prepared the manuscript with contributions from all co-authors. UL, SK, and MS contributed with conceptualization, research supervision, and discussions of the results. KE oversaw data management at the University of Cologne and advised in the analysis and selection of data sets. MM provided the long-term radiosonde data set and insights into the local conditions at Ny-Ålesund.

Competing interests. Matthew D. Shupe is an editor for the special issue "Arctic mixed-phase clouds as studied during the ACLOUD/PASCAL campaigns in the framework of $(AC)^3$".

Special issue statement. This article is part of the special issue "Arctic mixed-phase clouds as studied during the ACLOUD/PASCAL campaigns in the framework of $(AC)^3$ (ACP/AMT/ESSD inter-journal SI)". It is not associated with a conference.

Acknowledgements. We gratefully acknowledge the funding by the Deutsche Forschungsgemeinschaft (DFG, German Research Foundation) – project no. 268020496 – TRR 172, within the Transregional Collaborative Research Center "ArctiC Amplification: Climate Relevant Atmospheric and SurfaCe Processes, and Feedback Mechanisms $(AC)^3$". Contributions by Stefan Kneifel were funded by the German Research Foundation (DFG) under grant KN 1112/2-1 as part of the Emmy-Noether Group "Optimal combination of Polarimetric and Triple Frequency radar techniques for Improving Microphysical process understanding of cold clouds (OPTIMIce)". Contributions by Matthew Shupe were funded by the U.S. National Oceanic and Atmospheric Administration's Earth System Research Laboratory. We wish to thank the Finnish Meteorological Institute, the Aerosol, Clouds, and Trace Gases Research Infrastructure (ACTRIS), and especially Ewan O'Conner for the Cloudnet algorithm. Furthermore, this work would have not been possible without Tobias Marke's assistance regarding Cloudnet and his providing the circulation weather type, as well as Tatiana Nomokonova, who compiled the cloud microphysical data set and assisted in the use of the MWR data. We further wish to thank Christoph Ritter and Maximilian Mahn for sharing ideas and insightful discussions and Birte Kulla for providing Fig. 1b. Last but not least, we are grateful for the AWIPEV station staff for technical support, maintenance, and operation of the instruments.

Financial support. This research has been supported by the Deutsche Forschungsgemeinschaft (DFG, German Research Foundation, project no. 268020496 and grant no. KN 1112/2-1) and the U.S. National Oceanic and Atmospheric Administration's Earth System Research Laboratory.

Review statement. This paper was edited by Radovan Krejci and reviewed by three anonymous referees.

References

Amante, C. and Eakins, B. W.: ETOPO1 1 Arc-Minute Global Relief Model: Procedures, Data Sources and Analysis, NOAA Technical Memorandum NESDIS NGDC-24, National Geophysical Data Center, https://doi.org/10.7289/V5C8276M, 2009.

Argentini, S., Viola, A. P., Mastrantonio, G., Maurizi, A., Georgiadis, T., and Nardino, M.: Characteristics of the boundary layerat Ny-Ålesund in the Arctic during the ARTIST field experiment, Ann. Geophys., 46, 2, https://doi.org/10.4401/ag-3414, 2003.

Beine, H., Argentini, S., Maurizi, A., Mastrantonio, G., and Viola, A.: The local wind field at Ny-Ålesund and the Zeppelin mountain at Svalbard, Meteorol. Atmos. Phys., 78, 107–113, 2001.

Brooks, I. M., Tjernström, M., Persson, P. O. G., Shupe, M. D., Atkinson, R. A., Canut, G., Birch, C. E., Mauritsen, T., Sedlar, J., and Brooks, B. J.: The Turbulent Structure of the Arctic Summer Boundary Layer During The Arctic Summer Cloud-Ocean Study, J. Geophys. Res.-Atmos., 122, 9685–9704, 2017.

Cesana, G., Kay, J., Chepfer, H., English, J., and De Boer, G.: Ubiquitous low-level liquid-containing Arctic clouds: New observations and climate model constraints from CALIPSO-GOCCP, Geophys. Res. Lett., 39, L20804, https://doi.org/10.1029/2012GL053385, 2012.

Chang, L., Song, S., Feng, G., Zhang, Y., and Gao, G.: Assessment of the uncertainties in Arctic low-level temperature inversion characteristics in radio occultation observations, IEEE T. Geosci. Remote, 55, 1793–1803, 2017.

Choi, Y.-S., Ho, C.-H., Park, C.-E., Storelvmo, T., and Tan, I.: Influence of cloud phase composition on climate feedbacks, J. Geophys. Res.-Atmos., 119, 3687–3700, 2014.

Crameri, F.: Scientific colour-maps, Zenodo, https://doi.org/10.5281/zenodo.1243862, 2018.

Crewell, S. and Löhnert, U.: Accuracy of Boundary Layer Temperature Profiles Retrieved With Multifrequency Multiangle Microwave Radiometry, IEEE T. Geosci. Remote, 45, 2195–2201, https://doi.org/10.1109/TGRS.2006.888434, 2007.

Dahlke, S. and Maturilli, M.: Contribution of Atmospheric Advection to the Amplified Winter Warming in the Arctic North Atlantic Region, Adv. Meteorol., 2017, 4928620, https://doi.org/10.1155/2017/4928620, 2017.

De Boer, G., Eloranta, E. W., and Shupe, M. D.: Arctic mixed-phase stratiform cloud properties from multiple years of surface-based measurements at two high-latitude locations, J. Atmos. Sci., 66, 2874–2887, 2009.

Dekhtyareva, A., Holmén, K., Maturilli, M., Hermansen, O., and Graversen, R.: Effect of seasonal mesoscale and microscale meteorological conditions in Ny-Ålesund on results of monitoring of long-range transported pollution, Polar. Res., 37, 1508196, https://doi.org/10.1080/17518369.2018.1508196, 2018.

Dong, X., Xi, B., Crosby, K., Long, C. N., Stone, R. S., and Shupe, M. D.: A 10 year climatology of Arctic cloud fraction and radiative forcing at Barrow, Alaska, J. Geophys. Res., 115, D17212, https://doi.org/10.1029/2009JD013489, 2010.

Ebell, K., Nomokonova, T., Maturilli, M., and Ritter, C.: Radiative effect of clouds at Ny-Ålesund, Svalbard, as inferred from ground-based remote sensing observations, J. Appl. Meteorol. Clim., 59, 3–22, https://doi.org/10.1175/JAMC-D-19-0080.1, 2019.

Eirund, G. K., Possner, A., and Lohmann, U.: Response of Arctic mixed-phase clouds to aerosol perturbations under different surface forcings, Atmos. Chem. Phys., 19, 9847–9864, https://doi.org/10.5194/acp-19-9847-2019, 2019.

Esau, I. and Repina, I.: Wind climate in Kongsfjorden, Svalbard, and attribution of leading wind driving mechanisms through turbulence-resolving simulations, Adv. Meteorol., 2012, 568454, https://doi.org/10.1155/2012/568454, 2012.

Hogan, R. J. and O'Connor, E. J.: Facilitating cloud radar and lidar algorithms: the Cloudnet Instrument Synergy/Target Categorization product, Cloudnet documentation, 1–14, 2004.

Hogan, R. J., Jakob, C., and Illingworth, A. J.: Comparison of ECMWF winter-season cloud fraction with radar-derived values, J. Appl. Meteorol., 40, 513–525, 2001.

Hogan, R. J., Mittermaier, M. P., and Illingworth, A. J.: The retrieval of ice water content from radar reflectivity factor and temperature and its use in evaluating a mesoscale model, J. Appl. Meteorol. Clim., 45, 301–317, 2006.

Illingworth, A., Hogan, R., O'connor, E., Bouniol, D., Brooks, M., Delanoë, J., Donovan, D., Eastment, J., Gaussiat, N., Goddard, J., Haeffelin, M., Baltink, H. K., Krasnov, O. A., Pelon, J., Piriou, J., Protat, A., Russchenberg, H. W., Seifert, A., Tompkins, A. M., van Zadelhoff, G., Vinit, F., Willén, U., Wilson, D. R., and Wrench, C. L.: Cloudnet: Continuous evaluation of cloud profiles in seven operational models using ground-based observations, B. Am. Meteorol. Soc., 88, 883–898, 2007.

Intrieri, J., Fairall, C., Shupe, M., Persson, P., Andreas, E., Guest, P., and Moritz, R.: An annual cycle of Arctic surface cloud forcing at SHEBA, J. Geophys. Res., 107, 8039, https://doi.org/10.1029/2000JC000439, 2002.

Jackson, R. C., McFarquhar, G. M., Korolev, A. V., Earle, M. E., Liu, P. S., Lawson, R. P., Brooks, S., Wolde, M., Laskin, A., and Freer, M.: The dependence of ice microphysics on aerosol concentration in Arctic mixed-phase stratus clouds during ISDAC and M-PACE, J. Geophys. Res., 117, D15207, https://doi.org/10.1029/2012JD017668, 2012.

Jenkinson, A. and Collison, F.: An initial climatology of gales over the North Sea, Synoptic Climatology Branch Memorandum, 62, 1–18, 1977.

Jocher, G., Karner, F., Ritter, C., Neuber, R., Dethloff, K., Obleitner, F., Reuder, J., and Foken, T.: The near-surface small-scale spatial and temporal variability of sensible and latent heat exchange in the Svalbard region: a case study, ISRN Meteorology, 2012.

Kalesse, H., de Boer, G., Solomon, A., Oue, M., Ahlgrimm, M., Zhang, D., Shupe, M. D., Luke, E., and Protat, A.: Understanding Rapid Changes in Phase Partitioning between Cloud Liquid and Ice in Stratiform Mixed-Phase Clouds: An Arctic Case Study, Mon. Weather Rev., 144, 4805–4826, 2016.

Kay, J. E. and Gettelman, A.: Cloud influence on and response to seasonal Arctic sea ice loss, J. Geophys. Res., 114, D18204, https://doi.org/10.1029/2009JD011773, 2009.

Kay, J. E., L'Ecuyer, T., Chepfer, H., Loeb, N., Morrison, A., and Cesana, G.: Recent Advances in Arctic Cloud and Climate Research, Current Climate Change Reports, 2, 159–169, 2016.

Kayser, M., Maturilli, M., Graham, R. M., Hudson, S. R., Rinke, A., Cohen, L., Kim, J.-H., Park, S.-J., Moon, W., and Granskog, M. A.: Vertical thermodynamic structure of the troposphere during the Norwegian young sea ICE expedition (N-ICE2015), J. Geophys. Res.-Atmos., 122, 10855–10872, 2017.

Keine, C.: Moods Median Test, GitHub, available at: https://www.github.com/ChristianKeine/Moods-Mediantest, last access: 1 February 2019.

Kim, B.-M., Hong, J.-Y., Jun, S.-Y., Zhang, X., Kwon, H., Kim, S.-J., Kim, J.-H., Kim, S.-W., and Kim, H.-K.: Major cause of unprecedented Arctic warming in January 2016: Critical role of an Atlantic windstorm, Scientific Reports, 7, 40051, https://doi.org/10.1038/srep40051, 2017.

Klein, S. A., McCoy, R. B., Morrison, H., Ackerman, A. S., Avramov, A., de Boer, G., Chen, M., Cole, J. N., Del Genio, A. D., Falk, M., Foster, M. J., Fridlind, A., Golaz, J.-C., Hashino, T., Harrington, J. Y., Hoose, C., Khairoutdinov, M. F., Larson, V. E., Liu, X., Luo, Y., McFarquhar, G. M., Menon, S., Neggers, R. A. J., Park, S., Poellot, M. R., Schmidt, J. M., Sednev, I., Shipway, B. J., Shupe, M. D., Spangenberg, D.A., Sud, Y. C., Turner, D. D., Veron, D. E., von Salzen, K., Walker, G. K., Wang, Z., Wolf, A. B., Xie, S., Xu, K.-M., Yang, F., and Zhang, G.: Intercomparison of model simulations of mixed-phase clouds observed during the ARM Mixed-Phase Arctic Cloud Experiment. I: Single-layer cloud, Q. J. Roy. Meteor. Soc., 135, 979–1002, 2009.

Knudsen, E. M., Heinold, B., Dahlke, S., Bozem, H., Crewell, S., Gorodetskaya, I. V., Heygster, G., Kunkel, D., Maturilli, M., Mech, M., Viceto, C., Rinke, A., Schmithüsen, H., Ehrlich, A., Macke, A., Lÿpkes, C., and Wendisch, M.: Meteorological conditions during the ACLOUD/PASCAL field campaign near Svalbard in early summer 2017, Atmos. Chem. Phys., 18, 17995–18022, https://doi.org/10.5194/acp-18-17995-2018, 2018.

Komurcu, M., Storelvmo, T., Tan, I., Lohmann, U., Yun, Y., Penner, J. E., Wang, Y., Liu, X., and Takemura, T.: Intercomparison of the cloud water phase among global climate models, J. Geophys. Res.-Atmos., 119, 3372–3400, 2014.

Korolev, A. and Isaac, G.: Phase transformation of mixed-phase clouds, Q. J. Roy. Meteor. Soc., 129, 19–38, 2003.

Küchler, N., Kneifel, S., Löhnert, U., Kollias, P., Czekala, H., and Rose, T.: A W-Band Radar–Radiometer System for Accurate and

Continuous Monitoring of Clouds and Precipitation, J. Atmos. Ocean. Tech., 34, 2375–2392, 2017.

Lamb, D. and Verlinde, J.: Physics and chemistry of clouds, Cambridge University Press, UK, 2011.

Li, Z., Xu, K.-M., and Cheng, A.: The Response of Simulated Arctic Mixed-Phase Stratocumulus to Sea Ice Cover Variability in the Absence of Large-Scale Advection, J. Geophys. Res.-Atmos., 122, 12335–12352, 2017.

Löhnert, U. and Crewell, S.: Accuracy of cloud liquid water path from ground-based microwave radiometry 1. Dependency on cloud model statistics, Radio Sci., 38, 8041, https://doi.org/10.1029/2002RS002654, 2003.

Maturilli, M. and Ebell, K.: Twenty-five years of cloud base height measurements by ceilometer in Ny-Ålesund, Svalbard, Earth Syst. Sci. Data, 10, 1451–1456, https://doi.org/10.5194/essd-10-1451-2018, 2018.

Maturilli, M. and Kayser, M.: Homogenized radiosonde record at station Ny-Ålesund, Spitsbergen, 1993–2014, PANGAEA, https://doi.org/10.1594/PANGAEA.845373, 2016.

Maturilli, M. and Kayser, M.: Arctic warming, moisture increase and circulation changes observed in the Ny-Ålesund homogenized radiosonde record, Theor. Appl. Climatol., 130, 1–17, 2017a.

Maturilli, M. and Kayser, M.: Homogenized radiosonde record at station Ny-Ålesund, Spitsbergen, 2015–2016, PANGAEA, https://doi.org/10.1594/PANGAEA.875196, 2017b.

Maturilli, M., Herber, A., and König-Langlo, G.: Climatology and time series of surface meteorology in Ny-Ålesund, Svalbard, Earth Syst. Sci. Data, 5, 155–163, https://doi.org/10.5194/essd-5-155-2013, 2013.

McCoy, D. T., Tan, I., Hartmann, D. L., Zelinka, M. D., and Storelvmo, T.: On the relationships among cloud cover, mixed-phase partitioning, and planetary albedo in GCMs, J. Adv. Model. Earth Sy., 8, 650–668, 2016.

Mech, M., Kliesch, L.-L., Anhäuser, A., Rose, T., Kollias, P., and Crewell, S.: Microwave Radar/radiometer for Arctic Clouds (MiRAC): first insights from the ACLOUD campaign, Atmos. Meas. Tech., 12, 5019–5037, https://doi.org/10.5194/amt-12-5019-2019, 2019.

Mioche, G., Jourdan, O., Ceccaldi, M., and Delanoë, J.: Variability of mixed-phase clouds in the Arctic with a focus on the Svalbard region: a study based on spaceborne active remote sensing, Atmos. Chem. Phys., 15, 2445–2461, https://doi.org/10.5194/acp-15-2445-2015, 2015.

Mioche, G., Jourdan, O., Delanoë, J., Gourbeyre, C., Febvre, G., Dupuy, R., Monier, M., Szczap, F., Schwarzenboeck, A., and Gayet, J.-F.: Vertical distribution of microphysical properties of Arctic springtime low-level mixed-phase clouds over the Greenland and Norwegian seas, Atmos. Chem. Phys., 17, 12845–12869, https://doi.org/10.5194/acp-17-12845-2017, 2017.

Morrison, A., Kay, J., Chepfer, H., Guzman, R., and Yettella, V.: Isolating the liquid cloud response to recent Arctic sea ice variability using spaceborne lidar observations, J. Geophys. Res.-Atmos., 123, 473–490, 2018.

Morrison, H., Shupe, M. D., Pinto, J. O., and Curry, J. A.: Possible roles of ice nucleation mode and ice nuclei depletion in the extended lifetime of Arctic mixed-phase clouds, Geophys. Res. Lett., 32, L18801, https://doi.org/10.1029/2005GL023614, 2005.

Morrison, H., Pinto, J. O., Curry, J. A., and McFarquhar, G. M.: Sensitivity of modeled Arctic mixed-phase stratocumulus to cloud condensation and ice nuclei over regionally varying surface conditions, J. Geophys. Res., 113, D05203, https://doi.org/10.1029/2007JD008729, 2008.

Morrison, H., De Boer, G., Feingold, G., Harrington, J., Shupe, M. D., and Sulia, K.: Resilience of persistent Arctic mixed-phase clouds, Nat. Geosci., 5, 11–17, 2012.

Nomokonova, T. and Ebell, K.: Cloud microphysical properties retrieved from ground-based remote sensing at Ny-Ålesund (10 June 2016–8 October 2018), University of Cologne, PANGAEA, https://doi.org/10.1594/PANGAEA.898556, 2019.

Nomokonova, T., Ebell, K., Löhnert, U., Maturilli, M., and Ritter, C.: The influence of anomalous atmospheric conditions at Ny-Ålesund on clouds and their radiative effect, Atmos. Chem. Phys. Discuss., https://doi.org/10.5194/acp-2019-985, in review, 2019a.

Nomokonova, T., Ebell, K., Löhnert, U., Maturilli, M., Ritter, C., and O'Connor, E.: Statistics on clouds and their relation to thermodynamic conditions at Ny-Ålesund using ground-based sensor synergy, Atmos. Chem. Phys., 19, 4105–4126, https://doi.org/10.5194/acp-19-4105-2019, 2019b.

Nomokonova, T., Ritter, C., and Ebell, K.: HATPRO microwave radiometer measurements at AWIPEV, Ny-Ålesund (2016–2018), PANGAEA, https://doi.org/10.1594/PANGAEA.902183, 2019c.

Norgren, M. S., de Boer, G., and Shupe, M. D.: Observed aerosol suppression of cloud ice in low-level Arctic mixed-phase clouds, Atmos. Chem. Phys., 18, 13345–13361, https://doi.org/10.5194/acp-18-13345-2018, 2018.

Norwegian Polar Institute: Kartdata Svalbard 1 : 100 000 (S100 Kartdata)/Map Data, Norwegian Polar Institute, Data set, https://doi.org/10.21334/npolar.2014.645336c7, 2014.

Pithan, F., Svensson, G., Caballero, R., Chechin, D., Cronin, T. W., Ekman, A. M., Neggers, R., Shupe, M. D., Solomon, A., Tjernström, M., and Wendisch, M.: Role of air-mass transformations in exchange between the Arctic and mid-latitudes, Nat. Geosci., 11, 805–812, 2018.

Qiu, S., Xi, B., and Dong, X.: Influence of Wind Direction on Thermodynamic Properties and Arctic Mixed-Phase Clouds in Autumn at Utqiaġvik, Alaska, J. Geophys. Res.-Atmos., 123, 9589–9603, 2018.

Quinn, P., Shaw, G., Andrews, E., Dutton, E., Ruoho-Airola, T., and Gong, S.: Arctic haze: current trends and knowledge gaps, Tellus B, 59, 99–114, 2007.

Rose, T., Crewell, S., Löhnert, U., and Simmer, C.: A network suitable microwave radiometer for operational monitoring of the cloudy atmosphere, Atmos. Res., 75, 183–200, 2005.

Savre, J., Ekman, A. M., Svensson, G., and Tjernström, M.: Large-eddy simulations of an Arctic mixed-phase stratiform cloud observed during ISDAC: sensitivity to moisture aloft, surface fluxes and large-scale forcing, Q. J. Roy. Meteor. Soc., 141, 1177–1190, 2015.

Scott, R. C. and Lubin, D.: Unique manifestations of mixed-phase cloud microphysics over Ross Island and the Ross Ice Shelf, Antarctica, Geophys. Res. Lett., 43, 2936–2945, 2016.

Sedlar, J., Shupe, M. D., and Tjernström, M.: On the relationship between thermodynamic structure and cloud top, and its climate significance in the Arctic, J. Climate, 25, 2374–2393, 2012.

Serreze, M. C., Barrett, A. P., Stroeve, J. C., Kindig, D. N., and Holland, M. M.: The emergence of surface-based Arctic amplification, The Cryosphere, 3, 11–19, https://doi.org/10.5194/tc-3-11-2009, 2009.

Serreze, M. C. and Barry, R. G.: Processes and impacts of Arctic amplification: A research synthesis, Global Planet. Change, 77, 85–96, 2011.

Sheskin, D.: Handbook of Parametric and Nonparametric Statistical Procedures, 2nd edn., CRC Press, USA, 2000.

Shupe, M. D.: Clouds at Arctic atmospheric observatories. Part II: Thermodynamic phase characteristics, J. Appl. Meteorol. Clim, 50, 645–661, 2011.

Shupe, M. D. and Intrieri, J. M.: Cloud radiative forcing of the Arctic surface: The influence of cloud properties, surface albedo, and solar zenith angle, J. Climate, 17, 616–628, 2004.

Shupe, M. D., Kollias, P., Matrosov, S. Y., and Schneider, T. L.: Deriving mixed-phase cloud properties from Doppler radar spectra, J. Atmos. Ocean. Tech., 21, 660–670, 2004.

Shupe, M. D., Matrosov, S. Y., and Uttal, T.: Arctic mixed-phase cloud properties derived from surface-based sensors at SHEBA, J. Atmos. Sci., 63, 697–711, 2006.

Shupe, M. D., Kollias, P., Persson, P. O. G., and McFarquhar, G. M.: Vertical motions in Arctic mixed-phase stratiform clouds, J. Atmos. Sci., 65, 1304–1322, 2008.

Shupe, M. D., Walden, V. P., Eloranta, E., Uttal, T., Campbell, J. R., Starkweather, S. M., and Shiobara, M.: Clouds at Arctic atmospheric observatories. Part I: Occurrence and macrophysical properties, J. Appl. Meteorol. Clim, 50, 626–644, 2011.

Shupe, M. D., Persson, P. O. G., Brooks, I. M., Tjernström, M., Sedlar, J., Mauritsen, T., Sjogren, S., and Leck, C.: Cloud and boundary layer interactions over the Arctic sea ice in late summer, Atmos. Chem. Phys., 13, 9379–9399, https://doi.org/10.5194/acp-13-9379-2013, 2013.

Solomon, A., Shupe, M. D., Persson, O., Morrison, H., Yamaguchi, T., Caldwell, P. M., and de Boer, G.: The sensitivity of springtime Arctic mixed-phase stratocumulus clouds to surface-layer and cloud-top inversion-layer moisture sources, J. Atmos. Sci., 71, 574–595, 2014.

Solomon, A., de Boer, G., Creamean, J. M., McComiskey, A., Shupe, M. D., Maahn, M., and Cox, C.: The relative impact of cloud condensation nuclei and ice nucleating particle concentrations on phase partitioning in Arctic mixed-phase stratocumulus clouds, Atmos. Chem. Phys., 18, 17047–17059, https://doi.org/10.5194/acp-18-17047-2018, 2018.

Solomon, S., Qin, D., Manning, M., Averyt, K., and Marquis, M.: Climate Change 2007: The Physical Science Basis. Contribution of Working Group I to the Fourth Assessment Report of the Intergovernmental Panel on Climate Change, vol. 4, edited by: Solomon, S., Qin, D., Manning, M., Chen, Z., Marquis, M., Averyt, K. B., Tignor, M., and Miller, H. L., Cambridge University Press, Cambridge, UK and New York, NY, USA, 2007.

Sotiropoulou, G., Sedlar, J., Tjernström, M., Shupe, M. D., Brooks, I. M., and Persson, P. O. G.: The thermodynamic structure of summer Arctic stratocumulus and the dynamic coupling to the surface, Atmos. Chem. Phys., 14, 12573–12592, https://doi.org/10.5194/acp-14-12573-2014, 2014.

Svendsen, H., Beszczynska-Møller, A., Hagen, J. O., Lefauconnier, B., Tverberg, V., Gerland, S., Børre Ørbæk, J., Bischof, K., Papucci, C., Zajaczkowski, M., Azzolini, R., Bruland, O., and Wiencke, C.: The physical environment of Kongsfjorden–Krossfjorden, an Arctic fjord system in Svalbard, Polar Res., 21, 133–166, 2002.

Wendisch, M., Macke, A., Ehrlich, A., Lüpkes, C., Mech, M., Chechin, D., Dethloff, K., Barientos, C., Bozem, H., Brückner, M., Clemen, H., Crewell, S., Donth, T., Dupuy, R., Ebell, K., Egerer, U., Engelmann, R., Engler, C., Eppers, O., Gehrmann, M., Gong, X., Gottschalk, M., Gourbeyre, C., Griesche, H., Hartmann, J., Hartmann, M., Heinold, B., Herber, A., Herrmann, H., Heygster, G., Hoor, P., Jafariserajehlou, S., Jäkel, E. Jërvinen, E., Jourdan, O., Kästner, U., Kecorius, S., Knudsen, E. M., Köllner, F., Kretzschmar, J., Lelli, L., Leroy, D., Maturilli, M., Mei, L., Mertes, S., Mioche, G., Neuber, R., Nicolaus, M., Nomokonova, T., Notholt, J., Palm, M., van Pinxteren, M., Quaas, J., Richter, P., Ruiz-Donoso, E., Schäfer, M., Schmieder, K., Schnaiter, M., Schneider, J., Schwarzenböck, A., Seifert, P., Shupe, M. D., Siebert, H., Spreen, G., Stapf, J., Stratmann, F., Vogl, T., Welti, A., Wex, H., Wiedensohler, A., Zanatta, M., and Zeppenfeld, S.: The Arctic Cloud Puzzle: Using ACLOUD/PASCAL Multiplatform Observations to Unravel the Role of Clouds and Aerosol Particles in Arctic Amplification, B. Am. Meteorol. Soc., 100, 841–871, 2019.

Wendish, M., Brückner, M., Burrows, J. P., Crewell, S., Dethloff, K., Ebell, K., Lüpkes, C., Macke, A., Notholt, J., Quaas, J., Rinke, A., and Tegen, I.: Understanding Causes and Effects of Rapid Warming in the Arctic, EOS, 98, https://doi.org/10.1029/2017EO064803, 2017.

Westbrook, C. D. and Illingworth, A. J.: Evidence that ice forms primarily in supercooled liquid clouds at temperatures $> -27\,^{\circ}$C, Geophys. Res. Lett., 38, L14808, https://doi.org/10.1029/2011GL048021, 2011.

Woods, C., Caballero, R., and Svensson, G.: Large-scale circulation associated with moisture intrusions into the Arctic during winter, Geophys. Res. Lett., 40, 4717–4721, 2013.

Yamartino, R. J.: A comparison of several "single-pass" estimators of the standard deviation of wind direction, J. Clim. Appl. Meteorol., 23, 1362–1366, 1984.

Young, G., Jones, H. M., Choularton, T. W., Crosier, J., Bower, K. N., Gallagher, M. W., Davies, R. S., Renfrew, I. A., Elvidge, A. D., Darbyshire, E., Marenco, F., Brown, P. R. A., Ricketts, H. M. A., Connolly, P. J., Lloyd, G., Williams, P. I., Allan, J. D., Taylor, J. W., Liu, D., and Flynn, M. J.: Observed microphysical changes in Arctic mixed-phase clouds when transitioning from sea ice to open ocean, Atmos. Chem. Phys., 16, 13945–13967, https://doi.org/10.5194/acp-16-13945-2016, 2016.

Zängl, G., Reinert, D., Rípodas, P., and Baldauf, M.: The ICON (ICOsahedral Non-hydrostatic) modelling framework of DWD and MPI-M: Description of the non-hydrostatic dynamical core, Q. J. Roy. Meteor. Soc., 141, 563–579, 2015.

Zhao, M. and Wang, Z.: Comparison of Arctic clouds between European Center for Medium-Range Weather Forecasts simulations and Atmospheric Radiation Measurement Climate Research Facility long-term observations at the North Slope of Alaska Barrow site, J. Geophys. Res., 115, D23202, https://doi.org/10.1029/2010JD014285, 2010.

Zuidema, P., Baker, B., Han, Y., Intrieri, J., Key, J., Lawson, P., Matrosov, S., Shupe, M., Stone, R., and Uttal, T.: An Arctic springtime mixed-phase cloudy boundary layer observed during SHEBA, J. Atmos. Sci., 62, 160–176, 2005.

IV Observational signatures of mixed-phase cloud structures revealed by radar Doppler spectrum skewness

9 Introduction

The first study (Chapter III) found that persistent low-level MPCs (P-MPC) are common above Ny-Ålesund, and that cloud properties are impacted by wind conditions and thermodynamical surface coupling. However, the differences between the different cloud categories are exceeded by the variability within the categories. For example, the LWP was on average higher for coupled than decoupled P-MPC, but the values span a similar range and other processes than surface coupling need to be considered for explaining the LWP for any specific cloud case. The analyses in the first study show that while the local and synoptic scale forcing impact the clouds, they are not sufficient to fully explain the observed variability in cloud properties and the evolution of the P-MPC. Furthermore, the mechanisms by which the environmental conditions modify the clouds were not examined. To address these questions a more detailed look into the processes within the cloud is required. This conclusions is also widely supported by the literature (Sect. 2.2). While the thermodynamic conditions are considered important, the central role of microphysical processes to steer the cloud life cycle is also recognized. It is therefore worth considering how the highly resolved Doppler radar data could be further utilized. The second study of the thesis focuses on the use of the cloud radar Doppler spectra for the research of Arctic MPCs.

There is an ongoing need for improved numerical representation of mixed-phase cloud processes (Sect. 2). To this end, observational datasets are required to evaluate model parameterizations. Vertically resolved and continuously operated remote sensing instruments can provide valuable information on cloud properties under variable atmospheric conditions, but lack the detailed description of hydrometeors (e.g. particle size distribution, ice crystal shape) that in situ observations can provide. The use of remote sensing datasets for model evaluation is challenging because it is often not possible to unambiguously attribute the measurements to exact process rates. However, certain features in the observed parameters can be indicative of specific processes, sometimes referred to as observational "fingerprints", and thereby provide constraints for model parameterizations. Previous studies have shown that microphysical processes such as drizzle formation riming, aggregation, and secondary ice production can be identified by a detailed analysis of radar Doppler spectra (Giangrande et al., 2016, Kalesse et al., 2016a, Kollias et al., 2011a, Rambukkange et al., 2011, Zawadzki et al., 2001). Particularly in warm clouds, parameters derived from the cloud radar Doppler spectra have proven useful for the evaluation of model parameterizations (Acquistapace, 2017, Rémillard et al., 2017). Because of a larger variability in hydrometeor populations and possible processes, observational fingerprints in cloud radar Doppler spectra are less well characterized for mixed-phase clouds.

The use of the lower moments of the radar Doppler spectra is commonplace in studies on Arctic mixed-phase clouds where a vertically pointing millimeter wavelength cloud radar (MMCR) is available. The lower moments of the Doppler spectra, taken here to refer to reflectivity (Z_e), mean Doppler velocity (V_m), and Doppler spectrum width (σ), provide key information about the occurrence and properties of hydrometeors. Specifically, the spectrum width has been used as an indicator for mixed-phase conditions (Shupe, 2007). Because the supercooled liquid droplets have a terminal fall velocity of $0\,\mathrm{m\,s^{-1}}$ while ice particles fall at 0.3–$1\,\mathrm{m\,s^{-1}}$, the presence of both liquid and ice in the radar measuring volume increases the spectrum width. Several studies have used mean profiles of the lower moments to study the effects of thermodynamical conditions on Arctic MPCs (Qiu et al., 2018, Sedlar et al., 2012, Sedlar and Tjernström, 2009, Sotiropoulou et al., 2014, 2016). These parameters are also used to inform model set-up and to evaluate model performance (Marsham et al., 2006, Norgren et al., 2018, Schemann and Ebell, 2020). Furthermore, the radar parameters can be used to retrieve microphysical properties such as liquid and ice water content and effective radii as well as eddy dissipation rate, although some of the techniques are only applicable for single-phase conditions (Shupe et al., 2012, 2015, 2008c, and references therein). In certain situations also microphysical processes can be detected from the lower moments, for example the increase in V_m in a layer containing liquid is indicative of riming (Kalesse et al., 2016a, Zawadzki et al., 2001). Only occasionally higher moments or further parameters derived from the Doppler spectra (e.g. number of peaks, left and right slope) are used in studies about mixed-phase clouds. This introduction covers the literature on radar Doppler spectra based techniques that go beyond the lower moments, with a focus on mixed-phase clouds but not limited to the Arctic.

Owing to the importance of phase-partitioning to radiative properties and the development of the cloud (Sect. 2.2) and the importance of detecting supercooled liquid for aviation safety (Wang et al., 2017), several studies have focused on using the Doppler spectra to determine hydrometeor phase and to detect super-cooled liquid in mixed-phase clouds. Because ceilometer and lidar attenuate by an optical depth of about 3, a reliable phase detection from cloud radar that can be applied to deep multi-layered clouds is desirable. Luke and Kollias (2007) used a range of parameters describing the Doppler spectrum (e.g. the moments, minimum and maximum detected velocity, left and right slope) to train a neural network for hydrometeor phase classification. Riihimaki et al. (2017) used k-means clustering of a set of spectral parameters for hydrometeor phase classification, and state that the variables most effective in detecting mixed-phase volumes where spectrum width, left slope and right slope. Recently, Silber et al. (2019a) showed that there are considerable limitations in accurately detecting super-cooled liquid with bulk-parameters such as the Doppler spectrum width. Luke et al. (2010) showed that by identifying peaks in the Doppler spectrum it is possible to detect the presence of super-cooled liquid in cloud regions where lidar and ceilometer cannot penetrate. Increasingly sophisticated methods to identify different peaks in the Doppler spectrum are carried out to facilitate phase classification as well as process studies (Kalesse et al., 2019, Melchionna et al., 2008, Radenz et al., 2019).

The identification of the liquid peak in the Doppler spectra opens further possibilities for retrieving cloud and atmospheric parameters. Decomposing the spectra to different vertically consistent modes allows the determination of reflectivity and mean Doppler velocity profiles for liquid and ice phase separately (Rambukkange et al., 2011, Shupe et al., 2004, Yu et al., 2014). Having obtained the Ze related to super-cooled liquid allows the application of retrievals for liquid water content and droplet effective radius (Shupe et al., 2004, Verlinde et al., 2007). Furthermore, cloud droplets can be used as tracers for air motions due to their negligible terminal velocity (Gossard, 1994, Kollias et al., 2001, Shupe et al., 2004). Identifying the liquid peak and associated Doppler velocity can therefore be used to estimate vertical motions and allows for the correction of ice particle Doppler velocities with air motions to get better estimates of the fall velocities (Shupe et al., 2004, Yu et al., 2014). In a more simple approach, the vertical motions can also be estimated from the slow falling edge of the spectra (Shupe et al., 2008a,b, Sokol et al., 2018, Zheng et al., 2017).

Already Zawadzki et al. (2001) suggested that the detailed consideration of Doppler spectrum profiles shows indicators of riming and secondary ice production in a deep stratiform cloud, although the X-band radar used in their study was not able to detect the super-cooled droplets. Later Rambukkange et al. (2011) and Giangrande et al. (2016) found corresponding structures in MMCR Doppler spectra, where also the super-cooled droplets were identifiable. In these studies ice falling into a layer of super-cooled liquid was found to increase in fall velocity, and within the liquid layer a new mode appeared in the Doppler spectra. Given the thermodynamic conditions were favorable (Rambukkange et al., 2011), and supported by air craft in situ and surface disdrometer observations (Giangrande et al., 2016), the new mode was attributed to new ice via rime-splintering, and the increase in fall velocity of the background ice to be due to riming. Kalesse et al. (2016a) further explored the use of such observational fingerprints of riming to constrain the riming process in a 1-D bin microphysical model. Verlinde et al. (2013) studied in detail an Arctic multi-layered mixed-phase cloud using Doppler spectra supported by aircraft in situ observations, and was additionally able to identify drizzle in the spectra. Verlinde et al. (2013) and Giangrande et al. (2016) demonstrate how aircraft observations can be used to guide the interpretation of the Doppler spectra, which then can be applied to describe the studied cloud system spatially and temporally beyond the very limited aircraft sampling. Another approach to support the interpretation of the features in the MMCR Doppler spectra is to combine it with a polarimetric radar. Oue et al. (2016), Oue et al. (2018) and Vogel and Fabry (2018) showed that this way additional insights to the riming process could be found. These examples of finding signatures of microphysical processes in a detailed analysis of single frequency non-polarimetric radar Doppler spectra are all from multi-layered clouds, and only a few (namely Kalesse et al., 2016a, Oue et al., 2016, 2018, Verlinde et al., 2013) are from the Arctic.

In the presence of hydrometeors with varying terminal velocity, the skewness of the Doppler spectrum gives an indication whether the spectral reflectivity is dominated by the slower or faster falling hydrometeors (Luke and Kollias, 2013). Note, that the skewness referred to in this work is the skewness of the cloud radar Doppler spectra and not the skewness of the vertical wind distribution. The Doppler spectrum skewness has been found to be a useful parameter to study drizzle onset (Acquistapace et al., 2019, Kollias et al., 2011b) and for retrieving microphysical parameters in ice clouds (Maahn et al., 2015, Maahn and Löhnert, 2017). The skewness-Z_e relationship in warm drizzling clouds is found so robust it has even been suggested as a potential method for radar calibration (Maahn et al., 2019). Also Kalesse et al. (2016a) presented the skewness of the super-cooled liquid mode to infer the presence of drizzle in the mixed-phase cloud in question. The skewness of the Doppler spectrum has the advantage that it is insensitive to absolute radar calibration or attenuation, but requires a careful processing of the data (Luke and Kollias, 2013, Williams et al., 2018). So far skewness has not had a correspondingly important role in the study of mixed-phase clouds as in the other cloud regimes mentioned. Some phase-classification algorithms utilize skewness (Luke and Kollias, 2007), although Riihimaki et al. (2017) and Silber et al. (2019a) state that the spectrum width and the left and right slope are the parameters contributing most to the mixed-phase detection. Giangrande et al. (2016) found that the part of the cloud where considerable riming and secondary ice production was identified was characterized by a strong negative skewness (defined as + up, see Fig.1c and 9b in Giangrande et al., 2016). Kalesse et al. (2016b) showed a time-height plot for skewness in a low-level stratiform MPC in the Arctic (Fig. 5h in Kalesse et al., 2016b). At cloud top, skewness indicates that cloud droplets are dominating the Doppler spectra, below which skewness changes sign when the ice starts to dominate. In the precipitating ice below the cloud a range of skewness values from zero to negative to positive are observed over the 1.5 day period the cloud was present above the site. Studies utilizing skewness in a statistical sense beyond individual case studies, such has been done with drizzle in warm clouds, are currently lacking for the mixed-phase cloud regime.

For Arctic low-level stratiform mixed-phase clouds the MMCR Doppler spectra beyond the lower moments has mainly been utilized as a tool for separating liquid and ice Z_e and V_m (e.g. Shupe et al., 2008c). The retrieval of vertical motions facilitated key findings for the way cloud scale dynamics modulate the amount of supercooled liquid and ice in the cloud (Shupe et al., 2008a), and the interaction of the cloud with the boundary layer (Shupe et al., 2013). Kalesse et al. (2016b) presented a skewness time series for this cloud regime and interpreted it in agreement with other observation and modeled conditions, but did not analyze the skewness further. The utilization of skewness is challenging in mixed-phase clouds due to the possibility of multiple co-existing hydrometeor populations and different combinations that may lead to similar signatures in the Doppler spectra (Oue et al., 2018). However, given the success of using skewness in combination with other radar parameters for studying warm rain processes, it is worth considering the possibilities of skewness for investigating MPCs. Furthermore, very few measurement techniques exist that can observe the interplay between supercooled liquid and ice, and any approaches that can probe the development of mixed-phase cloud volumes have the potential to be beneficial.

This second study of the dissertation explores the possibility of using cloud radar Doppler spectrum skewness for studying microphysical processes in the cloud top liquid layer of the persistent low-level mixed-phase clouds (P-MPC). Due to the strong size dependency of Z_e, skewness could provide insights to the growth of ice particles and the early stages of precipitation formation. In the right conditions skewness could also indicate if supercooled liquid or ice dominate the radar signal, as described by Kalesse et al. (2016b). The P-MPC are identified following the criteria described in Sect. 8, but a longer time series is included here as more radar data (Sect. 4.1) has become available since the conclusion of the first study. Data collected from 10 June 2016 to 8 October 2018 and 14 June

2019 to 31 December 2019 are analyzed. Furthermore, only profiles that are mixed-phase according to Cloudnet are considered, and for each P-MPC case a combined minimum of 10 minute (20 Cloudnet profiles) of mixed-phase profiles was required. This is of course limited to the ability to Cloudnet to correctly identify supercooled liquid and ice, which has known limitations (Sect. 5), but including profiles that a priori are not expected to include mixed-phase clouds to analyze mixed-phase conditions would be counterproductive. A cloud with a single liquid layer is the most basic kind of MPC, and a good starting point for developing the basis of exploiting skewness in MPCs in general. Furthermore, the analysis of the Doppler spectra is predominantly focused on cases where supercooled liquid is producing an identifiable radar signal. First, additional processing of the Doppler spectrum data was carried out (Sect. 10). Sect. 11 focuses on building an understanding of the radar Doppler spectra and its moments in P-MPCs to develop a conceptual model of Doppler spectrum skewness in the liquid containing layer. Selected case studies are investigated, and key assumptions and challenges are discussed. In Sect. 12 skewness profiles with a distinct layered structure are analyzed in more detail. An algorithm to detect the feature, and its commonality and the connections with other cloud properties are investigated. In Sect. 13 possible ways forward are discussed. The summary and conclusions (Sect. 14) close the chapter.

10 Additional processing of the radar Doppler spectra

The instruments, measurement set-up, data processing and quality control have been described in Chapter II. Specifically for this study, additional processing steps for the radar Doppler spectra were applied and are briefly described here.

As in any observational data, also the cloud radar Doppler spectrum contains random noise. Given an adequate signal-to-noise ratio, this does not impose considerable issues for the integrated reflectivity (Ze) or mean Doppler velocity (V_m). However, higher moments increasingly suffer from noisiness in the data (Lenschow et al., 2000) and the noise interferes with the analysis of the Doppler spectra. To mitigate these issues, a 5-point moving mean was applied on the radar power spectra. Significant peaks were identified using the peak noise level calculated from the unaveraged spectra (see Sect. 4.1). Only peaks with at least 5 consecutive bins above the peak noise level were considered. After identifying the peaks, the peak edges were set to be the first and last bin where the power was above the peak noise floor, and the noise was removed. For this study the moments are calculated following Equations 11–14 including all significant peaks (and not only the strongest peak as was done for example by Williams et al., 2018, or Kalesse et al., 2016a). Figs. 6a and b show two examples of Doppler spectra for a MPC observed at Ny-Ålesund on 23 November 2016, and the moments calculated before and after applying the moving mean on the spectra. As can be expected, the moving mean makes the major features of the spectra more prominent. The lower moments are not strongly affected, but for the higher moments the difference can be considerable. Figs. 6c and d show a timeseries of skewness (S_k) profiles without and with, respectively, the moving mean applied on the Doppler spectra. The main features of the skewness field are not altered, but Fig. 6d is overall slightly less cluttered. To further improve the quality, a 3-by-3 moving mean (± 1 range gate and ± 1 time step) was applied on the moments timeseries. Fig. 6e shows the example skewness timeseries after this last step, demonstrating a less noisy skewness signal compared to Fig. 6c.

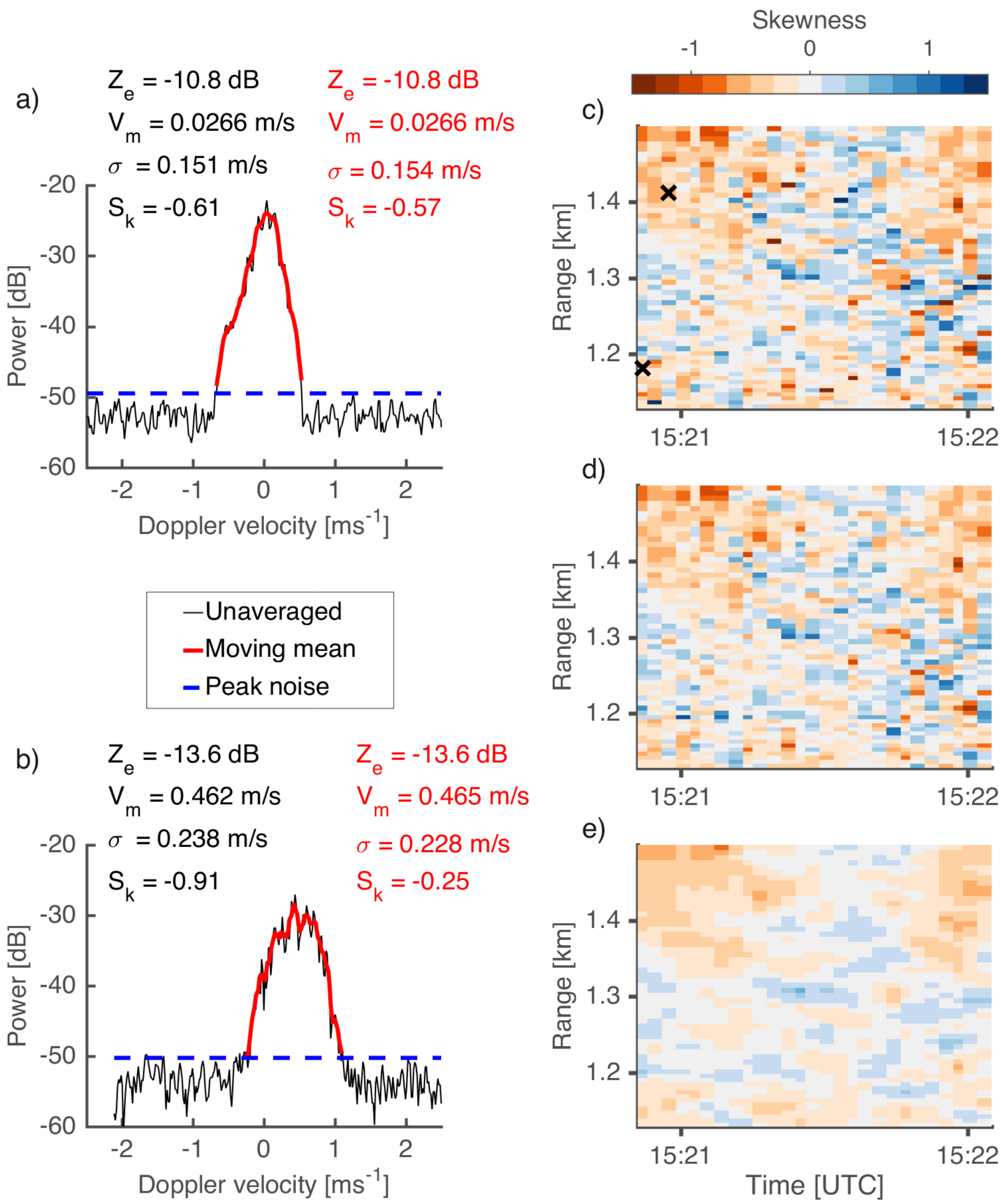

Figure 6: Examples for the cloud radar power spectrum (a, b) and skewness time height cross sections (c-e) at different processing steps: c) before additional processing, d) after applying a low-pass filter on the spectra, and e) after applying a low-pass filter on the skewness field (see text for details). In a) and b), the power spectra before (black) and after (red) applying a 5-point moving mean and the identification of significant peaks is shown. The moments given in black and red are calculated from the spectra without and with the moving mean, respectively. The corresponding time and height of the example spectra are shown by the black crosses in panel c, a) at 1.41 km and b) at 1.18 km.

Different number of bins for the moving mean of the Doppler spectra were tested. A very narrow averaging window did not result to considerable improvements in the quality of the spectra or the moments, where as a broad window led to a loss of features in the spectra. The value used (5) was chosen as a compromise between these effects. It should be noted that the treatment used here is only one option, chosen for simplicity, and alternative techniques are available (Williams et al., 2018).

11 Radar Doppler spectra in low-level mixed-phase clouds

Here, the Doppler spectrum and its moments are investigated through examples of P-MPC cases observed above Ny-Ålesund. In the following, three different P-MPC cases are considered. The cases are chosen to represent clouds with different characteristics, all of which fall under the label of "persistent stratiform MPC" at Ny-Ålesund. All of the cases feature a persistent liquid layer at cloud top, but the amount of liquid and precipitation vary. The Doppler spectra is interpreted with the support of auxiliary data and existing literature. The first case (Sect. 11.1) is presented in more detail, as it will be returned to in the next section. The second and third case (Sect. 11.2 and 11.3) will be only shortly introduced and the focus is plainly on the Doppler spectra. The last part of this section summarizes the findings of the case studies to build a conceptual understanding of how the Doppler spectrum skewness (S_k) describes the P-MPC and which processes influence it. Also key challenges of interpreting S_k are discussed. At the end, assumptions required for further analysis are stated.

Throughout this section, only low-level MPC with a single liquid layer are considered and the focus is on the liquid-containing layer at the top of the cloud. All cases selected are chosen to be free from other clouds above because this makes it possible to attribute all of the measured LWP to the low-level cloud, and processes such as seeding or radiative coupling with a cloud above can be excluded. Individual profiles shown in this section are labeled as A, B, C,... in the order in which they are discussed. The labeling continues through Sects. 11.1–11.3 to avoid ambiguity.

11.1 5 November 2016: Mixed-phase cloud ideal for investigating the Doppler spectra

Case overview

The first case considered is a mixed-phase cloud present above Ny-Ålesund for the entire day on the 5 November 2016 (Fig. 7). The previous day deep multi-layered clouds were observed, which gave way to a low-level cloud shortly after midnight. According to the Cloudnet classification the low-level cloud was mixed-phase, with a liquid layer at cloud top and continuous ice precipitation (Fig. 7b). In the early morning, the cloud top height was close to 1 km and the liquid base around 600 m. During the day the cloud slowly lifted and the liquid layer became thicker so that by late evening the base of the liquid layer had reached 1 km and cloud top was nearing 2 km. No further clouds above the low cloud were detected before the evening when a mid-level cloud appeared (Fig. 7a,b). Although the Cloudnet target classification shows a rather steady low-level MPC, inspecting the radar reflectivity (Z_e) and liquid water path (LWP) timeseries reveal considerable variability (Fig. 7a,c). At the beginning of the day Z_e was relatively high (at -10 dBz) but decreased quickly. Over most of the day Z_e stayed low, with slightly higher values starting from

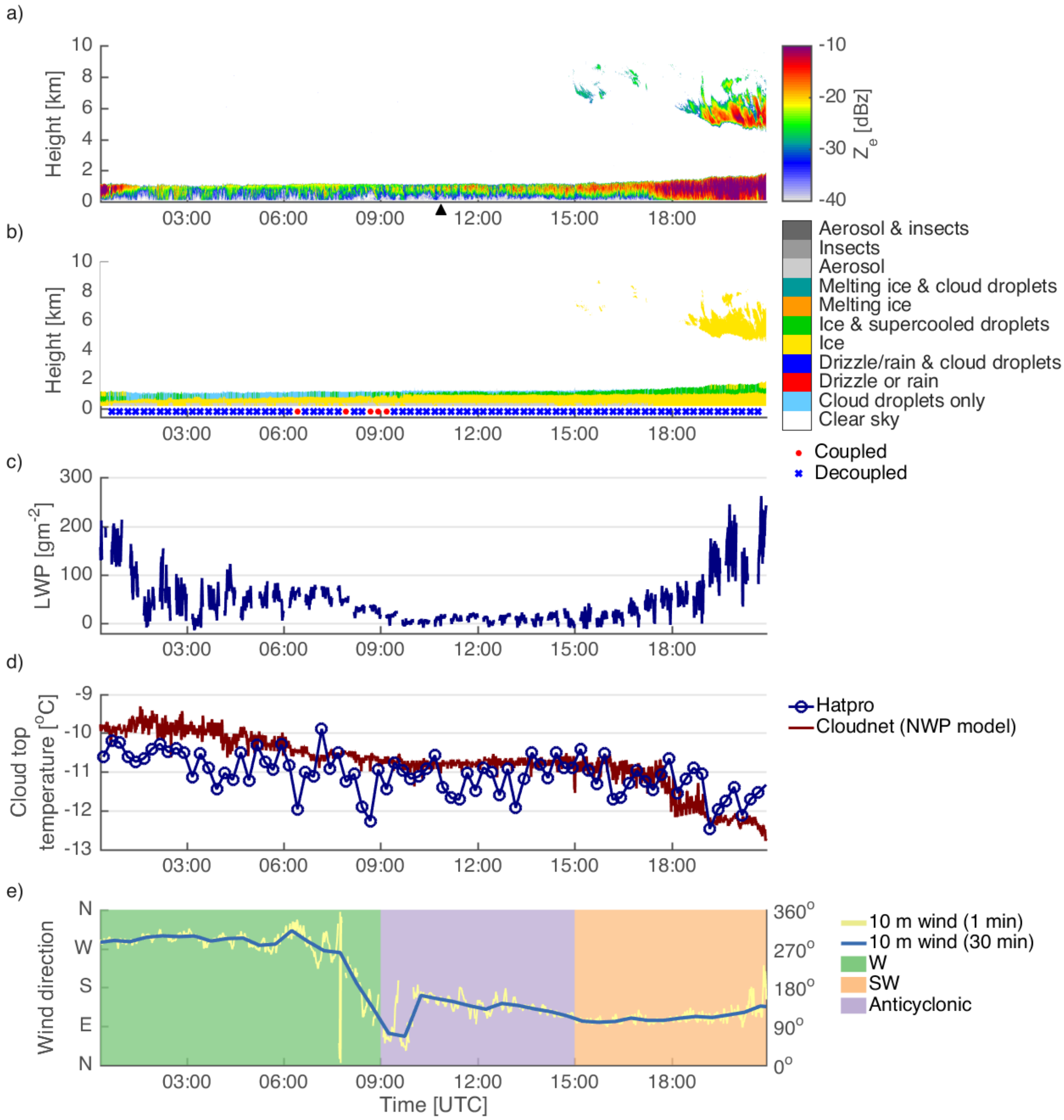

Figure 7: Overview of the P-MPC case observed above Ny-Ålesund on 5 November 2016. a) Reflectivity; b) Cloudnet target classification (Sect. 5) and surface coupling detection developed in Sect. 8. This cloud was classified as predominantly decoupled; c) Liquid water path from HATPRO (Sect. 6.1); d) Cloud top temperature estimated by the Cloudnet NWP model and HATPRO elevation scan (Sect. 6.3); e) Wind conditions. For 10 m wind direction both 1 min and 30 min mean values are shown. The Circulation Weather Type (CWT, Sect. 7.1) available every 6 hours is indicated by the background color. The time of the sounding shown in Fig. 8 is indicated by the black triangle in panel a.

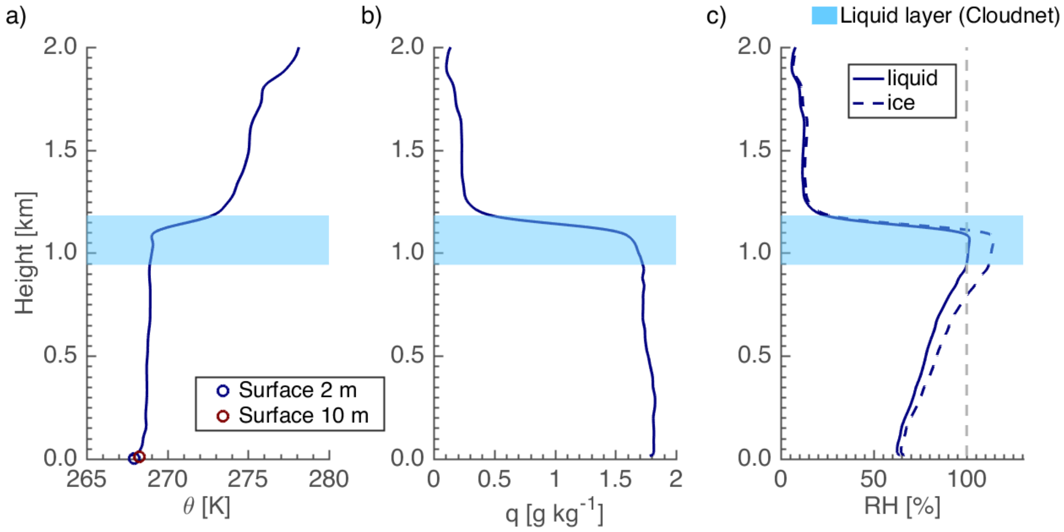

Figure 8: Thermodynamical profiles from the radiosounding started at 10:52 UTC on 5 November 2016. a) Potential temperature, b) specific humidity, c) relative humidity with respect to liquid (solid line) and ice (dashed line). Half an hour mean potential temperature from the surface observations is also shown in panel a. The light blue area indicates the height where Cloudnet identified liquid during the sounding time.

noon and a rapid increase at 17 UTC. Except for the last hours of the case, precipitation sublimates before reaching the ground. Similarly to Z_e, LWP was also initially high and then decreased first to below $100\,\mathrm{g\,m^{-2}}$ within the first 2 hours and further to almost zero by 9 UTC. In the afternoon LWP starts to increase again together with the deepening liquid layer and increase in Z_e. Although the highest LWP values are beyond the range of what is typical for the P-MPC at Ny-Ålesund, the case mean at $46\,\mathrm{g\,m^{-2}}$ represents rather average conditions (Sect. 8).

The cloud was formed within westerly wind (Fig. 7e). The large scale weather conditions consisted of a strong high pressure system over Greenland and low pressure over Europe. The 12 UTC CWT classification (Sect. 7.1) was anticyclonic, probably related to a small perturbation in the large scale flow (not shown). Until 7 UTC the 10 m wind was steadily from west, aligned with the free-tropospheric wind and following the Kongsfjorden valley from sea to inland. Within couple of hours the 10 m wind turns first south and then southeast to be channeled in the opposite direction along the fjord. The conditions present for the rest of the day are very typical for Ny-Ålesund: southeast surface wind underlying southwest 850 hPa wind.

The sounding at 11 UTC indicates a temperature inversion at cloud top and a well-mixed layer below the cloud (Fig. 8a). The liquid layer seems to have extended into the temperature inversion, which would suggest that the very top of the cloud was stably stratified. However, judging from the relative humidity profile (Fig. 8c) the sonde passed through the cloud at a location where the liquid layer was particularly thin and the liquid layer top height from Cloudnet might be overestimated in Fig. 8. The potential temperature profile indicates a weak surface based inversion. The method to continuously evaluate surface coupling developed in the first study (Sect. 8) indicates that the cloud was mostly decoupled with some profiles classified as coupled between 6 and 9:30 UTC (Fig. 7b). Correspondingly, the cloud case is classified as predominantly decoupled. The sounding profile, taken shortly after the coupled profiles were detected, indicates that the mixing layer reached from the cloud almost to the surface and also the temperature inversion presented by surface observations (2 and 10 m temperature) was weak (Fig. 8a), which support the weak decoupling classification. The instances of surface coupling occurred simultaneously as the wind conditions were changing (Fig. 7b,e), which could be related. The southeasterly surface wind present from 10 UTC onwards might have acted to stabilize the surface layer and strengthen the decoupling of the cloud (see Sect. 8 for a detailed discussion). Unfortunately no further soundings were performed on this day to confirm the development of the coupling state.

The surface based inversion suggests that the turbulence in the mixing layer was driven by the cloud or forced mechanically. Radiative cooling at cloud top may generate negative buoyancy and by that turbulent kinetic energy (Shupe et al., 2013). During the day the cloud top temperature was gradually decreasing (Fig. 7d), although it should be remembered that neither of the methods used to estimate cloud top temperature have a better accuracy than $1-2$ K (Sect. 6.3). The temperature decrease present in the NWP model timeseries could also be due to the rising cloud top. As no other cloud was present above the low-level MPC for most of the day and the data does suggest a decrease in cloud top temperature, it is plausible that sufficient radiative cooling at cloud top took place to drive mixing in the sub-cloud layer. Additionally, in the afternoon wind shear was present, as the surface wind direction deviated strongly from that in the free-troposphere (Fig. 7e). This wind shear might have been another source of turbulence. However, to draw definite conclusions about the dominating mechanisms or how turbulence intensity developed during the day would require further analysis.

The absolute humidity above the cloud was low at the time of the sounding ($<0.5\,\mathrm{g\,m^{-3}}$; Fig. 8b), indicating that the free troposphere did not provide a source of humidity for the cloud. Since the cloud was also mostly decoupled from the surface, the cloud probably did not have a sufficient source of humidity to compensate for the continuous sink via precipitation, thus causing the decrease in LWP during the first half of the day. The relative humidity profile shows that the layer saturated with respect to ice did not extend far below the liquid layer (Fig. 8b), explaining the sublimation of precipitation indicated by the radar measurements (Fig. 7a). The sublimation of precipitation together with the turbulent layer extending below the cloud might have allowed for recycling of humidity and thus enabling the cloud to persist despite the continuous precipitation and lack of humidity sources (Solomon et al., 2014, 2011). In the evening the cloud gets thicker and a mid-level cloud appears, suggesting a change in atmospheric conditions. The integrated water vapor (IWV) starts to increase from 15 UTC onwards, and the sounding made the next day shows higher absolute humidity ($> 1\,\mathrm{g\,m^{-3}}$) near the top of the low-level cloud (not shown). The presence of a humidity source from the free-troposphere provides a possible explanation for the strong increase in the LWP, Z_e, and the thickness of the cloud after 17 UTC.

Overall, the low-level cloud above Ny-Ålesund on the 5 November 2016 exhibits many of the typical characteristics of an Arctic MPC repeatedly observed at other sites (Sect. 2.2): A thin but persistent super-cooled liquid layer producing continuous precipitation, a strong temperature inversion at cloud top and a turbulent layer driven (at least to some extent) by cloud top radiative cooling. At the time of the sounding no humidity inversion near cloud top was found, but it is possible that one emerged later during the day. The cloud exhibits a noteworthy persistency despite the changing wind and thermodynamic conditions, a defining feature for these kind of clouds.

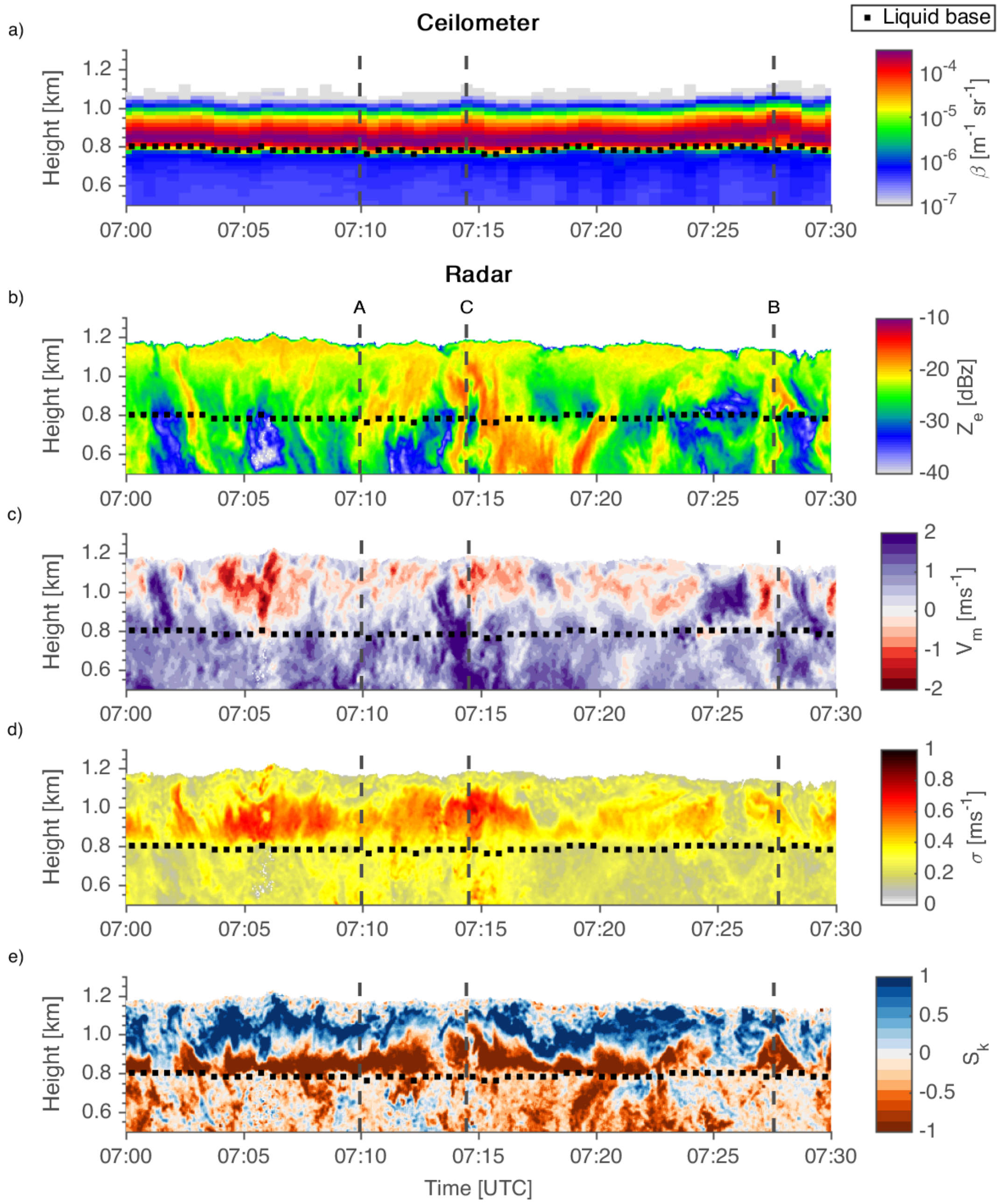

Figure 9: Excerpt of the P-MPC case on 5 November 2016. a) Ceilometer attenuated backscatter and radar moments: b) reflectivity, c) mean Doppler velocity, d) Doppler spectrum width, and e) skewness. The black dots indicate the liquid base height retrieved by Cloudnet (Sect. 5). The dashed vertical lines show the times for which profiles are shown in Figs. 10 –14, corresponding to labels A-C.

Radar observations

To identify detailed structures in the radar Doppler spectra and the moments in the 5 November 2016 P-MPC case, a shorter example time period in the early morning is shown in Fig. 9. The ceilometer shows a strong backscatter between 800 m and 1.1 km, above which the signal disappears (Fig. 9a). The strong gradient in the attenuated backscatter (β') around 800 m indicates the base of a liquid layer, which is well retrieved by the Cloudnet algorithm (indicated by black dots in Fig. 9). The initial strong increase in backscatter is quickly reduced again as the ceilometer signal gets attenuated and diminishes before reaching cloud top. Below the liquid base β'-values are small, as the ceilometer is less sensitive to the low number of large precipitating particles. The layer containing liquid likely spans from the liquid base, indicated by the ceilometer, to cloud top. Due to the cold temperature (Fig. 7d), Cloudnet assumes that the precipitation was ice. For simplicity, the layer between the ceilometer detected liquid base and cloud top is referred to as the mixed-phase layer (MPL), as both phases are expected within the layer even if it is not certain that they are found in every part of it.

The ceilometer time series looks very steady, while the radar parameters are variable and show many structures in the cloud. Within the MPL, Z_e varied from -30 to -15 dBz in the half an hour period presented in Fig. 9. Variation in Z_e is caused by the changing number and size of droplets and ice particles, although attributing the measured Z_e to specific values of these parameters in mixed-phase volumes is not trivial (Shupe et al., 2008c). The mean Doppler velocity (V_m) is a superposition of the terminal fall velocity of the hydrometeors and the vertical air motions, neither of which can be directly inferred from the timeseries in Fig. 9b. However, knowing that hydrometeors always fall downwards, any V_m that is upwards has to be related to an updraft. More upwards Doppler velocities were present in the upper parts of the MPL, and below the liquid base a more consistently downwards V_m was observed. In the upper part of the MPL the ice particles are likely to have been relatively small and thus having less of an impact on V_m. The V_m was therefore closer to the Doppler velocity of the liquid droplets, which can be assumed to be tracers for air motions (Shupe et al., 2004). Below the liquid base V_m was heavily influenced by the fall velocity of the precipitating particles. The evaluation of V_m in the upper part of the MPL suggests narrow strong downdrafts and broader updraft regions, as would be expected for a cloud top driven mixing layer. The Doppler spectrum width (σ) had the highest values in the first half of the investigated period, reaching up to 0.8 m s^{-1}. In most profiles σ was larger in the lower parts or middle of the MPL, indicating mixed-phase or heavily turbulent cloud volumes. Skewness (S_k) shows some interesting features within the MPL. For most of the time a layered structure was present with a region of strongly negative S_k above the liquid base followed by a layer with strongly positive S_k. At the very top of the cloud S_k was often close to zero. Below the liquid base S_k was mostly negative, but the features were less strong and more patchy compared to those within the MPL.

Doppler spectra

To be able to interpret the radar moments, the Doppler spectrum across one profile (i. e. a spectograph) at 7:09:57 UTC is shown in Fig. 10f. At this instance, the liquid base is identified at 773 m and LWP was about 70 g m^{-2}. The spectograph features two distinct modes in the MPL, one only present in the MPL and increasing with height and another one appearing 100 m below cloud top, growing with decreasing height and continuing be-

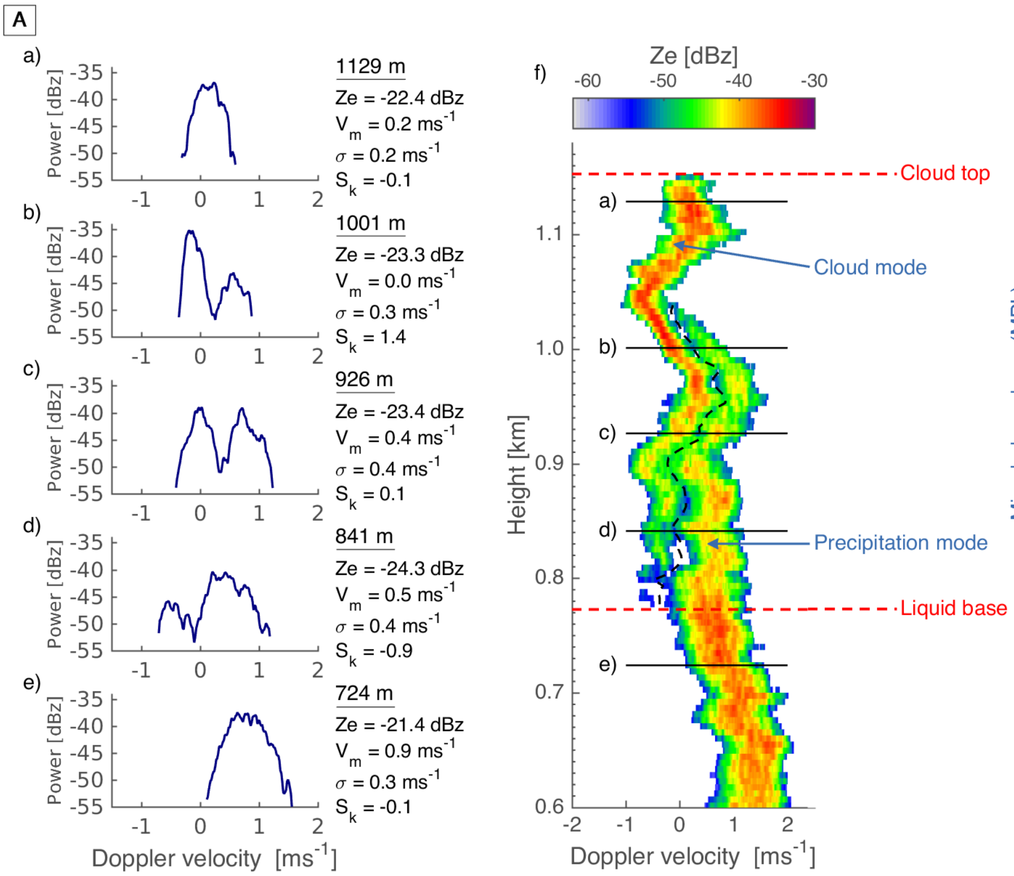

Figure 10: Spectograph measured at 07:09:57 UTC on 5 November 2016 (profile A in Fig. 9) in f), and Doppler spectra at selected heights in a)-e). For each spectra in a)-e) the moments corresponding to the spectra are given, and the height of the spectra are shown by black lines in f). The red dashed lines indicate the liquid base and cloud top as given by Cloudnet, where the liquid base height is derived from the ceilometer and cloud top is defined here as the edge between the last bin with detected hydrometer and the above empty bin. The black dashed line in f) shows where the spectra is split for evaluating the cloud and precipitation mode separately in Fig. 11 (see text for details).

low the liquid base. Here, everything below liquid base is considered precipitation, and the mode related to precipitation will generally be referred to as the precipitation mode. Considering the clearly sub-zero temperature near cloud top where the precipitation is formed (Figs. 7d), the precipitation is likely to be ice. It seems that ice is initiated rather close to cloud top and grows towards cloud base eventually falling out as precipitation, in agreement with previous observational and model based studies of Arctic MPCs (Section 2.2). Above the liquid base, another mode is present in the spectra. The second, smaller mode has a lower fall velocity than the precipitation mode. Because of the lower fall velocity and the increase towards cloud top, the second mode is very likely to be associated with cloud droplets. This assumption is supported by the ceilometer's detection of liquid base close to the altitude where the mode appears in the spectra. Also the MWR measurements indicate the presence of $70\,\mathrm{g\,m^{-2}}$ liquid somewhere in the column, and since no other cloud is detected above the low-level cloud this liquid is most likely located within the MPL. The two modes present in the spectograph can therefore be considered to relate to super-cooled liquid droplets (the cloud mode) and ice generated in the MPL and falling out (the precipitation mode).

To understand how the different features of spectra relate to the moments, Fig. 10 also includes Doppler spectra at selected heights together with the moments calculated for each spectrum. At cloud top (Fig. 10a), the Doppler spectrum presents one mode with moderate reflectivity, a rather small spectrum width, and skewness close to zero. Moving 130 m lower (Fig. 10b), the precipitation mode has additionally appeared in the spectrum, increasing the reflectivity and spectrum width somewhat and turning the skewness strongly positive. The Doppler spectrum is clearly asymmetric with the slower falling cloud mode dominating, which corresponds to a positive skewness when + is defined down towards the radar (Sect. 4.1). In the middle of the cloud (Fig. 10c) both modes are of similar size so that skewness is small while spectrum width has further increased. Moving further down to about 80 m above the liquid base (Fig. 10d), the spectra has again become strongly asymmetric, this time with the precipitation mode dominating and hence negative skewness. The spectrum width remains sizable. As the precipitation mode increases while the cloud mode shrinks from cloud top to liquid base, there is no considerable change in the total reflectivity from 1012 m to 852 m (Fig. 10b–d). In the precipitation below the liquid base, the Doppler spectra presents one mode with a moderate reflectivity and spectrum width, and skewness close to zero (Fig. 10e). The impact of vertical air motions shifting the Doppler velocity is particularly clear in the zig-zag pattern in the spectograph above 900 m, which makes it difficult to interpret the mean Doppler velocity across the profile.

The two modes in Fig. 10f are so distinct, it is trivial to separate them and consider the reflectivity and mean Doppler velocity of each mode separately. The spectra in the bins where both modes are present was split at the most prominent minimum between the two peaks, or simply at the gap if such is present (black dashed line in Fig. 10f). After separating the spectra, Z_e and V_m for each mode were calculated and are shown in Fig. 11a–b. The mean Doppler velocity of the cloud mode can now be used to evaluate the vertical motions in the MPL (assuming the cloud droplets act as a tracer for vertical air motions following Shupe et al., 2004). Within the one profile, both up- and downwards motions are present as the vertical wind varies from $-0.68\,\mathrm{m\,s^{-1}}$ to $0.43\,\mathrm{m\,s^{-1}}$ (Fig. 11b). Such variation in vertical motions with height can be explained by the presence of rather small eddies, the occurrence of which agrees with the turbulent nature of the cloud layer. Further, it is possible to subtract the vertical air motions from the mean Doppler velocity of the precipitation mode, resulting to a profile of precipitation fall velocity in the layer where the cloud mode is present (Fig. 11b). When the precipitation mode first appears, it has a fall velocity of $0.56\,\mathrm{m\,s^{-1}}$. The fall velocity gradually increases towards liquid base, where it reaches $1.1\,\mathrm{m\,s^{-1}}$. The relative low reflectivity of the precipitation mode (below -20 dBz) suggests light snowfall, which is not unusual for this type of clouds (Morrison et al., 2012). Z_e values between -25 and -20 dBz are close to the medians of Z_e-distributions within the MPL reported at other sites (see for example Qiu et al., 2018, Sedlar et al., 2012, Sotiropoulou et al., 2014).

The joint increase of Z_e and V_m of the precipitation mode suggests the ice particles were gradually growing while falling through the MPL. The temperature near cloud top was about -10 °C at the time of the profile (Fig. 7d), which corresponds to plate-like ice crystal habits (Pruppacher and Klett, 1997). The fall velocity was in a range common for pristine ice crystals and small aggregates and graupel (Barthazy and Schefold, 2006, Brandes et al., 2008). The precipitation mode also becomes broader with decreasing height, reaching a

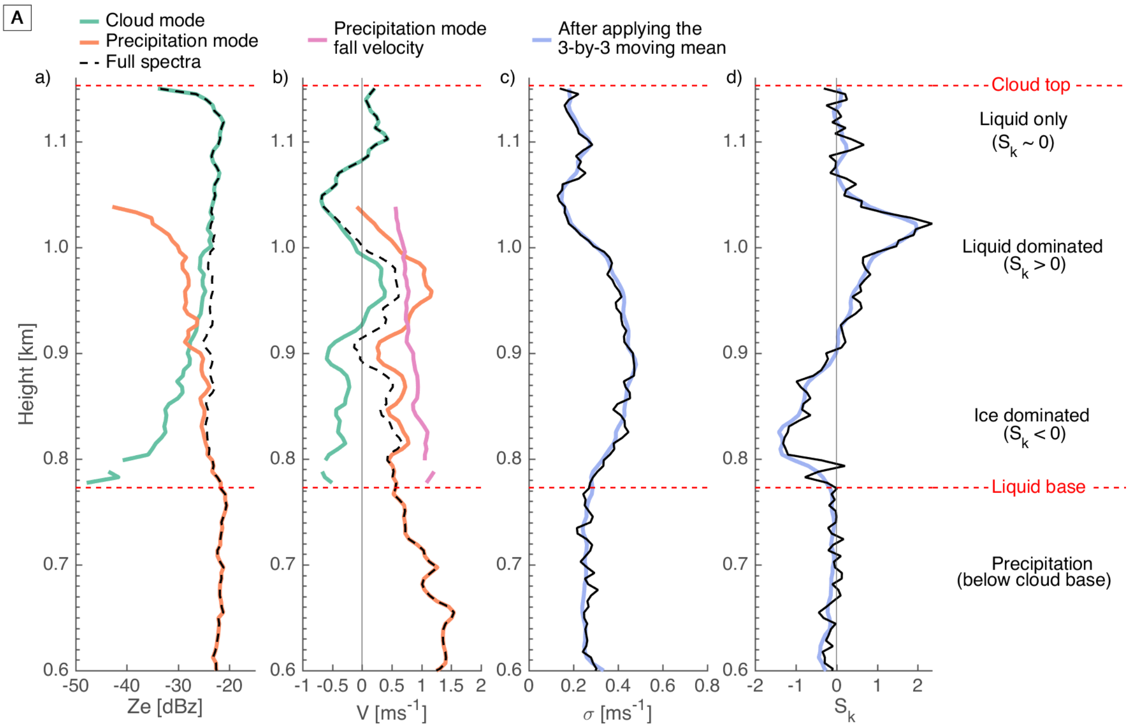

Figure 11: Moments corresponding to spectograph in Fig. 10 (profile A). For reflectivity (a) and mean Doppler velocity (b) profiles calculated for the cloud mode, the precipitation mode, and the full spectra are presented. In b) also the fall velocity of the precipitation mode is given. In all figures the black line (dashed or solid) corresponds to the values calculated from the spectograph in Fig. 10 without further processing. For Doppler spectrum width (c) and skewness (d) the profile also after applying the 3-by-3 moving mean (Sect. 10) is shown.

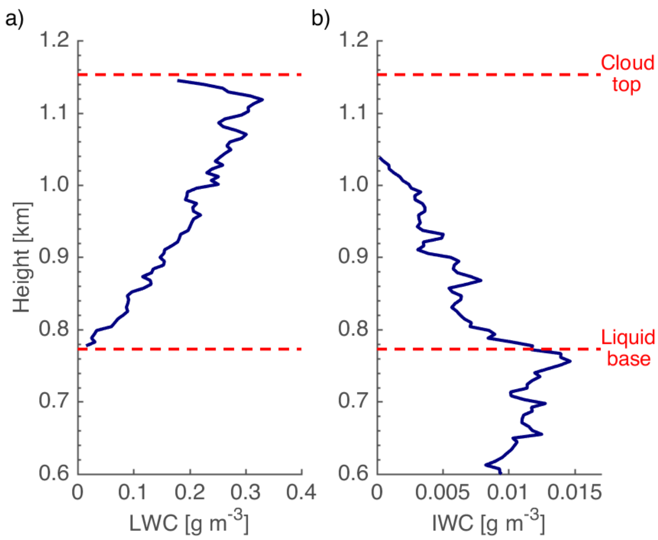

Figure 12: a) LWC and b) IWC calculated based on cloud and precipitation mode Z_e profiles, respectively, shown in Fig. 11a. For the IWC retrieval the temperature from the sounding at 10:52 UTC (Fig. 8) was used.

spectrum width of $0.3\,\mathrm{m\,s^{-1}}$ at the liquid base (Fig. 10, Fig. 11c). Aggregation, riming and splintering all may broaden the Doppler spectrum (Barrett et al., 2019, Giangrande et al., 2016, Kneifel et al., 2016), but so does also the increase in turbulence or wind shear (Shupe et al., 2008b). The repeatedly occurring negative skewness below the liquid base (Fig. 9e) suggests that in the precipitation a tail of slower falling particles occur, and hence the presence of multiple ice habits. However, the Doppler spectra do not represent features distinct enough to determine which processes might have taken place, other than the general increase in size within the MPL indicated by the increase in reflectivity and fall velocity.

The inspection of Figs. 10–11 leads to an interpretation of skewness within the mixed-phase layer. At cloud top, only the cloud mode was present and skewness is close to zero. If any ice was present above 1.04 km, it was below the detection limit of the radar. The skewness becomes positive when the second mode appears in the spectra, and remains positive as long as the cloud mode has a higher reflectivity and thus dominates the signal (Fig. 11a,d). The change from positive to negative skewness indicates a change in the dominating mode. At 900 −930 m height the Z_e of the two modes is approximately equal and skewness is close to zero. In the lower parts of the MPL skewness is negative as the faster falling precipitation mode dominates the signal. In the example shown in Fig. 11 skewness becomes rather close to zero at liquid base. This, as already discussed, was not always the case (Fig. 9e). Note, that the dominating mode (Fig. 11e) in the MPL is defined in terms of radar reflectivity and not the particle mass or number concentration.

To relate the skewness profile to hydrometeor mass and partitioning between the phases, the liquid and ice water content (LWC and IWC, respectively) profiles are calculated based on the reflectivity of each mode (Fig. 11a) using the retrievals given in Sects. 6.2. For the IWC retrieval the temperature profile from the sounding at 10:52 UTC (Fig. 8) was used. The application of the retrievals in this manner requires that the Z_{precip} and Z_{cloud} have been obtained, and might therefore not be possible for other profiles. The LWC exhibits a quasi-adiabatic profile (Fig. 12a), and the values are close to the average LWC reported from aircraft in situ observations by Mioche et al. (2017) for MPCs in the Svalbard region. The IWC increases towards liquid base, where it reaches its maximum value and then slowly decreases again (Fig. 12b). The IWC is on the low end of the IWC values reported by Mioche et al. (2017) but not out of range, and similarly low IWC have been reported on other Arctic sites (De Boer et al., 2009). The profile is also from a time when Z_e was rather low (Fig. 7) and estimating IWC later during the day would result to higher values. It is also worth mentioning that the IWC-retrieval by Hogan et al. (2006) was developed for thick mid-latitude frontal clouds and might not perform as well for a thin Arctic cloud. The MPL was heavily liquid dominated. LWC was an order of magnitude higher than the IWC although the reflectivities of the cloud and precipitation mode were comparable. This demonstrates the strong dependency of radar reflectivity on particle size ($Z_e \propto D^6$, see Sect. 4.1): the same mass distributed over a low number of larger particles causes a higher Z_e than when spread over a large number of small particles. Furthermore, ice particles have a lower density than liquid droplets. The high liquid fraction (ratio of liquid to total condensed water) is common for low-level MPC in the Arctic (De Boer et al., 2009, Mioche et al., 2017, Shupe et al., 2008c), and in terms of the LWC and IWC profiles the 5 November 2016 case does not present anything unusual.

In Fig. 11 the values calculated from the spectograph presented and after applying the 3-by-3 moving mean (Sect. 10) are shown for the σ and S_k the profiles. The values

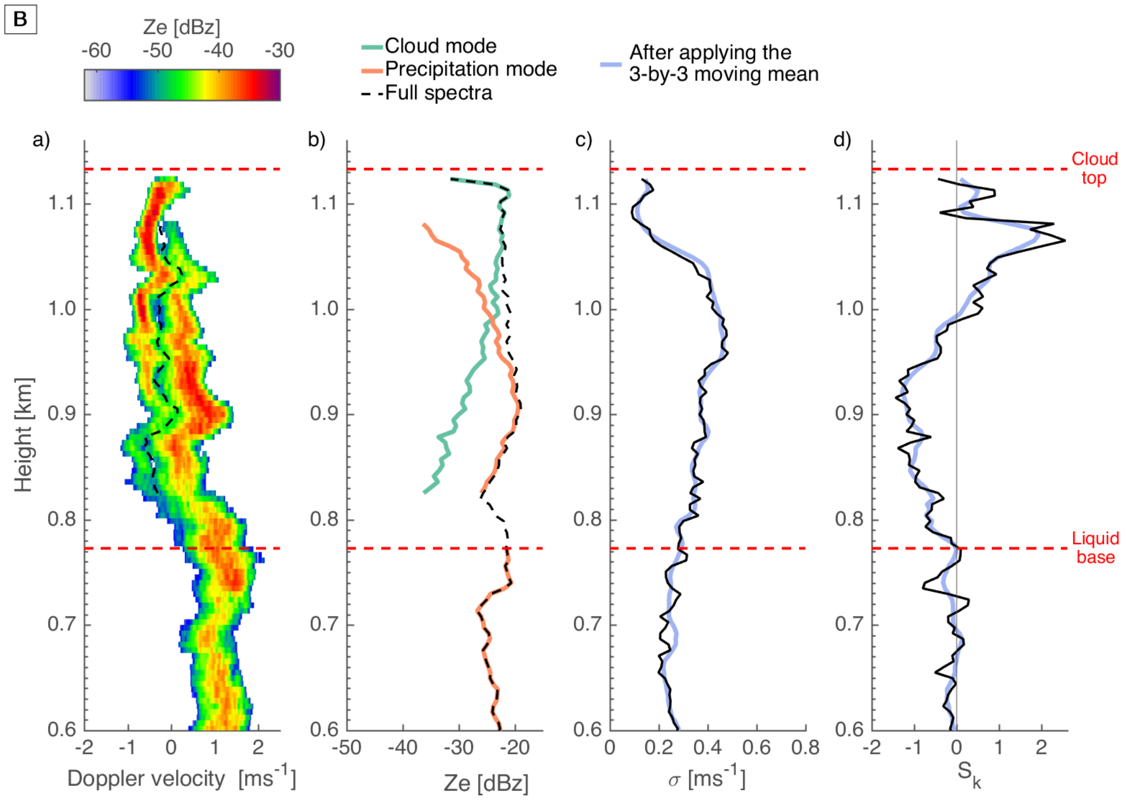

Figure 13: Spectograph measured at 07:27:34 UTC on 5 November 2016 (profile B in Fig. 9) and associated moments. a) as Fig. 10f, b)–d) as Fig. 11.

calculated for the particular spectra presented are shown to facilitate the understanding of how the specific spectra correspond to the values of the moments. The noisiness of the parameters is evident in the profiles and demonstrate the need for additional smoothing to facilitate further analysis of the data.

Another example profile from the same case is shown in Fig. 13. Similarly to the first spectograph presented in Fig. 10f, in Fig. 13a two distinct modes are present. The cloud mode becomes clearly distinguishable from the precipitation mode only 60 m above the ceilometer detected liquid base. Although the spectra cannot be neatly separated to two modes in the lowest part of the MPL, the cloud mode is still visible in the spectograph and causes a negative skewness (Fig. 13d). Compared to the spectograph in Fig. 10f, in Fig. 13a the precipitation mode appears closer to cloud top, and starts to dominate higher up in the MPL (Fig. 13a, b). Correspondingly, the layer of positive skewness has moved upwards and is shallower. Overall, the skewness profile follows the reflectivities of the cloud and precipitation modes as described above: a positive skewness in the layer where the cloud mode dominates ($1-1.08$ km), zero skewness at the height where the reflectivities of each mode are equal (0.99 km), and negative skewness in the precipitation mode dominated layer ($0.77-0.99$ km). The reflectivity of the precipitation mode in Fig. 13b does not show a monotonic increase with decreasing height, but instead decreases from 900 m downwards and has a kink at 730 m. The most likely explanation for this peculiar behavior is the nature of the measurement: the radar observation is a snapshot of a dynamic 3-dimensional structure observed in an Eulerian framework, and even though it is common to interpret a radar profile as presenting a continuous development in the hydrometeor population, this

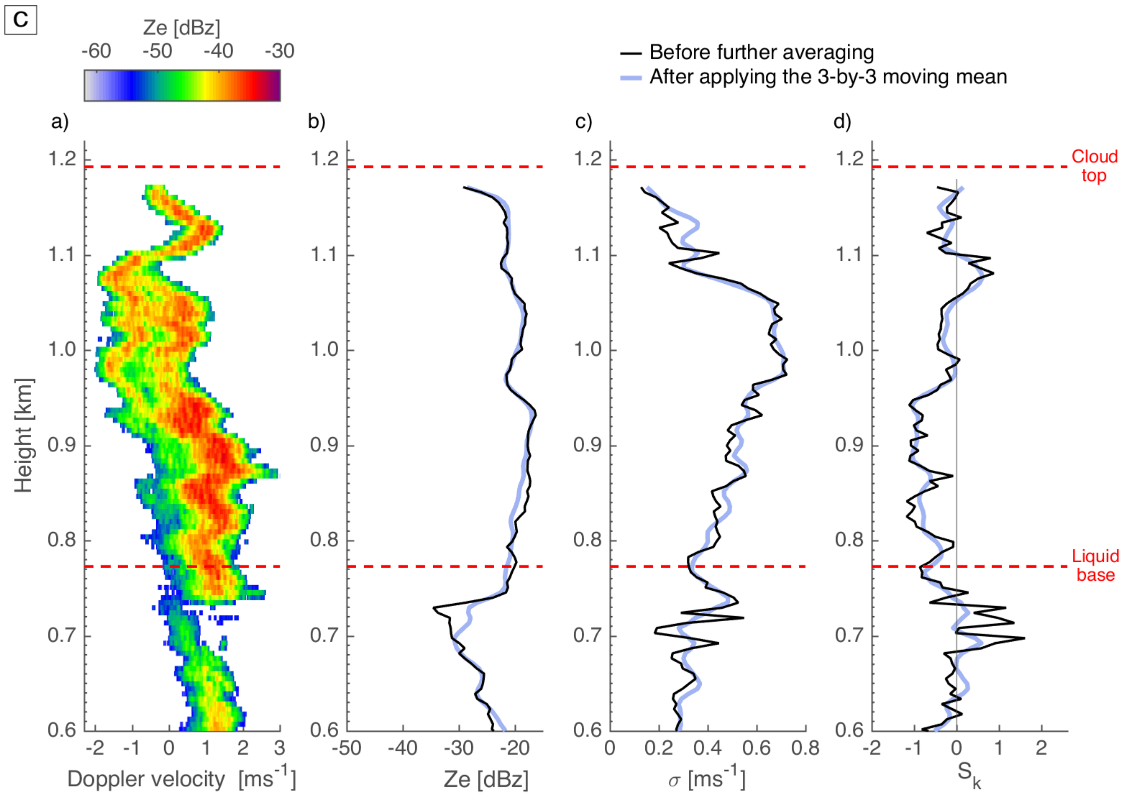

Figure 14: As Fig. 13 for 7:14:29 UTC on 5 November 2016 (profile C in Fig. 9).

is in reality not the case. Returning to the timeseries in Fig. 9, some structures appear slanted as the cloud is advected above the observatory and the horizontal wind pushes the falling hydrometeors. Few studies have suggested evaluating the spectra along fall streaks (Kalesse et al., 2016a, Pfitzenmaier et al., 2017), however, this approach does not provide an all-conclusive solution for the problem. The measurement technique only gives a partial picture of the development of the cloud, and this limitation needs to be kept in mind when interpreting the results. With a statistical approach that compiles long term measurements it is assumed that clouds are sampled at different parts and development stages of the cloud regime in question, thus producing a representative distribution of cloud parameters.

The last spectograph considered was measured at 07:14:59 (Fig. 14). Two modes can be identified in the spectograph but for most of the profile it is not trivial to separate them. Here decomposing the spectra would require more sophisticated approaches and it is not necessarily possible in all bins. Although it is not possible to quantitatively determine the mode with larger Z_e, the visual inspection of Fig. 14a suggests that the skewness is still reflecting the dominating mode of the spectra as described before. Moreover, the individual modes in Fig. 14a appear broader compared to the two previous spectographs (Figs. 10f, 13a). Also the width of the complete spectrum is larger (Fig. 11c, 13a, 14b). The Doppler spectrum width is influenced by microphysical properties (e.g. the presence of multiple hydrometeor habits) and dynamical conditions (Sec. 4.1). In mixed-phase volumes larger σ is expected, and Figs. 10-14 show that σ was generally larger ($> 0.3\,\mathrm{m\,s^{-1}}$) when multiple modes were present in the spectograph. In Fig. 14 turbulence is likely to cause broadening of the spectra. Particularly at 1-1.1 km both modes are similarly affected, which suggests a dynamic rather than microphysical cause for the increased spectrum width. Hence, it seems

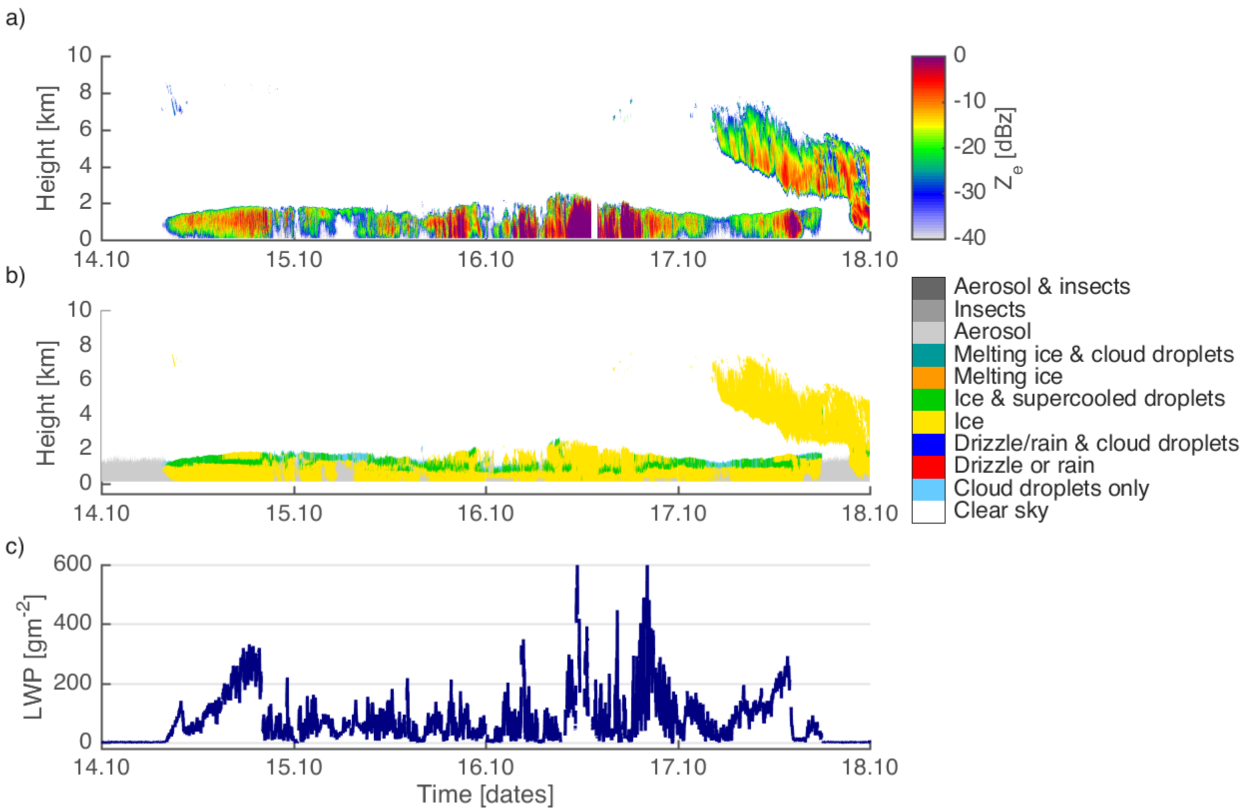

Figure 15: Overview of the clouds observed above Ny-Ålesund on 14–17 October 2019. a) Reflectivity; b) Cloudnet target classification; c) Liquid water path. The dates on the x-axis are placed at midnight and indicate the start of the corresponding day. Note the different LWP and Z_e scales compared to Fig. 7. The gap in the radar data on the 16 October was due to connection issues between the instrument and the measurement PC.

that the largest spectrum width corresponds to spectra with multiple modes combined with higher levels of turbulence. The larger σ in the lower parts of the MPL that was seen in Fig. 9d is caused by the mixed-phase conditions (broad bimodal spectra). The larger σ in the first half of the time period could be attributed to more turbulence at this time.

11.2 17 October 2019: Mixed-phase cloud with less well defined Doppler spectra

Since the morning of 14 October 2019 until the afternoon of 17 October there was an almost continuous low cloud cover over Ny-Ålesund (Fig. 15). On few occasions above 6 km barely detectable cirrus clouds occurred. In the morning of 17 October a mid-level cloud appeared, which descended during the day reaching near the ground by the evening. During 14–17 October the low-level cloud was changing a lot. At times it was deeper and contained multiple liquid layers while on some occasions no liquid was measured (Fig. 15b,c). At the end of 16 October the cloud becomes a steadily liquid topped MPC for several hours. Due to the variability in cloud structure the entire time period when the low-level cloud was present was not classified as a P-MPC (for criteria see Sect. 3.1 in Gierens et al., 2020, provided in Sect. 8). The details of the evolution of the cloud would require a lengthy discussion that is beside the focus of this study. I will therefore limit the analysis in this section to the first hours of 17 October to investigate the radar Doppler spectra of the mixed-phase layer in a time period that was relatively steady.

Fig. 16 shows a 20 min period of radar moments and ceilometer backscatter shortly after midnight on the 17 October 2019. Compared to the case of 5 November 2016 described in the previous section (Fig. 9), the cloud in Fig. 16 exhibits clearly higher Z_e and less strong skewness features. The heavier precipitation is also visible in the ceilometer attenuated backscatter as higher values below the liquid base, but the liquid base is still clearly identifiable as a sharp increase in β' (Fig. 16a). The reason for the smaller absolute values of S_k becomes clear when investigating the spectograph at 01:50:42 (Fig. 17). On 5 November 2016 most spectographs exhibited two clearly separated modes (Fig. 10f, 13a, 14a), while in this case the spectra is more ambiguous. Between 1.2 and 1.4 km the spectra seems to represent two modes merged together (Figs. 17c and d) but the distinction is not nearly as clear as it was in the previous case. The skewness does not reach as large absolute values since the spectra are less asymmetric (Fig. 17h). However, although the decomposition of the spectra to evaluate Z_e for the cloud and precipitation mode separately is not easily done here, the skewness is still providing an indication about the balance between the two modes. At the very top, only few radar bins appear to have a single mode and S_k close to zero. The very top-most bins in Fig. 17 show a positive skewness, but this should be interpreted carefully because at the edge of the cloud partial beam filling may distort the measurement. The difference between the instant and averaged S_k profiles (black and light purple lines in Fig. 17g) suggests that S_k in the topmost 100 m of the cloud varied considerably, but on average the skewness at cloud top was zero. When the second mode appears in the spectograph, skewness is positive for a few bins. In 100 m from cloud top, skewness has turned negative with the precipitation mode dominating the signal and the cloud mode being barely detectable as a additional mode on the slow edge of the spectra.

Why do the spectra in this second case not exhibit the same clear bimodality as in the first case? At the time of the spectograph the LWP was 95 g m^{-2}, which is higher than the LWP corresponding to any of the spectographs presented in the previous section (Figs. 10-14). The Z_e associated with the cloud mode near cloud top was -20 dBz (Fig. 17a), which is similar to the Z_e in this region shown in Figs. 11a, 13b, and 14b. The difficulty of detecting the cloud mode in the spectra can therefore not be explained by a too low reflectivity of the cloud mode. As already discussed in the previous section, turbulent broadening of the spectra makes the modes less distinguishable. Turbulence could also be playing a role in the 17 October 2019 case, at least the modes in the spectra in Fig. 17a-d appear broader than in Fig. 10a-d. The spectrum width, however, is overall smaller on the 17 October 2019 than the 5 November 2016 case (Fig. 9d, 16d). A further aspect to consider is the difference in fall velocity between the cloud and precipitation mode. A smaller difference in fall velocity between the two modes causes them to occupy more of the same region in the Doppler velocity space and therefore appear less separated in the Doppler spectra. The terminal velocity of ice particles is determined by their area-to-mass ratio and is therefore habit dependent (Karrer et al., 2020). Hence, the degree of the separation of the cloud and precipitation will vary depending on ice particle properties.

11.3 14 April 2017: A mixed-phase cloud without skewness features

The two cases presented in Sections 11.1 and 11.2 exhibit consistent features in the skewness timeseries. However, this is not always the case, as will be shown for the P-MPC observed

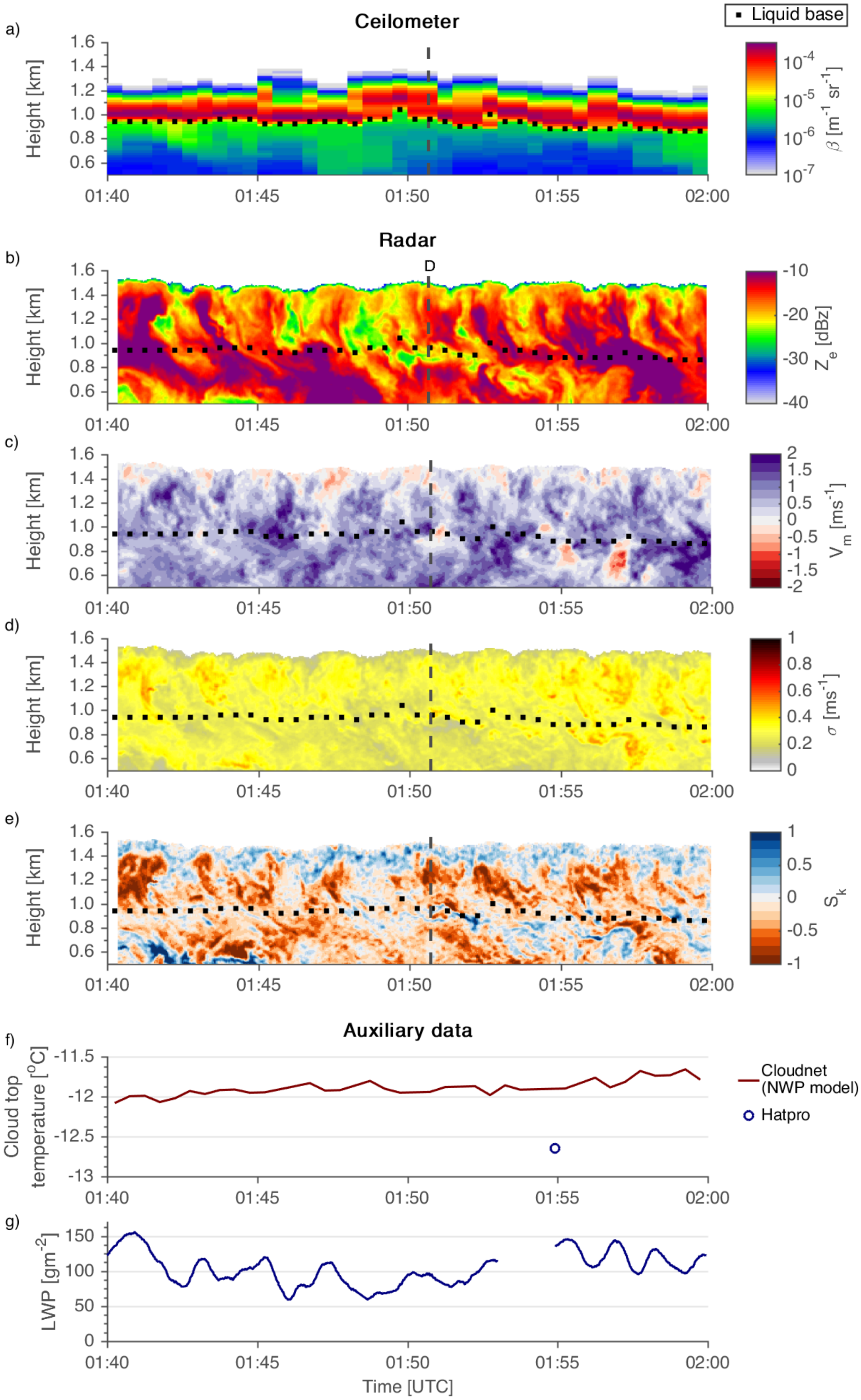

Figure 16: Excerpt of the P-MPC case on 17 October 2019. a)–e) as in Fig. 9, f)–g) as in Fig. 7. The dashed vertical line in a)-e) indicate the time for the profile D shown in Fig. 17.

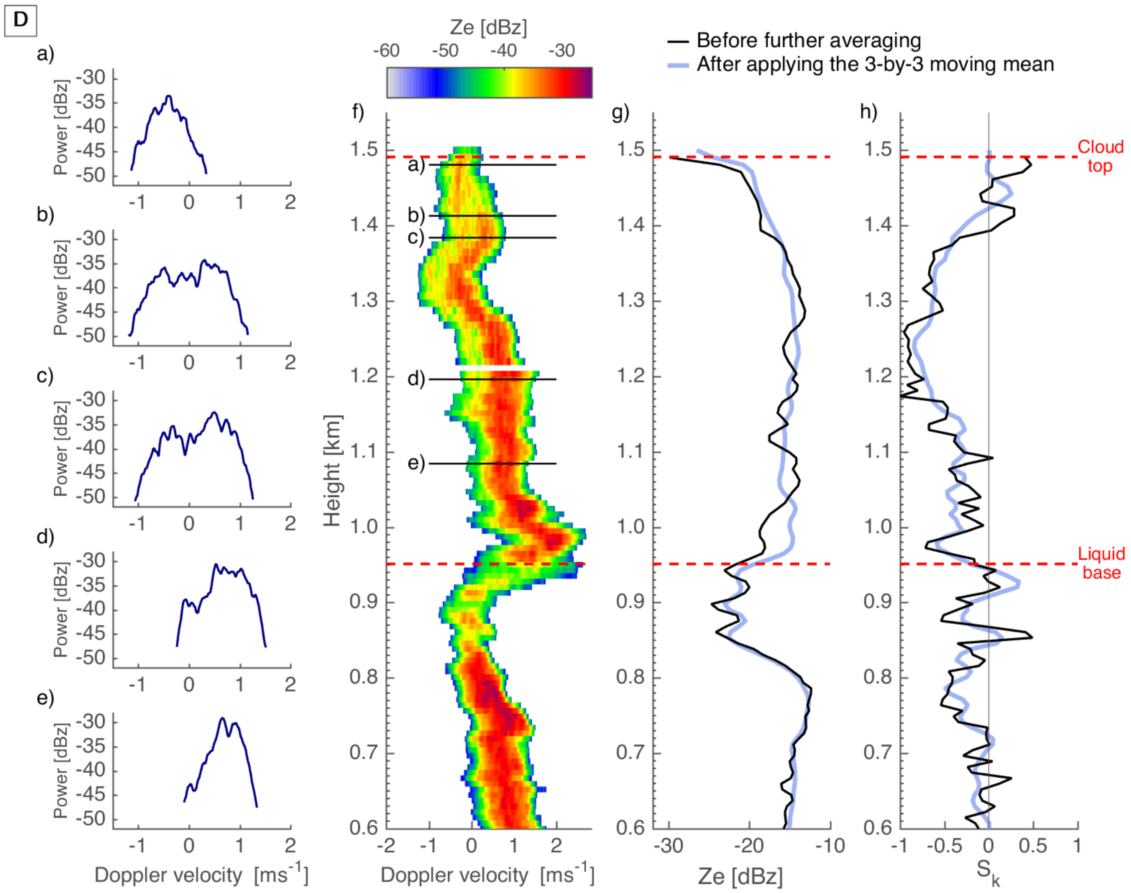

Figure 17: a)–f) as in Fig. 10 for 10:50:42 UTC on 17 October 2019 (profile D in Fig. 16), and corresponding profiles of g) reflectivity and h) skewness. The red dashed lines indicate the liquid base and cloud top. The small gap at 1.2 km in f) shows the edge of the chirp sections, which is associated with a change in the Doppler velocity resolution and a jump in sensitivity (Sect. 4.1).

above Ny-Ålesund on the 14 April 2017. An overview of the case is given in Fig. 18. Before and after the P-MPC no further clouds were observed, and the lonely cloud was quite low with cloud top below 1 km. Cloud top temperature was a couple of degrees lower than in the previous two cases, and the LWP was considerably lower (Fig. 18c, d). During the case LWP did not exceed 50 g m^{-2} and the case average LWP was merely 8 g m^{-2}. Fig. 19 shows the radar moments for a half an hour period in the middle of the case. Although Z_e and V_m are variable, the time-height plot of S_k is very uninteresting. The values are small, and no structures emerge. Also σ is low in the MPL, mostly staying below 0.2 m s^{-1}.

The spectographs in Fig. 20 explain the lack of skewness features in the cloud. The precipitation mode is strong but the cloud mode is not identifiable. The profile is unimodal and hence S_k and σ are small. The lack of skewness features in the 14 April 2017 case is therefore explained by the absence of the cloud mode in the Doppler spectra. In this case also the precipitation mode is very symmetric and exhibits less variation below the liquid base than in the previous two cases (Figs. 9e, 16e, 19e). The high Z_e (reaching to 0 dBz) combined with the low LWP indicate a lower liquid fraction in the MPL compared to the two previous cases. Because the temperature is closer to -15 °C, the difference in the saturation vapor pressure over liquid and ice is larger and the Wegener-Bergeron-Findeisen

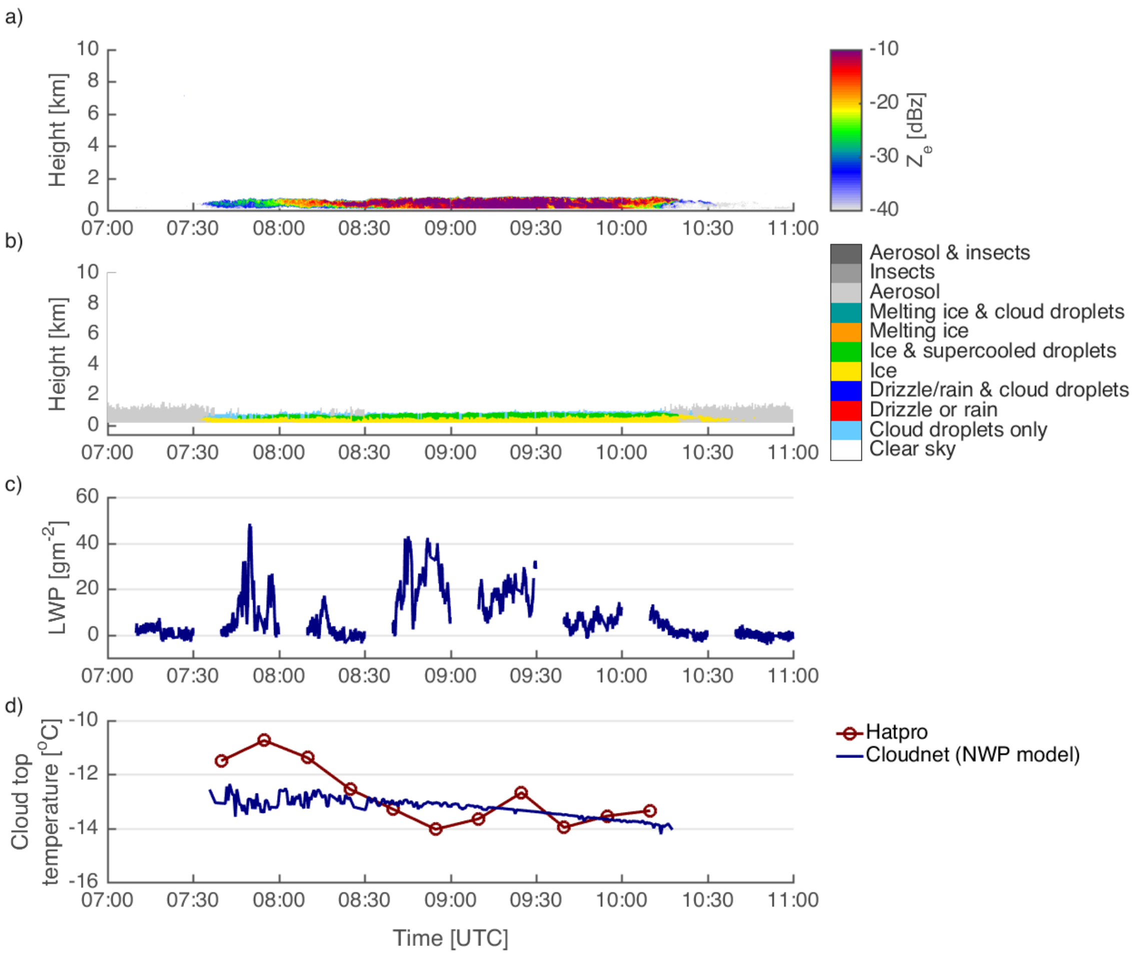

Figure 18: Overview of the P-MPC case observed above Ny-Ålesund on 14 April 2017. a) Reflectivity; b) Cloudnet target classification; c) Liquid water path; d) Cloud top temperature estimated by the Cloudnet NWP model and HATPRO elevation scan (Sect. 4.2).

process (WBF) therefore more efficient, possibly explaining the lower liquid fraction on the 14 April 2017. Furthermore, conditions such as available INP also modulate the phase-partitioning (Eirund et al., 2019, Norgren et al., 2018). It is also possible that the cloud is at the later stages of its lifecycle moving towards glaciation, and has at earlier stages featured higher levels of LWP which by the time it is observed above Ny-Ålesund has already depleted.

The P-MPC on the 14 April 2017 reveals a limitation of using millimeter wavelength cloud radar Doppler spectra to study mixed-phase clouds. When the amount of liquid is very low, as it is in this case, the sensitivity of the radar is not sufficient to detect the cloud droplets. Although the presence of super-cooled droplets could in some cases be indirectly inferred (Zawadzki et al., 2001), any feature that relies on an explicit signal from the droplets is necessarily limited to the cases where the amount of liquid sufficiently exceeds the detection limit of the instrument. For most of the case the LWP is also close to the detection limit of the MWR. The detection of super-cooled liquid in the cloud is based on the ceilometer, which is more sensitive to the small droplets.

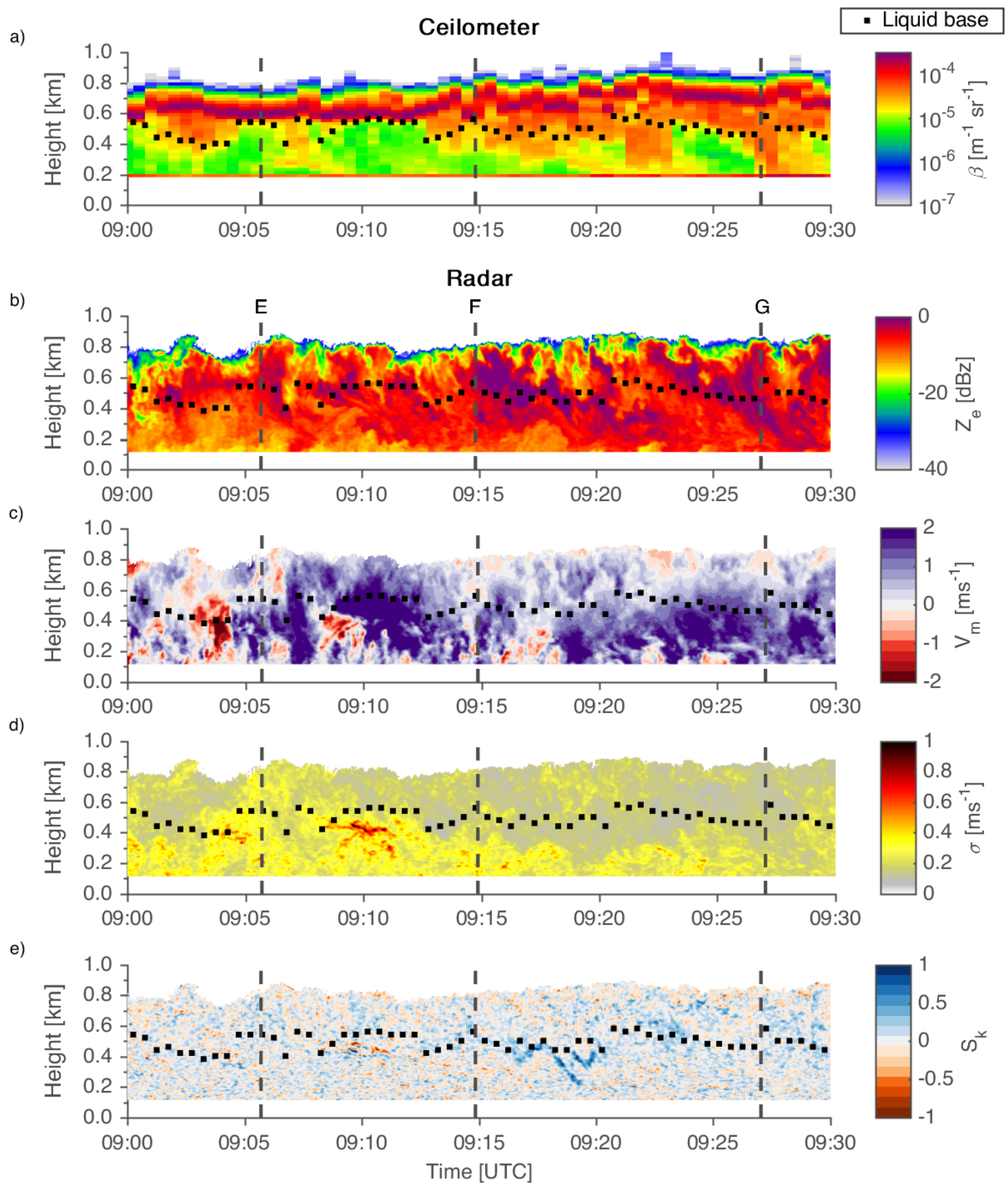

Figure 19: As Fig. 9 for 14 April 2017. The dashed vertical lines show the times for which profiles are shown in Fig. 20.

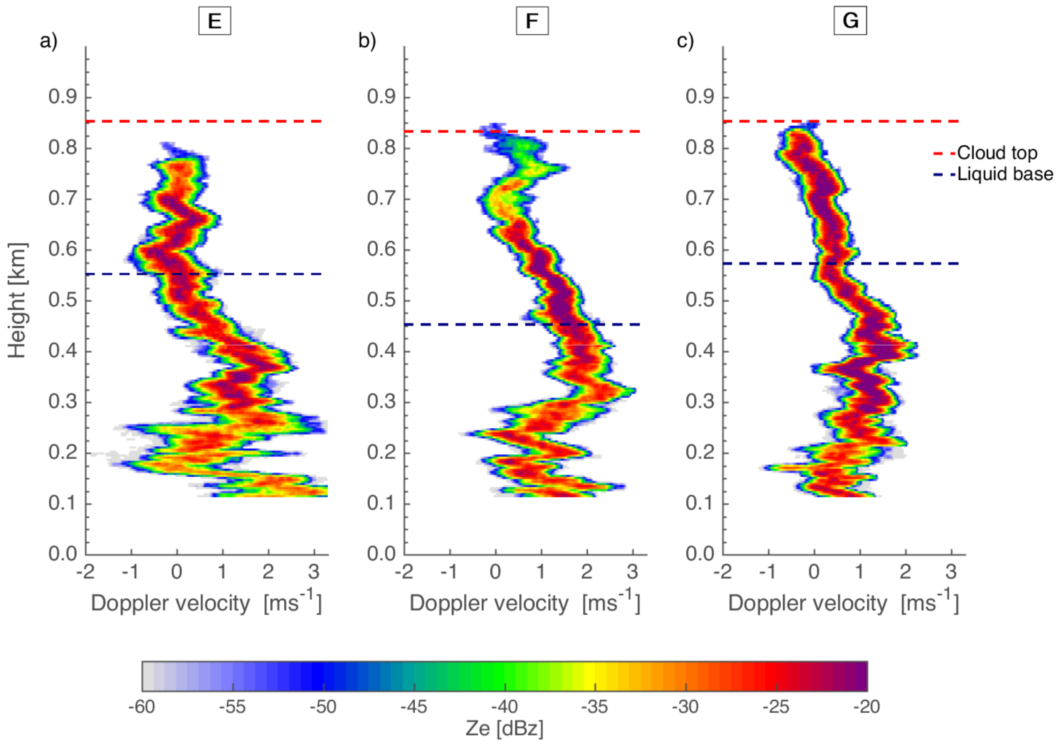

Figure 20: Spectographs measured at a) 09:05:42 UTC, b) 09:14:51 UTC, and c) 09:27:02 UTC on 14 April 2017, labeled E–G in Fig. 19. Note the different color scale compared to Figs. 10–14 and 17.

11.4 Interpretation of Doppler spectrum skewness in the mixed-phase layer

The three cases covered in Sections 11.1–11.3 represent a variety of flavors of the P-MPC frequently observed at AWIPEV. All cases depict the well-known model of an Arctic MPC (Sect. 2.2): a layer of super-cooled liquid persisting over several hours, with ice continuously forming close to cloud top, growing and falling out of the cloud as precipitation. The values of Z_e, LWP, and other parameters were within the range commonly reported for low-level MPCs at Ny-Ålesund and other sites. Although the amount of liquid and ice certainly differed between and within the cases, none of the clouds included is particularly extraordinary.

Although the evaluation of spectographs is informative, it is not feasible to analyze all of the full spectra even for one cloud case. Already the half an hour time period included in Fig. 9 consists of 664 profiles and 141843 Doppler spectra. Furthermore, not all measured spectra are neatly bimodal such as the ones presented for the 5 November 2016 case (Sect. 11.1) which complicates any analysis relying on peak identification and separation. Approaches based on the moments of the spectra are beneficial, because they allow the analysis of larger data sets which improves the statistical significance and generability of the results. However, an understanding of how the moments relate to the conditions in the cloud is required. Based on the case studies (Sect. 11.1-11.3), here a conceptual model for the interpretation of the Doppler spectrum skewness for the cloud top mixed-phase layer is proposed, and key challenges and limitations are considered. Lastly, the assumptions required for the further analysis are stated.

Conclusions from case studies

While the changes in Z_e across the MPL could be minor, the degree at which the cloud and precipitation mode contribute to the total Z_e changed from one extreme (cloud mode only) to the other (precipitation mode only). The profiles of Z_e and V_m give little indication of the presence of two modes or the shift of the relative contribution of each mode (Figs. 10–14, 17, 19). An increase in σ indicates the presence of multiple modes, but σ is also influenced by other factors which makes its interpretation difficult. Skewness appears sensitive to the presence of multiple modes of different sizes in the Doppler spectra. When the modes are broader and less well defined (e.g. Figs. 14, 17) the absolute value of S_k is smaller than in profiles with well defined and clearly separated modes (e.g. Figs. 11, 13). Still, by definition, the sign of S_k indicates if the reflectivity of the slow or faster falling side of the spectra is stronger. Whether the faster and slower falling particles correspond to supercooled liquid and ice, or to ice particles with different terminal fall velocities, cannot directly be inferred from the skewness.

As demonstrated by Sect. 11.3, when phase-classification carried out with instrument synergy finds a cloud layer mixed-phase, it is possible that the radar is only measuring a signal from the ice particles. In other words, the cloud is not mixed-phase from the viewpoint of the radar observation. However, although not explicitly measured, the supercooled liquid may still play a role in the microphysical processes and influence the ice particles, and thus also influence the radar measurement in an indirect way. Without going into the difficulties of the definition of mixed-phase (see Sect. 2.1), it is reasonable to assume that genuine MPCs exist where the radar can only measure the ice component of the cloud because of its limited sensitivity to detect low numbers of small droplets. Hence, for the analysis of skewness and further parameters derived from radar observations, it is proposed that cloud volumes classified as mixed-phase based on instrument synergy should be categorized as I) apparently mixed-phase, when the radar measures a clear signal from both liquid and ice, II) ice-dominated, when the radar receives a signal from liquid but the signal is dominated by the ice such that the main features of the Doppler spectra are determined by the ice phase, or III) ice-only, when the radar only measures a signal from the ice particles. Such distinction is required to answer the question "which processes can the Doppler spectrum skewness describe in a MPC?" because the answer differs for the different categories.

Fig. 21 summarizes the conceptual view of Doppler spectrum skewness in the mixed-phase layer at cloud top for the different radar observation categories. For the apparently mixed-phase (Fig. 21.I), Sections 11.1 and 11.2 showed that skewness seems quite robust as a metric to infer whether liquid or ice is dominating the radar signal. When both the cloud and the precipitation mode were present in the spectograph, the shift in the relative contribution of each mode was related to a distinct skewness profile (Fig. 11d). At cloud top, if only the cloud mode is present skewness is close to zero. The appearance of the precipitation mode turns the skewness positive. With the growth of the precipitation mode and the shrinking of the cloud mode when moving towards liquid base, the reflectivities of each mode become first equal and then the precipitation mode becomes larger. Correspondingly, skewness becomes first zero and then negative. Not always is a liquid-only layer detected at cloud top. In such cases, the skewness starts directly positive and no layer of zero skewness is present at cloud top. It is also possible that already at the very top of the cloud Z_{precip} is relatively large and the turn from positive to negative skewness

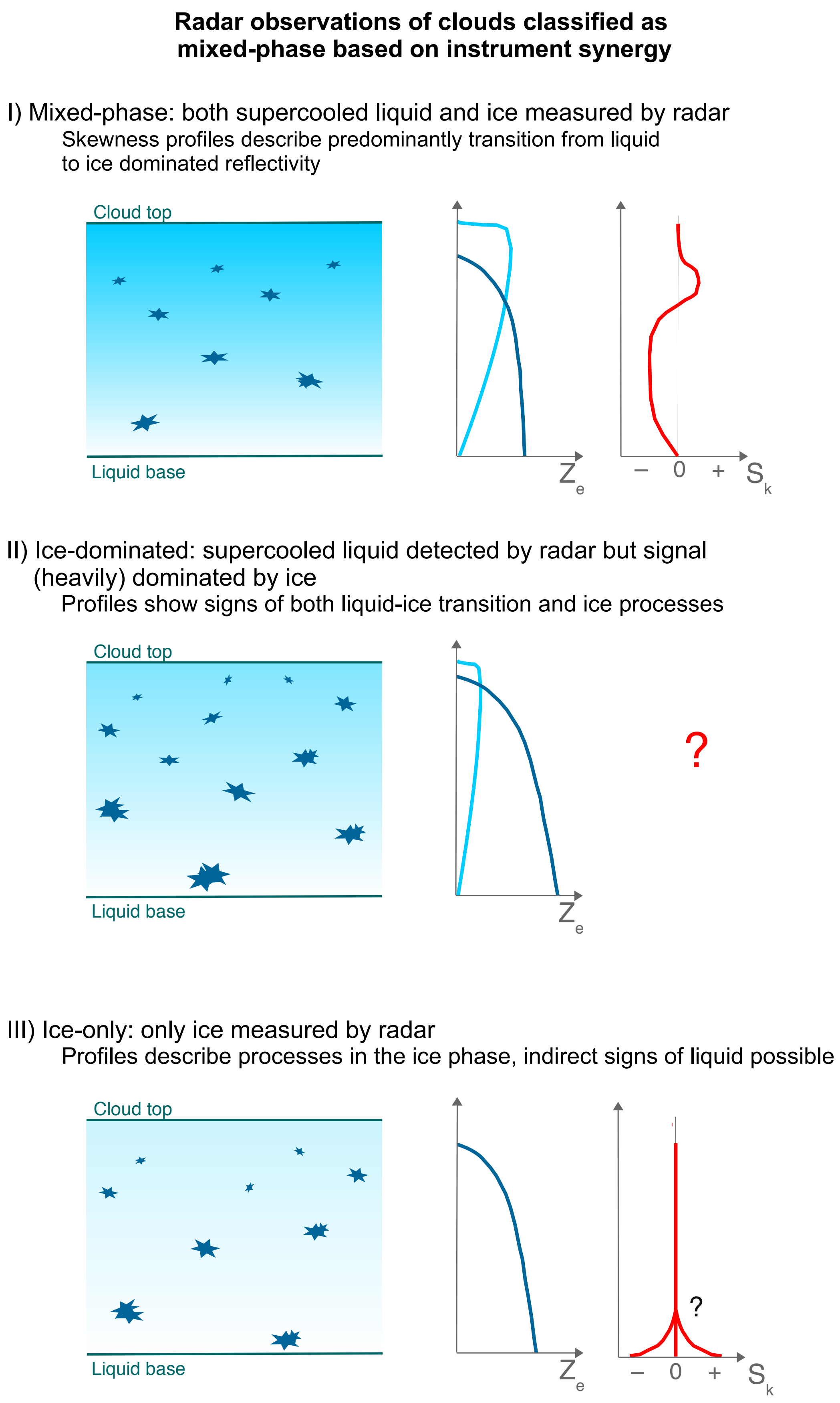

Figure 21: Conceptual model for Doppler spectrum skewness in the mixed-phase layer at cloud top. Light blue color corresponds to supercooled liquid, dark blue to ice particles.

happens very close to the top (Fig. 17), or that skewness is negative in the entire MPL (not shown).

The apparently mixed-phase profiles were chosen as the main focus of this study, which is reflected in the selection of case studies for Sections 11.1–11.3. Hence, the analysis presented does not provide much insight for the features of the skewness profile in the ice-dominated and ice-only radar observations (Fig. 21.II and III). The variation in skewness in the precipitation below the liquid layer (Fig. 9e, 16e) indicates that processes influencing the ice particles can lead to skewness of the Doppler spectrum. On the other hand, Figs. 19 and 20 show that in the absence of a liquid signal the skewness can be more or less zero. The ice-only skewness profiles (Fig. 21.III) might therefore be constantly zero, and if skewness in the Doppler spectrum is developing it is more likely found in the lower parts of the MPL. At cloud top all ice particles are expected to be relatively small and pristine, which corresponds to a symmetric Doppler spectra. For the Doppler spectra to become skewed requires variation in the terminal fall velocities of the ice particles, i. e. differences in size and density, which can develop trough aggregation when the ice particles are falling through the MPL. Also newly nucleated ice particles co-existing with larger ice falling from higher up in the MPL would cause skewness in the Doppler spectrum. Riming is unlikely to be an important process for the ice-only skewness profiles, as the amount of supercooled liquid is necessarily small. The skewness profile in the ice-dominated profiles (Fig. 21.II) might be similar to the ice-only, or might include a feature resembling that of the apparently mixed-phase profile (Fig. 21.I) near cloud top and skewness related to processes in the ice phase below, resulting in a complicated profile to predict or interpret.

Challenges

A major challenge for the analysis of Doppler spectra in mixed-phase clouds is that no direct information about hydrometeor phase is available. The labeling of certain features in the spectra to relate to ice or liquid phase in Sections 11.1–11.3 was done based on interpretation that utilizes other instruments and relationships between fall speed and reflectivity that are characteristic for certain hydrometeor type. Secondly, knowledge on how microphysical processes in mixed-phased clouds are revealed by the radar Doppler spectra is sparse, and therefore it is not known which processes define the skewness of the spectra. The classification outlined in Fig. 21 proposes a framework to separate the MPCs in regimes where the dominant features in the Doppler spectra are expected to differ. Whether or not the governing microphysical processes are different or not, the observational fingerprints left on the Doppler spectra certainly differ. But as with any categorization of observational data, it might not be trivial to apply the proposed classification to measured profiles. The radars ability to detect the supercooled liquid is limited by its sensitivity and concerns particularly the low-LWP cases. A LWP threshold could therefore be used to exclude ice-only (III) profiles from the analysis. It is also possible that while the radar is measuring a signal from the liquid, a broad precipitation mode can overlap with the cloud mode in the spectra, and although technically there is a signal from the liquid it can only barely, or not at all, be distinguished in the Doppler spectra. Hence, for the separation of apparently mixed-phase (I) and ice-dominated (II) profiles, limits on Z_e could be a possibility. By way of identifying a specific characteristic, such as the Ƨ-shaped skewness profile that was found to prevail in the apparently mixed-phase profiles in Sections 11.1 and 11.2, this characteristic can be used to define appropriate thresholds and to refine the categorization. In such iterative process it is possible - even likely - that further categories need to be added when the view of the Doppler spectra in mixed-phase clouds gets refined.

A single Doppler radar without polarimetric capabilities falls short in the study of the ice-only and ice-dominated MPCs (Fig. 21.III and II). The reflectivity as a function of Doppler velocity does not provide enough information to constrain the ice particle properties, but without detecting changes in parameters such mass, density and shape it is difficult to investigate microphysical processes. Polarimetric radars additionally measure depolarization of the radar signal which provides information about the shape of ice particles (Myagkov et al., 2016) and have been used to investigate microphysical processes in deep multi-layered MPCs (Moisseev et al., 2015, Oue et al., 2016). Oue et al. (2018) and Oue et al. (2015) also showed the benefits of combining Doppler spectra with the analysis of polarimetric variables to distinguish different layers with bimodal Doppler spectra. Furthermore, the multi-frequency approach combines two or three radars with different wavelengths, and provides constrains on the ice particle size distribution (Mason et al., 2018, Matrosov, 1998). For example Kneifel et al. (2016, 2015) have shown that triple-frequency signatures can provide insights to riming and aggregation processes. Hence, the investigation of ice-only and ice-dominated regimes would benefit from these more capable radar techniques.

The lack of information on hydrometeor phase poses an issue for the apparently mixed-phase MPCs (Fig. 21.I). While the slower falling cloud mode can fairly confidently be assumed to relate to super-cooled liquid droplets based on the auxiliary measurements (namely ceilometer and MWR), no definite information about the phase of precipitation is available in the radar Doppler spectra. Unfortunately drizzle droplets and small ice particles populate the same region of the Doppler spectra as they do not have distinctly different fall velocities. It is therefore impossible to determine with certainty the phase of the hydrometeors with a moderate terminal velocity in any specific spectra. Similar skewness structures as described in Sections 11.1–11.2, with positive S_k in the upper parts and negative S_k in the lower parts of the cloud, have been found in warm drizzling clouds (Acquistapace et al., 2019, Kollias et al., 2011b). Furthermore, although large supercooled droplets may hamper with the interpretation of the Doppler spectra in mixed-phase volumes, they might actually be relevant for microphysical processes. The presence of larger droplets have been associated with higher ice production rates (Rangno and Hobbs, 2001), an large droplets also have a central role in the Hallett-Mossop process (Andronache, 2017). The key question is therefore not if drizzle droplets ever occur in the P-MPC data set, but how they change the Doppler spectrum skewness and if drizzle can also be responsible for the skewness profile sketched in Fig. 21.I. It is therefore worth considering the likelihood of supercooled drizzle occurring in the P-MPC dataset. Supercooled drizzle is most often observed in moderately supercooled clouds at temperatures close to 0 °C and the occurrence of super-cooled drizzle declines rapidly with decreasing temperature (Cortinas Jr. et al., 2004, Zhang et al., 2017). Although in warm clouds drizzle is usually not formed when LWP is low, in pristine Arctic air masses with low CCN and INP concentrations larger droplets may form at lower LWP than what would be typical for stratiform clouds at lower latitudes (Silber et al., 2019b). Criteria such as low LWP or low temperature cannot be used to rule out the possibility of drizzle completely, but by excluding moderately supercooled P-MPC the fraction of cases with drizzle is likely to be reduced significantly. Furthermore, in situ observations in MPCs have found precipitation from Arctic low-level MPCs more often in ice than liquid phase (McFarquhar et al., 2007, Mioche et al., 2017). Mioche et al. (2017)

also found liquid droplets larger than 100 µm most often near cloud top, and never below cloud base. They also did not find drizzle droplets at temperatures below -12 °C. Hence, although it is not possible to rule out the occurrence of drizzle droplets in any specific case, it is unlikely that drizzle comprises the majority of precipitation produced by the P-MPC.

The so called kinematic broadening of the Doppler spectrum smooths the features of the spectra and thus acts to decrease the skewness (Fig. 14). The main contributions to kinematic broadening are the turbulent motions in the radar sampling volume and the contribution of horizontal wind due to the finite beam width (Doviak and Zrnić, 2006). Additionally, the noise level impacts the features that can be detected in the Doppler spectrum, as clearly demonstrated in Sect 10. Furthermore, the sensitivity of the radar determines the weakest signal that can be detected. The strength of the microphysical signals in the spectra is therefore not only influenced by the properties of the cloud but also the technical specifications of the radar and the measurement strategy employed. However, not all kinematic effects reduce the skewness of the Doppler spectrum. Heterogeneous vertical wind within the sampling volume may also induce skewness in the spectrum (Luke and Kollias, 2013). Luckily, this effect is not constant in time and therefore any temporally consistent skewness features should be microphysical.

Assumptions for further skewness analysis

Despite the challenges discussed above, very few remote sensing techniques are available for studying the interplay between liquid and ice in mixed-phase clouds, and any parameter that could shed some light into the complex processes is worth considering. The identification of steady features in skewness found in Sections 11.1 and 11.2 is promising and warrants further analysis, which is carried out in the next section.

For the analysis of skewness profiles, it is assumed that:

1. The Z_e associated with the cloud droplets increases from liquid base to cloud top.

2. The Z_e associated with ice particles is zero at cloud top and increases toward liquid base.

3. In apparently mixed-phase clouds (Fig. 21.I), skewness indicates whether the cloud or precipitation mode dominates the measured Z_e. Assuming both modes are Gaussian, the $S_k = 0$ point corresponds to $Z_{precip} \approx Z_{cloud}$.

12 Using skewness features to characterize MPC

Section 11 showed that the radar Doppler spectrum skewness often displays a profile resembling an Ƨ-shape. Although not all skewness profiles exhibit this structure (e.g. Fig. 19e), it appears as a frequent feature in the first two cases (Figs. 9e, 16e). This section focuses on the analysis of such Ƨ-shaped skewness profiles. To detect the specific kind of S_k profile, and to quantify it in the context of the mixed-phase layer, an algorithm to detect the transition from a predominantly negative to positive skewness was developed (Sect. 12.1). The detection of the skewness transition height is done in combination with the discrimination of the type of the skewness profile. After developing the tool to identify the skewness feature of interest, the prevalence of this feature in the P-MPC dataset is evaluated (Sect. 12.2) and the use of the skewness transition height as a cloud parameter

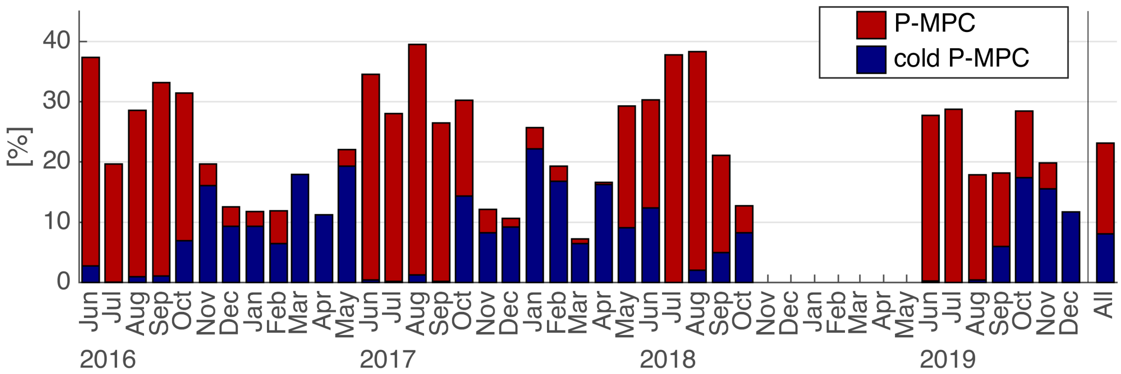

Figure 22: Percentage of measured profiles with P-MPC (see Sect. 8 for criteria) and a subset of the P-MPC (labeled 'cold P-MPC') including only mixed-phase profiles for cases where cloud top temperature did not exceed -5 °C.

is considered (Sect. 12.3). In Sect. 12.4 the method is applied on a case study, followed by a statistical analysis of the skewness transition height in the P-MPC data set in Sect. 12.5.

In this section the entire dataset from June 2016 to December 2019 was utilized. As mentioned in Sect. 9, only mixed-phase profiles were included in this study. Furthermore, as suggested in Sect. 11.4, all cases where cloud top temperature exceeded -5 °C were excluded to lessen the influence of drizzle on the analysis. These two criteria cause a reduction of the size of the dataset compared to Chapter III, where also liquid only profiles have been included. While the frequency of occurrence of the P-MPC in the measurement period was 23%, only 8% of the measured profiles are included in the cold P-MPC dataset (Fig. 22). Due to temperature criteria the amount of data is low particularly in summer. Still, 238 cases consisting of about 2.2×10^6 radar profiles remain to be analyzed.

12.1 Detecting skewness transition

Before applying the algorithm to detect the skewness transition height, preparatory data processing steps were carried out. Despite the additional treatment of the Doppler spectra and moments described in Sect. 10, the S_k profile can still appear somewhat noisy (e.g. Fig. 14d). To facilitate the automatic detection of structures further noise reduction was implemented. A moving average of 3 time steps and 7 range gates was applied (about 9 seconds and 35–50 meters depending on the vertical resolution, respectively). All data below the liquid base were removed in order to only detect features in the MPL. The outcome of these processing steps is presented in Fig. 23 for the S_k timeseries that were shown for the case studies in Sect. 11.

Each skewness profile was normalized to 200 data points between the first and last height where radar data is available in the MPL in order to mitigate the effect of changing MPL depth and vertical resolution on the analysis. The height at which S_k turns from negative to positive was identified by finding the maximum of the following function:

$$\zeta(z) = -\sum_{i=z_{lb}}^{z} S_i + \sum_{i=z}^{z_{ct}} S_i \tag{17}$$

where S_z is the Doppler spectrum skewness at height z, z_{lb} is the liquid base height and z_{ct} is the cloud top height. Fig. 24 illustrates the behavior of $\zeta(z)$ and its relationship to the

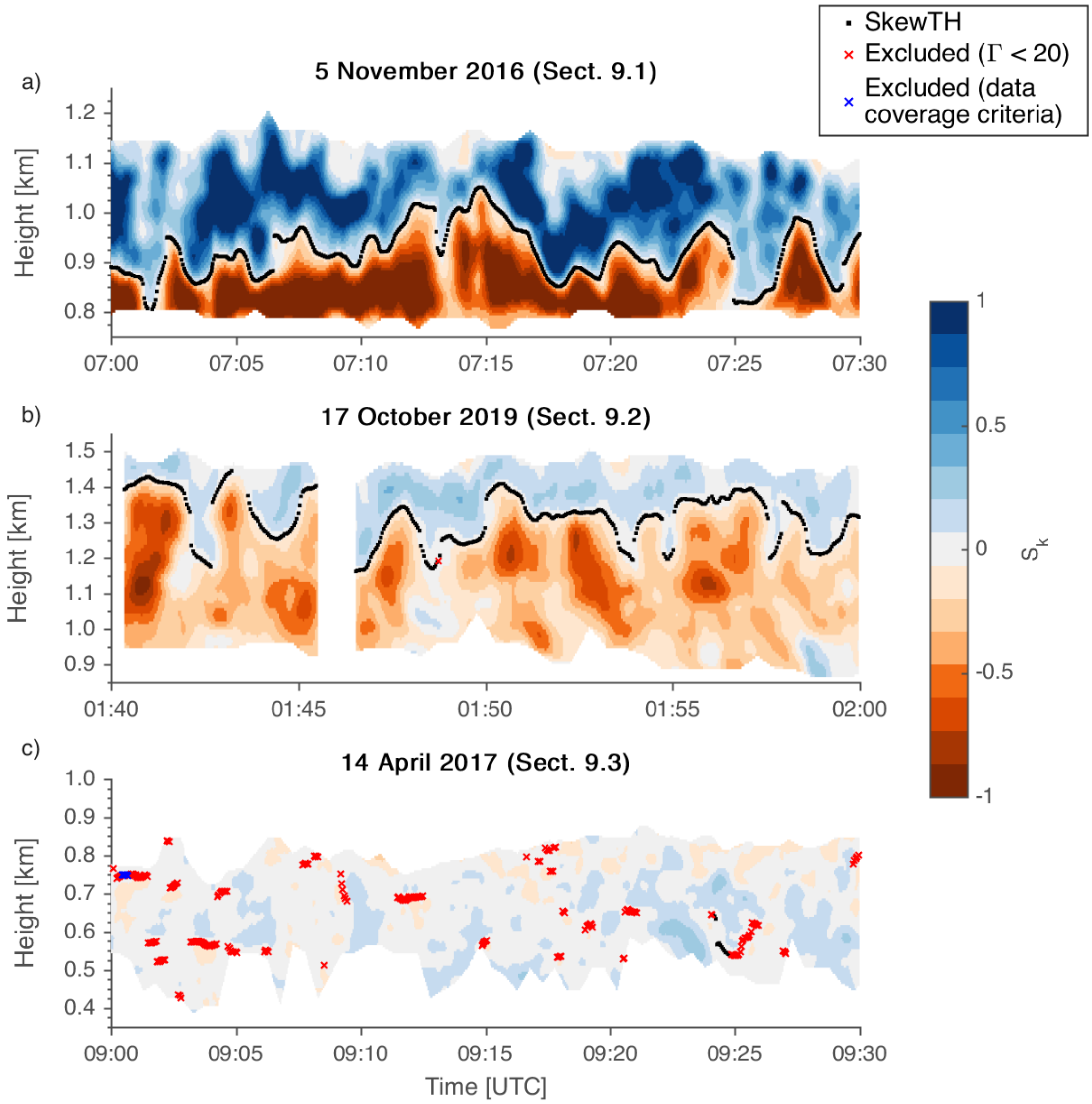

Figure 23: The skewness timeseries after additional processing and the identified SkewTH (see text for details). The excluded SkewTH are shown with red and blue markers. The time periods in a), b) and c) correspond to those shown in Figs. 9, 16 and 19, respectively. The 1 minute gap at 17 October 2019 01:46 UTC is due to the cloud not fulfilling all the criteria for P-MPC in two Cloudnet profiles.

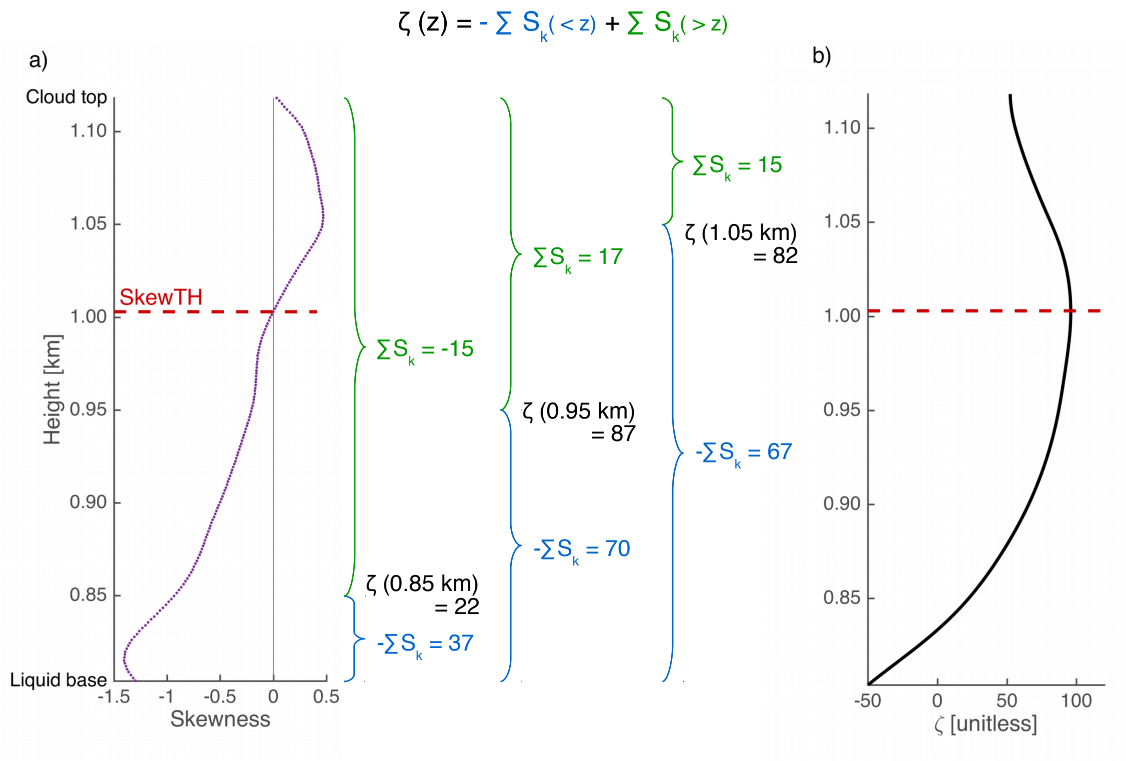

Figure 24: a) An example skewness profile and b) the corresponding ζ-profile (Eq. 17). Three examples (at 0.85, 0.95 and 1.05 km height) for computing $\zeta(z)$ are shown. Further examples are shown in Fig. 25.

skewness profile, and further examples are shown in Fig. 25. $\zeta(z)$ gets its largest value at the height where skewness turns from negative to positive, so that the skewness transition height (SkewTH) is simply given by

$$SkewTH = z_{\max(\zeta)} \quad . \tag{18}$$

In case skewness moves from negative to positive several times, local maximum and minimum in $\zeta(z)$ denote the change in the sign and $\zeta(z)$ gets its largest value at the height above which the skewness is most strongest positive and below which it is most negative (Example 1 in Fig. 25). Any max(ζ) at liquid base or cloud top are ignored because they cannot correspond to a transition point but result from a throughout dominantly positive or negative skewness profile (Example 2 in Fig. 25). Furthermore, the examples in Fig. 25 show that the values of $\zeta(z)$ depend on the magnitude of the skewness values and how clearly the skewness profile exhibits the layered structure with negative values below and positive values above. Hence, $\zeta(z)$ can be used as a measure of the "strength" of the skewness feature. For this purpose

$$\Gamma = \max(\zeta(z)) - \min(\zeta(z)) \tag{19}$$

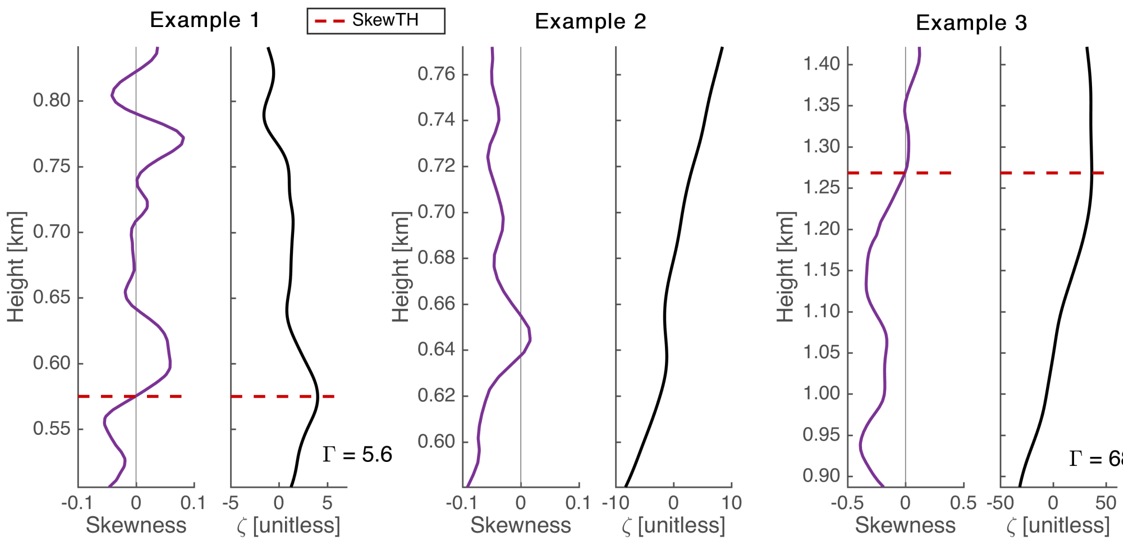

Figure 25: Examples of skewness- and the corresponding ζ-profiles. The SkewTH given by Eq. 18 and Γ given by Eq. 19 are shown where applicable. Note that the scales differ considerably between the examples.

was calculated for each profile. Based on inspection of various profiles in different cloud cases, skewness profiles with $\Gamma < 20$ were deemed to exhibit the desired skewness feature too weakly and were excluded from further analysis.

As a last step to assure the quality of the SkewTH dataset, sporadically occurring data points were removed. For each SkewTH data point, a data coverage of at least 30% relative to the available skewness profiles in a $\pm$ 1 minute window was required. This criteria was applied iteratively until no further data were removed. The purpose of this processing step is to dismiss profiles from the analysis that do not exhibit a temporally consistent feature. The resulting SkewTH for the example cases presented in Sect. 11 are shown in Fig. 23. The clear features in the 5 November 2016 and 17 October 2019 cases (Sect. 11.1 and 11.2) are well captured. In the 14 April 2017 case (Sect. 11.3) most of the time no SkewTH is found. The $\Gamma < 20$ criteria removes many of the initially detected SkewTH and the data coverage criteria removes some more, resulting in only a few SkewTH being recognized at 9:24–9:25 UTC. It should be emphasized that the algorithm specifically detects a structure with predominantly negative skewness in the lower part with a predominantly positive skewness in the upper part of the MPL. Opposite structure or any other kind of feature are not identified.

12.2 Occurrence and required conditions for skewness transition height

The skewness transition height (SkewTH) was identified in 32% of all of the skewness profiles analyzed. The fraction of S_k-profiles with SkewTH within each cold P-MPC case is shown in Fig. 26a. In 60% of the cases the SkewTH was found at least 10% of the time. Considering the rather strict quality criteria imposed on the detection of the SkewTH, these cases can fairly confidently be assumed to have exhibited the skewness feature at least temporarily. Similarly, the 6% of the cold P-MPCs where the SkewTH was present over 70% of the time can be considered clouds where the layered skewness structure (negative in the bottom and positive at the top) was rather continuous. In most cold P-MPCs the SkewTH was partially present, which could be related to an intermittency of the feature or

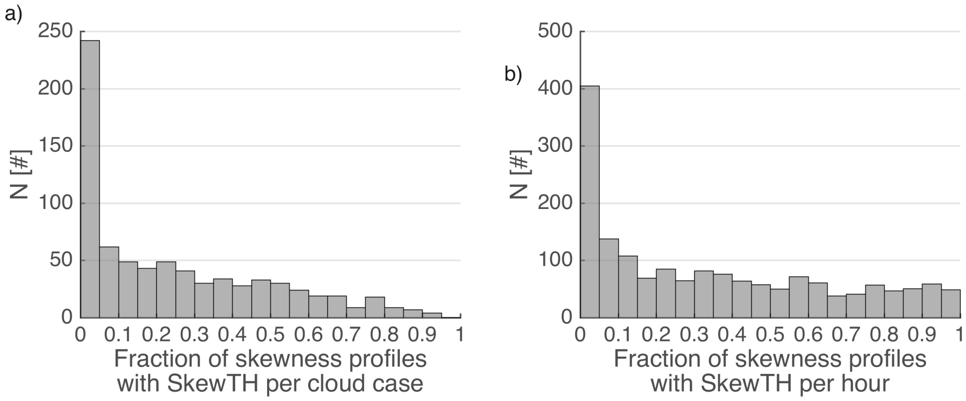

Figure 26: The fraction of S_k profiles with SkewTH identified in a) each cold P-MPC case and b) hourly time periods.

to the strength of the feature not being continuously strong enough. The duration of the different P-MPC cases varies, and it is possible that a cloud was present over Ny-Ålesund for several hours and exhibited the S_k feature for a period of time but then developed to a state without any S_k structures, ending up with a low SkewTH fraction despite the feature being strong for some time. Therefore, each cold P-MPC case exceeding two hours was split into hourly time periods. The frequency of occurrence of SkewTH in these shorter time periods, shown in Fig. 26b, was often higher than it was when considering the entire duration of the P-MPC. 18% of the hourly time periods feature the SkewTH over 70% of the time, and 6% over 90% of the time. On the other hand, in 11% of the hourly periods SkewTH was completely absent. Hence, it seems that a cloud can have phases with rather continuous or completely missing SkewTH. Although the SkewTH is more often absent than present, more than half of the cold P-MPCs feature the skewness transition at least part of the time.

When evaluating how often the SkewTH was detected, it is worth considering in which conditions it appeared. As discussed in Sect. 11, low amounts of liquid are challenging for a radar based analysis. Indeed, low LWP conditions were associated with infrequent SkewTH detection, and with increasing LWP the fraction of profiles with SkewTH increased until about $90\,\mathrm{g\,m^{-2}}$ (Fig. 27b). Above this value the portion of profiles with SkewTH levels at approximately 50%. At low LWP the radar lacks the required sensitivity to detect the small droplets rendering it impossible to collect measurements such as depicted in Fig. 21a. With increasing LWP the chances for the radar to detect the cloud droplets increases and also the Z_{cloud} becomes stronger, which promotes the Ƨ-shaped skewness profile, hence the increase in the frequency of SkewTH observations.

Besides the Ƨ-shaped skewness profile (Fig. 21a), numerous profiles with constantly nearly zero S_k were observed (Figs. 19). Here, profiles with mean($|S_k|$) < 0.05 were taken to not considerably differ from zero, hereafter referred to as ZeroSkew-profiles. For the threshold different values from 0.01 to 0.1 were tested, and the tendencies described here were not found sensitive to the choice of the threshold. Skewness profiles without SkewTH were separated into ZeroSkew-profiles and the rest. The ZeroSkew-profiles were particularly common at low LWP, and with increasing LWP the portion of profiles with no significant skewness features decreased (Fig. 27b). Above a LWP of $50\,\mathrm{g\,m^{-2}}$ less than 10% belonged to the ZeroSkew-category, indicating that throughout symmetric and unimodal profiles were rare for the cold P-MPC at moderate to large LWP. A considerable portion

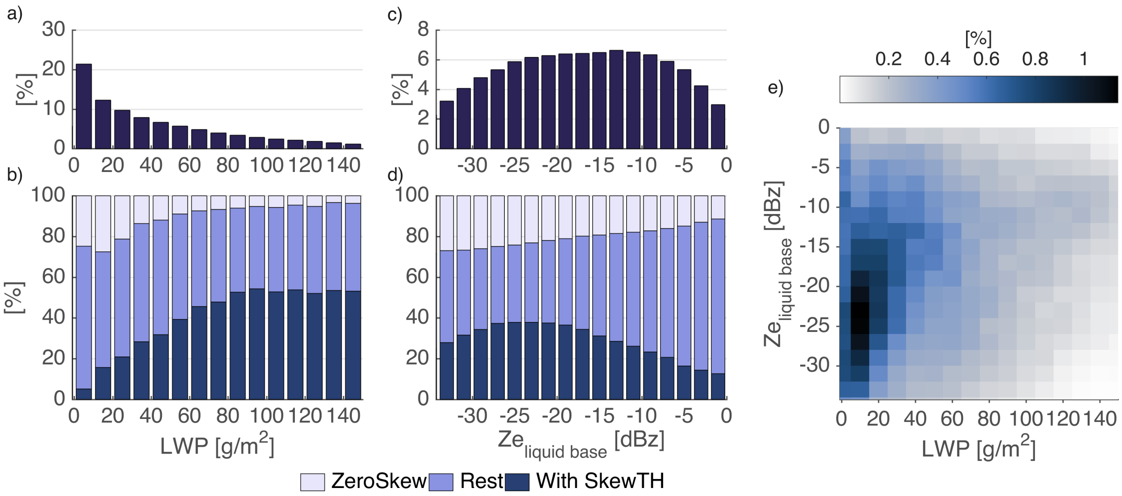

Figure 27: Distributions of a) LWP, c) Z_e at liquid base and e) the bivariate distribution of LWP and Z_e at liquid base in the cold P-MPC dataset, and the fraction of profiles in SkewTH, ZeroSkew and "Rest" categories in each LWP (b) and $Z_{liquidbase}$ (d) bin.

of the skewness profiles ends up in the "Rest"-category (Fig. 27b). These profiles include everything that did not fit the criteria of the two other categories: completely positive or negative profiles, profiles in which SkewTH was excluded by the quality criteria (Sect. 12.1), or skewness profiles with negative skewness above a layer of positive skewness. Specifically at low LWP, the profiles in the "Rest"-category are likely exhibiting features related to processes in the ice phase.

The skewness profile as described in Fig. 21a does not only depend on the cloud liquid, but also the ice phase is crucial. A high amount of ice could lead to a throughout negative skewness profile (e.g. Fig. 23b at 01:43 UTC) or to the skewness mainly exhibiting signs of processes in the ice phase, in which cases the skewness profile might have a different shape. Z_e at one range gate below the liquid base ($Z_{liquidbase}$), where there is no or only minimal (in case of inaccuracy in the detection of the liquid base height) contribution from the cloud mode to the total reflectivity, was taken as a proxy for the amount of ice in the MPL. Similarly as with LWP, the increase in $Z_{liquidbase}$ was decreasing the portion of profiles classified as ZeroSkew (Fig. 27d). However, the fraction of profiles with SkewTH was first slightly growing and then shrinking with increasing $Z_{liquidbase}$. At the large end of the distribution $Z_{liquidbase}$ is so large that Z_{precip} is likely to heavily dominate the MPL, and the skewness profiles mainly exhibit signs of processes modifying the precipitation mode. At low reflectivities the precipitating ice particles are necessarily small and few, limiting the possible interactions that could lead to skewness in the Doppler spectra and thus the ZeroSkew-profiles were more common. To explain the increase in the fraction of SkewTH at $Z_{liquidbase}$ below -25 dBz it is necessary to again consider the liquid phase. The bivariate distribution shown in Fig. 27e indicates that from -35 to -20 dBz the average LWP was increasing with increasing $Z_{liquidbase}$. As SkewTH was more often detected with increasing LWP (Fig. 27b), a slight increase can be expected in the occurrence of SkewTH with the increase of $Z_{liquidbase}$, as it coincides with an increase in LWP.

Since the occurrence of SkewTH is tied to both LWP and $Z_{liquidbase}$, it is worth considering the two parameters together to explain why SkewTH was occasionally identified at very low LWP or high $Z_{liquidbase}$ (Fig. 27b, d). Fig. 28a shows that SkewTH could be identified in low LWP conditions when $Z_{liquidbase}$ was also low, and in higher $Z_{liquidbase}$

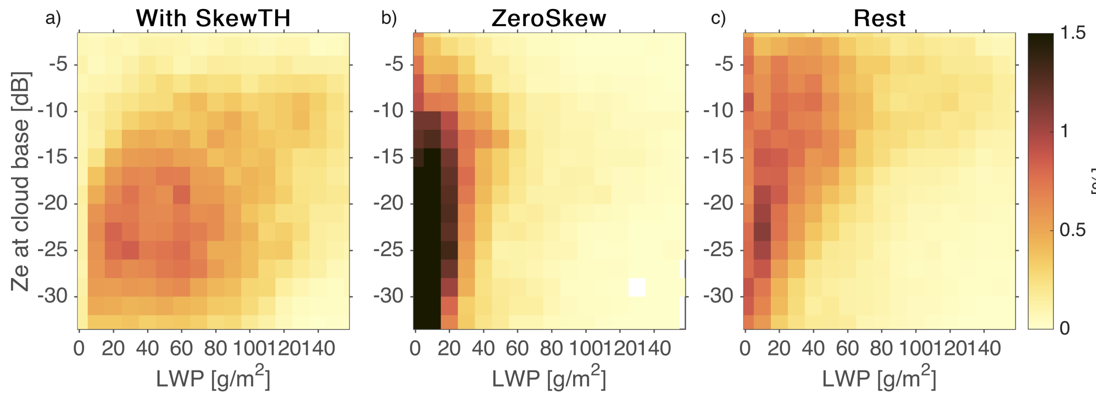

Figure 28: Bivariate distribution of LWP and Z_e at liquid base for profiles with a) SkewTH, b) ZeroSkew and c) the "Rest" categories.

conditions when also LWP was larger. Still, SkewTH were rare when $Z_{liquidbase}$ was above -6 dBz. Skewness inherently does not contain information about the magnitude of Z_e associated with the cloud or the precipitation mode per se, but about the relationship between the two (or more) modes. For skewness to exhibit the Ƨ-shaped profile, detected by the identification of the SkewTH, requires both the cloud and the precipitation mode to be sufficiently strong but not too overly dominant compared to the other mode. Because at the liquid base the cloud mode disappears while the precipitation mode remains, the cloud mode is not expected to dominate the entire MPL as long as precipitation is formed. The circumstances where one of the modes dominates the entire MPL therefore relate to the precipitation mode dominating, which explains why at the high end of the $Z_{liquidbase}$ distribution profiles with SkewTH were rare.

As already shown by Fig. 27b and d, the ZeroSkew-profiles were focused in the low LWP region, but span a range of $Z_{liquidbase}$ (Fig. 28b). These are likely profiles where the cloud mode was absent in the Doppler spectra (as for example in the 14 April 2017 case described in Sect. 11.3), and riming, aggregation, or secondary ice production were either not taking place or too weak to impact the shape of the Doppler spectra. Assuming the classification of the profiles as mixed-phase is correct, the ZeroSkew-profiles probably consists of clouds where ice nucleation and depositional growth were the only processes modifying the Doppler spectra. Because the "Rest" category is a mix of profiles with different characteristics and contains probably the profiles with the most complicated mixtures of varied hydrometeors and processes, the possibilities to draw conclusions from Fig. 28c are limited. Aggregation can produce large snowflakes that may cause high Z_{precip} in the MPL, and at least some of the profiles at the large end of the $Z_{liquidbase}$ probably contain signs of aggregation. In Fig. 28 at the lower half of the $Z_{liquidbase}$ the "Rest" category overlaps with the other two groups, which could be related to profiles close to the thresholds of the classification criteria which might have been misclassified. Overall, Fig. 28 shows that with LWP above about 30 g m^{-2} the skewness profile almost always exhibits some features, either related to mixed- or ice-phase processes. Also, above -10 dBz of $Z_{liquidbase}$ other than the Ƨ-shaped skewness profile is common, which is not surprising considering that at such reflectivities the ice mode is strongly dominating the MPL and it could be expected that its shape and changes determine the skewness profile.

The analysis presented in this section shows that the occurrence of SkewTH depends on the amounts of liquid and ice in the MPL in rather predictable ways. Profiles with too low amounts of liquid (as measured by the LWP) or large amounts of ice (estimated by the Z_e of the precipitation falling out of the MPL) were usually associated with skewness profiles that do not exhibit a clear transitioning from negative to positive skewness. Thus, conclusions drawn from the analysis of the SkewTH represent P-MPC in a specific phase-partitioning regime defined by the radar reflectivity of the cloud and precipitation modes. The moderate frequency of occurrence (32%) of SkewTH in the cold P-MPC dataset follows particularly from the commonality of low LWP (Fig. 27a). Excluding all profiles with LWP $< 30\,\mathrm{g\,m^{-2}}$ raises the fraction of skewness profiles with SkewTH to 51%, and further excluding all profiles with $Z_{liquidbase} >$ -10 dBz to 58%. These thresholds are exemplary as Fig. 28a does not provide a basis of setting definite thresholds, and serve to illustrate that estimating a commonality of a feature is dependent on the regime considered. In conditions where Z_{cloud} is sufficiently strong and not overshadowed by a large Z_{precip} the Ƨ-shaped skewness profile sketched in Fig. 21a was commonplace. Hence, the specific skewness feature is relevant in the context of the low-level MPC at Ny-Ålesund, and could provide insights into the processes in the MPL.

12.3 Skewness transition height as a cloud parameter

Identifying the SkewTH does not only allow the evaluation of the occurrence of the specific kind of skewness profile, but also opens possibilities to analyze these profiles in more detail. To combine clouds at different heights and with varying MPL depth, further measures to describe the SkewTH in the context of the MPL are defined: the distance of SkewTH from cloud top

$$SkewTH_{ct} = z_{ct} - SkewTH \quad , \tag{20}$$

the distance of SkewTH from liquid base

$$SkewTH_{lb} = SkewTH - z_{lb} \quad , \tag{21}$$

and the skewness transition height normalized between liquid base and cloud top

$$SkewTH_{norm} = \frac{SkewTH - z_{lb}}{z_{ct} - z_{lb}} \quad , \tag{22}$$

where $SkewTH_{norm}$ at z_{lb} and z_{ct} correspond to 0 and 1, respectively. As will be shown later in Sect. 12.5, the different normalizations provide alternative perspectives that are necessary to properly interpret the skewness transition height.

With the detection and quantification of SkewTH in place it is now possible to inspect the radar profiles using this new measure. Fig. 29 shows the distributions of the radar moments in the MPL for profiles with different $SkewTH_{norm}$. First of all, the SkewTH is successfully sorting the skewness profiles in distinct categories. All skewness profiles in Fig. 29p–t exhibit the Ƨ-shaped profile sketched in Fig. 21a, but the height where skewness changes from negative to positive is changing depending on the $SkewTH_{norm}$. Below the SkewTH both the median and most of the distribution are negative, and above the SkewTH positive. Hence, the detection of SkewTH and the discrimination of profiles based on $SkewTH_{norm}$ works as intended.

The Z_e and V_m distributions for different $SkewTH_{norm}$ can be used to evaluate the interpretation of the skewness profile to describe the relative strength of the cloud and precipitation modes in the Doppler spectra. With low $SkewTH_{norm}$ ($<$ 0.2) the Z_e-

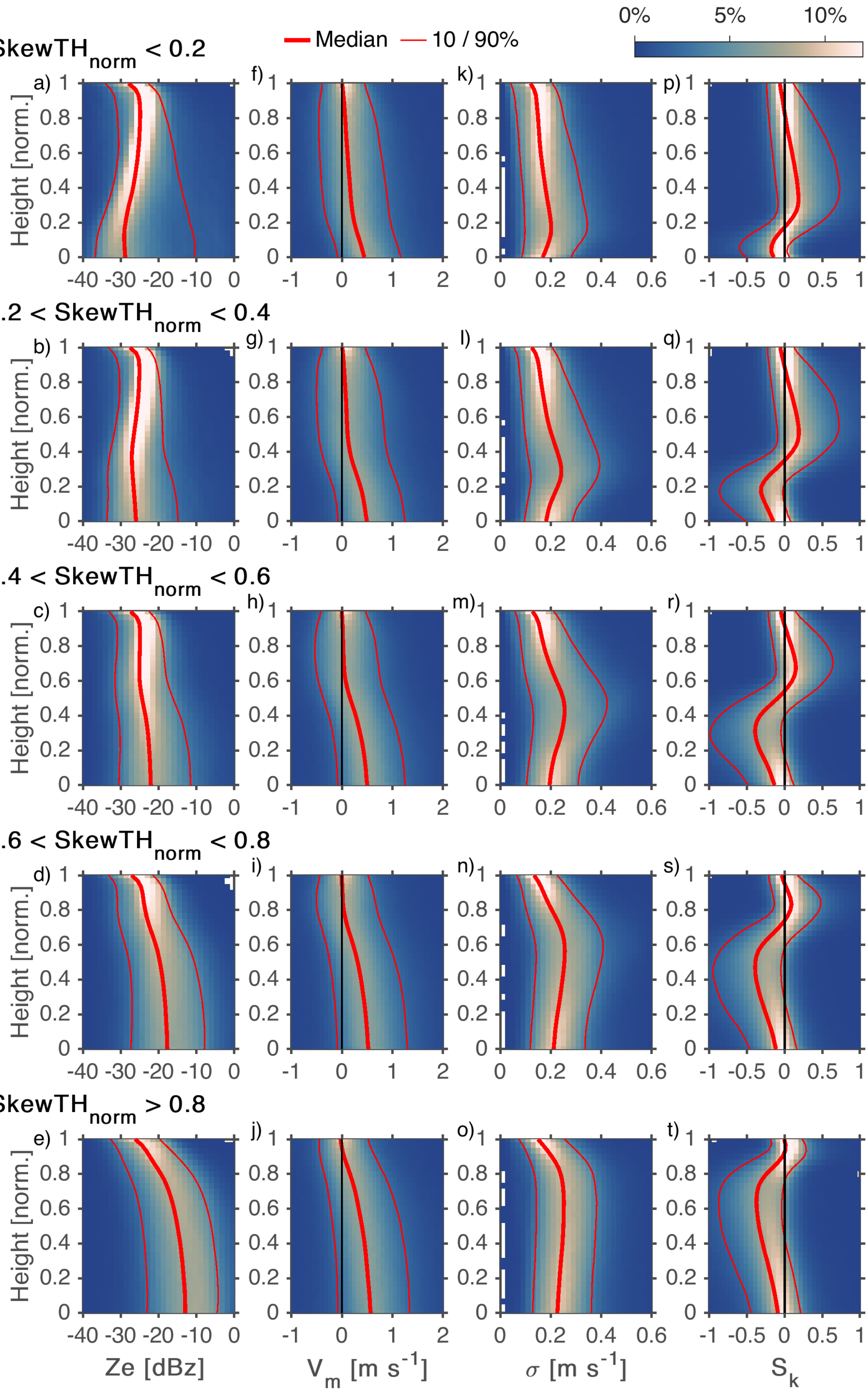

Figure 29: Distributions of radar moments (columns) with different $SkewTH_{norm}$ (rows). The height of the profiles is normalized with respect to the liquid layer, so that 0 indicates liquid base and 1 cloud top (Eq. 22). In each figure, the distribution of values is shown relative to the total number of observations at a given height.

profile is increasing towards cloud top (Fig. 29a) as would be expected for profiles largely dominated by the cloud mode. The V_m is on average zero at the top of the cloud and remains close to zero down to the height with the SkewTH where it abruptly increases (Fig. 29f–j). Turbulence modulates the V_m, but the average vertical wind velocity should be zero when averaged over a long enough time period (Stull, 1988). The distribution of V_m is therefore broadened, but the median values should present the terminal fall velocities of the hydrometeors. Above the SkewTH the cloud mode is dominating, thus the V_m is dominated by the cloud droplets terminal velocity that averages at zero. At the SkewTH the precipitation mode takes over and the V_m becomes dominated by the falling particles, hence the clear increase in V_m at the SkewTH and below. Fig. 29a–e show the change in the Z_e distribution as the height where the precipitation mode takes over shifts towards cloud top. In Fig. 29b the upper part of the MPL is similar than in Fig. 29a with Z_e increasing with height, but in the lower parts the Z_e distribution is more broad and the median Z_e-profile is rather constant. In Fig. 29c the portion of the Z_e-profile increasing with height is focused on the very top of the MPL, and below the SkewTH a clear increase in Z_e caused by the growing ice particles is seen. With $SkewTH_{norm} > 0.8$ (Fig. 29e) Z_e increases all the way from cloud top to liquid base and the median V_m is constantly positive, indicating that precipitation is dominating the radar signal in the entire MPL except the very top. Overall, Fig. 29a–j are in agreement with the interpretation of the skewness profile depicted in Sect. 11.4, i.e. that above the SkewTH the cloud mode dominates the radar signal and below the precipitation mode.

The Doppler spectrum width profiles differ between the $SkewTH_{norm}$ classes (Fig. 29k–o). When $SkewTH_{norm} < 0.6$, σ gets the largest values at the height of the SkewTH. At the SkewTH both the cloud and the precipitation mode are strong causing a large spectrum width (Fig. 29k–m). Ignoring kinematic effects broadening the Doppler spectrum, the σ is large when multiple modes with different fall velocities are present. Because the cloud mode has a terminal velocity of $0\,\mathrm{m\,s^{-1}}$ and the terminal velocity of the precipitation mode increases from cloud top downwards, the difference in fall velocity between the two modes is expected to increase from cloud top to liquid base. Thus σ reaches higher values at SkewTH when $SkewTH_{norm}$ is low. With $SkewTH_{norm} > 0.6$ (Fig. 29n–o) σ increases from cloud top downwards but does not decrease again below the SkewTH as it does in Fig. 29k–m. To explain the σ profile below the SkewTH when $SkewTH_{norm}$ is higher up in the cloud requires considering the precipitation mode. The spectographs shown in Figs. 10–20 suggest that the width of the precipitation mode increases as it grows towards liquid base. The spectrum width below the SkewTH when the transition in skewness takes place close to cloud top (Fig. 29o) is hence a result of both the bimodality of the spectra and the increasing width of the precipitation mode due to the growth of the precipitating particles. Additionally, it could be possible that different turbulence conditions are associated with the different $SkewTH_{norm}$, which would further impact the spectrum width.

Fig. 29a–j shows that Z_e and V_m are larger at cloud base when $SkewTH_{norm}$ is closer to cloud top. The median Z_e at liquid base increased from -29 dBz for $SkewTH_{norm} < 0.2$ to -13 dBz for $SkewTH_{norm} > 0.8$, and the V_m from 0.41 to $0.56\,\mathrm{m\,s^{-1}}$, respectively. Larger Z_e at liquid base indicate the MPL is producing more precipitation. Since Z_{cloud} increases with height and Z_{precip} decreases, for Z_{precip} to dominate close to cloud top requires Z_{precip} to be rather large already at the upper part of the cloud, and as it continues to grow it is also larger at liquid base. Because the median V_m is quite modest even for $SkewTH_{norm}$ > 0.8 suggesting relatively small ice particles, the larger Z_e at liquid base might be due to increase in ice particle number concentration. Furthermore, it seems that considerable riming which would increase the fall velocity (Kneifel and Moisseev, 2020) is not frequent. At the base of the MPL skewness was on average slightly negative, with the median S_k varying from -0.18 to -0.10 in the different $SkewTH_{norm}$ groups. The negative skewness at the liquid base could be caused by an inaccuracy of the detection of the liquid base height from the ceilometer β'-profile or the coarser resolution of the measurement, but it could also be a indicator of processes effecting the precipitation mode.

To summarize, Fig. 29 shows that the interpretation of SkewTH is supported by the bulk parameters in the cold P-MPC data set. Secondly, despite omitting potentially relevant details such as the depth of the MPL, temperature, or LWP, indicators for the occurrence of certain processes could be found by just sorting the data based on the $SkewTH_{norm}$. However, a more detailed analysis that considers further aspects is warranted. Before further analyzing the larger dataset, the SkewTH is examined in more detail for a case study to facilitate a better understanding on how the skewness profile relates to other cloud parameters and which processes might be influencing it.

12.4 Application to a case study

To better understand the skewness transition height, attention is turned again to the MPC case on the 5 November 2016 that was introduced in Sect. 11.1. A two hour time period is analyzed, from 6:00 to 8:00 UTC (Fig. 30). Fig. 30d shows how the SkewTH clearly splits the MPL to the upper part with predominantly positive skewness and the lower part with predominantly negative skewness. SkewTH varies from the bottom of the layer (at 7:01 UTC) to close to the top (7:33 UTC), but averages at 130 m above liquid base and 210 m below cloud top. A close inspection of the time series reveals some interesting features. Fig. 30a suggests that an increase in SkewTH coincides with an increase in the reflectivity (6:35 UTC, 7:15-7:18 UTC, 7:30-7:34 UTC). This relationship is confirmed by Fig. 31a, which shows a clear correlation between the MPL mean Z_e and SkewTH. Fig. 31b further shows that higher SkewTH is associated with higher Z_e specifically at the height of the skewness transition. At higher SkewTH, the Z_e related to precipitation starts to dominate the total Z_e closer to cloud top. Since Z_{cloud} increases with height and Z_{precip} decreases, for Z_{precip} to dominate close to cloud top requires Z_{precip} to be rather large already at the upper part of the cloud. The larger Z_{precip} could for example be caused by a higher ice nucleation rate increasing the ice particle number concentration. Hence, Z_e at SkewTH is larger when the SkewTH is higher. A higher SkewTH is also related to a higher Z_e below the skewness transition height (as already shown by Fig. 29a–e), since the ice crystals continue to grow when falling through the mixed-phase layer (Fig. 31c). Similarly to Fig. 29a, the timeseries in Fig. 30a shows an increase in Z_e in the layer above the SkewTH when SkewTH is close to the liquid base. The increase in Z_e with height above the SkewTH, which is caused by the cloud mode dominating the radar signal in this layer, explains why the mean Z_e is higher above than below the SkewTH when the SkewTH is low (Fig. 31c) .

The assumption that the layer above the SkewTH is dominated by the super-cooled liquid can be tested using the LWP measurement, which is independent from the cloud radar observations. Although some liquid is expected in the lower parts of the MPL, the liquid in the upper parts dominates the LWP due to the increase in LWC with height (Morrison et al., 2008). Fig. 32a shows a clear relationship between the mean Z_e between

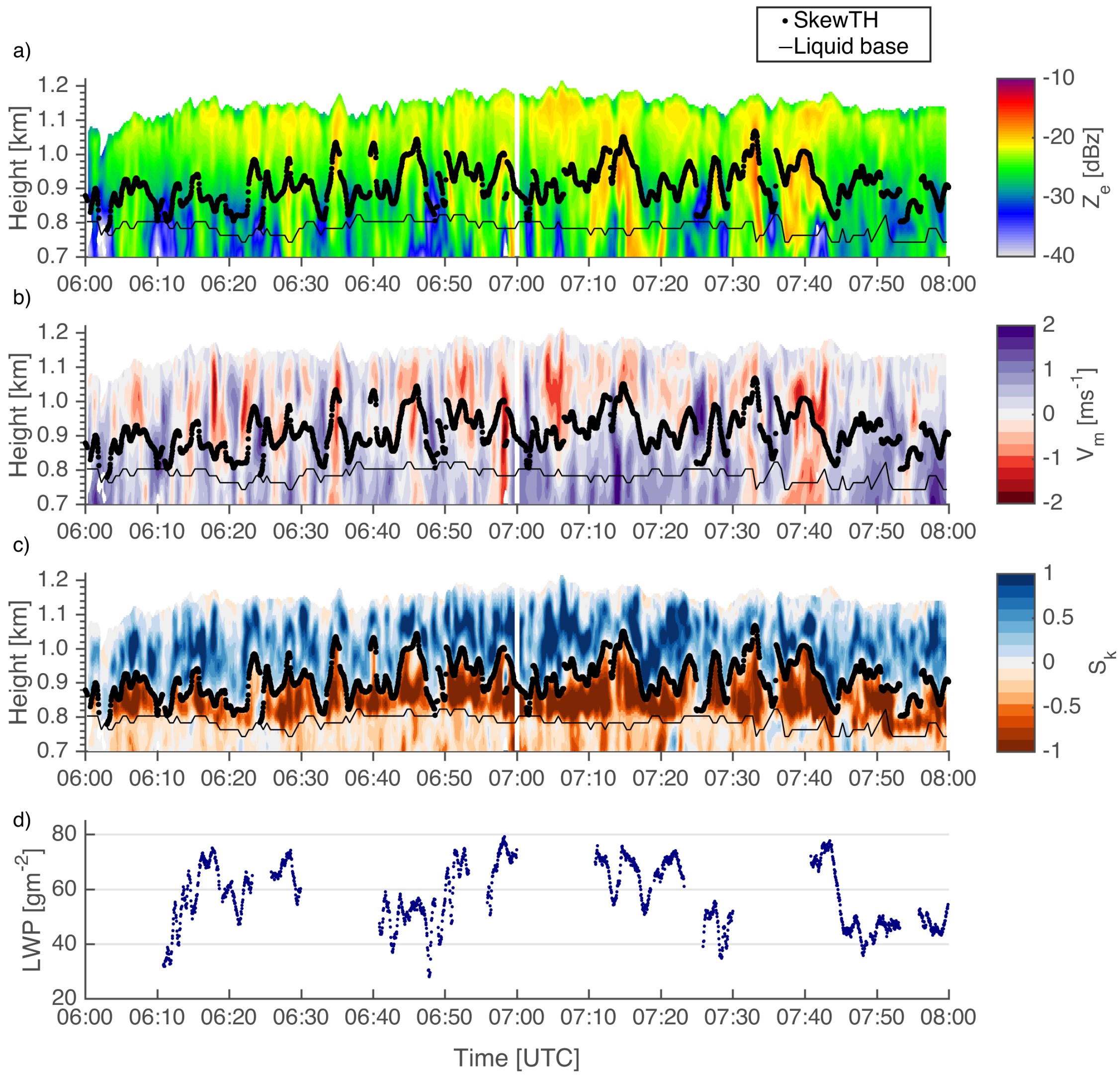

Figure 30: Time series of the parameters used for the time period analyzed in Sect. 12.4: a) reflectivity, b) mean Doppler velocity, c) Doppler spectrum skewness, and d) liquid water path (LWP). The regular gaps in the LWP timeseries are caused by scanning interrupting the zenith pointing the observations (Sect. 6.1).

SkewTH and cloud top, and the LWP. In other words, the LWP is correlated with Z_e in the part of the MPL where the radar signal is believed to be dominated by liquid. This result gives further confidence in the interpretation of the skewness profile. The scatter in Fig. 32a can be explained by the variable portion of the MPL that is considered when calculating the mean Z_e for the layer above the SkewTH. Z_{cloud} increases with height, and so Z_e would be expected to be higher when the part of the MPL that is included in the average above the SkewTH is more focused to cloud top. Indeed, Fig. 32a shows that for a given LWP, higher Z_e above the SkewTH is related to a higher SkewTH. Additionally, the precipitation mode is also contributing to Z_e in variable amounts. As discussed above, a higher SkewTH seems to be related to a larger Z_{precip}. The contribution of Z_{precip} to the total Z_e above the SkewTH could therefore be larger when the SkewTH is high, in agreement with Fig. 32a.

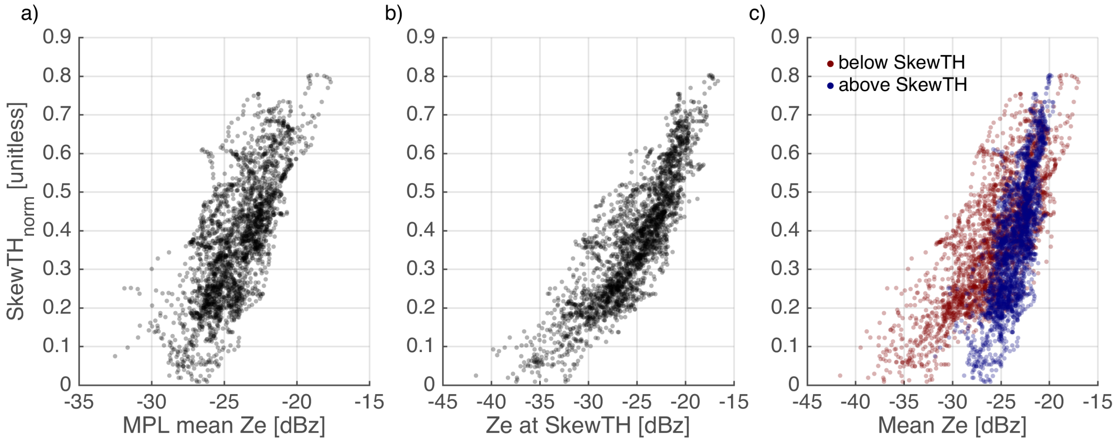

Figure 31: a) Mean Z_e in the mixed-phase layer, b) Z_e at the SkewTH, c) mean Z_e from liquid base to SkewTH (red) and from the SkewTH to cloud top (blue).

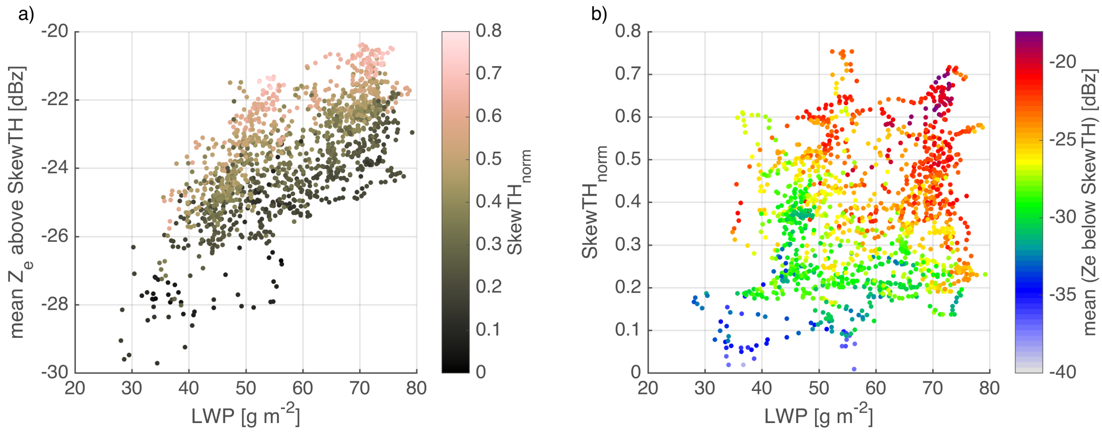

Figure 32: a) The relationship between the LWP and the mean Z_e of the layer from SkewTH to cloud top. The color indicates $SkewTH_{norm}$. b) LWP, $SkewTH_{norm}$ and the mean Z_e in the MPL below the SkewTH (indicated by color).

Fig. 32a suggests that the SkewTH is independent of LWP. This is further illustrated by Fig. 32b, which confirms the lack of correlation between the two parameters. The result seems to contradict the assumptions made about the skewness profile, as the SkewTH is understood to represent the height where the balance between Z_{cloud} and Z_{precip} shifts and therefore should closely relate to the amount of liquid in the cloud. For a fixed Z_{precip} profile, a stronger Z_{cloud} (i.e. larger LWP) should move the SkewTH downwards. Using the Z_e below the SkewTH as a proxy for Z_{precip} in the MPL, Fig. 32b indicates that for a given Z_e the increase in LWP does indeed relate to lower SkewTH. Hence, the lack of correlation between LWP and SkewTH is not a sign of mistaken assumptions, but the microphysical processes in play. For a given LWP, a large variation in the amount of ice is possible, indicated by the variability in Z_e below the SkewTH in Fig. 32b. It follows that large variability in the radar reflectivity weighted phase partitioning, as represented by the SkewTH, is also present. Furthermore, the impact the LWP has on the SkewTH-Z_e-relationship shown in Fig. 31 is considered. A larger LWP relates to an increase in Z_e at the SkewTH (Fig. 33). This behavior can be explained by considering the assumption that at the SkewTH both liquid and ice contribute approximately equally to the total reflectivity.

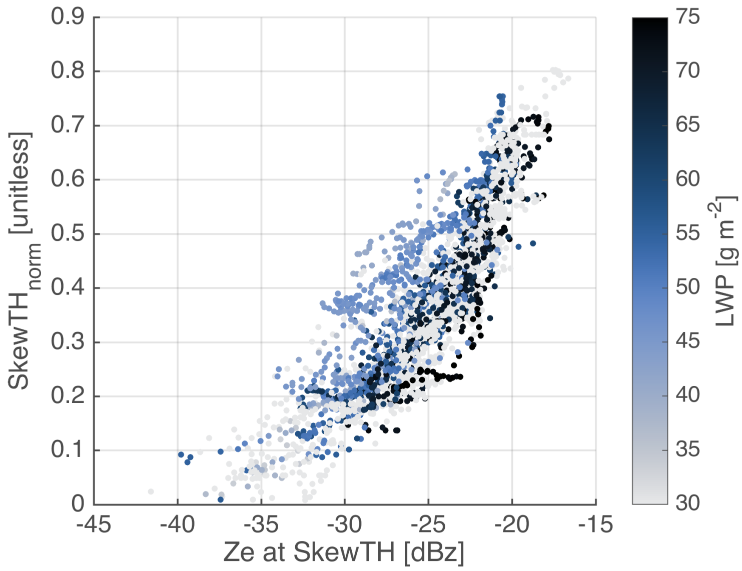

Figure 33: The influence of LWP on the relationship between SkewTH and Z_e at SkewTH.

A larger LWP shifts the Z_{cloud} profile to higher values, requiring a larger Z_{precip} in order for the SkewTH to stay at the same height. Hence, a higher LWP is associated with a slight increase in Z_e at SkewTH.

Fig. 32b shows, despite the scatter, that larger Z_e below the SkewTH are related to higher LWP, indicating that an increase in cloud liquid is related to an increase in the amount of ice. This result is in agreement with previous studies (e.g. De Boer et al., 2011, Korolev and Isaac, 2003, Morrison et al., 2005, Rangno and Hobbs, 2001). That the SkewTH is clearly correlated with Z_e but not LWP could indicate that the phase-partitioning in this MPC is to a large degree controlled by the ice phase, at least when viewed in terms of radar reflectivity. That ice is controlling a parameter determined based on reflectivity would be expected given the strong size dependency of Z_e.

Returning to the time series of radar moments, the mean Doppler velocity in the layer above the SkewTH shows more variation than the layer below (Fig. 30b). Particularly, V_m above the SkewTH shows clearly more upward velocities. In the upper part of the MPC where liquid dominates the radar signal, V_m is indicative of vertical motions although still biased to some extent by Z_{precip}. Below the SkewTH the precipitation mode dominates the signal, and V_m shows a more consistent downward motion. Only in very strong updrafts (e.g. 6:33-6:35 UTC, 6:55-7:00 UTC, 7:30-7:43UTC) does the upwards air motion overcome the terminal velocity of the ice and the mean Doppler velocity is upwards. That the skewness transition height so nicely maps the layer in the upper part of the cloud where vertical motions are identifiable in the radar V_m is in agreement with the interpretation of the skewness transition height separating the liquid dominated and ice dominated layers of the MPL.

It is generally recognized that vertical motions in the Arctic low-level MPC play a role via modulating the cloud liquid (Morrison et al., 2012, Shupe et al., 2008a). Here, the slow edge of the Doppler spectra is used as a tracer for air motions, and the mean within the MPL is taken to describe the average vertical wind within the layer. The time series in Fig. 30a and d show that the vertical motions pose a forcing to LWP by decreasing and increasing the LWP rather than determining the absolute values. The deviation of the

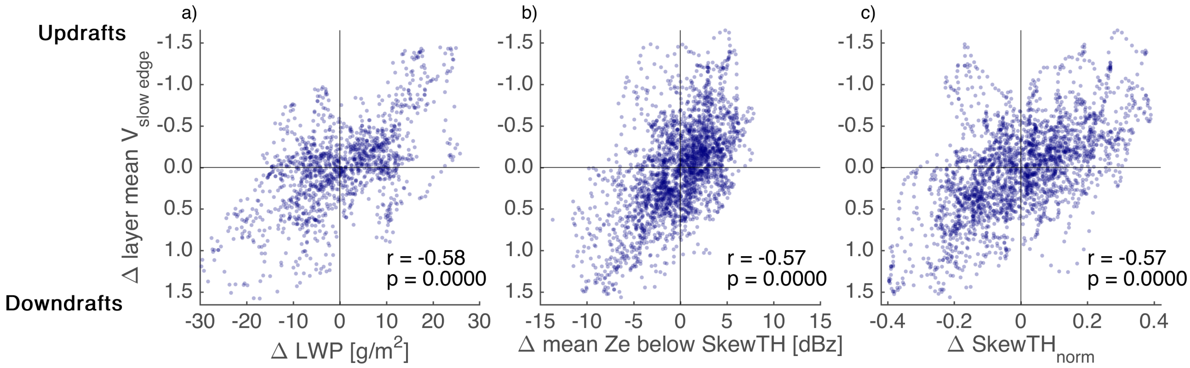

Figure 34: The influence of vertical wind on a) LWP, b) MPL mean Z_e and c) SkewTH. For each parameter the deviation of the instant value from the 30 min mean is used. The Doppler velocity of the edge of the Doppler spectra at the slower falling end is used to estimate vertical air motions.

instant values from a 30 min mean is therefore considered. Fig. 34a shows that in general increased (decreased) LWP values are associated with updrafts (downdrafts), although the correlation was not particularly strong (r = -0.58). In this regard the cloud above Ny-Ålesund on the 5 November 2016 follows the behavior expected for an Arctic MPC. Shupe et al. (2008a) further showed that in the case analyzed in their study, vertical velocities where linked to the amount of ice in the MPC. Also in our case an association between the ice in the cloud (estimated via the Z_e in the bottom part of the MPL) and vertical motions can be found (Fig. 34b). Overall, updrafts increase both the amount of liquid and ice in the MPL.

Interestingly, a relationship between vertical motions and SkewTH can be identified in Fig. 30b. Strong downdrafts (e.g. 6:33 UTC, 7:26 UTC, 7:35 UTC) seem to push the SkewTH downwards. The relationship becomes evident in Fig 34c, which shows a correlation between vertical motions and SkewTH. The relationship between SkewTH and vertical motions suggests that although updrafts increase the amount of both liquid and ice in the MPL, the impact on Z_{precip} is stronger leading to a more ice dominated MPL and a higher SkewTH. On the other hand, in downdrafts both liquid and ice are decreased, but the decrease in Z_{cloud} is relatively smaller and the MPL becomes more liquid dominated with a lower SkewTH. In the MPC analyzed by Shupe et al. (2008a), the downdrafts decreased the IWP more than LWP so that the liquid fraction was increased in downdrafts. Hence, Fig. 34c qualitatively agrees with the findings of Shupe et al. (2008a). In the view of the relationship between vertical motions and SkewTH and Z_e, Fig. 35a shows how vertical motions impact the relationship between SkewTH and Z_e. Updrafts (downdrafts) are related with the highest (lowest) SkewTH and Z_e. For average SkewTH it seems that strong updrafts are related to an increase on Z_e at SkewTH, but otherwise the vertical wind does not seem to influence the relationship between SkewTH and Z_e. Could the vertical motions explain the variability between SkewTH and LWP shown in Fig. 32b? For a similar LWP the amount of ice could vary between up- and downdrafts. Fig. 35b shows this to be the case to some extent, but the larger differences between up- and downdrafts are seen in the LWP level. A particularly strong updraft is associated with LWP between 70 and 80 g m^{-2}, and since higher LWP was found to increase Z_e at SkewTH (Fig. 33) the higher Z_e at SkewTH related to strong updraft could actually be due to the higher LWP associated with the updraft instead of the updraft itself. Therefore, although vertical

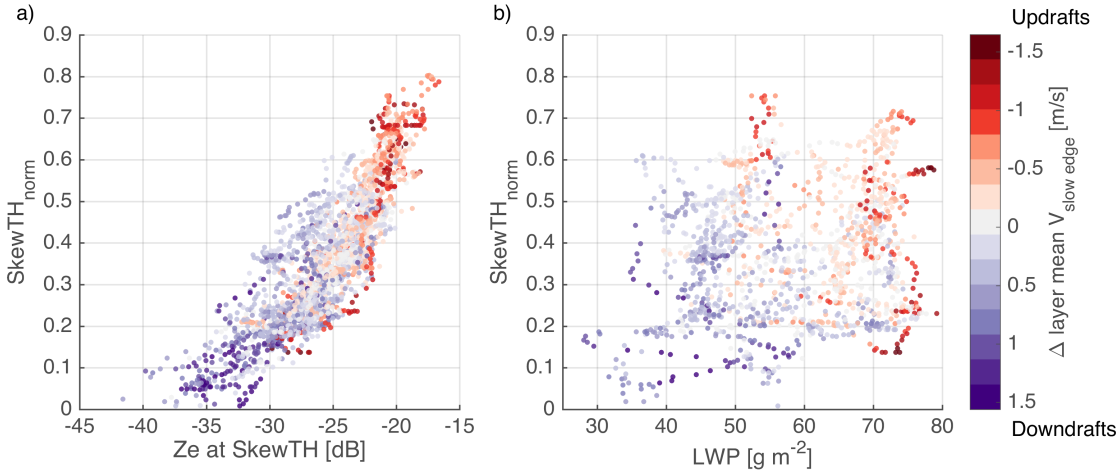

Figure 35: Impact of up- and downdrafts on the relationship between SkewTH and a) the Z_e at SkewTH, b) LWP.

motions clearly influence the phase partitioning of the MPL, it does not seem to largely influence the relationship between SkewTH and Z_e or LWP.

Two possibilities for the observed behavior in the variation of ice with vertical motions can be considered. Firstly, the increase in Z_{precip} in updrafts could be caused by a higher ice nucleation rate. The increase in ice particle number concentration when more supercooled liquid is present is well documented, although the precise mechanisms responsible for the phenomena are not clear (De Boer et al., 2011, Rangno and Hobbs, 2001). Hence, updrafts where LWP is increasing may be associated with more ice nucleation. The second possibility for an increased Z_{precip} in updrafts is related to the growth of the ice particles. As long as liquid is present, the MPL can be assumed to have a vapor pressure saturated with respect to ice. However, the growth rate is temperature and supersaturation dependent (Pruppacher and Klett, 1997) and might thus be modulated by the vertical motions. Additionally, the size of the ice particle at the time when it falls out of the MPL is not only determined by the growth rate, but also the time the particle had to grow, i.e. the residence time of the ice particle in the MPL. In updrafts the ice particle remains in the MPL for a longer time because its falling is slowed down, while in downdrafts the ice particle is pushed out of the MPL faster than its terminal velocity would allow. The simulations carried out by Solomon et al. (2011) showed slightly more depositional growth in downdrafts than updrafts, and the significance of vertical transport in the differences ice water tendencies between up- and downdrafts. From the measurements available and the analysis presented it is not possible to state which of these mechanisms play a role in determining the impact vertical motions have on phase-partitioning in the studied MPC.

The results presented for the case on 5 November 2016 refine the picture of the SkewTH and the way it represents the partitioning between liquid and ice in the MPL. Further simplified, the Z_e above the SkewTH can be considered a proxy for the strength of the cloud mode, and the Z_e below the SkewTH roughly represents the amount of precipitation in the MPL. Using these coarse estimates, SkewTH was found to vary as expected in response to increasing or decreasing Z_{precip} and Z_{cloud} (Figs. 31-32a). With an increase in Z_e below SkewTH (proxy for Z_{precip}), SkewTH moves upwards closer to cloud top (Fig. 31), indicating a more ice dominated MPL. With an increase in LWP, both Z_{cloud} and Z_{precip} (estimated by LWP and Z_e below SkewTH, respectively) are increasing, posing competing effects on the SkewTH and leading to a lack of direct correlation between the LWP and the SkewTH (Fig. 32b). However, a higher LWP combined with a low Z_e below SkewTH coincides with a SkewTH close to liquid base, correctly implying the MPL is to a large degree dominated by cloud liquid. Using SkewTH as a proxy for phase-partitioning, the relationship between vertical motions and phase-partitioning was found to agree with existing literature. A strong relationship between the SkewTH and Z_e was found, undisturbed by vertical motions (Fig. 35). The depth of the MPL in the time period evaluated does not vary considerably (the mean MPL depth was 330 m with a standard deviation of 30 m), and is therefore not an important factor for considering the skewness transition height in this specific case.

12.5 Extension to larger dataset

In this section, the analysis of the skewness transition height is extended to include all profiles where SkewTH was identified in the 3-year dataset (Sect. 12.1). Some of the findings of Sect. 12.4 are considered again to investigate the influence of factors such as the change in MPL depth and temperature. In this section SkewTH is given as distance from cloud top, liquid base, and normalized within the MPL (Sect. 12.3) to demonstrate the differences between the parameters and to find out if for certain analysis a specific parameter is best suited. The relationship between SkewTH and LWP and Z_e is further analyzed to refine the interpretation of SkewTH and how its location in the MPL relates to the amount of ice and liquid in the layer.

Depth of the mixed-phase layer

Sect. 12.4 showed that for a rather constant MPL depth the SkewTH could still vary considerably, following the changes in Z_{cloud} and Z_{precip}. In this case, when $SkewTH_{norm}$ moved up or down, it was always related to a corresponding change in the distance of the skewness transition height from liquid base and cloud top. Combining multiple cases in the analysis, the depth of the MPL varies considerably (Fig. 36a). When comparing profiles with different MPL depth, it is possible that the SkewTH in one profiler is higher up relative to the layer than in another profile, but if the MPL is thicker the absolute distance from both liquid base and cloud top are both larger. Similarly, in a thinner layer the absolute distance of the SkewTH to cloud top and liquid base is smaller although the SkewTH might be at the same height relative to the layer. Fig. 36c and d show how the distributions of $SkewTH_{lb}$ (Eq. 21) and $SkewTH_{ct}$ (Eq. 20) become broader as the depth of the MPL increases. The SkewTH can not be further away from the liquid base or cloud top than the depth of the layer allows, but Fig. 36b further suggests that in deeper MPL the $SkewTH_{norm}$ is higher up in the MPL. The median of $SkewTH_{ct}$ moves away from cloud top with increasing MPL depth until 500 m, but although larger $SkewTH_{ct}$ values are possible with even deeper MPL the median does not increase anymore (Fig. 36b). It is possible that in some cases the boundaries of the MPL are misidentified. A 700 m deep MPL might in reality be two or more liquid layers nearby mistakenly considered as one continuous layer, and the SkewTH in the uppermost liquid layer would in such case be counted as very close to cloud top relative to the artificially deep layer. In the sampling of the data care was taken to minimize such effects, but due to the limitations in the detection of thin liquid layers by the available remote sensing instrumentation and the Cloudnet algorithm the possibility of multiple liquid layers to be counted as one cannot be

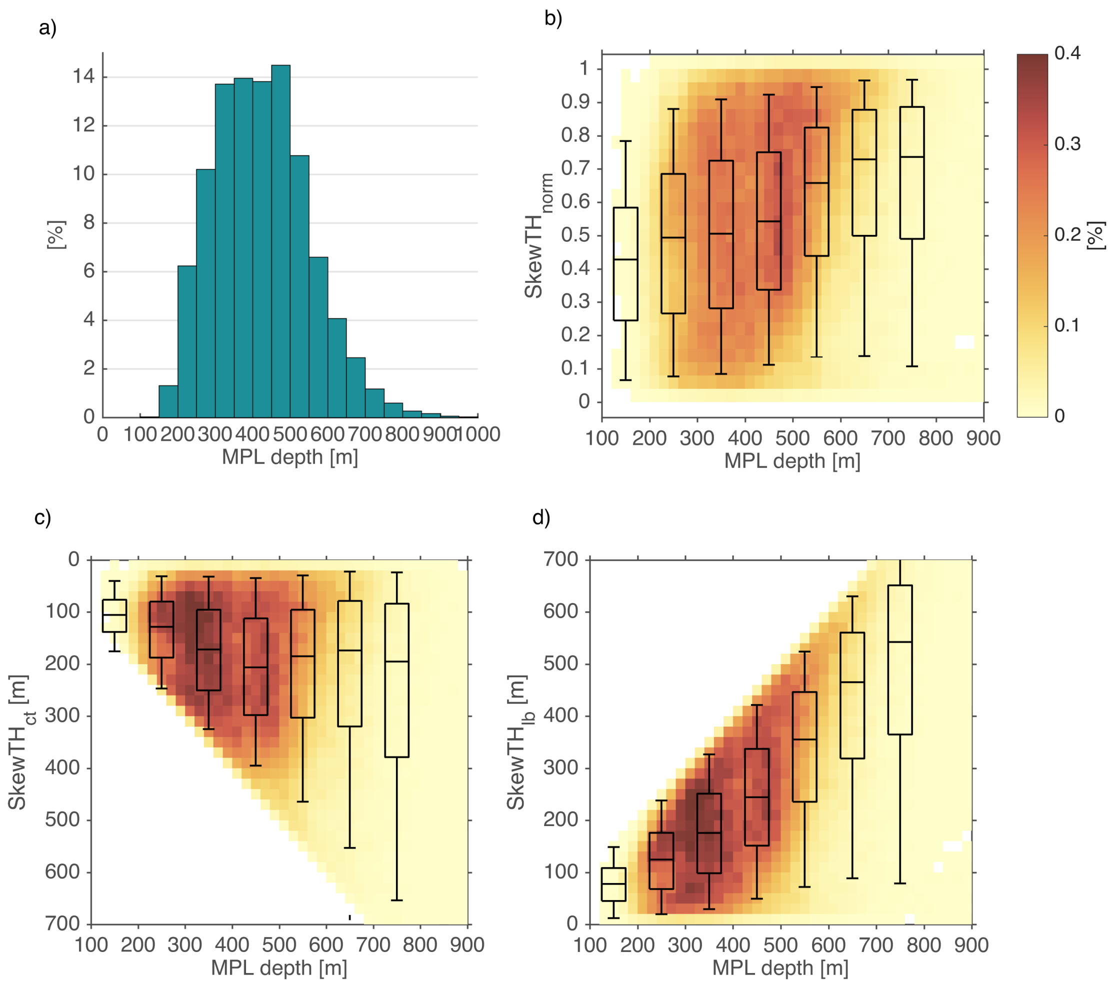

Figure 36: a) Distribution of the mixed-phase layer (MPL) depth for profiles with SkewTH, and bivariate distributions of MPL depth and b) $SkewTH_{norm}$, c) $SkewTH_{ct}$, and d) $SkewTH_{lb}$. Box and whiskers in b)–d) indicate 5, 25, 50, 75 and 95-percentiles for 100 m MPL depth bins.

excluded. Otherwise the sampling criteria (Sect. 12.1) should not favor SkewTH close to cloud top.

It is worth considering that the conditions might vary with MPL depth. Fig. 37a shows that an increase in LWP is associated with an increase in the MPL depth. In situ and modeling studies agree on the general behavior of cloud droplet number concentration staying rather constant while the size of the droplets increases from liquid base to cloud top leading to an increase in the LWC profile (Jackson et al., 2012, Mioche et al., 2017, Morrison et al., 2008). Since LWC increases with height and LWP is the integral of the LWC-profile, a larger LWP is expected for a deeper MPL. However, because the amount of water vapor the air can hold is temperature dependent (Pruppacher and Klett, 1997), an adiabatic profile at a colder temperature corresponds to a lower LWC (Pinsky et al., 2015). Hence for the same MPL depth, an adiabatic LWC profile yields a lower LWP at colder temperatures. This can be seen in Fig. 37b, which shows that for a given MPL depth, a decrease in temperature decreases the mean LWP. With shallow MPL (< 250 m) the temperature

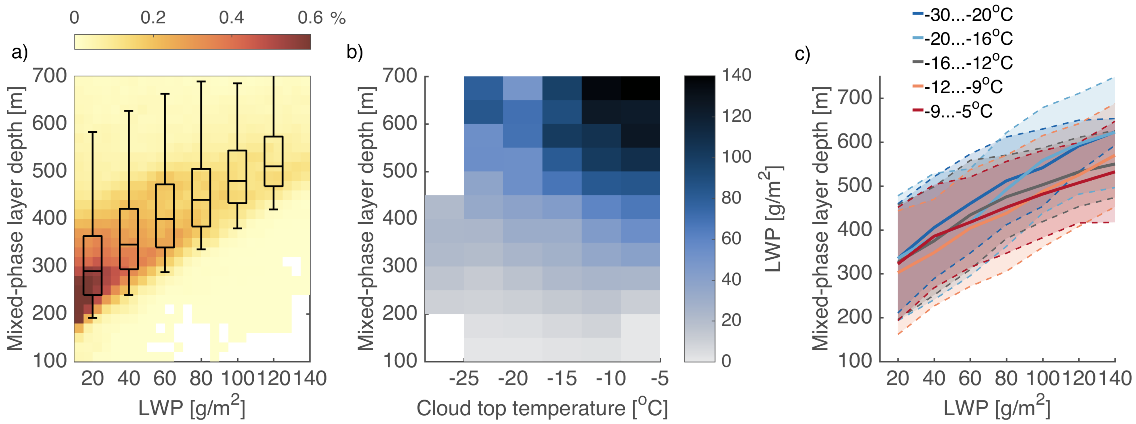

Figure 37: a) Bivariate distribution of MPL depth and LWP. Box and whiskers in indicate 5, 25, 50, 75 and 95-percentiles. b) The mean LWP for each 4 °C cloud top temperature bin and 50 m MPL depth bin. c) The mean (thick solid line) ± standard deviation (shaded area with a dash line boundary) MPL depth at different temperatures. LWP bin size in a) and c) is $20\,\mathrm{g\,m^{-2}}$, and bins with less than 200 data points are omitted.

does not seem to have an effect, and at temperature below -25 °C the MPL depth does not seem to matter, but these outcomes could be due to the measurement uncertainty at the very low LWP that are associated with both of these conditions. Fig. 37b only shows the mean value, so to illustrate the extent to which temperature can provide an explanation for the variation in Fig. 37a, Fig. 37c shows the mean ± standard deviation in the MPL depth for given LWP at different temperatures. For LWP below $50\,\mathrm{g\,m^{-2}}$ one cannot conclude that the distributions differ. With larger LWP the colder temperatures are associated with deeper MPL depth, as would be expected. Considerable variation is still present, and the difference between the mean values at different temperatures rarely exceeds the standard deviations. A simple adiabatic parcel model (such as used by Pinsky et al., 2015) is not capable of describing the turbulent mixed-phase layer that is not in thermodynamic equilibrium. In situ observations from aircraft (Jackson et al., 2012, Mioche et al., 2017) and estimates based on ground based remote sensing (Shupe et al., 2008a) have found the liquid water content in the MPL to often be sub-adiabatic. Importantly, ice particles play a role in determining LWC as they limit the humidity available for liquid droplets (Korolev, 2008, Pinsky et al., 2015), and a larger sink of humidity on the ice phase at colder temperatures might also contribute to the temperature effects shown by Fig. 37.

A deeper MPL is also related to a larger Z_e at liquid base ($Z_{liquidbase}$), which represents the precipitation formed in the MPL (Fig. 38a). The amount of ice at liquid base is determined by the number of ice particles on one hand and the mass of the particles on the other hand. The ice particle number concentration depends on the ice formation mechanisms (heterogeneous nucleation and secondary ice processes, see Sect. 2.1). As already discussed, supercooled liquid and specifically large droplets may promote ice nucleation. Since the droplets increase in size from liquid base to cloud top, large droplets are more likely found in the upper parts of thicker MPL given high enough LWP. The higher $Z_{liquidbase}$ in deeper MPL might therefore be related to higher ice nucleation induced by the larger amount of liquid. Secondly, the mass of the ice particles at liquid base is influenced by the time the ice crystals have had to grow and the growth rate, which is dependent on the temperature, water vapor pressure and ventilation around the particle. In the right conditions riming

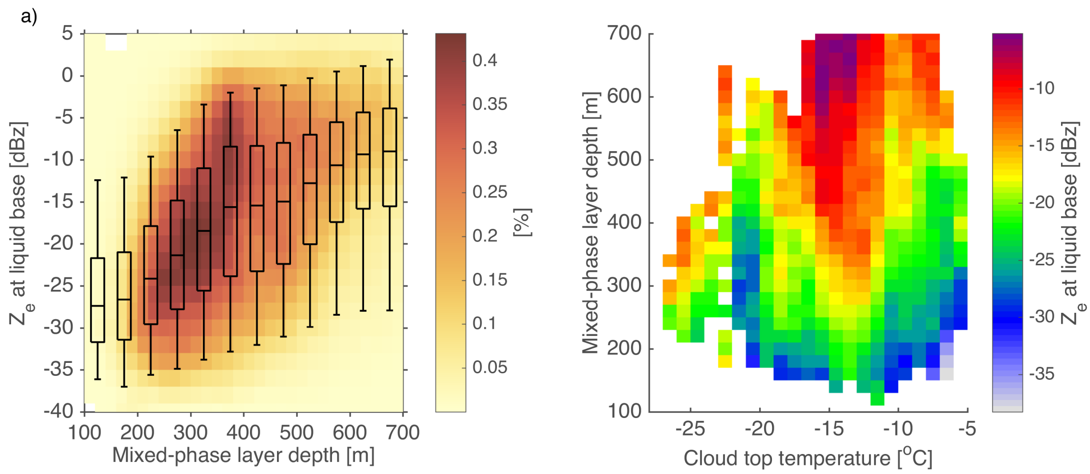

Figure 38: a) Bivariate distribution of MPL depth and $Z_{liquidbase}$. Box and whiskers in indicate 5, 25, 50, 75 and 95-percentiles for 50 m MPL depth bins. b) The mean $Z_{liquidbase}$ for each 1 °C cloud top temperature bin and 20 m MPL depth bin. Bins with less than 300 data points are omitted.

can also play a role in increasing the ice mass. Radar reflectivity might also be increased by aggregation which increases the size of ice particles but does not increase the IWC. Assuming ice is mainly nucleated at cloud top followed by diffusional growth in the continuously with-respect-to-ice super-saturated mixed-phase layer, the size of the ice particle when they have fallen to the level of the liquid base is dependent on their residence time in the mixed-phase layer. This again is influenced by the fall speed of the particle and the thickness of the layer. Although the fall speed of the ice particles vary because of different mass-size relations, in a deeper mixed-phase layer ice particles of different sizes, shapes and densities all have more time to grow because the distance they have to fall before reaching the liquid base is longer. A longer residence time in the mixed-phase layer might also add to the ice mass through an increased likelihood of riming, as more collisions with liquid droplets may occur. Hence, it is possible to explain why a deeper mixed-phase layer is related to higher $Z_{liquidbase}$, and also that the large scatter in Fig. 38a should be expected due to the other factors (ice particle number concentration, habit, and fall speed) that also largely influence the $Z_{liquidbase}$, but it is difficult to determine the relative importance of different processes.

The role of ice nucleation and the growth of the particles for defining the Z_e of the precipitation falling out of the MPL is discussed in the light of the available evidence. Fig. 36b and c showed that SkewTH is closer to cloud top in deeper MPL indicating that independent of how much further below the SkewTH the MPL extends, in the deep MPL there is already more ice near cloud top. The SkewTH close to cloud top is also associated with higher $Z_{liquidbase}$ (Fig. 29a–e). Thus the early stages of precipitation formation are relevant for the amount of ice produced by the MPL, and increased ice nucleation seems to play a role in the increased $Z_{liquidbase}$ in deeper MPL. However, it is still possible that also the quicker growth of the particles could move the SkewTH upwards. The difference in the saturation vapor pressure between liquid and ice is temperature dependent, and the ice particle growth rate at liquid saturation is at its highest around -14 to -15 °C (Pruppacher and Klett, 1997). The dendritic growth at this temperature regime can also enhance aggregation. On the other hand, the number concentration of particles that may act as INP is strongly temperature dependent (Kanji et al., 2017) and increases with decreasing temperature. Fig. 38b shows the mean $Z_{liquidbase}$ for a given cloud top temperature and MPL depth. Fig. 38b agrees with Fig. 38a in that deeper MPL produce more precipitation, but for a given MPL depth the $Z_{liquidbase}$ peaks around -14 °C. The temperature dependency of $Z_{liquidbase}$ suggests that the growth rate of the ice particles has an impact on the the amount of ice produced by the MPL. At cloud top temperature below -22 °C, the $Z_{liquidbase}$ is larger possibly due to increased ice nucleation. Below -20 °C only few P-MPC cases with SkewTH are found, so the result is quite sensitive to the properties of these individual cases. In conclusion, it seems that the higher Z_e at liquid base is related to both higher ice nucleation and more growth in the deeper MPL.

It is important to keep in mind that the results presented concern a specific subset of all low-level MPC. On the other hand, it is possible that narrowing the sample makes it possible to find certain signatures for different processes as the range of possible realizations of P-MPC is reduced. One important aspect that has not been addressed so far is the role of the aerosol loading and the impact of INP and CCN concentrations on the P-MPC. Several studies have found that both INP and CCN concentrations have an impact on the evolution and properties of MPC (Eirund et al., 2019, Lohmann and Hoose, 2009, Morrison et al., 2008, Norgren et al., 2018, Possner et al., 2017, Solomon et al., 2018). Finding observational evidence for aerosol-cloud-interactions is a difficult task (Jackson et al., 2012, Maahn et al., 2017) and beyond the scope of this study. Furthermore, no reliable long-term measurements of INP and CCN at cloud level were available. Assuming that the statistics cover a range of conditions from low to high INP and CCN concentrations, the results are hints of mechanisms that are at play independent of the aerosol regime. However, this only holds if the sampling of the data set is not biased to a certain aerosol regime, which is hard to estimate. If high INP concentrations lead to a quick glaciation of the cloud or to an overall ice dominated MPC (as suggested by several modeling studies), such clouds are not included in the analysis of the SkewTH. The analysis in Sect. 12.2 showed that for SkewTH to be identified, a sufficient amount of liquid compared to ice needs to be present (e.g. Fig. 28a). Therefore, it is possible that the significance of ice particle growth for the amount of ice in the MPL (Fig. 38b) might only be valid in a low-INP regime where ice nucleation is limited.

Z_e at the skewness transition height

In Sect. 12.4 the relationship between the skewness transition height and the reflectivity at SkewTH (Z_{SkewTH}) was found that was not disturbed by vertical motions (Fig. 35). Fig. 39 shows the Z_{SkewTH} distributions for the different definitions of SkewTH. Fig. 39b ($SkewTH_{lb}$) resembles Fig. 31b, but Fig. 39a ($SkewTH_{ct}$) is quite different. To understand this behavior it is necessary to remember what defines the skewness transition height (Sect. 11.4). Very close to liquid base Z_{cloud} is always low because regardless of the number concentration the droplets are small. If SkewTH is very close to the liquid base, the reflectivity at this height is small because Z_{precip} needs to be comparably small to the Z_{cloud}, otherwise the SkewTH would not be identified at this height (Fig. 21a). With increasing distance from liquid base the Z_{cloud} increases in size, and so does the Z_{precip} that is required for the Doppler spectrum to have a zero skewness. The relationship between the Z_{cloud} profile and the definition of SkewTH results in the clear correlation between $SkewTH_{lb}$ and Z_{SkewTH}. Some spread in the distribution of Z_{SkewTH} at a given

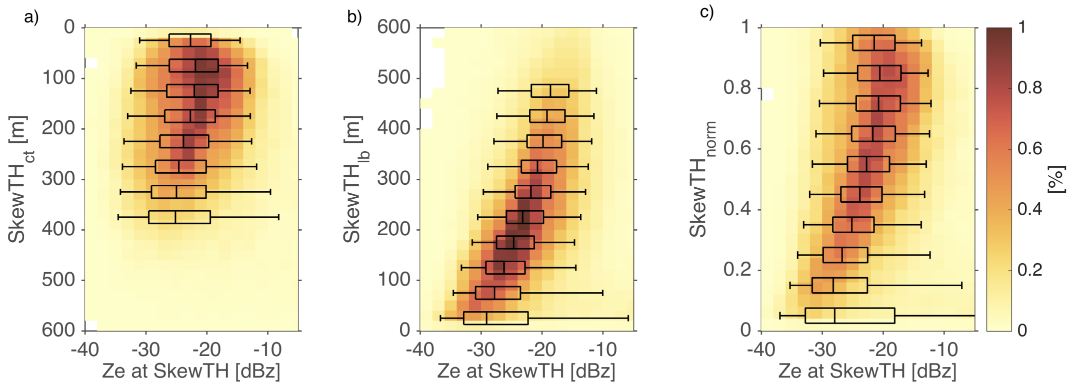

Figure 39: Bivariate distributions of Z_e at the skewness transition height and a) $SkewTH_{ct}$, b) $SkewTH_{lb}$, and c) $SkewTH_{norm}$. Boxes and whiskers as in Fig. 38.

distance from liquid base is present, as Z_{cloud} can vary depending on the LWC and droplet size distribution.

While Z_{SkewTH} is clearly associated with the $SkewTH_{lb}$, no such relationship between Z_{SkewTH} and $SkewTH_{ct}$ exists (Fig. 39a). When SkewTH is at a given distance from the liquid base the Z_e is relatively well defined, however, how much further the MPL still extends above the SkewTH varies. For example, when SkewTH is 200 m above the liquid base, Z_e is -23 $\pm$ 5 dBz (mean $\pm$ standard deviation), but the depth of the MPL may be 300 m or 500 m (Fig. 36d). Thus, the corresponding $SkewTH_{ct}$ may be 100 m or 300 m. Hence, for a given $SkewTH_{lb}$ a range of $SkewTH_{ct}$ are possible, resulting to the broad and rather undefined distribution shown by Fig. 39a. The clear relationship between $SkewTH_{lb}$ and Z_{SkewTH} was explained by the fact that the Z_{cloud} always increases from cloud base upwards and therefore the Z_e related to SkewTH must also increase as a distance from cloud base. As Z_{precip} also starts at zero and increases with distance from cloud top, should there not be a similar behavior of Z_{SkewTH} increasing as a distance from cloud top? Firstly, the liquid base was defined as the height where liquid droplets occur, where as the cloud top is not defined as the height where ice particles appear but it may extend higher if a liquid-only layer is present at cloud top. 100 m below cloud top Z_{precip} might still be zero (Fig. 11) or it might already dominate the radar signal (Fig. 36c). Secondly, the magnitude and growth of Z_{precip} is not as constrained as the Z_{cloud}. The variability in the efficiency of ice nucleation mechanisms influence the ice number concentration and the different growth mechanisms (depositional growth, aggregation, riming) depend on factors such as temperature, particle habit, ventilation, particle size distribution and fall velocity, which leads to a larger variability in the IWC profile and the Z_e profile related to a given IWC. All that said, inspecting Fig. 39c reveals that the reflectivity at SkewTH does increase slightly with distance from the cloud top in the upper most 20% of the MPL. It is worth remembering that the distributions in Fig. 39 do not describe an average Z_e profile, but the Z_e that is associated with the SkewTH at a given height. This behavior might be related that the ice particles do need to grow first and no matter how high the ice nucleation or growth rate, Z_{precip} can only dominate the radar signal in the top most 10% of the MPL if the Z_{cloud} is modest, and for higher Z_{cloud} more growth is required and in these cases the SkewTH cannot be too close to the cloud top. At the edge of the cloud Z_{cloud} also goes to zero, so that right at the top less ice is required to dominate the

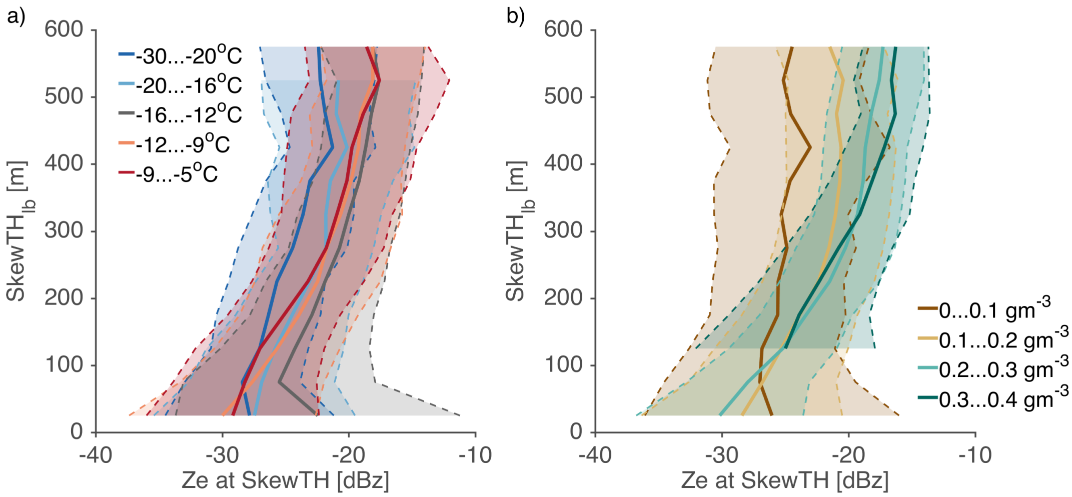

Figure 40: Z_{SkewTH} distributions as a function of $SkewTH_{lb}$ for different a) cloud top temperature and b) normalized LWP (= LWP / MPL depth) classes. The thick lines show the mean, and the dashed lines filled with shaded areas the standard deviation for $SkewTH_{lb}$ bins of 50 m, and bins with less than 300 data points were omitted.

signal. Overall Fig. 39c ($SkewTH_{norm}$) resembles Fig. 39b ($SkewTH_{lb}$), the distributions just appear somewhat broader.

When the SkewTH is in the first 100 m above liquid base (Fig. 39b) or the lowest 20% of the MPL (Fig. 39c) the Z_{SkewTH} distribution is strongly skewed and the 90-percentiles, which may exceed -10 dBz, are deviating from the general pattern (Fig. 39b, c). The profiles with SkewTH close to cloud base with unexpectedly large Z_e are likely misclassified in the sense that skewness in these cases is not describing the change from liquid to ice dominated radar signal. Reflectivities exceeding -10 dBz certainly have a fair amount of ice, which as discussed in Sect. 12.2 also in itself can produce changes in the skewness. Also it would be expected that such profiles appear especially at the lower parts of the MPL, as the ice particles need to grow and interact with each other or the liquid droplets to develop changes in fall velocities that would appear as skewness of the Doppler spectra. Secondly, the skewness profile must somehow resemble that depicted in Fig. 21a, otherwise it would not be included in this analysis. The large Z_e close to liquid base are in violation with the assumptions made, because it is generally thought that the reflectivity of liquid droplets does not exceed -20 dBz so that Z_{cloud} could hardly be expected to exceed -20 dBz in the lowest 100 m of the liquid layer. In the cases where SkewTH is identified close to liquid base, the Z_{SkewTH} could be used as an additional criteria for discriminating ice only or ice dominated skewness profiles that have similar skewness features.

The distinct relationship between $SkewTH_{lb}$ and Z_{SkewTH} (Fig. 39b) was explained by the dependency of Z_{cloud} on the increase in droplet size (and thus LWC) from liquid base upwards. The temperature dependency of LWC discussed before should therefore be reflected in the Z_{SkewTH}. Indeed, Fig. 40a shows that at a given height from the liquid base Z_{SkewTH} is lower at colder temperatures. The differences are small near cloud base, where droplets are always small, and increase with distance from liquid base. However, similarly as in Fig. 37c the dependency on temperature is rather limited. The warmer temperature classes do not differ from each other indicating that other mechanisms must be important in determining Z_{cloud}. It should be remembered that the temperature is thought to impact LWC which in turn is related to Z_{cloud} and hence Z_{SkewTH}. Instead of testing the temperature dependency, it is possible to consider directly if the amount of liquid is related to Z_{SkewTH}. For this purpose a normalized LWP is defined as $LWP* =$ LWP / MPL depth. $LWP*$ corresponds to the LWC associated with a MPL of given depth and LWP if the LWC were constant. Such an approximation is not suggested, instead the aim is to evaluate the amount of liquid in layers of different depths. Fig. 40b shows that larger $LWP*$ are associated with larger Z_{SkewTH}, and the influence of $LWP*$ on the Z_{SkewTH} is stronger than the influence of temperature. Some variation is still to be expected as the LWC profile still can vary within the $LWP*$ classes, and differences in the droplet number concentration for a given LWC also alter Z_{cloud}. The influence of temperature and $LWP*$ on Z_{SkewTH} are worth keeping in mind when interpreting results from SkewTH.

SkewTH as a measure for phase-partitioning

So far, the possibility to use SkewTH as a radar reflectivity weighted measure for phase-partitioning has only been touched briefly. For this purpose, $SkewTH_{norm}$ could be used. $SkewTH_{lb}$ defines how many meters from liquid base the Z_{precip} is dominating the radar signal, and $SkewTH_{ct}$ how many meters from cloud top the Z_{cloud} dominates, but neither bears any information about how much further the MPL extends. $SkewTH_{norm}$ describes which portion of the MPL is dominated by which mode, and as such is a measure of the phase-partitioning of the MPL defined by the reflectivity of liquid and ice in the cloud. For $SkewTH_{norm} = 1$ the radar reflectivity in the entire MPL is dominated by ice, and when $SkewTH_{norm} = 0$ by liquid. Figs. 11a and 12 show that although the Ze of the cloud and precipitation mode are comparable, the liquid largely outweighs the ice in terms of mass, which is due to the D^6 dependence of the radar reflectivity and the larger size of the ice particles. The radar-reflectivity weighted measure for phase-partitioning should therefore not be confused with a metric based on the condensed mass, which is often reported in the literature (Korolev et al., 2017). Since the ice crystals so quickly start to dominate the radar signal, such Z_e-based metric would be most useful to the study of liquid dominated (in terms of mass) clouds, as otherwise the ice is always dominant, and the processes related to ice formation at the low ice-mass-fraction end of the MPC regime. The case study already showed that $SkewTH_{norm}$ as a phase-partitioning measure could be used to reproduce results related to the impact of vertical motions (Fig. 34). Fig. 32b further showed that $SkewTH_{norm}$ is related to the amount of liquid and ice in the MPL as is suitable for a phase-partitioning measure: for a given amount of ice the increase in liquid decreases $SkewTH_{norm}$, and for a given amount of liquid the increase in ice increases $SkewTH_{norm}$.

13 Potential of radar Doppler spectrum skewness for the study of mixed-phase clouds

The multitude of possible processes and combinations of different hydrometeors and influences of dynamics (such as turbulence) makes the use of the Doppler spectra to study MPCs a challenging endeavor. However, the existence of persistent features that are repeatedly found and agree with the general understanding of the cloud structure is promising. Sect. 12 showed that the analysis of the specific skewness feature produced results that are in agreement with the assumptions made in Sect. 11.4, and could also reproduce some findings from previous studies. Here, the potential use of the Doppler spectrum skewness is discussed and suggestions for next steps are outlined.

13.1 Retrieving microphysical quantities

The retrieval of microphysical quantities such as ice and liquid water content and effective radii (r_{eice} and r_{eliq}, respectively) from radar observations is particularly challenging for mixed-phase clouds (Shupe et al., 2008c). These parameters are required for radiative transfer simulations of the cloudy atmosphere (Ebell et al., 2020, Shupe et al., 2015), which are used to study the cloud radiative effect and are therefore important for investigating the role of clouds in the Arctic climate system. Many of the commonly used retrievals have been developed for liquid or ice clouds and require Z_e that is associated only with the hydrometeor population whose properties are being retrieved (e.g. Delanoë et al., 2007, Frisch et al., 1998, 2002, Hogan et al., 2006, Matrosov et al., 2002). Applying such retrievals for mixed-phase clouds is often done by assuming the radar reflectivity is dominated by the ice phase, and the IWC and r_{eice} retrievals are applied using the measured Z_e. Consequently, the Z_e-dependent retrievals for LWC and r_{eliq} cannot be applied, and adiabatic or LWP-scaled values for LWC are used instead (Illingworth et al., 2007, Nomokonova and Ebell, 2019, Shupe et al., 2015). In some case studies the Doppler spectra was decomposed to the contribution of liquid (Z_{liquid}) and ice (Z_{ice}), and thus the aforementioned retrievals could be applied for each phase separately (Shupe et al., 2004, Verlinde et al., 2007, Yu et al., 2014). Despite the efforts made in the development of peak-detection algorithms for radar Doppler spectra (Kalesse et al., 2019, Radenz et al., 2019), the decomposition of spectra is not always possible and this approach is unlikely to provide robust retrievals for the full range of mixed-phase clouds observed.

Skewness could be used to gain additional information for the benefit of the retrieval of microphysical quantities (Küchler et al., 2018, Maahn and Löhnert, 2017). Although skewness does not make it possible to derive the complete Z_{liquid} and Z_{ice} profiles, it could be used to constrain the profiles at least for the cases defined in Sect. 12. For example, above the SkewTH ice does not dominate the radar signal. In this layer the error in Z_{ice} following the $Z_{ice} \approx Z_e$ assumption is at least 50% (3 dB), which corresponds to an uncertainty of 40–46% in the retrieved IWC in the temperature range from -30 °C to -5 °C (Eq. 15, Sect. 6.2). Although the uncertainty of the retrieval might be as high as 100% (Hogan et al., 2006), skewness can be used to reduce the overestimation that is caused by mixed-phase Z_e being fully attributed to the ice phase. On the other hand, the lack of Doppler spectrum skewness could be used as a sign that the supercooled liquid is not significantly contributing to the measured radar reflectivity and the use of the measured Z_e for computing IWC and r_{eice} is justified.

13.2 Constraining numerical models

Features found in the radar observations can be used to confront numerical models. Forward simulating modeled clouds allows the comparison of models and observations in the observational space, and makes it possible to test whether models can reproduce statistical relationships found in the observations. Advanced forward simulators such as the Passive and Active Microwave TRAnsfer (PAMTRA) model (Mech et al., 2020) are able to simulate the full radar Doppler spectrum for a specific observational setup. Comparing the

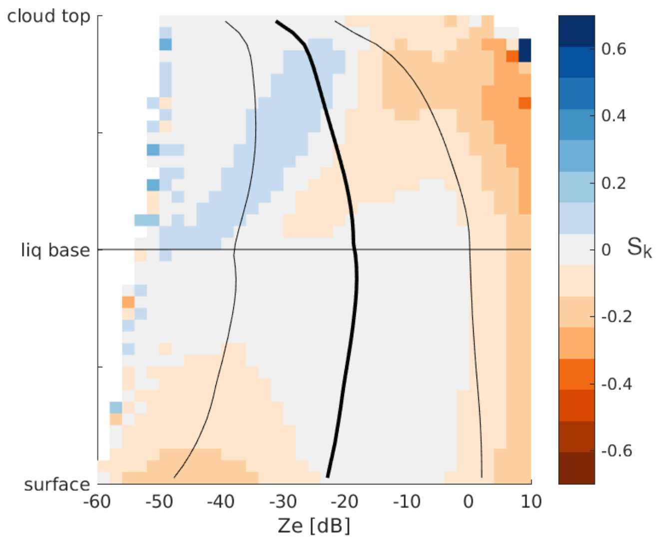

Figure 41: The mean skewness (indicated by color) in each Z_e and normalized height bin. The thick and thin black lines show the median and 5/95-percentiles of Z_e, respectively. All P-MPC are included in the figure.

model and observation in the observational space circumvents the challenge of retrieving microphysical quantities from the radar measurement, which is burdened with significant uncertainties specifically in the mixed-phase regime. However, the task of finding the appropriate radar parameters for the model evaluation must still be resolved. Fig. 11 showed that moving from the liquid-only layer at cloud top to the precipitation below the liquid base might not be associated with much changes in Z_e. V_m is not only a mixture of the terminal fall velocities of the different hydrometeors, but further influenced by vertical wind. Higher moments of the Doppler spectra can provide additional constrains for microphysical processes or the development of phase-partitioning. Because radar reflectivity is strongly dependent on the size of the scatterers, skewness is sensitive to the occurrence of the somewhat larger and faster falling ice particles in the Doppler spectra. Hence, skewness could be used for studying the early stages of ice formation and the transition from liquid to ice.

Schemann and Ebell (2020) performed simulations with the high-resolution ICOsahedral Nonhydrostatic Large-Eddy Model (ICON-LEM) around Ny-Ålesund for 11 days in June 2017. The model output was forward simulated with PAMTRA and compared with the same cloud radar measurements as used in this study. Schemann and Ebell found an underestimation of Z_e in the model compared to the observations, which was attributed to too small ice particles in the model. The reason for this was thought to be related to the limitations of the INP and CCN parameterizations, and possibly also the description of the growth of the ice particles. Adding the Doppler spectrum skewness to the analysis might provide means to get a better understanding of the behavior of the model and where it differs from the observations. The work by Schemann and Ebell shows that while high-resolution modeling can quite successfully produce a mixed-phase cloud, at least in some cases if not all, there is room for improvement in the detailed representation of clouds in the model. Moreover, Schemann and Ebell (2020) demonstrate that the necessary tools to carry out such model-measurement comparisons in the observational space are available and ready for the implementation of any radar-based parameters made available.

In Sect. 12 the skewness profile was reduced to one parameter and the height where the skewness transitions from negative to positive was analyzed. In this manner a better understanding of what defines the sign of S_k in the mixed-phase layer could be developed. With the increased knowledge it is now possible to provide a more general relationship between skewness and reflectivity, which could be used as a starting point for model comparison. Fig. 41 shows the mean skewness for a given Z_e and height in the MPL. The figure reiterates what was learned in Sect. 12.4–12.5, but also provides some additional information. The liquid dominated region spans from -40 dBz at liquid base to -20 dBz at cloud top. In the lower reflectivity side of positive S_k a region of zero skewness is found, which probably describes liquid only conditions. The strongest negative skewness is found at higher reflectivities relatively high up in the cloud. In this region the precipitation mode is large, but as the cloud mode is also considerably strong the skewness gets large absolute values. Lower down in the cloud with the same reflectivity the skewness gets smaller as the cloud mode decreases in size. Close to cloud base with Z_e above -20 dBz the cloud mode is not sufficiently strong anymore to produce any significant skewness.

13.3 Next steps

Some possibilities for continuing the research utilizing Doppler spectrum skewness are outlined above, for which immediate next steps can be recommended. Firstly, the measurement set-up could be optimized for providing a detailed spectra with a noise level as low as possible. Parameters such as the range resolution and averaging time have an impact on the noise level and kinematic broadening of the Doppler spectra, which again affect the skewness that will be computed from the spectra. Furthermore, uncertainties in the skewness that follow from uncertainties in the measured Doppler spectra should be quantified. To move towards process studies, whether observational or with model comparison, a detailed study focusing on the processes that define the skewness profile should be carried out. A combination of a microphysical bin model and a radar forward simulator proved useful for warm drizzling clouds (Acquistapace, 2017), and a similar approach could be taken for mixed-phase clouds.

14 Conclusions

This study explored the possibilities of using cloud radar Doppler spectrum skewness to research Arctic mixed-phase clouds. Contrasting case studies were used to develop an understanding of the variation of the Doppler spectra and its skewness in different conditions. In MPC with enough liquid and not too much ice skewness describes which phase dominates the radar signal. The change from liquid dominated cloud top to ice dominating below was found to be associated with a distinct skewness profile. A method to identify such profiles was developed and applied on the 3-year dataset of persistent low-level MPCs. The skewness profile exhibiting a change from liquid to ice dominated layer was found in 32% of the measured radar profiles and in 51% of the profiles with LWP above $30\,\mathrm{g\,m^{-2}}$. The investigation of a case study and the 3-year dataset showed that the analysis of the skewness transition height produce results that are consistent with the assumptions made and in agreement with findings in previous studies. Following from the definition of skewness the transition from negative to positive is defined by the reflectivity of ice relative to liquid, but not the absolute values. The Z_e of cloud liquid closely relates to the LWC profile and is thus to a large degree defined by thermodynamical conditions. The processes controlling the amount and size of ice particles are more varied, not to mention that their larger size dominates the reflectivity, thus variation in skewness was often associated with the variability of the Z_e associated with the ice phase. Furthermore, a radar reflectivity weighted measure for phase-partitioning in the mixed-phase layer could be derived from the skewness profile.

It is worth highlighting that not all radar measurements of mixed-phase clouds contain clear features related to supercooled liquid. When the amount of liquid is very low, the radar may lack the required sensitivity to measure the small droplets. This instrument specific technical limit sets boundaries to the range of cloud conditions that are explicitly measured as mixed-phase by a cloud radar. Moreover, also when the cloud liquid can be measured, the backscattered power from the ice particles can be so much stronger that it overshadows any signal from the liquid and the radar measurement predominantly describes processes in the ice phase. Doppler radar observations of MPCs therefore cover a range from ice only over ice dominated to apparently mixed-phase measurements. The interpretation of the Doppler spectra in these different measurement regimes require different frameworks. For example, even when droplets cannot be measured by the radar the presence of supercooled liquid can in some cases be inferred from the influence it has on the ice phase, but the assumptions required for such analysis differ from those used in this study. When discussing the potential use of radar Doppler spectra for the study of MPCs, clarity in the applicability of the approach is called for. The quantitative analysis in this work (Sect. 12) focused on MPCs where the signal from the supercooled liquid in the radar Doppler spectra was strong and significantly altered the features of the spectra. The skewness of the Doppler spectrum describes the phase (ice or liquid) dominating the spectra within this regime, which was found to be limited to Z_e at liquid base below -5 dBz. At the low end of the LWP distribution even lower $Z_{liquidbase}$ was required. Furthermore, the interpretation of skewness was only considered for liquid at cloud top and might not be applicable for embedded liquid layers. Further studies specifying the features and their interpretation in more ice dominated Doppler spectra are still needed.

Mixed-phase clouds are notoriously difficult to measure. Only few remote sensing instruments, namely cloud radars and to some extent lidars, can provide vertically resolved measurements of both supercooled liquid and ice. The approach presented in this work allows the investigation of the early stages of precipitation formation in the liquid layer at cloud top. The details of ice nucleation mechanisms and the discrepancy between the observed INP and ice particle number concentrations are some of the central unanswered questions concerning MPCs. With the insights gained from this work on the interpretation of the Doppler spectrum skewness, further studies can now be designed to find cues on the mechanisms altering the ice formation and liquid-to-ice transition at cloud top. Particularly for the ice-dominated and ice-only radar observation regimes (Fig. 21), polarimetric (Oue et al., 2016) and multi-frequency techniques (Kneifel et al., 2015) could prove beneficial. A handful of observatories in the high Arctic operate long term cloud radar measurements, supplemented with campaign deployments, and the approach developed in this study can readily be applied to the datasets obtained at different sites. This work also makes a contribution towards determining observational constrains for the evaluation of numerical models, particularly in terms of precipitation formation and the mechanisms altering phase-partitioning in the upper parts of mixed-phase clouds.

V Conclusions

14 Summary

Low-level mixed-phase clouds are ubiquitous, persistent, and play a central role in the Arctic climate system due to the multiple ways the clouds interact with the surface and the lower troposphere. Climate models struggle with the representation of these clouds, which has been associated with deficiencies in describing microphysical processes, contributing to uncertainties in future climate predictions. Observations are needed to provide constrain for model parameterizations on one hand, and to improve process understanding on the other hand. Remote sensing techniques provide long-term cloud measurements that can be obtained in (nearly) all weather conditions. Specifically, ground-based cloud radars provide highly vertically and temporally resolved profiles for the entire troposphere. Only few sites with long-term cloud radar operation exist in the high Arctic, most of them on the western hemisphere. Furthermore, the information available from cloud radar Doppler spectra is not yet fully capitalized for the mixed-phase cloud regime.

This dissertation presents the first work investigating a multi-year dataset of remote sensing observations of persistent low-level mixed-phase clouds (P-MPC) above Ny-Ålesund, Svalbard. The Scientific Study I provided a characterization of the cloud regime, evaluating the potential local and regional influences of the complex fjord environment to P-MPC occurrence and properties. The Scientific Study II expanded the observational toolkit available for analyzing microphysical properties in mixed-phase volumes by investigating the information that can be gained from Doppler spectrum skewness, and provides relationships that can be used for constraining numerical models. It is well recognized that both environmental conditions, such as advection and surface interactions, as well as microphysical processes within the cloud play a role in the life cycle of P-MPCs. The studies made address both of these aspects, considering the P-MPCs above Ny-Ålesund in interaction with their surroundings as well as investigating a new approach to evaluate the liquid-ice partitioning inside the mixed-phase layer. The two scientific studies employ complimentary approaches for filling the observational gaps in studying Arctic low-level MPCs by providing a description of the complex features influencing the P-MPCs observed at a supersite in the eastern Arctic (Study I) and by expanding the understanding of possibilities available from the analysis of the cloud radar Doppler spectrum skewness (Study II). In the following, the main results and conclusions of the scientific studies are summarized, followed by a discussion and outlook for future research.

Scientific Study I. Characterization of low-level mixed-phase clouds at Ny-Ålesund

In this study, 2.5 years of cloud observations above Ny-Ålesund were analyzed. A method to identify P-MPCs based on the Cloudnet target classification product was developed. The cloud sampling scheme, identifying low-level mixed-phase clouds with a liquid layer persisting for at least one hour, forms the basis of the analysis of both scientific studies. Furthermore, a method to continuously evaluate the thermodynamical coupling of the P-MPC with the surface was developed, and using a combination of 10 m wind direction and the circulation weather type (CWT, Sect. 7.1) the influence of wind conditions could be analyzed. Using the developed methodologies, the analysis required to answer the questions posed in Sect. 3 could be carried out. The main findings are summarized below.

- What is the frequency of occurrence of P-MPCs above Ny-Ålesund, and what are their typical properties (altitude, liquid and ice water path)? Do these parameters exhibit seasonal variation?

The P-MPCs were found to occur 23% of the time, with the highest frequency of occurrence in summer and lowest in winter. The P-MPCs were mostly close to the surface, as would be expected, with a median liquid base height of 760 m. The liquid base height exhibited a clear seasonality, with the P-MPCs being lowest in summer and highest in winter, in agreement with previous studies (e.g. Maturilli and Ebell, 2018, Nomokonova et al., 2019, Shupe et al., 2011). The LWP was typically low (mean $35\,\mathrm{g\,m^{-2}}$ with standard deviation of $45\,\mathrm{g\,m^{-2}}$). The IWP distributions were strongly skewed towards lower values, such that the mean IWP was $12\,\mathrm{g\,m^{-2}}$ but the median only $2.1\,\mathrm{g\,m^{-2}}$. Hence, the P-MPCs were usually heavily liquid dominated, but occasionally formed higher amounts of ice. The LWP did not exhibit a seasonal variation, which could be related to the sampling criteria being selective to a specific cloud regime. On the other hand, a strong seasonal variation in the IWP was found, with lowest values in summer and autumn and a clear maximum in spring. The low IWP in summer and autumn (median 0.2 and $1.0\,\mathrm{g\,m^{-2}}$, respectively) can be explained by the relatively warmer temperatures of these seasons. Despite lower temperatures in winter than in spring, the median IWP in spring ($7.5\,\mathrm{g\,m^{-2}}$) was almost double that of the median IWP in winter ($4.0\,\mathrm{g\,m^{-2}}$). A possible explanation for the high IWP in spring could be a larger amount of INPs being available in this season, as aerosol concentrations in the region peak in spring.

- How can the thermodynamical coupling of the P-MPC with the surface be evaluated from the continuous observations? How often are P-MPCs above Ny-Ålesund found to be coupled, and does thermodynamical coupling of the cloud with the surface influence the amount of liquid and ice in the cloud?

A method combining HATPRO temperature profiles and surface ambient temperature and pressure observations to evaluate the thermodynamical coupling of the P-MPC with the surface was developed. The new approach was evaluated against the coupling state estimated from the potential temperature profiles from radiosoundings, and a satisfactory agreement was found. Compared to radiosonde profiles that are available spuriously (rarely more than one sounding was taken during a P-MPC case), the new method developed allows for a continuous evaluation of the development of the (de)coupling of the cloud. Using this new method, 63% of the observed P-MPC cases where found to be fully decoupled while only 15% were coupled, the rest 22% classified as predominantly decoupled. Coupling was found to occur most frequently in summer. A low liquid base seemed to favor surface coupling, which might contribute to the seasonal cycle of coupling as the P-MPCs were lower in summer. The median LWP of coupled P-MPCs was $46\,\mathrm{g\,m^{-2}}$, clearly higher than the medians of the fully (predominantly) decoupled P-MPCs at $29\,\mathrm{g\,m^{-2}}$ ($25\,\mathrm{g\,m^{-2}}$). No statistically significant differences in IWP depending on the coupling state was found.

- How are the large-scale and local wind conditions in the fjord influencing the occurrence and properties of P-MPCs? How does the location of the measurement site on a mountainous coastline impact the observed P-MPCs?

Clear relationships were found between the observed P-MPC properties and the regional free-tropospheric wind direction, represented by the CWT. The P-MPCs occurred predominantly under weather types from south to west, and these wind directions were also associated with higher LWP and IWP. The weather types from north to east present the other extreme, being associated with least frequent P-MPCs and lowest LWP and IWP. Furthermore, a strong dependency between CWT and liquid base height was found. The P-MPC brought to the site by easterly (westerly) winds had the highest (lowest) mean liquid base heights at or above 1.2 km (around 700 m). No general relationships between surface wind direction and P-MPC occurrence, LWP or IWP were found. However, it is possible that the approach used to describe the wind field in the valley was too simplified. Furthermore, decoupling was more common with southeast and southwest surface wind, directions associated with katabatic winds in previous studies.

From the results, answers for the second question can be provided. Distinct differences were found in the occurrence and properties (namely altitude, LWP and IWP) between the P-MPCs advected to the site from the sea (westerly wind) and from inland (easterly wind). These differences could not be fully explained by different airmass characteristics (lower tropospheric temperature and humidity), indicating that the island is influencing the clouds. This is most obviously seen by the distribution of the liquid base height, which clearly shows that low (below 1 km) P-MPCs could not be advected to the site from the east due to the mountains. The liquid base height was most often found around the height of the mountaintops, but determining whether this is caused by the presence of the mountains or a mere coincidence requires further investigation. Furthermore, the thermodynamical coupling of the P-MPC with the surface was found to be related to the surface wind direction, such that surface wind directions associated with katabatic winds were coinciding with decoupled P-MPC. Since the katabatic wind is a direct result of the local orography, the influence of katabatic winds stabilizing the surface layer (as shown by Argentini et al., 2003) and promoting decoupling is clearly a local phenomena. Thus, the results related to the frequency of (de)coupling, or the connection between coupling state and LWP or IWP cannot be considered representative for the Arctic in general, but represent the conditions in Kongsfjorden.

Overall, it can be concluded that low-level MPCs above Ny-Ålesund are not special in themselves. They are most often found in the lowest 1 km and have low LWP and IWP, similar to what has been reported for low-level MPCs at other sites (e.g. De Boer et al., 2009, Shupe, 2011). The persistent low-level MPCs were found to occur in variable synoptic and local wind conditions, across temperatures ranging from 0 to -30 °C, and in all seasons, demonstrating the ability of these clouds to maintain themselves under various forcing conditions. However, the low-level MPCs above Ny-Ålesund have some distinct flavors, which need to be kept in mind when analyzing observations from this site.

Scientific Study II. Observational signatures of mixed-phase cloud structures revealed by radar Doppler spectrum skewness

This study explored the possibilities of using cloud radar Doppler spectrum skewness to study the P-MPCs. Combining case studies and statistical analysis, a conceptual model relating the reflectivities of the supercooled liquid and ice to the skewness profile in the mixed-phase layer (MPL) at cloud top was developed and tested. The analysis carried out using a 3-year data set of P-MPCs with cloud top temperature below -5 °C confirmed the assumptions made about the interpretation of the skewness profile. An algorithm to detect skewness profiles resembling an Ƨ-shape was developed, which allowed to estimate the commonality of the feature identified in the case studies and enabled further analysis of the relationships between the skewness profile and other cloud parameters. The main outcomes of the extensive analysis are shortly described below in the view of the research questions posed in Sect. 3.

- In which conditions can skewness provide additional information about the microphysical properties in a mixed-phase volume?

The evaluation of contrasting case studies found that answering this question is not possible in a general way. Instead, three regimes for the radar observation of mixed-phase volumes were recognized: I) apparently mixed-phase, when the radar measures a clear signal from both liquid and ice, II) ice-dominated, when the radar receives a signal from liquid but the signal is dominated by the ice such that the main features of the Doppler spectra are determined by the ice phase, and III) ice-only, when the radar only measures a signal from the ice particles. Although skewness could potentially provide information about microphysical properties in all of these regimes, the main processes controlling the Doppler spectrum skewness are likely to differ. In which category a particular profile falls depends both on the properties of the cloud (the amount of supercooled liquid and ice as well as turbulence) but also the technical aspects of the measurement set-up (sensitivity of the radar and noise level of the spectra). Furthermore, the occurrence of quasi-zero skewness profiles within the MPL were analyzed, and these were found to occur mainly at low LWP ($< 30\,\mathrm{g\,m^{-2}}$). These represent profiles where skewness cannot provide insights on any processes. Most of the analysis carried out in this study focused on the apparently mixed-phase MPL, and the rest of this summary is dedicated to this category.

The analysis of the case studies showed that the MPL, where a signal from supercooled liquid and ice could be distinguished in the Doppler spectra, exhibited a skewness profile resembling an Ƨ-shape. Such profiles comprised 32% of the dataset analyzed, and 51% of the profiles with LWP above $30\,\mathrm{g\,m^{-2}}$. Furthermore, the Ƨ-shaped skewness profile were rare when reflectivity at the liquid base (descriptive of the amount of ice within the MPL) exceeded -10 dBz. Thus, such skewness profiles were very common when sufficient liquid but not too much ice was present, and represents conditions when skewness can be used to describe the microphysical properties of the MPL.

- What defines the skewness of the Doppler spectrum of a vertically pointing cloud radar in a mixed-phase cloud?

In general terms, the Doppler spectrum skewness gives an indication if the spectral reflectivity is dominated by the slower or faster falling hydrometeors. For the apparently mixed-phase volumes, this leads to the skewness indicating whether the reflectivity of the cloud liquid (Z_{cloud}) or precipitating ice (Z_{precip}) is dominating the overall reflectivity. Hence, skewness is providing a radar reflectivity weighted measure of phase-partitioning in the MPL. Furthermore, Z_{cloud} increases from liquid base towards cloud top, while Z_{precip} increases with distance from cloud top following the growth of the ice particles falling through the liquid layer. The opposing gradients lead to the characteristic Ƨ-shape of the skewness profile. In the upper parts of the MPL Z_{cloud} dominates and skewness is positive, while closer to liquid base Z_{precip} dominates and skewness is negative. At the height where skewness changes sign (i.e. the skewness transition height, SkewTH), the reflectivities of both liquid and ice are approximately equal. A strong relationship between the reflectivity at SkewTH and the distance of the SkewTH from liquid base was found. This was understood to result from the definition of SkewTH as the height where the reflectivities of liquid and ice are approximately equal together with the Z_{cloud}-profile being to a large extent constrained by thermodynamical conditions. However, the results suggested that the location of SkewTH for a given profile was mainly driven by Z_{precip}.

- Which microphysical processes leave hints in the Doppler spectra that could be studied with the help of the skewness of the spectrum?

As already mentioned, the skewness provides a reflectivity weighted measure of phase-partitioning in the MPL. Although phase-partitioning in itself is not a microphysical process, analyzing the mechanisms influencing phase-partitioning can give hints about the processes in play. As an example, it was shown for a case study that the expected variation in phase-partitioning with vertical wind could be reproduced using $SkewTH_{norm}$.

Furthermore, ice was found to define the SkewTH to a large degree. The skewness profile could therefore be used for studying the precipitation formation in the MPL. The analysis revealed that in certain conditions Z_{precip} was already large very close to cloud top, possibly indicative of a higher ice nucleation rate. Secondly, conditions promoting the growth of the ice particles within the liquid layer were found to be associated with a higher reflectivity of the precipitation falling out of the MPL, suggesting that growth processes are important for determining how much ice is produced in the layer. It is difficult to state whether an increase in Z_{precip} is caused by diffusional growth or aggregation. However, riming was found not to be of large importance for the P-MPCs analyzed. Thus, it is concluded that the Doppler spectrum skewness of the MPL at cloud top contains information about the formation of ice, but further studies are required to determine the precise microphysical processes that determine the skewness profile.

The central conclusion of this study is that cloud radar Doppler spectrum skewness, a parameter that has been so far under-utilized for MPCs, contains information about the microphysical properties within the mixed-phase layer worth exploring. Furthermore, the statistical analysis carried out revealed steady relationships that can provide observational constrain for the evaluation of microphysical parameterizations applied in numerical models.

15 Discussion and Outlook

The representativeness of the observations collected at Ny-Ålesund is an obvious question to be raised. Schemann and Ebell (2020) used a high resolution model to evaluate the horizontal heterogeneity of LWP, and not surprisingly found that the heterogeneity around Ny-Ålesund surpassed the heterogeneity over open sea, sea ice, or the interior of Spitsbergen. However, even if the local conditions modify the low-level clouds, large scale phenomena such as intrusions of warm air from lower latitudes or synoptic systems such as fronts and cyclones might not necessarily be largely impacted by the local fjord climatology and the occurrence and properties of such systems at Ny-Ålesund might well be representative for the region. Additionally, the representativeness of cloud observations could be improved by selective sampling based on wind direction at cloud level. For example, when comparing cloud properties measured at Ny-Ålesund with measurements carried out on a ship on the Greenland sea, the Ny-Ålesund data could be sampled to only include clouds advected to the site from the sea. For processes in the boundary layer, which by definition is influenced by surface properties and is also impacted by meso-scale circulation, Study I showed that the local scale phenomena cannot be ignored. The azimuth scans performed by HATPRO (Sect. 4.2), as well as high resolution modeling such as used by Schemann and Ebell (2020), could be utilized to further understand the local mechanisms impacting low-level MPCs in Kongsfjorden.

The case study presented in Sect. 11.1 (Fig. 7) highlights the benefit of continuously monitoring the development of the coupling state of the cloud. First, the coupling indicated by one profile is not necessarily representative for the cloud case, especially if the cloud is very persistent. Second, the assessment of the development of the coupling state revealed an interesting connection with the local wind. As discussed in Sect. 11.1, the P-MPC on 5 November 2016 was mostly decoupled, and the instances of coupling occurred at the same time when the surface wind direction turned around. Although it could be a coincidence, other cases with similar behavior have been identified. This is an interesting aspect to further consider to better understand the connections between the thermodynamical coupling of the low-level clouds and the local wind conditions in Kongsfjorden. Furthermore, it would be interesting to see if the skewness profiles reveal any differences between coupled and decoupled clouds, or in situations with changing wind conditions inducing coupling with the surface, which would indicate microphysical processes being altered by the dynamics.

The question of the representativeness of the Ny-Ålesund site notwithstanding, there are investigations that are not sensitive to local processes. An obvious example here is the Study II, which investigated a specific approach for the analysis of the Doppler spectra and was not negatively impacted by local conditions. However, also in such studies it is good to be aware of the characteristics of the measurement site to be able to identify any consequences it might have on the analyzed parameters. Furthermore, mechanisms within the cloud, or the clouds interaction with the boundary layer and surface can be identified. The generability of such results or their relevance would be required to be tested at other measurements sites.

Possibly the most significant contribution of this dissertation are the relationships found between Doppler spectrum skewness and other cloud parameters. As already discussed in Sect. 13.2, the results can be used to evaluate numerical models. Using a forward simulator, the modeled microphysical properties can be translated to the observational space, i.e. to corresponding radar Doppler spectrum and its moments, and an analysis analogous to that presented in Sect. 12 can be carried out. Whether or not the figures produced from an ensemble of simulated P-MPCs resemble those shown in Study II remains to be seen. To test and improve microphysical parameterizations, a range of observational constrains are required. Models may contain compensating errors, and might appear to reproduce the observed behavior when evaluated with one set of measured parameters but not with another. The nature of the analysis carried out in this work consisting of a large dataset provides robust constrains against which to evaluate model performance. Furthermore, only few of the measurement techniques available are able to provide information of both liquid and ice through the entire mixed-phase layer, and the sensitivity of skewness to provide information on the development of phase-partitioning could make it particularly powerful for evaluating microphysical parameterizations.

In the near future, a new polarimetric, vertically scanning Ka-band radar is going to be installed at AWIPEV. In addition to the polarimetric variables, the co-located measurements of the W- and Ka-band radars also allow the use of dual-frequency techniques. Furthermore, a depolarizing micro-pulse lidar has been recently installed at AWIPEV. The combination of these new observational capabilities allows to further develop the ideas presented in this work to more complex sceneries, such as multi-layered mixed-phase clouds and clouds consisting of a mixture of supercooled liquid droplets, drizzle and ice particles.

Recent and ongoing measurement campaigns in the central Arctic and North Atlantic provide exciting opportunities to analyze the observations at Ny-Ålesund in a regional context. The Multidisciplinary drifting Observatory for the Study of Arctic Climate (MOSAiC) is a year long expedition to the central Arctic, which among a vast array of other measurements also deploys a range of remote sensing instrumentation for measuring cloud properties. Within the recently concluded Cold-air Outbreaks in the Marine Boundary Layer Experiment (COMBLE), cloud observations were carried out in northern Scandinavia and Bear Island. Combining the observations from COMBLE, AWIPEV and MOSAiC provide unprecedented opportunities for studying the evolution of meridionally transported airmasses and the associated clouds.

Acknowledgments

The PhD work was carried out as part of and funded by the Transregional Collaborative Research Center (TR 172) 'Climate Relevant Atmospheric and Surface Processes, and Feedback Mechanisms (AC)^3' funded by the German Research Foundation (Deutsche Forschungsgemeinschaft). Also the Graduate School of Geosciences is acknowledged for support and travel funds. Karin, thank you for your continuous work to provide support and to improve the graduate school.

From the bottom of my heart, I thank my supervisors. This work would not be same without you. Each one of you is unique, and you have thought me a lot. I want to thank Uli for pushing me to do better, and for believing in me also when I didn't believe in myself. I want to thank Matt for sharing from his vast experience and knowledge. And I thank Stefan for his endless encouragement, optimism and devotion for my work.

I also thank the Inferno group and further colleagues at the institute who provided support and friendships. Special thanks goes to the postdocs providing advice and guidance, and the fellow PhD students both in Cologne and in (AC)^3 for the comradery. Sabrina, thank you for walking the last steps together with me. I also wish to thank Marion and Christoph from AWI, who were willingly sharing from their knowledge and experience. In particular, I want to thank those people whose work makes it possible for me to do mine: Nadine, Dagmar and our brilliant technicians Pavel and Rainer. I'm grateful for the AWIPEV staff for their support and continuous work for maintaining the instruments, for Ewan for providing Cloudnet, for Tobias for the CWT product, and for Kerstin for managing the data. Thank you to everyone who contributed to the thesis by reading and providing comments: Vera, Kerstin, and Nils, and for Marek with the assistance with formatting the bibliography.

I am lucky to have some incredible friends. This thesis would not have been written without the love and support that I got during the years. Thank you for keeping me grounded and reminding me who I am outside of academic work. An meine liebe WG: Danke, das ihr meinen Fuß festhaltet, wenn mein Kopf in den Wolken schwebt und meine Hand nehmt, wenn der Boden unter meinen Füßen wackelt. And thank you Nils for everything, who knows where I would be without you. My family has supported me from early on, fostering the curiosity to explore the world and encouraged me to pursue my interests in science and technology. Kiitos isä ja äiti. Tuuli, olet korvaamaton.

Abbreviations

AWI Alfred Wegener Institute for Polar and Marine Research

BSRN Baseline Surface Radiation Network

CCN Cloud condensation nucleus

CWT Circulation weather type

FMCW Frequency modulated continuous wave

HATPRO Humidity and temperature profiler (a microwave radiometer)

ICON-LEM ICOsahedral Nonhydrostatic Large-Eddy Model

INP Ice nucleating particle

IPEV Polar Institute Paul Emile Victor

IWC Ice water content

IWV Integrated water vapor

JOYCE Jülich Observatory for Cloud Evolution

JOYRAD-94 JOYCE Radar–94 GHz

LES Large eddy simulation

LWC Liquid water content

LWP Liquid water path

MiRAC Microwave Radar/Radiometer for Arctic Clouds

MiRAC-A Microwave Radar/Radiometer for Arctic Clouds - Active component

MMCR Millimeter wavelength cloud radar

MPC Mixed-phase cloud

MPL Mixed-phase layer

MWR Microwave radiometer

N_d Droplet number concentration

N_i Ice particle number concentration

NWP Numerical weather prediction

P-MPC Persistent low-level mixed-phase cloud

PAMTRA Passive and Active Microwave TRAnsfer (forward model)

RMSE Root mean square error

SIP Secondary ice production

SkewTH Skewness transition height

SLD Supercooled large droplets

WBF Wegener-Bergeron-Findeisen process

ZeroSkew Skewness profile not considerably differing from zero, specifically mean($|S_k|$) $<$ 0.05

Symbols

β' Attenuated backscatter

η Radar reflectivity

Γ Variable used for implementing quality criteria on the strength of the skewness feature (Eq. 19)

θ Half power beam width

κ_w Dielectric factor for water

λ Wavelength

σ_B Scattering cross section

σ Doppler spectrum width

$\zeta(z)$ Sum function used to determine the skewness transition height (Eq. 17)

B Chirp bandwidth

c Speed of light

D Diameter

f^2 Normalized power density pattern

f_B Frequency of the beat signal, i.e. the frequency difference of the transmitted and received signal

G_T Antenna gain of the transmitter

$LWP*$ LWP normalized by MPL depth

$N(D)$ Particle size distribution

N_{chirp} Number of chirp repetitions

N_l Number of range gates in a liquid cloud

P_R Returned power

P_T Transmitted power

δr Range resolution

r Range

r_{eice} Effective radius of ice particles

r_{eliq} Effective radius of liquid droplets

$SkewTH_{ct}$ Skewness transition height measured as distance from cloud top (Eq. 20)

$SkewTH_{lb}$ Skewness transition height measured as distance from liquid base (Eq. 21)

$SkewTH_{norm}$ Skewness transition height normalized between liquid base and cloud top (Eq. 22)

Z_{precip} Reflectivity of the precipitation mode

S_k Doppler spectrum skewness

T_B Brightness temperature

T_c Chirp duration

T Temperature

t Time

V_m Mean Doppler velocity

V_{nyq} Nyquist velocity, i.e. the largest unambiguous Doppler velocity that can be obtained by a radar

δV_D Doppler velocity resolution

V_D Doppler velocity

Z_{SkewTH} Reflectivity at the skewness transition height

Z_{cloud} Reflectivity of the cloud mode

Z_{ice} Reflectivity of ice

$Z_{liquidbase}$ Reflectivity at liquid base height

Z_{liquid} Reflectivity of liquid

Z_e Equivalent radar reflectivity

Z Radar reflectivity factor

z Height above the ground

z_{ct} Cloud top height

z_{lb} Liquid base height

Bibliography

Acquistapace, C., 2017: Investigation of drizzle onset in liquid clouds using ground-based active and passive remote sensing instruments. Ph.D. thesis, Institut für Geophysik und Meteorologie der Universität zu Köln.

Acquistapace, C., S. Kneifel, U. Löhnert, P. Kollias, M. Maahn, and M. Bauer-Pfundstein, 2017: Optimizing observations of drizzle onset with millimeter-wavelength radars. *Atmospheric Measurement Techniques*, **10 (5)**, 1783–1802, doi: 10.5194/amt-10-1783-2017.

Acquistapace, C., U. Löhnert, M. Maahn, and P. Kollias, 2019: A New Criterion to Improve Operational Drizzle Detection with Ground-Based Remote Sensing. *Journal of Atmospheric and Oceanic Technology*, **36 (5)**, 781–801, doi: 10.1175/JTECH-D-18-0158.1.

AMAP, 2017: Snow, Water, Ice and Permafrost. Summary for Policy-makers. *Arctic Monitoring and Assessment Programme (AMAP), Oslo, Norway.*

Andersen, A. O., J. Flora, K. L. Johansen, M.-P. Heide-Jørgensen, and A. Mosbech, 2017: *Piniariarneq: from interdisciplinary research towards a new resource management*. Institut for Antropologi, Københavns Universitet.

Andronache, C., 2017: *Mixed-Phase Clouds: Observations and Modeling*. Elsevier.

Ansmann, A., M. Tesche, P. Seifert, D. Althausen, R. Engelmann, J. Fruntke, U. Wandinger, I. Mattis, and D. Müller, 2009: Evolution of the ice phase in tropical altocumulus: SAMUM lidar observations over Cape Verde. *Journal of Geophysical Research: Atmospheres*, **114 (D17)**.

Argentini, S., A. P. Viola, G. Mastrantonio, A. Maurizi, T. Georgiadis, and M. Nardino, 2003: Characteristics of the boundary layer at Ny-Ålesund in the Arctic during the ARTIST field experiment. *Annals of Geophysics*, **46 (2)**.

Armour, K. C., N. Siler, A. Donohoe, and G. H. Roe, 2019: Meridional atmospheric heat transport constrained by energetics and mediated by large-scale diffusion. *Journal of Climate*, **32 (12)**, 3655–3680.

Avramov, A. and J. Y. Harrington, 2010: Influence of parameterized ice habit on simulated mixed phase Arctic clouds. *Journal of Geophysical Research: Atmospheres*, **115 (D3)**, doi: 10.1029/2009JD012108.

Baek, E.-H., J.-H. Kim, S. Park, B.-M. Kim, and J.-H. Jeong, 2020: Impact of poleward heat and moisture transports on Arctic clouds and climate simulation. *Atmospheric Chemistry and Physics*, **20 (5)**, 2953–2966, doi: 10.5194/acp-20-2953-2020.

Barrett, A. I., C. D. Westbrook, J. C. Nicol, and T. H. M. Stein, 2019: Rapid ice aggregation process revealed through triple-wavelength Doppler spectrum radar analysis. *Atmospheric Chemistry and Physics*, **19 (8)**, 5753–5769, doi: 10.5194/acp-19-5753-2019.

Barthazy, E. and R. Schefold, 2006: Fall velocity of snowflakes of different riming degree and crystal types. *Atmospheric research*, **82 (1-2)**, 391–398.

Beard, K. V. and I. Ochs, Harry T., 1993: Warm-Rain Initiation: An Overview of Microphysical Mechanisms. *Journal of Applied Meteorology*, **32 (4)**, 608–625, doi: 10.1175/1520-0450(1993)032<0608:WRIAOO>2.0.CO;2.

Beine, H., S. Argentini, A. Maurizi, G. Mastrantonio, and A. Viola, 2001: The local wind field at Ny-Ålesund and the Zeppelin mountain at Svalbard. *Meteorol. Atmos. Phys.*, **78 (1-2)**, 107–113.

Bergeron, T., 1935: On the physics of clouds and precipitation. *Proces Verbaux de l'Association de Météorologie*, 156–175.

Block, K., F. A. Schneider, J. Mülmenstädt, M. Salzmann, and J. Quaas, 2020: Climate models disagree on the sign of total radiative feedback in the Arctic. *Tellus A: Dynamic Meteorology and Oceanography*, **72 (1)**, 1–14.

Bodas-Salcedo, A., J. Mulcahy, T. Andrews, K. Williams, M. Ringer, P. Field, and G. Elsaesser, 2019: Strong dependence of atmospheric feedbacks on mixed-phase microphysics and aerosol-cloud interactions in HadGEM3. *Journal of Advances in Modeling Earth Systems*, **11 (6)**, 1735–1758, doi: 10.1029/2019MS001688.

Bony, S., R. Colman, V. M. Kattsov, R. P. Allan, C. S. Bretherton, J.-L. Dufresne, A. Hall, S. Hallegatte, M. M. Holland, W. Ingram, D. A. Randall, B. J. Soden, G. Tselioudis, and M. J. Webb, 2006: How well do we understand and evaluate climate change feedback processes? *Journal of Climate*, **19 (15)**, 3445–3482, doi: 10.1175/JCLI3819.1.

Brandes, E. A., K. Ikeda, G. Thompson, and M. Schöhuber, 2008: Aggregate Terminal Velocity/Temperature Relations. *Journal of Applied Meteorology and Climatology*, **47 (10)**, 2729–2736, doi: 10.1175/2008JAMC1869.1.

Brooks, I. M., M. Tjernström, P. O. G. Persson, M. D. Shupe, R. A. Atkinson, G. Canut, C. E. Birch, T. Mauritsen, J. Sedlar, and B. J. Brooks, 2017: The Turbulent Structure of the Arctic Summer Boundary Layer During The Arctic Summer Cloud-Ocean Study. *J. Geophys. Res.-Atmos.*, **122 (18)**, 9685–9704.

CC BY 3.0, 2007: Creative Commons Attribution 3.0 Unported License. URL: `https://creativecommons.org/licenses/by/3.0`.

CC BY 4.0, 2013: Creative Commons Attribution 4.0 International License. URL: `https://creativecommons.org/licenses/by/4.0`.

Ceppi, P., F. Brient, M. D. Zelinka, and D. L. Hartmann, 2017: Cloud feedback mechanisms and their representation in global climate models. *Wiley Interdisciplinary Reviews: Climate Change*, **8 (4)**, e465.

Cesana, G., D. Waliser, X. Jiang, and J.-L. Li, 2015: Multimodel evaluation of cloud phase transition using satellite and reanalysis data. *Journal of Geophysical Research: Atmospheres*, **120 (15)**, 7871–7892.

Chance, R. J., J. F. Hamilton, L. J. Carpenter, S. C. Hackenberg, S. J. Andrews, and T. W. Wilson, 2018: Water-soluble organic composition of the Arctic sea surface microlayer and association with ice nucleation ability. *Environmental science & technology*, **52 (4)**, 1817–1826.

Chang, L., S. Song, G. Feng, Y. Zhang, and G. Gao, 2017: Assessment of the uncertainties in Arctic low-level temperature inversion characteristics in radio occultation observations. *IEEE T. Geosci. Remote*, **55 (3)**, 1793–1803.

Cober, S. G., G. A. Isaac, and J. W. Strapp, 2001: Characterizations of Aircraft Icing Environments that Include Supercooled Large Drops. *Journal of Applied Meteorology*, **40 (11)**, 1984–2002, doi: 10.1175/1520-0450(2001)040<1984:COAIET>2.0.CO;2.

Cober, S. G., J. W. Strapp, and G. A. Isaac, 1996: An Example of Supercooled Drizzle Drops Formed through a Collision-Coalescence Process. *Journal of Applied Meteorology*, **35 (12)**, 2250–2260, doi: 10.1175/1520-0450(1996)035<2250:AEOSDD>2.0.CO;2.

Cohen, J., X. Zhang, J. Francis, T. Jung, R. Kwok, J. Overland, et al., 2020: Divergent consensuses on Arctic amplification influence on midlatitude severe winter weather. *Nature Climate Change*, **10**, 20–29, doi: 10.1038/s41558-019-0662-y.

Colman, R., J. Fraser, and L. Rotstayn, 2001: Climate feedbacks in a general circulation model incorporating prognostic clouds. *Climate Dynamics*, **18 (1-2)**, 103–122.

Conen, F., E. Stopelli, and L. Zimmermann, 2016: Clues that decaying leaves enrich Arctic air with ice nucleating particles. *Atmospheric environment*, **129**, 91–94.

Cortinas Jr., J. V., B. C. Bernstein, C. C. Robbins, and J. Walter Strapp, 2004: An Analysis of Freezing Rain, Freezing Drizzle, and Ice Pellets across the United States and Canada: 1976–90. *Weather and Forecasting*, **19 (2)**, 377–390, doi: 10.1175/1520-0434(2004)019<0377:AAOFRF>2.0.CO;2.

Costa, A., J. Meyer, A. Afchine, A. Luebke, G. Günther, J. R. Dorsey, M. W. Gallagher, A. Ehrlich, M. Wendisch, D. Baumgardner, H. Wex, and M. Krämer, 2017: Classification of Arctic, midlatitude and tropical clouds in the mixed-phase temperature regime. *Atmospheric Chemistry and Physics*, **17 (19)**, 12 219–12 238, doi: 10.5194/acp-17-12219-2017.

Crewell, S. and U. Löhnert, 2003: Accuracy of cloud liquid water path from ground-based microwave radiometry 2. Sensor accuracy and synergy. *Radio Sci.*, **38 (3)**, 7–1.

Crewell, S. and U. Löhnert, 2007: Accuracy of Boundary Layer Temperature Profiles Retrieved With Multifrequency Multiangle Microwave Radiometry. *IEEE T. Geosci. Remote*, **45 (7)**, 2195–2201, doi: 10.1109/TGRS.2006.888434.

Crook, J. A., P. M. Forster, and N. Stuber, 2011: Spatial patterns of modeled climate feedback and contributions to temperature response and polar amplification. *Journal of Climate*, **24 (14)**, 3575–3592.

Cui, Z., K. S. Carslaw, Y. Yin, and S. Davies, 2006: A numerical study of aerosol effects on the dynamics and microphysics of a deep convective cloud in a continental environment. *Journal of Geophysical Research: Atmospheres*, **111 (D5)**.

Curry, J. A., 1986: Interactions among turbulence, radiation and microphysics in Arctic stratus clouds. *J. Atmos. Sci.*, **43 (1)**, 90–106.

Curry, J. A., 1995: Interactions among aerosols, clouds, and climate of the Arctic Ocean. *Science of the total environment*, **160**, 777–791.

Curry, J. A., P. V. Hobbs, M. D. King, D. A. Randall, P. Minnis, G. A. Isaac, J. O. Pinto, T. Uttal, A. Bucholtz, D. G. Cripe, H. Gerber, C. W. Fairall, T. J. Garrett, J. Hudson, J. M. Intrieri, C. Jakob, T. Jensen, P. Lawson, D. Marcotte, L. Nguyen, P. Pilewskie, A. Rangno, D. C. Rogers, K. B. Strawbridge, F. P. J. Valero, A. G. Williams, and D. Wylie, 2000: FIRE Arctic clouds experiment. *Bulletin of the American Meteorological Society*, **81 (1)**, 5–30, doi: 10.1175/1520-0477(2000)081<0005:FACE>2.3.CO;2.

Dahlke, S. and M. Maturilli, 2017: Contribution of Atmospheric Advection to the Amplified Winter Warming in the Arctic North Atlantic Region. *Adv. Meteorol.*, **2017**.

De Boer, G., W. Chapman, J. E. Kay, B. Medeiros, M. D. Shupe, S. Vavrus, and J. Walsh, 2012: A characterization of the present-day Arctic atmosphere in CCSM4. *J. Climate*, **25 (8)**, 2676–2695.

De Boer, G., E. W. Eloranta, and M. D. Shupe, 2009: Arctic mixed-phase stratiform cloud properties from multiple years of surface-based measurements at two high-latitude locations. *J. Atmos. Sci.*, **66 (9)**, 2874–2887.

De Boer, G., H. Morrison, M. Shupe, and R. Hildner, 2011: Evidence of liquid dependent ice nucleation in high-latitude stratiform clouds from surface remote sensors. *Geophysical Research Letters*, **38 (1)**.

De Boer, G., M. Shupe, P. Caldwell, S. E. Bauer, O. Persson, J. Boyle, M. Kelley, S. Klein, and M. Tjernström, 2014: Near-surface meteorology during the Arctic Summer Cloud Ocean Study (ASCOS): evaluation of reanalyses and global climate models. *Atmos. Chem. Phys.*, **14 (1)**, 427–445.

Dee, D. P., S. M. Uppala, A. J. Simmons, P. Berrisford, P. Poli, S. Kobayashi, et al., 2011: The ERA-Interim reanalysis: configuration and performance of the data assimilation system. *Quarterly Journal of the Royal Meteorological Society*, **137 (656)**, 553–597, doi: 10.1002/qj.828.

Dekhtyareva, A., K. Holmén, M. Maturilli, O. Hermansen, and R. Graversen, 2018: Effect of seasonal mesoscale and microscale meteorological conditions in Ny-Ålesund on results of monitoring of long-range transported pollution. *Polar. Res.*, **37 (1)**, 1508 196.

Delanoë, J., A. Protat, D. Bouniol, A. Heymsfield, A. Bansemer, and P. Brown, 2007: The characterization of ice cloud properties from Doppler radar measurements. *Journal of applied meteorology and climatology*, **46 (10)**, 1682–1698.

DeVoe, H., 1964: Optical Properties of Molecular Aggregates. I. Classical Model of Electronic Absorption and Refraction. *The Journal of Chemical Physics*, **41 (2)**, 393–400, doi: 10.1063/1.1725879.

DeVoe, H., 1965: Optical Properties of Molecular Aggregates. II. Classical Theory of the Refraction, Absorption, and Optical Activity of Solutions and Crystals. *The Journal of Chemical Physics*, **43 (9)**, 3199–3208, doi: 10.1063/1.1697294.

Doviak, R. J. and D. S. Zrnić, 2006: *Doppler radar and weather observations*. 3d ed., Dover Publications, Inc.

Ebell, K., T. Nomokonova, M. Maturilli, and C. Ritter, 2020: Radiative effect of clouds at Ny-Ålesund, Svalbard, as inferred from ground-based remote sensing observations. *Journal of Applied Meteorology and Climatology*, **59 (1)**, 3–22, doi: 10.1175/JAMC-D-19-0080.1.

Egerer, U., M. Gottschalk, H. Siebert, A. Ehrlich, and M. Wendisch, 2019: The new BELUGA setup for collocated turbulence and radiation measurements using a tethered balloon: first applications in the cloudy Arctic boundary layer. *Atmospheric Measurement Techniques*, **12 (7)**, 4019–4038, doi: 10.5194/amt-12-4019-2019.

Eirund, G. K., A. Possner, and U. Lohmann, 2019: Response of Arctic mixed-phase clouds to aerosol perturbations under different surface forcings. *Atmospheric Chemistry and Physics*, **19 (15)**, 9847–9864, doi: 10.5194/acp-19-9847-2019.

Emeis, S., 2011: *Surface-based remote sensing of the atmospheric boundary layer*. Springer Science+Business Media B.V., Dordrecht.

English, J. M., J. E. Kay, A. Gettelman, X. Liu, Y. Wang, Y. Zhang, and H. Chepfer, 2014: Contributions of clouds, surface albedos, and mixed-phase ice nucleation schemes to Arctic radiation biases in CAM5. *Journal of Climate*, **27 (13)**, 5174–5197.

Engström, A., J. Karlsson, and G. Svensson, 2014: The importance of representing mixed-phase clouds for simulating distinctive atmospheric states in the Arctic. *Journal of climate*, **27 (1)**, 265–272.

Esau, I. and I. Repina, 2012: Wind climate in Kongsfjorden, Svalbard, and attribution of leading wind driving mechanisms through turbulence-resolving simulations. *Adv. Meteorol.*, **2012**.

Fan, J., S. Ghan, M. Ovchinnikov, X. Liu, P. J. Rasch, and A. Korolev, 2011: Representation of Arctic mixed-phase clouds and the Wegener-Bergeron-Findeisen process in climate models: Perspectives from a cloud-resolving study. *Journal of Geophysical Research: Atmospheres*, **116 (D1)**.

Field, P. R., R. J. Hogan, P. R. A. Brown, A. J. Illingworth, T. W. Choularton, and R. J. Cotton, 2005: Parametrization of ice-particle size distributions for mid-latitude stratiform cloud. *Quarterly Journal of the Royal Meteorological Society*, **131 (609)**, 1997–2017, doi: 10.1256/qj.04.134.

Field, P. R., R. P. Lawson, P. R. A. Brown, G. Lloyd, C. Westbrook, D. Moisseev, A. Miltenberger, A. Nenes, A. Blyth, T. Choularton, P. Connolly, J. Buehl, J. Crosier, Z. Cui, C. Dearden, P. DeMott, A. Flossmann, A. Heymsfield, Y. Huang, H. Kalesse, Z. A. Kanji, A. Korolev, A. Kirchgaessner, S. Lasher-Trapp, T. Leisner, G. McFarquhar, V. Phillips, J. Stith, and S. Sullivan, 2017: Secondary ice production: Current state of the science and recommendations for the future. *Meteorological Monographs*, **58**, 7.1 – 7.20, doi: 10.1175/AMSMONOGRAPHS-D-16-0014.1.

Findeisen, W., 1938: Kolloid-meteorologische Vorgänge bei Neiderschlags-bildung. *Meteor. Z*, **55**, 121–133.

Fridlind, A. M., B. van Diedenhoven, A. S. Ackerman, A. Avramov, A. Mrowiec, H. Morrison, P. Zuidema, and M. D. Shupe, 2012: A FIRE-ACE/SHEBA Case Study of Mixed-Phase Arctic Boundary Layer Clouds: Entrainment Rate Limitations on Rapid Primary Ice Nucleation Processes. *Journal of the Atmospheric Sciences*, **69 (1)**, 365–389, doi: 10.1175/JAS-D-11-052.1.

Frisch, A., G. Feingold, C. Fairall, T. Uttal, and J. Snider, 1998: On cloud radar and microwave radiometer measurements of stratus cloud liquid water profiles. *Journal of Geophysical Research: Atmospheres*, **103 (D18)**, 23 195–23 197.

Frisch, S., M. Shupe, I. Djalalova, G. Feingold, and M. Poellot, 2002: The retrieval of stratus cloud droplet effective radius with cloud radars. *Journal of Atmospheric and Oceanic Technology*, **19 (6)**, 835–842.

Fu, S., X. Deng, M. D. Shupe, and H. Xue, 2019: A modelling study of the continuous ice formation in an autumnal Arctic mixed-phase cloud case. *Atmospheric Research*, **228**, 77–85.

GDAS1, .: URL: `https://www.ready.noaa.gov/gdas1.php`.

Ghatak, D. and J. Miller, 2013: Implications for Arctic amplification of changes in the strength of the water vapor feedback. *Journal of Geophysical Research: Atmospheres*, **118 (14)**, 7569–7578.

Giangrande, S. E., T. Toto, A. Bansemer, M. R. Kumjian, S. Mishra, and A. V. Ryzhkov, 2016: Insights into riming and aggregation processes as revealed by aircraft, radar, and disdrometer observations for a 27 April 2011 widespread precipitation event. *Journal of Geophysical Research: Atmospheres*, **121 (10)**, 5846–5863.

Gierens, R., S. Kneifel, M. D. Shupe, K. Ebell, M. Maturilli, and U. Löhnert, 2020: Low-level mixed-phase clouds in a complex Arctic environment. *Atmospheric Chemistry and Physics*, **20 (6)**, 3459–3481, doi: 10.5194/acp-20-3459-2020.

Goosse, H., J. E. Kay, K. C. Armour, A. Bodas-Salcedo, H. Chepfer, D. Docquier, A. Jonko, P. J. Kushner, O. Lecomte, F. Massonnet, and H. S. Park, 2018: Quantifying climate feedbacks in polar regions. *Nature communications*, **9 (1)**, 1–13, doi: 10.1038/s41467-018-04173-0.

Gordon, N., A. Jonko, P. Forster, and K. Shell, 2013: An observationally based constraint on the water-vapor feedback. *Journal of Geophysical Research: Atmospheres*, **118 (22)**, 12–435.

Gossard, E. E., 1994: Measurement of cloud droplet size spectra by Doppler radar. *Journal of Atmospheric and Oceanic Technology*, **11 (3)**, 712–726.

Grazioli, J., J.-B. Madeleine, H. Gallée, R. M. Forbes, C. Genthon, G. Krinner, and A. Berne, 2017: Katabatic winds diminish precipitation contribution to the Antarctic ice mass balance. *Proceedings of the National Academy of Sciences*, **114 (41)**, 10 858–10 863, doi: 10.1073/pnas.1707633114.

Gunsch, M. J., R. M. Kirpes, K. R. Kolesar, T. E. Barrett, S. China, R. J. Sheesley, A. Laskin, A. Wiedensohler, T. Tuch, and K. A. Pratt, 2017: Contributions of transported Prudhoe Bay oil field emissions to the aerosol population in Utqiaġvik, Alaska. *Atmospheric Chemistry and Physics*, **17 (17)**, 10 879–10 892, doi: 10.5194/acp-17-10879-2017.

Guo, Z., M. Wang, Y. Peng, and Y. Luo, 2020: Evaluation on the vertical distribution of liquid and ice phase cloud fraction in Community Atmosphere Model version 5.3 using spaceborne lidar observations. *Earth and Space Science*, **7 (3)**, e2019EA001 029, doi: https://doi.org/10.1029/2019EA001029.

Hall, A., 2004: The role of surface albedo feedback in climate. *Journal of Climate*, **17 (7)**, 1550–1568.

Hallett, J. and S. Mossop, 1974: Production of secondary ice particles during the riming process. *Nature*, **249 (5452)**, 26–28.

Hansen, J., R. Ruedy, M. Sato, and K. Lo, 2010: Global surface temperature change. *Reviews of Geophysics*, **48 (4)**.

Harrington, J. Y., T. Reisin, W. R. Cotton, and S. M. Kreidenweis, 1999: Cloud resolving simulations of Arctic stratus: Part II: Transition-season clouds. *Atmos. Res.*, **51 (1)**, 45–75.

Herenz, P., H. Wex, S. Henning, T. B. Kristensen, F. Rubach, A. Roth, S. Borrmann, H. Bozem, H. Schulz, and F. Stratmann, 2018: Measurements of aerosol and CCN properties in the Mackenzie River delta (Canadian Arctic) during spring–summer transition in May 2014. *Atmospheric Chemistry and Physics*, **18 (7)**, 4477–4496, doi: 10.5194/acp-18-4477-2018.

Heymsfield, A. J., A. Protat, D. Bouniol, R. T. Austin, R. J. Hogan, J. Delanoë, H. Okamoto, K. Sato, G.-J. van Zadelhoff, D. P. Donovan, and Z. Wang, 2008: Testing IWC Retrieval Methods Using Radar and Ancillary Measurements with In Situ Data. *Journal of Applied Meteorology and Climatology*, **47 (1)**, 135–163, doi: 10.1175/2007JAMC1606.1.

Hildebrand, P. H. and R. S. Sekhon, 1974: Objective Determination of the Noise Level in Doppler Spectra. *Journal of Applied Meteorology*, **13 (7)**, 808–811, doi: 10.1175/1520-0450(1974)013<0808:ODOTNL>2.0.CO;2.

Hillmer-Pegram, K., 2014: A synthesis of existing, planned, and proposed infrastructure and operations supporting oil and gas activities and commercial transportation in arctic Alaska. Program Report. *University of Alaska Fairbanks, Political Science Department, Resilience and Adaptation Program, Fairbanks, Alaska.*

Hobbs, P. V. and A. L. Rangno, 1998: Microstructures of low and middle-level clouds over the Beaufort Sea. *Q. J. Roy. Meteor. Soc.*, **124 (550)**, 2035–2071.

Hobbs, P. V., A. L. Rangno, M. Shupe, and T. Uttal, 2001: Airborne studies of cloud structures over the Arctic Ocean and comparisons with retrievals from ship-based remote sensing measurements. *J. Geophys. Res.-Atmos*, **106 (14)**, 15 029–15 044.

Hogan, R. J., M. P. Mittermaier, and A. J. Illingworth, 2006: The retrieval of ice water content from radar reflectivity factor and temperature and its use in evaluating a mesoscale model. *J. Appl. Meteorol. Clim*, **45 (2)**, 301–317.

Hogan, R. J. and E. J. O'Connor, 2004: Facilitating cloud radar and lidar algorithms: the Cloudnet Instrument Synergy/Target Categorization product. *Cloudnet documentation*.

Huffman, G. J. and J. Norman, Gene Alfred, 1988: The Supercooled Warm Rain Process and the Specification of Freezing Precipitation. *Monthly Weather Review*, **116 (11)**, 2172–2182, doi: 10.1175/1520-0493(1988)116<2172:TSWRPA>2.0.CO;2.

Illingworth, A. J., R. J. Hogan, E. O'Connor, D. Bouniol, M. E. Brooks, J. Delanoë, D. P. Donovan, J. D. Eastment, N. Gaussiat, J. W. F. Goddard, M. Haeffelin, H. K. Baltink, O. A. Krasnov, J. Pelon, J.-M. Piriou, A. Protat, H. W. J. Russchenberg, A. Seifert, A. M. Tompkins, G.-J. van Zadelhoff, F. Vinit, U. Willén, D. R. Wilson, and C. L. Wrench, 2007: Cloudnet: Continuous evaluation of cloud profiles in seven operational models using ground-based observations. *B. Am. Meteorol. Soc.*, **88 (6)**, 883–898, doi: 10.1175/BAMS-88-6-883.

Intrieri, J., C. Fairall, M. Shupe, P. Persson, E. Andreas, P. Guest, and R. Moritz, 2002: An annual cycle of Arctic surface cloud forcing at SHEBA. *J. Geophys. Res.-Oceans*, **107 (C10)**.

IPCC, 2013: Climate Change 2013: The Physical Science Basis. Contribution of Working Group I to the Fifth Assessment Report of the Intergovernmental Panel on Climate Change [Stocker, T.F., D. Qin, G.-K. Plattner, M. Tignor, S.K. Allen, J. Boschung, A. Nauels, Y. Xia, V. Bex and P.M. Midgley (eds.)]. *Cambridge University Press, Cambridge, United Kingdom and New York, NY, USA.*

IPCC, 2018: Summary for Policymakers. In: Global Warming of 1.5^{o}C. An IPCC Special Report on the impacts of global warming of 1.5^{o}C above pre-industrial levels and related global greenhouse gas emission pathways, in the context of strengthening the global response to the threat of climate change, sustainable development, and efforts to eradicate poverty [Masson-Delmotte, V., P. Zhai, H.-O. Pörtner, D. Roberts, J. Skea, P.R. Shukla, A. Pirani, W. Moufouma-Okia, C. Péan, R. Pidcock, S. Connors, J.B.R. Matthews, Y. Chen, X. Zhou, M.I. Gomis, E. Lonnoy, T. Maycock, M. Tignor, and T. Waterfield (eds.)]. *World Meteorological Organization, Geneva, Switzerland*.

IPCC, 2019: Summary for Policymakers. In: IPCC Special Report on the Ocean and Cryosphere in a Changing Climate [H.-O. Pörtner, D.C. Roberts, V. Masson-Delmotte, P. Zhai, M. Tignor, E. Poloczanska, K. Mintenbeck, A. Alegría, M. Nicolai, A. Okem, J. Petzold, B. Rama, N.M. Weyer (eds.)]. *World Meteorological Organization, Geneva, Switzerland*.

Irish, V. E., P. Elizondo, J. Chen, C. Chou, J. Charette, M. Lizotte, L. A. Ladino, T. W. Wilson, M. Gosselin, B. J. Murray, E. Polishchuk, J. P. D. Abbatt, L. A. Miller, and A. K. Bertram, 2017: Ice-nucleating particles in Canadian Arctic sea-surface microlayer and bulk seawater. *Atmospheric Chemistry and Physics*, **17 (17)**, 10 583–10 595, doi: 10.5194/acp-17-10583-2017.

Irish, V. E., S. J. Hanna, Y. Xi, M. Boyer, E. Polishchuk, M. Ahmed, J. Chen, J. P. D. Abbatt, M. Gosselin, R. Chang, L. A. Miller, and A. K. Bertram, 2019: Revisiting properties and concentrations of ice-nucleating particles in the sea surface microlayer and bulk seawater in the Canadian Arctic during summer. *Atmospheric Chemistry and Physics*, **19 (11)**, 7775–7787, doi: 10.5194/acp-19-7775-2019.

Isaac, G., J. Ayers, M. Bailey, L. Bissonnette, B. Bernstein, S. Cober, N. Driedger, W. Evans, F. Fabry, A. Glazer, I. Gultepe, J. Hallett, D. Hudak, A. Korolev, and D. Marcotte, 2005: First results from the Alliance Icing Research Study II. *43rd AIAA Aerospace Sciences Meeting and Exhibit*, doi: 10.2514/6.2005-252.

Jaakkola, J. J., S. Juntunen, and K. Näkkäläjärvi, 2018: The holistic effects of climate change on the culture, well-being, and health of the Saami, the only indigenous people in the European Union. *Current environmental health reports*, **5 (4)**, 401–417, doi: 10.1007/s40572-018-0211-2.

Jackson, R. C., G. M. McFarquhar, A. V. Korolev, M. E. Earle, P. S. Liu, R. P. Lawson, S. Brooks, M. Wolde, A. Laskin, and M. Freer, 2012: The dependence of ice microphysics on aerosol concentration in Arctic mixed-phase stratus clouds during ISDAC and M-PACE. *J. Geophys. Res.-Atmos.*, **117 (D15)**.

Jakobson, E. and T. Vihma, 2010: Atmospheric moisture budget in the Arctic based on the ERA-40 reanalysis. *International Journal of Climatology*, **30 (14)**, 2175–2194.

Jenkinson, A. and F. Collison, 1977: An initial climatology of gales over the North Sea. *Synoptic climatology branch memorandum*, **62**, 18.

Jiang, H., W. R. Cotton, J. O. Pinto, J. A. Curry, and M. J. Weissbluth, 2000: Cloud resolving simulations of mixed-phase Arctic stratus observed during BASE: Sensitivity to concentration of ice crystals and large-scale heat and moisture advection. *J. Atmos. Sci.*, **57 (13)**, 2105–2117.

Jocher, G., F. Karner, C. Ritter, R. Neuber, K. Dethloff, F. Obleitner, J. Reuder, and T. Foken, 2012: The near-surface small-scale spatial and temporal variability of sensible and latent heat exchange in the Svalbard region: a case study. *ISRN Meteorology*, **2012**.

Kalesse, H., W. Szyrmer, S. Kneifel, P. Kollias, and E. Luke, 2016a: Fingerprints of a riming event on cloud radar Doppler spectra: observations and modeling. *Atmospheric Chemistry and Physics*, **16 (5)**, 2997–3012, doi: 10.5194/acp-16-2997-2016.

Kalesse, H., T. Vogl, C. Paduraru, and E. Luke, 2019: Development and validation of a supervised machine learning radar Doppler spectra peak-finding algorithm. *Atmospheric Measurement Techniques*, **12 (8)**, 4591–4617, doi: 10.5194/amt-12-4591-2019.

Kalesse, H., G. de Boer, A. Solomon, M. Oue, M. Ahlgrimm, D. Zhang, M. D. Shupe, E. Luke, and A. Protat, 2016b: Understanding Rapid Changes in Phase Partitioning between Cloud Liquid and Ice in Stratiform Mixed-Phase Clouds: An Arctic Case Study. *Mon. Weather Rev.*, **144 (12)**, 4805–4826.

Kanamitsu, M., 1989: Description of the NMC global data assimilation and forecast system. *Weather and Forecasting*, **4 (3)**, 335–342, doi: 10.1175/1520-0434(1989)004<0335:DOTNGD>2.0.CO;2.

Kanji, Z. A., L. A. Ladino, H. Wex, Y. Boose, M. Burkert-Kohn, D. J. Cziczo, and M. Krämer, 2017: Overview of ice nucleating particles. *Meteorological Monographs*, **58**, 1–1.

Karlsson, J. and G. Svensson, 2013: Consequences of poor representation of Arctic sea-ice albedo and cloud-radiation interactions in the CMIP5 model ensemble. *Geophys. Res. Lett.*, **40 (16)**, 4374–4379.

Karrer, M., A. Seifert, C. Siewert, D. Ori, A. von Lerber, and S. Kneifel, 2020: Ice Particle Properties Inferred From Aggregation Modelling. *Journal of Advances in Modeling Earth Systems*, **12 (8)**, e2020MS002 066, doi: 10.1029/2020MS002066, e2020MS002066 10.1029/2020MS002066.

Kay, J. E. and A. Gettelman, 2009: Cloud influence on and response to seasonal Arctic sea ice loss. *J. Geophys. Res.-Atmos.*, **114 (D18)**.

Kay, J. E., T. L'Ecuyer, A. Gettelman, G. Stephens, and C. O'Dell, 2008: The contribution of cloud and radiation anomalies to the 2007 Arctic sea ice extent minimum. *Geophys. Res. Lett.*, **35 (8)**.

Kay, J. E., T. L'Ecuyer, H. Chepfer, N. Loeb, A. Morrison, and G. Cesana, 2016: Recent Advances in Arctic Cloud and Climate Research. *Current Climate Change Reports*, **2 (4)**, 159–169.

Kayser, M., M. Maturilli, R. M. Graham, S. R. Hudson, A. Rinke, L. Cohen, J.-H. Kim, S.-J. Park, W. Moon, and M. A. Granskog, 2017: Vertical thermodynamic structure of the troposphere during the Norwegian young sea ICE expedition (N-ICE2015). *J. Geophys. Res.-Atmos.*, **122 (20)**, 10–855.

Kim, H., S.-W. Yeh, S.-I. An, J.-H. Park, B.-M. Kim, and E.-H. Baek, 2020: Arctic sea ice loss as a potential trigger for Central Pacific El Niño events. *Geophysical Research Letters*, **n/a (n/a)**, e2020GL087 028, doi: 10.1029/2020GL087028, e2020GL087028 2020GL087028.

Klein, S. A., R. B. McCoy, H. Morrison, A. S. Ackerman, A. Avramov, G. d. Boer, et al., 2009: Intercomparison of model simulations of mixed-phase clouds observed during the ARM Mixed-Phase Arctic Cloud Experiment. I: Single-layer cloud. *Q. J. Roy. Meteor. Soc.*, **135 (641)**, 979–1002, doi: 10.1002/qj.416.

Kneifel, S., P. Kollias, A. Battaglia, J. Leinonen, M. Maahn, H. Kalesse, and F. Tridon, 2016: First observations of triple-frequency radar Doppler spectra in snowfall: Interpretation and applications. *Geophysical Research Letters*, **43 (5)**, 2225–2233, doi: 10.1002/2015GL067618.

Kneifel, S. and D. Moisseev, 2020: Long-term statistics of riming in non-convective clouds derived from ground-based Doppler cloud radar observations. *Journal of the Atmospheric Sciences*, 1–47, doi: 10.1175/JAS-D-20-0007.1.

Kneifel, S., A. von Lerber, J. Tiira, D. Moisseev, P. Kollias, and J. Leinonen, 2015: Observed relations between snowfall microphysics and triple-frequency radar measurements. *Journal of Geophysical Research: Atmospheres*, **120 (12)**, 6034–6055, doi: 10.1002/2015JD023156.

Kollias, P., B. Albrecht, R. Lhermitte, and A. Savtchenko, 2001: Radar observations of updrafts, downdrafts, and turbulence in fair-weather cumuli. *Journal of the atmospheric sciences*, **58 (13)**, 1750–1766.

Kollias, P., J. Rémillard, E. Luke, and W. Szyrmer, 2011a: Cloud radar Doppler spectra in drizzling stratiform clouds: 1. Forward modeling and remote sensing applications. *Journal of Geophysical Research: Atmospheres*, **116 (D13)**, doi: 10.1029/2010JD015237.

Kollias, P., W. Szyrmer, J. Rémillard, and E. Luke, 2011b: Cloud radar Doppler spectra in drizzling stratiform clouds: 2. Observations and microphysical modeling of drizzle evolution. *Journal of Geophysical Research: Atmospheres*, **116 (D13)**, doi: 10.1029/2010JD015238.

Komurcu, M., T. Storelvmo, I. Tan, U. Lohmann, Y. Yun, J. E. Penner, Y. Wang, X. Liu, and T. Takemura, 2014: Intercomparison of the cloud water phase among global climate models. *J. Geophys. Res.-Atmos.*, **119 (6)**, 3372–3400.

Korolev, A., 2007: Limitations of the Wegener–Bergeron–Findeisen mechanism in the evolution of mixed-phase clouds. *Journal of the Atmospheric Sciences*, **64 (9)**, 3372–3375.

Korolev, A. and P. R. Field, 2008: The effect of dynamics on mixed-phase clouds: Theoretical considerations. *J. Atmos. Sci.*, **65 (1)**, 66–86.

Korolev, A. and G. Isaac, 2003: Phase transformation of mixed-phase clouds. *Q. J. Roy. Meteor. Soc.*, **129 (587)**, 19–38.

Korolev, A., G. Isaac, and J. Hallett, 1999: Ice particle habits in Arctic clouds. *Geophysical research letters*, **26 (9)**, 1299–1302.

Korolev, A., G. Mcfarquhar, P. R. Field, C. Franklin, P. Lawson, Z. Wang, E. Williams, S. J. Abel, D. Axisa, S. Borrmann, J. Crosier, J. Fugal, M. Krämer, U. Lohmann, O. Schlenczek, and M. Wendisch, 2017: Ice Formation and Evolution in Clouds and Precipitation: Measurement and Modeling Challenges. Chapter 5: Mixed-phase clouds: progress and challenges. *Meteorological Monographs*, **58**, 5–1.

Korolev, A. V., 2008: Rates of phase transformations in mixed-phase clouds. *Quarterly Journal of the Royal Meteorological Society*, **134 (632)**, 595–608.

Korolev, A. V. and G. A. Isaac, 2000: Drop Growth Due to High Supersaturation Caused by Isobaric Mixing. *Journal of the Atmospheric Sciences*, **57 (10)**, 1675–1685, doi: 10.1175/1520-0469(2000)057<1675:DGDTHS>2.0.CO;2.

Kretzschmar, J., M. Salzmann, J. Mülmenstädt, and J. Quaas, 2019: Arctic clouds in ECHAM6 and their sensitivity to cloud microphysics and surface fluxes. *Atmospheric Chemistry and Physics*, **19 (16)**, 10 571–10 589, doi: 10.5194/acp-19-10571-2019.

Küchler, N., 2019: Ground-based remote sensing of warm low-level stratified clouds - new perspectives and applications. Ph.D. thesis, Institut für Geophysik und Meteorologie der Universität zu Köln.

Küchler, N., S. Kneifel, P. Kollias, and U. Löhnert, 2018: Revisiting liquid water content retrievals in warm stratified clouds: The modified Frisch. *Geophysical Research Letters*, **45 (17)**, 9323–9330.

Küchler, N., S. Kneifel, U. Löhnert, P. Kollias, H. Czekala, and T. Rose, 2017: A W-Band Radar–Radiometer System for Accurate and Continuous Monitoring of Clouds and Precipitation. *J. Atmos. Ocean. Tech.*, **34 (11)**, 2375–2392.

Kulla, B. S. and C. Ritter, 2019: Water Vapor Calibration: Using a Raman Lidar and Radiosoundings to Obtain Highly Resolved Water Vapor Profiles. *Remote Sensing*, **11 (6)**, 616.

Larsen, J., O. Anisimov, A. Constable, A. Hollowed, N. Maynard, P. Prestrud, T. Prowse, and J. Stone, 2014: Polar regions. In: Climate Change 2014: Impacts, Adaptation, and Vulnerability. Part B: Regional Aspects. Contribution of Working Group II to the Fifth Assessment Report of the Intergovernmental Panel on Climate Change [Barros, V.R.,C.B. Field, D.J. Dokken, M.D. Mastrandrea, K.J. Mach, T.E. Bilir, M. Chatterjee, K.L. Ebi, Y.O. Estrada, R.C. Genova,B. Girma, E.S. Kissel, A.N. Levy, S. MacCracken, P.R. Mastrandrea, and L.L. White (eds.)]. *Cambridge University Press, Cambridge, United Kingdom and New York, NY, USA.*, 1567–1612.

Lasher-Trapp, S., S. Anderson-Bereznicki, A. Shackelford, C. H. Twohy, and J. G. Hudson, 2008: An Investigation of the Influence of Droplet Number Concentration and Giant Aerosol Particles upon Supercooled Large Drop Formation in Wintertime Stratiform Clouds. *Journal of Applied Meteorology and Climatology*, **47 (10)**, 2659–2678, doi: 10.1175/2008JAMC1807.1.

Lauer, M., K. Block, M. Salzmann, and J. Quaas, 2020: CO_2-forced changes of Arctic temperature lapse rates in CMIP5 models. *Meteorologische Zeitschrift*.

Leaitch, W. R., A. Korolev, A. A. Aliabadi, J. Burkart, M. D. Willis, J. P. D. Abbatt, H. Bozem, P. Hoor, F. Köllner, J. Schneider, A. Herber, C. Konrad, and R. Brauner, 2016: Effects of 20–100 nm particles on liquid clouds in the clean summertime Arctic. *Atmospheric Chemistry and Physics*, **16 (17)**, 11 107–11 124, doi: 10.5194/acp-16-11107-2016.

Lenschow, D. H., V. Wulfmeyer, and C. Senff, 2000: Measuring Second- through Fourth-Order Moments in Noisy Data. *Journal of Atmospheric and Oceanic Technology*, **17 (10)**, 1330–1347, doi: 10.1175/1520-0426(2000)017<1330:MSTFOM>2.0.CO;2.

Lhermitte, R., 1990: Attenuation and Scattering of Millimeter Wavelength Radiation by Clouds and Precipitation. *Journal of Atmospheric and Oceanic Technology*, **7 (3)**, 464–479, doi: 10.1175/1520-0426(1990)007<0464:AASOMW>2.0.CO;2.

Li, Z., K.-M. Xu, and A. Cheng, 2017: The Response of Simulated Arctic Mixed-Phase Stratocumulus to Sea Ice Cover Variability in the Absence of Large-Scale Advection. *J. Geophys. Res.-Atmos.*, **122 (22)**, 12–335.

Liu, Y., J. R. Key, Z. Liu, X. Wang, and S. J. Vavrus, 2012: A cloudier Arctic expected with diminishing sea ice. *Geophysical Research Letters*, **39 (5)**.

Loewe, K., A. M. L. Ekman, M. Paukert, J. Sedlar, M. Tjernström, and C. Hoose, 2017: Modelling micro- and macrophysical contributors to the dissipation of an Arctic mixed-phase cloud during the Arctic Summer Cloud Ocean Study (ASCOS). *Atmospheric Chemistry and Physics*, **17 (11)**, 6693–6704, doi: 10.5194/acp-17-6693-2017.

Lohmann, U. and C. Hoose, 2009: Sensitivity studies of different aerosol indirect effects in mixed-phase clouds. *Atmospheric Chemistry and Physics*, **9 (22)**, 8917–8934, doi: 10.5194/acp-9-8917-2009.

Löhnert, U. and S. Crewell, 2003: Accuracy of cloud liquid water path from ground-based microwave radiometry 1. Dependency on cloud model statistics. *Radio Sci.*, **38 (3)**.

Lowenthal, D. H., R. D. Borys, W. Cotton, S. Saleeby, S. A. Cohn, and W. O. Brown, 2011: The altitude of snow growth by riming and vapor deposition in mixed-phase orographic clouds. *Atmospheric environment*, **45 (2)**, 519–522.

Luke, E. and P. Kollias, 2007: A high resolution hydrometeor phase classifier based on analysis of cloud radar Doppler spectra. *Proc. of the 33rd Conf. on Radar Meteorology*.

Luke, E. P. and P. Kollias, 2013: Separating cloud and drizzle radar moments during precipitation onset using Doppler spectra. *Journal of Atmospheric and Oceanic Technology*, **30 (8)**, 1656–1671, doi: 10.1175/JTECH-D-11-00195.1.

Luke, E. P., P. Kollias, and M. D. Shupe, 2010: Detection of supercooled liquid in mixed-phase clouds using radar Doppler spectra. *J. Geophys. Res.-Atmos.*, **115 (D19)**.

Maahn, M., G. de Boer, J. M. Creamean, G. Feingold, G. M. McFarquhar, W. Wu, and F. Mei, 2017: The observed influence of local anthropogenic pollution on northern Alaskan cloud properties. *Atmospheric Chemistry and Physics*, **17 (23)**, 14 709–14 726, doi: 10.5194/acp-17-14709-2017.

Maahn, M., F. Hoffmann, M. D. Shupe, G. de Boer, S. Y. Matrosov, and E. P. Luke, 2019: Can liquid cloud microphysical processes be used for vertically pointing cloud radar calibration? *Atmospheric Measurement Techniques*, **12 (6)**, 3151–3171, doi: 10.5194/amt-12-3151-2019.

Maahn, M. and P. Kollias, 2012: Improved Micro Rain Radar snow measurements using Doppler spectra post-processing. *Atmospheric Measurement Techniques*, **5 (11)**, 2661–2673, doi: 10.5194/amt-5-2661-2012.

Maahn, M., U. Löhnert, P. Kollias, R. C. Jackson, and G. M. McFarquhar, 2015: Developing and evaluating ice cloud parameterizations for forward modeling of radar moments using in situ aircraft observations. *J. Atmos. Ocean. Tech.*, **32 (5)**, 880–903.

Maahn, M. and U. Löhnert, 2017: Potential of Higher-Order Moments and Slopes of the Radar Doppler Spectrum for Retrieving Microphysical and Kinematic Properties of Arctic Ice Clouds. *J. Appl. Meteorol. Clim*, **56 (2)**, 263–282, doi: 10.1175/JAMC-D-16-0020.1.

Magono, C. and C. W. Lee, 1966: Meteorological classification of natural snow crystals. *Journal of the Faculty of Science, Hokkaido University. Series 7, Geophysics*, **2 (4)**, 321–335.

Marsham, J., S. Dobbie, and R. Hogan, 2006: Evaluation of a large-eddy model simulation of a mixed-phase altocumulus cloud using microwave radiometer, lidar and Doppler radar data. *Quarterly Journal of the Royal Meteorological Society*, **132 (618)**, 1693–1715.

Mason, S. L., C. J. Chiu, R. J. Hogan, D. Moisseev, and S. Kneifel, 2018: Retrievals of Riming and Snow Density From Vertically Pointing Doppler Radars. *Journal of Geophysical Research: Atmospheres*, **123 (24)**, 13,807–13,834, doi: 10.1029/2018JD028603.

Matrosov, S. Y., 1998: A Dual-Wavelength Radar Method to Measure Snowfall Rate. *Journal of Applied Meteorology*, **37 (11)**, 1510–1521, doi: 10.1175/1520-0450(1998)037<1510:ADWRMT>2.0.CO;2.

Matrosov, S. Y., A. V. Korolev, and A. J. Heymsfield, 2002: Profiling cloud ice mass and particle characteristic size from Doppler radar measurements. *J. Atmos. Ocean. Tech.*, **19 (7)**, 1003–1018.

Mattingly, K. S., C. A. Ramseyer, J. J. Rosen, T. L. Mote, and R. Muthyala, 2016: Increasing water vapor transport to the Greenland Ice Sheet revealed using self-organizing maps. *Geophysical Research Letters*, **43 (17)**, 9250–9258.

Maturilli, M., 2020: Continuous meteorological observations at station Ny-Ålesund (2011-08 et seq). PANGAEA, URL: `https://doi.pangaea.de/10.1594/PANGAEA.914979`.

Maturilli, M. and K. Ebell, 2018: Twenty-five years of cloud base height measurements by ceilometer in Ny-Ålesund, Svalbard. *Earth Syst. Sci. Data*, **10**, 1451–1456.

Maturilli, M., A. Herber, and G. König-Langlo, 2013: Climatology and time series of surface meteorology in Ny-Ålesund, Svalbard. *Earth System Science Data*, **5 (1)**, 155–163, doi: 10.5194/essd-5-155-2013.

Maturilli, M., A. Herber, and G. König-Langlo, 2015: Surface radiation climatology for Ny-Ålesund, Svalbard (78.9° N). *Theor. Appl. Climatol.*, **120**, 331–339, doi: https://doi.org/10.1007/s00704-014-1173-4.

Maturilli, M. and M. Kayser, 2016: Homogenized radiosonde record at station Ny-Ålesund, Spitsbergen, 1993-2014. PANGAEA, doi: 10.1594/PANGAEA.845373.

Maturilli, M. and M. Kayser, 2017: Arctic warming, moisture increase and circulation changes observed in the Ny-Ålesund homogenized radiosonde record. *Theor. Appl. Climatol.*, **130 (1-2)**, 1–17.

Mauritsen, T., J. Sedlar, M. Tjernström, C. Leck, M. Martin, M. Shupe, S. Sjogren, B. Sierau, P. O. G. Persson, I. M. Brooks, and E. Swietlicki, 2011: An Arctic CCN-limited cloud-aerosol regime. *Atmospheric Chemistry and Physics*, **11 (1)**, 165–173, doi: 10.5194/acp-11-165-2011.

McCoy, D. T., I. Tan, D. L. Hartmann, M. D. Zelinka, and T. Storelvmo, 2016: On the relationships among cloud cover, mixed-phase partitioning, and planetary albedo in GCMs. *J. Adv. Model. Earth Sy.*, **8 (2)**, 650–668.

McFarquhar, G. M., G. Zhang, M. R. Poellot, G. L. Kok, R. McCoy, T. Tooman, A. Fridlind, and A. J. Heymsfield, 2007: Ice properties of single-layer stratocumulus during the Mixed-Phase Arctic Cloud Experiment: 1. Observations. *J. Geophys. Res.-Atmos.*, **112 (D24)**.

McFarquhar, G. M., S. Ghan, J. Verlinde, A. Korolev, J. W. Strapp, B. Schmid, et al., 2011: Indirect and semi-direct aerosol campaign: The impact of Arctic aerosols on clouds. *Bulletin of the American Meteorological Society*, **92 (2)**, 183–201.

McFiggans, G., P. Artaxo, U. Baltensperger, H. Coe, M. C. Facchini, G. Feingold, S. Fuzzi, M. Gysel, A. Laaksonen, U. Lohmann, T. F. Mentel, D. M. Murphy, C. D. O'Dowd, J. R. Snider, and E. Weingartner, 2006: The effect of physical and chemical aerosol properties on warm cloud droplet activation. *Atmospheric Chemistry and Physics*, **6 (9)**, 2593–2649, doi: 10.5194/acp-6-2593-2006.

McIlhattan, E. A., T. S. L'Ecuyer, and N. B. Miller, 2017: Observational Evidence Linking Arctic Supercooled Liquid Cloud Biases in CESM to Snowfall Processes. *Journal of Climate*, **30 (12)**, 4477–4495, doi: 10.1175/JCLI-D-16-0666.1.

Mech, M., L.-L. Kliesch, A. Anhäuser, T. Rose, P. Kollias, and S. Crewell, 2019: Microwave Radar/radiometer for Arctic Clouds (MiRAC): first insights from the ACLOUD campaign. *Atmospheric Measurement Techniques*, **12 (9)**, 5019–5037, doi: 10.5194/amt-12-5019-2019.

Mech, M., M. Maahn, S. Kneifel, D. Ori, E. Orlandi, P. Kollias, V. Schemann, and S. Crewell, 2020: PAMTRA 1.0: A Passive and Active Microwave radiative TRAnsfer tool for simulating radiometer and radar measurements of the cloudy atmosphere. *Geoscientific Model Development*, **13 (9)**, 4229–4251, doi: 10.5194/gmd-13-4229-2020.

Melchionna, S., M. Bauer, and G. Peters, 2008: A new algorithm for the extraction of cloud parameters using multipeak analysis of cloud radar data–first application and preliminary results. *Meteorologische Zeitschrift*, **17 (5)**, 613–620.

Melvin, A. M., P. Larsen, B. Boehlert, J. E. Neumann, P. Chinowsky, X. Espinet, J. Martinich, M. S. Baumann, L. Rennels, A. Bothner, D. J. Nicolsky, and S. S. Marchenko, 2017: Climate change damages to Alaska public infrastructure and the economics of proactive adaptation. *Proceedings of the National Academy of Sciences*, **114 (2)**, E122–E131, doi: 10.1073/pnas.1611056113.

Meredith, M., M. Sommerkorn, S. Cassotta, C. Derksen, A. Ekaykin, A. Hollowed, G. Kofinas, A. Mackintosh, J. Melbourne-Thomas, M. Muelbert, G. Ottersen, H. Pritchard, and E. Schuur, 2019: Polar Regions. In: IPCC Special Report on the Ocean and Cryosphere in a Changing Climate [H.-O. Pörtner, D.C. Roberts, V. Masson-Delmotte, P. Zhai, M. Tignor, E. Poloczanska, K. Mintenbeck, A. Alegría, M. Nicolai, A. Okem, J. Petzold, B. Rama, N.M. Weyer (eds.)]. *World Meteorological Organization, Geneva, Switzerland.*

Meta, A., 2006: Signal processing of FMCW Synthetic Aperture Radar data. Ph.D. thesis, Delft University of Technology, Faculty of Electrical Engineering, Mathematics & Computer Science.

Mewes, D. and C. Jacobi, 2019: Heat transport pathways into the Arctic and their connections to surface air temperatures. *Atmospheric Chemistry and Physics*, **19 (6)**, 3927–3937.

Miller, N. B., M. D. Shupe, C. J. Cox, D. Noone, P. O. G. Persson, and S. Konrad, 2017: Surface energy budget responses to radiative forcing at Summit, Greenland. *The Cryosphere*, **11 (1)**, 497.

Mioche, G., O. Jourdan, M. Ceccaldi, and J. Delanoë, 2015: Variability of mixed-phase clouds in the Arctic with a focus on the Svalbard region: a study based on spaceborne active remote sensing. *Atmos. Chem. Phys.*, **15 (5)**, 2445–2461.

Mioche, G., O. Jourdan, J. Delanoë, C. Gourbeyre, G. Febvre, R. Dupuy, M. Monier, F. Szczap, A. Schwarzenboeck, and J.-F. Gayet, 2017: Vertical distribution of microphysical properties of Arctic springtime low-level mixed-phase clouds over the Greenland and Norwegian seas. *Atmos. Chem. Phys.*, **17 (20)**, 12 845–12 869, doi: 10.5194/acp-17-12845-2017.

Moisseev, D. N., S. Lautaportti, J. Tyynela, and S. Lim, 2015: Dual-polarization radar signatures in snowstorms: Role of snowflake aggregation. *Journal of Geophysical Research: Atmospheres*, **120 (24)**, 12 644–12 655, doi: 10.1002/2015JD023884.

Moore, R. H., R. Bahreini, C. A. Brock, K. D. Froyd, J. Cozic, J. S. Holloway, A. M. Middlebrook, D. M. Murphy, and A. Nenes, 2011: Hygroscopicity and composition of Alaskan Arctic CCN during April 2008. *Atmospheric Chemistry and Physics*, **11 (22)**, 11 807–11 825, doi: 10.5194/acp-11-11807-2011.

Morrison, A. L., 2019: Engaging in Climate Change: Arctic Cloud-Sea Ice Feedbacks in Observations, Climate Models, and the Classroom. Ph.D. thesis, University of Colorado.

Morrison, H., G. De Boer, G. Feingold, J. Harrington, M. D. Shupe, and K. Sulia, 2012: Resilience of persistent Arctic mixed-phase clouds. *Nat. Geosci.*, **5 (1)**, 11–17.

Morrison, H., J. O. Pinto, J. A. Curry, and G. M. McFarquhar, 2008: Sensitivity of modeled Arctic mixed-phase stratocumulus to cloud condensation and ice nuclei over regionally varying surface conditions. *J. Geophys. Res.-Atmos.*, **113 (D5)**.

Morrison, H., M. D. Shupe, J. O. Pinto, and J. A. Curry, 2005: Possible roles of ice nucleation mode and ice nuclei depletion in the extended lifetime of Arctic mixed-phase clouds. *Geophys. Res. Lett.*, **32 (18)**.

Morrison, H., P. Zuidema, A. S. Ackerman, A. Avramov, G. de Boer, J. Fan, A. M. Fridlind, T. Hashino, J. Y. Harrington, Y. Luo, M. Ovchinnikov, and B. Shipway, 2011: Intercomparison of cloud model simulations of Arctic mixed-phase boundary layer clouds observed during SHEBA/FIRE-ACE. *J. Adv. Model. Earth Sy.*, **3 (2)**, doi: 10.1029/2011MS000066.

Myagkov, A., P. Seifert, U. Wandinger, J. Bühl, and R. Engelmann, 2016: Relationship between temperature and apparent shape of pristine ice crystals derived from polarimetric cloud radar observations during the ACCEPT campaign. *Atmospheric Measurement Techniques*, **9 (8)**, 3739–3754, doi: 10.5194/amt-9-3739-2016.

Neggers, R. A. J., J. Chylik, U. Egerer, H. Griesche, V. Schemann, P. Seifert, H. Siebert, and A. Macke, 2019: Local and Remote Controls on Arctic Mixed-Layer Evolution. *Journal of Advances in Modeling Earth Systems*, **11 (7)**, 2214–2237, doi: 10.1029/2019MS001671.

Nomokonova, T., 2020: Arctic cloud properties derived from ground-based sensor synergy at Ny-Ålesund. Ph.D. thesis, Institut für Geophysik und Meteorologie der Universität zu Köln.

Nomokonova, T. and K. Ebell, 2019: Cloud microphysical properties retrieved from ground-based remote sensing at Ny-Ålesund (10 June 2016 - 8 October 2018). PANGAEA, doi: 10.1594/PANGAEA.898556.

Nomokonova, T., K. Ebell, U. Löhnert, M. Maturilli, and C. Ritter, 2020: The influence of water vapor anomalies on clouds and their radiative effect at Ny-Ålesund. *Atmospheric Chemistry and Physics*, **20 (8)**, 5157–5173, doi: 10.5194/acp-20-5157-2020.

Nomokonova, T., K. Ebell, U. Löhnert, M. Maturilli, C. Ritter, and E. O'Connor, 2019: Statistics on clouds and their relation to thermodynamic conditions at Ny-Ålesund using ground-based sensor synergy. *Atmos. Chem. Phys.*, **19 (6)**, 4105–4126, doi: 10.5194/acp-19-4105-2019.

Norgren, M. S., G. d. Boer, and M. D. Shupe, 2018: Observed aerosol suppression of cloud ice in low-level Arctic mixed-phase clouds. *Atmos. Chem. Phys.*, **18 (18)**, 13 345–13 361.

O'Connor, E. J., A. J. Illingworth, and R. J. Hogan, 2004: A Technique for Autocalibration of Cloud Lidar. *Journal of Atmospheric and Oceanic Technology*, **21 (5)**, 777–786, doi: 10.1175/1520-0426(2004)021<0777:ATFAOC>2.0.CO;2.

Osborne, E., J. Richter-Menge, and M. Jeffries, 2018: Arctic Report Card 2018. *https://www.arctic.noaa.gov/Report-Card.*

Oshima, K., K. Yamazaki, et al., 2004: Seasonal variation of moisture transport in polar regions and the relation with annular modes. *Polar Meteorol. Glaciol*, **18**, 30–53.

Oue, M., M. Galletti, J. Verlinde, A. Ryzhkov, and Y. Lu, 2016: Use of X-Band Differential Reflectivity Measurements to Study Shallow Arctic Mixed-Phase Clouds. *Journal of Applied Meteorology and Climatology*, **55 (2)**, 403–424, doi: 10.1175/JAMC-D-15-0168.1.

Oue, M., P. Kollias, A. Ryzhkov, and E. P. Luke, 2018: Toward exploring the synergy between cloud radar polarimetry and Doppler spectral analysis in deep cold precipitating systems in the Arctic. *Journal of Geophysical Research: Atmospheres*, **123 (5)**, 2797–2815.

Oue, M., M. R. Kumjian, Y. Lu, Z. Jiang, E. E. Clothiaux, J. Verlinde, and K. Aydin, 2015: X-Band Polarimetric and Ka-Band Doppler Spectral Radar Observations of a Graupel-Producing Arctic Mixed-Phase Cloud. *Journal of Applied Meteorology and Climatology*, **54 (6)**, 1335–1351, doi: 10.1175/JAMC-D-14-0315.1.

Ovchinnikov, M., A. S. Ackerman, A. Avramov, A. Cheng, J. Fan, A. M. Fridlind, S. Ghan, J. Harrington, C. Hoose, A. Korolev, G. M. McFarquhar, H. Morrison, M. Paukert, J. Savre, B. J. Shipway, M. D. Shupe, A. Solomon, and K. Sulia, 2014: Intercomparison of large-eddy simulations of Arctic mixed-phase clouds: Importance of ice size distribution assumptions. *Journal of Advances in Modeling Earth Systems*, **6 (1)**, 223–248, doi: 10.1002/2013MS000282.

Payne, A. E., M. F. Jansen, and T. W. Cronin, 2015: Conceptual model analysis of the influence of temperature feedbacks on polar amplification. *Geophysical Research Letters*, **42 (21)**, 9561–9570.

Pfitzenmaier, L., Y. Dufournet, C. M. H. Unal, and H. W. J. Russchenberg, 2017: Retrieving Fall Streaks within Cloud Systems Using Doppler Radar. *Journal of Atmospheric and Oceanic Technology*, **34 (4)**, 905–920, doi: 10.1175/JTECH-D-16-0117.1.

Philipp, A., C. Beck, P. Esteban, F. Kreienkamp, T. Krennert, K. Lochbihler, S. P. Lykoudis, K. Pianko-Kluczynska, P. Post, D. R. Alvarez10, et al., 2014: cost733class-1.2 User guide. Technical report.

Phillips, V., T. Choularton, A. Illingworth, R. Hogan, and P. Field, 2003: Simulations of the glaciation of a frontal mixed-phase cloud with the Explicit Microphysics Model. *Quarterly Journal of the Royal Meteorological Society*, **129 (590)**, 1351–1371.

Pinsky, M., A. Khain, and A. Korolev, 2015: Phase transformations in an ascending adiabatic mixed-phase cloud volume. *Journal of Geophysical Research: Atmospheres*, **120 (8)**, 3329–3353, doi: 10.1002/2015JD023094.

Pinto, J. O., 1998: Autumnal mixed-phase cloudy boundary layers in the Arctic. *J. Atmos. Sci.*, **55 (11)**, 2016–2038.

Pithan, F., B. Medeiros, and T. Mauritsen, 2014: Mixed-phase clouds cause climate model biases in Arctic wintertime temperature inversions. *Climate dynamics*, **43 (1-2)**, 289–303.

Pithan, F., G. Svensson, R. Caballero, D. Chechin, T. W. Cronin, A. M. Ekman, R. Neggers, M. D. Shupe, A. Solomon, M. Tjernström, and M. Wendisch, 2018: Role of air-mass transformations in exchange between the Arctic and mid-latitudes. *Nat. Geosci.*, **11 (11)**, 805, doi: 10.1038/s41561-018-0234-1.

Pobanz, B. M., J. D. Marwitz, and M. K. Politovich, 1994: Conditions Associated with Large-Drop Regions. *Journal of Applied Meteorology*, **33 (11)**, 1366–1372, doi: 10.1175/1520-0450(1994)033<1366:CAWLDR>2.0.CO;2.

Politovich, M. K., 1989: Aircraft Icing Caused by Large Supercooled Droplets. *Journal of Applied Meteorology*, **28 (9)**, 856–868, doi: 10.1175/1520-0450(1989)028<0856:AICBLS>2.0.CO;2.

Possner, A., A. M. Ekman, and U. Lohmann, 2017: Cloud response and feedback processes in stratiform mixed-phase clouds perturbed by ship exhaust. *Geophysical Research Letters*, **44 (4)**, 1964–1972.

Pruppacher, H. R. and J. D. Klett, 1997: *Microphysics of clouds and precipitation*. 2d ed., Kluwer Academic Publishers.

Qiu, S., B. Xi, and X. Dong, 2018: Influence of Wind Direction on Thermodynamic Properties and Arctic Mixed-Phase Clouds in Autumn at Utqiaġvik, Alaska. *J. Geophys. Res.-Atmos.*, **123 (17)**, 9589–9603.

Radenz, M., J. Bühl, P. Seifert, H. Griesche, and R. Engelmann, 2019: peakTree: a framework for structure-preserving radar Doppler spectra analysis. *Atmospheric Measurement Techniques*, **12 (9)**, 4813–4828, doi: 10.5194/amt-12-4813-2019.

Rambukkange, M. P., J. Verlinde, E. W. Eloranta, C. J. Flynn, and E. E. Clothiaux, 2011: Using Doppler spectra to separate hydrometeor populations and analyze ice precipitation in multilayered mixed-phase clouds. *IEEE Geoscience and Remote Sensing Letters*, **8 (1)**, 108–112.

Rangno, A. L. and P. V. Hobbs, 2001: Ice particles in stratiform clouds in the Arctic and possible mechanisms for the production of high ice concentrations. *J. Geophys. Res.*, **106**, 15.

Rasmussen, R. M., I. Geresdi, G. Thompson, K. Manning, and E. Karplus, 2002: Freezing drizzle formation in stably stratified layer clouds: The role of radiative cooling of cloud droplets, cloud condensation nuclei, and ice initiation. *Journal of the atmospheric sciences*, **59 (4)**, 837–860.

Richter-Menge, J., M. Druckenmiller, and M. Jeffries, 2019: Arctic Report Card 2019. *https://www.arctic.noaa.gov/Report-Card*.

Riihimaki, L. D., J. M. Comstock, E. Luke, T. J. Thorsen, and Q. Fu, 2017: A case study of microphysical structures and hydrometeor phase in convection using radar Doppler spectra at Darwin, Australia. *Geophysical Research Letters*, **44 (14)**, 7519–7527.

Rinke, A., B. Segger, S. Crewell, M. Maturilli, T. Naakka, T. Nygård, T. Vihma, F. Alshawaf, G. Dick, J. Wickert, et al., 2019: Trends of Vertically Integrated Water Vapor over the Arctic during 1979–2016: Consistent Moistening All Over? *Journal of Climate*, **32 (18)**, 6097–6116.

Rose, T., 2015: *RPG-FMCW-94-SP/DP 94 GHz W-band Cloud Doppler Radar Operation and Software Guide (Version 3.50-1).*

Rose, T., S. Crewell, U. Löhnert, and C. Simmer, 2005: A network suitable microwave radiometer for operational monitoring of the cloudy atmosphere. *Atmos. Res.*, **75 (3)**, 183–200.

Rosenfeld, D., R. Chemke, P. DeMott, R. C. Sullivan, R. Rasmussen, F. McDonough, J. Comstock, B. Schmid, J. Tomlinson, H. Jonsson, K. Suski, A. Cazorla, and K. Prather, 2013: The common occurrence of highly supercooled drizzle and rain near the coastal regions of the western United States. *Journal of Geophysical Research: Atmospheres*, **118 (17)**, 9819–9833, doi: 10.1002/jgrd.50529.

Russotto, R. D. and M. Biasutti, 2020: Polar Amplification as an Inherent Response of a Circulating Atmosphere: Results From the TRACMIP Aquaplanets. *Geophysical Research Letters*, **47 (6)**, e2019GL086 771, doi: 10.1029/2019GL086771.

Rémillard, J., A. M. Fridlind, A. S. Ackerman, G. Tselioudis, P. Kollias, D. B. Mechem, H. E. Chandler, E. Luke, R. Wood, M. K. Witte, P. Y. Chuang, and J. K. Ayers, 2017: Use of Cloud Radar Doppler Spectra to Evaluate Stratocumulus Drizzle Size Distributions in Large-Eddy Simulations with Size-Resolved Microphysics. *Journal of Applied Meteorology and Climatology*, **56 (12)**, 3263–3283, doi: 10.1175/JAMC-D-17-0100.1.

Savre, J., A. M. Ekman, G. Svensson, and M. Tjernström, 2015: Large-eddy simulations of an Arctic mixed-phase stratiform cloud observed during ISDAC: sensitivity to moisture aloft, surface fluxes and large-scale forcing. *Q. J. Roy. Meteor. Soc.*, **141 (689)**, 1177–1190.

Schemann, V. and K. Ebell, 2020: Simulation of mixed-phase clouds with the ICON large-eddy model in the complex Arctic environment around Ny-Ålesund. *Atmospheric Chemistry and Physics*, **20 (1)**, 475–485, doi: 10.5194/acp-20-475-2020.

Schweiger, A., J. Zhang, R. Lindsay, and M. Steele, 2008: Did unusually sunny skies help drive the record sea ice minimum of 2007? *Geophys. Res. Lett.*, **35 (10)**.

Scott, R. C. and D. Lubin, 2016: Unique manifestations of mixed-phase cloud microphysics over Ross Island and the Ross Ice Shelf, Antarctica. *Geophys. Res. Lett.*, **43 (6)**, 2936–2945.

Sedlar, J. and M. Shupe, 2014: Characteristic nature of vertical motions observed in Arctic mixed-phase stratocumulus. *Atmos. Chem. Phys*, **14 (7)**, 3461–3478, doi: 10.5194/acp-14-3461-2014.

Sedlar, J., M. D. Shupe, and M. Tjernström, 2012: On the relationship between thermodynamic structure and cloud top, and its climate significance in the Arctic. *J. Climate*, **25 (7)**, 2374–2393, doi: 10.1175/JCLI-D-11-00186.1.

Sedlar, J. and M. Tjernström, 2009: Stratiform cloud—Inversion characterization during the Arctic melt season. *Boundary-layer meteorology*, **132 (3)**, 455–474.

Serreze, M. C. and R. G. Barry, 2011: Processes and impacts of Arctic amplification: A research synthesis. *Global Planet. Change*, **77 (1-2)**, 85–96.

Shupe, M., I. Brooks, and G. Canut, 2012: Evaluation of turbulent dissipation rate retrievals from Doppler cloud radar. *Atmospheric Measurement Techniques*, **5 (6)**, 1375–1385.

Shupe, M. D., 2007: A ground-based multisensor cloud phase classifier. *Geophysical Research Letters*, **34 (22)**.

Shupe, M. D., 2011: Clouds at Arctic atmospheric observatories. Part II: Thermodynamic phase characteristics. *J. Appl. Meteorol. Clim*, **50 (3)**, 645–661.

Shupe, M. D. and J. M. Intrieri, 2004: Cloud radiative forcing of the Arctic surface: The influence of cloud properties, surface albedo, and solar zenith angle. *J. Climate*, **17 (3)**, 616–628.

Shupe, M. D., P. Kollias, S. Y. Matrosov, and T. L. Schneider, 2004: Deriving mixed-phase cloud properties from Doppler radar spectra. *J. Atmos. Ocean. Tech.*, **21 (4)**, 660–670.

Shupe, M. D., P. Kollias, P. O. G. Persson, and G. M. McFarquhar, 2008a: Vertical motions in Arctic mixed-phase stratiform clouds. *J. Atmos. Sci.*, **65 (4)**, 1304–1322.

Shupe, M. D., P. Kollias, M. Poellot, and E. Eloranta, 2008b: On deriving vertical air motions from cloud radar Doppler spectra. *Journal of Atmospheric and Oceanic Technology*, **25 (4)**, 547–557.

Shupe, M. D., S. Y. Matrosov, and T. Uttal, 2006: Arctic mixed-phase cloud properties derived from surface-based sensors at SHEBA. *J. Atmos. Sci.*, **63 (2)**, 697–711.

Shupe, M. D., P. O. G. Persson, I. M. Brooks, M. Tjernström, J. Sedlar, T. Mauritsen, S. Sjogren, and C. Leck, 2013: Cloud and boundary layer interactions over the Arctic sea ice in late summer. *Atmos. Chem. Phys*, **13 (18)**, 9379–9399, doi: 10.5194/acp-13-9379-2013.

Shupe, M. D., D. D. Turner, A. Zwink, M. M. Thieman, E. J. Mlawer, and T. Shippert, 2015: Deriving Arctic cloud microphysics at Barrow, Alaska: algorithms, results, and radiative closure. *Journal of Applied Meteorology and Climatology*, **54 (7)**, 1675–1689.

Shupe, M. D., T. Uttal, S. Y. Matrosov, and A. S. Frisch, 2001: Cloud water contents and hydrometeor sizes during the FIRE Arctic Clouds Experiment. *J. Geophys. Res.-Atmos.*, **106 (D14)**, 15 015–15 028.

Shupe, M. D., V. P. Walden, E. Eloranta, T. Uttal, J. R. Campbell, S. M. Starkweather, and M. Shiobara, 2011: Clouds at Arctic atmospheric observatories. Part I: Occurrence and macrophysical properties. *J. Appl. Meteorol. Clim*, **50 (3)**, 626–644.

Shupe, M. D., J. S. Daniel, G. De Boer, E. W. Eloranta, P. Kollias, E. P. Luke, C. N. Long, D. D. Turner, and J. Verlinde, 2008c: A focus on mixed-phase clouds: The status of ground-based observational methods. *B. Am. Meteorol. Soc.*, **89 (10)**, 1549–1562.

Silber, I., A. M. Fridlind, J. Verlinde, L. M. Russell, and A. S. Ackerman, 2020: Nonturbulent Liquid-Bearing Polar Clouds: Observed Frequency of Occurrence and Simulated Sensitivity to Gravity Waves. *Geophysical Research Letters*, **47 (10)**, e2020GL087 099, doi: 10.1029/2020GL087099, e2020GL087099 2020GL087099.

Silber, I., J. Verlinde, G. Wen, and E. W. Eloranta, 2019a: Can Embedded Liquid Cloud Layer Volumes Be Classified in Polar Clouds Using a Single-Frequency Zenith-Pointing Radar? *IEEE Geoscience and Remote Sensing Letters*, **17 (2)**, 222–226.

Silber, I., A. M. Fridlind, J. Verlinde, A. S. Ackerman, Y.-S. Chen, D. H. Bromwich, S.-H. Wang, M. Cadeddu, and E. W. Eloranta, 2019b: Persistent Supercooled Drizzle at Temperatures Below -25°C Observed at McMurdo Station, Antarctica. *Journal of Geophysical Research: Atmospheres*, **124 (20)**, 10 878–10 895, doi: 10.1029/2019JD030882.

Singleton, F., 1960: Aircraft observations of rain and drizzle from layer clouds. *Quarterly Journal of the Royal Meteorological Society*, **86 (368)**, 195–204.

Sledd, A. and T. L'Ecuyer, 2019: How much do clouds mask the impacts of Arctic sea ice and snow cover variations? Different perspectives from observations and reanalyses. *Atmosphere*, **10 (1)**, 12.

Smith, L. C. and S. R. Stephenson, 2013: New Trans-Arctic shipping routes navigable by midcentury. *Proceedings of the National Academy of Sciences*, **110 (13)**, E1191–E1195.

Smith, P. L., 2010: The Unit Symbol for the Logarithmic Scale of Radar Reflectivity Factors. *Journal of Atmospheric and Oceanic Technology*, **27 (3)**, 615–616, doi: 10.1175/2009JTECHA1360.1.

Sokol, Z., J. Minářová, and P. Novák, 2018: Classification of hydrometeors using measurements of the ka-band cloud radar installed at the Milešovka Mountain (Central Europe). *Remote Sensing*, **10 (11)**, 1674.

Solomon, A., G. de Boer, J. M. Creamean, A. McComiskey, M. D. Shupe, M. Maahn, and C. Cox, 2018: The relative impact of cloud condensation nuclei and ice nucleating particle concentrations on phase partitioning in Arctic mixed-phase stratocumulus clouds. *Atmos. Chem. Phys.*, **18 (23)**, 17 047–17 059, doi: 10.5194/acp-18-17047-2018.

Solomon, A., G. Feingold, and M. D. Shupe, 2015: The role of ice nuclei recycling in the maintenance of cloud ice in Arctic mixed-phase stratocumulus. *Atmospheric Chemistry and Physics*, **15 (18)**, 10 631–10 643, doi: 10.5194/acp-15-10631-2015.

Solomon, A., M. D. Shupe, O. Persson, H. Morrison, T. Yamaguchi, P. M. Caldwell, and G. de Boer, 2014: The sensitivity of springtime Arctic mixed-phase stratocumulus clouds to surface-layer and cloud-top inversion-layer moisture sources. *J. Atmos. Sci.*, **71 (2)**, 574–595.

Solomon, A., M. D. Shupe, P. Persson, and H. Morrison, 2011: Moisture and dynamical interactions maintaining decoupled Arctic mixed-phase stratocumulus in the presence of a humidity inversion. *Atmospheric Chemistry & Physics Discussions*, **11 (5)**.

Sommer, M., R. Dirksen, and C. von Rohden, 2016: Brief Description of the RS92 GRUAN Data Product. Tech. rep., GRUAN Lead Centre. GRUAN-TD-4.

Sotiropoulou, G., J. Sedlar, M. Tjernström, M. D. Shupe, I. M. Brooks, and P. O. G. Persson, 2014: The thermodynamic structure of summer Arctic stratocumulus and the dynamic coupling to the surface. *Atmos. Chem. Phys.*, **14 (22)**, 12 573–12 592.

Sotiropoulou, G., M. Tjernström, J. Savre, A. M. L. Ekman, K. Hartung, and J. Sedlar, 2018: Large-eddy simulation of a warm-air advection episode in the summer Arctic. *Quarterly Journal of the Royal Meteorological Society*, **144 (717)**, 2449–2462, doi: 10.1002/qj.3316.

Sotiropoulou, G., M. Tjernström, J. Sedlar, P. Achtert, B. J. Brooks, I. M. Brooks, P. O. G. Persson, J. Prytherch, D. J. Salisbury, M. D. Shupe, P. E. Johnston, and D. Wolfe, 2016: Atmospheric Conditions during the Arctic Clouds in Summer Experiment (ACSE): Contrasting Open Water and Sea Ice Surfaces during Melt and Freeze-Up Seasons. *Journal of Climate*, **29 (24)**, 8721–8744, doi: 10.1175/JCLI-D-16-0211.1.

Stapf, J., A. Ehrlich, E. Jäkel, C. Lüpkes, and M. Wendisch, 2019: Reassessment of the common concept to derive the surface cloud radiative forcing in the Arctic: Consideration of surface albedo – cloud interactions. *Atmospheric Chemistry and Physics Discussions*, **2019**, 1–24, doi: 10.5194/acp-2019-534.

Stroeve, J. C., M. C. Serreze, M. M. Holland, J. E. Kay, J. Malanik, and A. P. Barrett, 2012: The Arctic's rapidly shrinking sea ice cover: a research synthesis. *Climatic change*, **110 (3-4)**, 1005–1027.

Stull, R. B., 1988: *An introduction to boundary layer meteorology*, Vol. 13. Springer Science & Business Media.

Tan, I. and T. Storelvmo, 2016: Sensitivity study on the influence of cloud microphysical parameters on mixed-phase cloud thermodynamic phase partitioning in CAM5. *Journal of the Atmospheric Sciences*, **73 (2)**, 709–728.

Tan, I. and T. Storelvmo, 2019: Evidence of Strong Contributions From Mixed-Phase Clouds to Arctic Climate Change. *Geophysical Research Letters*, **46 (5)**, 2894–2902.

Taylor, P. C., R. C. Boeke, Y. Li, and D. W. J. Thompson, 2019: Arctic cloud annual cycle biases in climate models. *Atmospheric Chemistry and Physics*, **19 (13)**, 8759–8782, doi: 10.5194/acp-19-8759-2019.

Tjernström, M., J. Sedlar, and M. D. Shupe, 2008: How well do regional climate models reproduce radiation and clouds in the Arctic? An evaluation of ARCMIP simulations. *J. Appl. Meteorol. Clim*, **47 (9)**, 2405–2422.

Tjernström, M., C. Leck, C. E. Birch, J. W. Bottenheim, B. J. Brooks, I. M. Brooks, et al., 2014: The Arctic Summer Cloud Ocean Study (ASCOS): overview and experimental design. *Atmospheric Chemistry and Physics*, **14 (6)**, 2823–2869, doi: 10.5194/acp-14-2823-2014.

Ulaby, F. and D. Long, 2014: *Microwave radar and radiometric remote sensing*. The University of Michigan Press.

Uttal, T., J. A. Curry, M. G. McPhee, D. K. Perovich, R. E. Moritz, J. A. Maslanik, P. S. Guest, H. L. Stern, J. A. Moore, R. Turenne, A. Heiberg, M. C. Serreze, D. P. Wylie, O. G. Persson, C. A. Paulson, C. Halle, J. H. Morison, P. A. Wheeler, A. Makshtas, H. Welch, M. D. Shupe,

J. M. Intrieri, K. Stamnes, R. W. Lindsey, R. Pinkel, W. S. Pegau, T. P. Stanton, and T. C. Grenfeld, 2002: Surface heat budget of the Arctic Ocean. *Bulletin of the American Meteorological Society*, **83 (2)**, 255–276, doi: 10.1175/1520-0477(2002)083<0255:SHBOTA>2.3.CO;2.

Vaisala, 2010: *USERS GUIDE Vaisala Ceilometer CL51.*

Vali, G., P. DeMott, O. Möhler, and T. Whale, 2015: A proposal for ice nucleation terminology. *Atmospheric Chemistry & Physics*, **15 (18)**.

Vassel, M., L. Ickes, M. Maturilli, and C. Hoose, 2019: Classification of Arctic multilayer clouds using radiosonde and radar data in Svalbard. *Atmospheric Chemistry and Physics*, **19 (7)**, 5111–5126, doi: 10.5194/acp-19-5111-2019.

Verlinde, J., M. P. Rambukkange, E. E. Clothiaux, G. M. McFarquhar, and E. W. Eloranta, 2013: Arctic multilayered, mixed-phase cloud processes revealed in millimeter-wave cloud radar Doppler spectra. *J. Geophys. Res.-Atmos.*, **118 (23)**.

Verlinde, J., J. Y. Harrington, G. M. McFarquhar, V. T. Yannuzzi, A. Avramov, S. Greenberg, N. Johnson, G. Zhang, M. R. Poellot, J. H. Mather, D. D. Turner, E. W. Eloranta, B. D. Zak, A. J. Prenni, J. S. Daniel, G. L. Kok, D. C. Tobin, R. Holz, K. Sassen, D. Spangenberg, P. Minnis, T. P. Tooman, M. D. Ivey, S. J. Richardson, C. P. Bahrmann, M. Shupe, P. J. DeMott, A. J. Heymsfield, and R. Schofield, 2007: The mixed-phase Arctic cloud experiment. *B. Am. Meteorol. Soc.*, **88 (2)**, 205–221, doi: 10.1175/BAMS-88-2-205.

Vignesh, P. P., J. H. Jiang, P. Kishore, H. Su, T. Smay, N. Brighton, and I. Velicogna, 2020: Assessment of CMIP6 Cloud Fraction and Comparison With Satellite Observations. *Earth and Space Science*, **7 (2)**, e2019EA000 975.

Vogel, J. M. and F. Fabry, 2018: Contrasting Polarimetric Observations of Stratiform Riming and Nonriming Events. *Journal of Applied Meteorology and Climatology*, **57 (2)**, 457–476, doi: 10.1175/JAMC-D-16-0370.1.

Walker, D. and J. Pierce, 2015: Rapid Arctic Transitions due to Infrastructure and Climate (RATIC): A contribution to ICARP III. *Alaska Geobotany Center, University of Alaska Fairbanks.*

Wang, J., J. Ge, Q. Zhang, P. Fan, M. Wei, and X. Li, 2017: Study of aircraft icing warning algorithm based on millimeter wave radar. *Journal of Meteorological Research*, **31 (6)**, 1034–1044.

Wegener, A., 1911: *Thermodynamik der atmosphäre.* J.A. Barth, 331 pp.

Wendisch, M., M. Brückner, J. P. Burrows, S. Crewell, K. Dethloff, K. Ebell, C. Lüpkes, A. Macke, J. Notholt, J. Quaas, A. Rinke, and I. Tegen, 2017: Understanding Causes and Effects of Rapid Warming in the Arctic. *Eos*, **98**, doi: 10.1029/2017EO064803.

Wendisch, M. et al., 2019a: Proposal for the Second Funding Period of the Transregional Collaborative Research Centre TR 172. ArctiC Amplification: Climate Relevant Atmospheric and SurfaCe Processes, and Feedback Mechanisms $(AC)^3$, phase II.

Wendisch, M., A. Macke, A. Ehrlich, C. Lüpkes, M. Mech, D. Chechin, et al., 2019b: The Arctic Cloud Puzzle: Using ACLOUD/PASCAL Multiplatform Observations to Unravel the Role of Clouds and Aerosol Particles in Arctic Amplification. *Bulletin of the American Meteorological Society*, **100 (5)**, 841–871, doi: 10.1175/BAMS-D-18-0072.1.

Westbrook, C. and A. Illingworth, 2013: The formation of ice in a long-lived supercooled layer cloud. *Q. J. Roy. Meteor. Soc.*, **139 (677)**, 2209–2221.

Westbrook, C. D. and A. J. Illingworth, 2011: Evidence that ice forms primarily in supercooled liquid clouds at temperatures > -27°C. *Geophys. Res. Lett.*, **38 (14)**, doi: 10.1029/2011GL048021.

Wex, H., L. Huang, W. Zhang, H. Hung, R. Traversi, S. Becagli, R. J. Sheesley, C. E. Moffett, T. E. Barrett, R. Bossi, H. Skov, A. Hünerbein, J. Lubitz, M. Löffler, O. Linke, M. Hartmann, P. Herenz, and F. Stratmann, 2019: Annual variability of ice-nucleating particle concentrations at different Arctic locations. *Atmospheric Chemistry and Physics*, **19 (7)**, 5293–5311, doi: 10.5194/acp-19-5293-2019.

Whyte, K., 2017: Indigenous climate change studies: Indigenizing futures, decolonizing the Anthropocene. *English Language Notes*, **55 (1)**, 153–162.

Williams, C. R., M. Maahn, J. C. Hardin, and G. de Boer, 2018: Clutter mitigation, multiple peaks, and high-order spectral moments in 35 GHz vertically pointing radar velocity spectra. *Atmospheric Measurement Techniques*, **11 (9)**, 4963–4980, doi: 10.5194/amt-11-4963-2018.

Wilson, T. W., L. A. Ladino, P. A. Alpert, M. N. Breckels, I. M. Brooks, J. Browse, S. M. Burrows, K. S. Carslaw, J. A. Huffman, C. Judd, W. P. Kilthau, R. H. Mason, G. McFiggans, L. A. Miller, J. J. Nájera, E. Polishchuk, S. Rae, C. L. Schiller, M. Si, J. V. Temprado, T. F. Whale, J. P. S. Wong, O. Wurl, J. D. Yakobi-Hancock, J. P. D. Abbatt, J. Y. Aller, A. K. Bertram, D. A. Knopf, and B. J. Murray, 2015: A marine biogenic source of atmospheric ice-nucleating particles. *Nature*, **525 (7568)**, 234–238, doi: 10.1038/nature14986.

Winton, M., 2006: Surface albedo feedback estimates for the AR4 climate models. *Journal of Climate*, **19 (3)**, 359–365.

Woods, C., R. Caballero, and G. Svensson, 2013: Large-scale circulation associated with moisture intrusions into the Arctic during winter. *Geophys. Res. Lett.*, **40 (17)**, 4717–4721.

Yau, M. K. and R. R. Rogers, 1996: *A short course in cloud physics*. 3d ed., Elsevier.

Young, G., H. M. Jones, T. W. Choularton, J. Crosier, K. N. Bower, M. W. Gallagher, R. S. Davies, I. A. Renfrew, A. D. Elvidge, E. Darbyshire, F. Marenco, P. R. A. Brown, H. M. A. Ricketts, P. J. Connolly, G. Lloyd, P. I. Williams, J. D. Allan, J. W. Taylor, D. Liu, and M. J. Flynn, 2016: Observed microphysical changes in Arctic mixed-phase clouds when transitioning from sea ice to open ocean. *Atmos. Chem. Phys.*, **16 (21)**, 13 945–13 967, doi: 10.5194/acp-16-13945-2016.

Yu, G., J. Verlinde, E. Clothiaux, and Y.-S. Chen, 2014: Mixed-phase cloud phase partitioning using millimeter wavelength cloud radar Doppler velocity spectra. *J. Geophys. Res.-Atmos.*, **119 (12)**, 7556–7576.

Yumashev, D., K. van Hussen, J. Gille, and G. Whiteman, 2017: Towards a balanced view of Arctic shipping: estimating economic impacts of emissions from increased traffic on the Northern Sea Route. *Climatic Change*, **143 (1-2)**, 143–155.

Zängl, G., D. Reinert, P. Rípodas, and M. Baldauf, 2015: The ICON (ICOsahedral Non-hydrostatic) modelling framework of DWD and MPI-M: Description of the non-hydrostatic dynamical core. *Q. J. Roy. Meteor. Soc.*, **141 (687)**, 563–579.

Zawadzki, I., F. Fabry, and W. Szyrmer, 2001: Observations of supercooled water and secondary ice generation by a vertically pointing X-band Doppler radar. *Atmospheric Research*, **59**, 343–359.

Zelinka, M. D., S. A. Klein, and D. L. Hartmann, 2012: Computing and partitioning cloud feedbacks using cloud property histograms. Part II: Attribution to changes in cloud amount, altitude, and optical depth. *Journal of Climate*, **25 (11)**, 3736–3754.

Zelinka, M. D., T. A. Myers, D. T. McCoy, S. Po-Chedley, P. M. Caldwell, P. Ceppi, S. A. Klein, and K. E. Taylor, 2020: Causes of higher climate sensitivity in CMIP6 models. *Geophysical Research Letters*, **47 (1)**, e2019GL085 782.

Zelinka, M. D., D. A. Randall, M. J. Webb, and S. A. Klein, 2017: Clearing clouds of uncertainty. *Nature Climate Change*, **7 (10)**, 674–678.

Zeppenfeld, S., M. van Pinxteren, M. Hartmann, A. Bracher, F. Stratmann, and H. Herrmann, 2019: Glucose as a Potential Chemical Marker for Ice Nucleating Activity in Arctic Seawater and Melt Pond Samples. *Environmental science & technology*, **53 (15)**, 8747–8756.

Zhang, D., Z. Wang, T. Luo, Y. Yin, and C. Flynn, 2017: The occurrence of ice production in slightly supercooled Arctic stratiform clouds as observed by ground-based remote sensors at the ARM NSA site. *Journal of Geophysical Research: Atmospheres*, **122 (5)**, 2867–2877.

Zhang, M., X. Liu, M. Diao, J. J. D'Alessandro, Y. Wang, C. Wu, D. Zhang, Z. Wang, and S. Xie, 2019: Impacts of Representing Heterogeneous Distribution of Cloud Liquid and Ice on Phase Partitioning of Arctic Mixed-Phase Clouds with NCAR CAM5. *Journal of Geophysical Research: Atmospheres*, **124 (23)**, 13 071–13 090, doi: 10.1029/2019JD030502.

Zheng, J., L. Liu, K. Zhu, J. Wu, and B. Wang, 2017: A method for retrieving vertical air velocities in convective clouds over the Tibetan Plateau from TIPEX-III Cloud Radar Doppler spectra. *Remote Sensing*, **9 (9)**, 964.

Zygmuntowska, M., T. Mauritsen, J. Quaas, and L. Kaleschke, 2012: Arctic Clouds and Surface Radiation – a critical comparison of satellite retrievals and the ERA-Interim reanalysis. *Atmospheric Chemistry and Physics*, **12 (14)**, 6667–6677, doi: 10.5194/acp-12-6667-2012.

Erklärung zur Dissertation

Hiermit versichere ich an Eides statt, dass ich die vorliegende Dissertation selbstständig und ohne die Benutzung anderer als der angegebenen Hilfsmittel und Literatur angefertigt habe. Alle Stellen, die wörtlich oder sinngemäß aus veröffentlichten und nicht veröffentlichten Werken dem Wortlaut oder dem Sinn nach entnommen wurden, sind als solche kenntlich gemacht. Ich versichere an Eides statt, dass diese Dissertation noch keiner anderen Fakultät oder Universität zur Prüfung vorgelegen hat; dass sie - abgesehen von unten angegebenen Teilpublikationen und eingebundenen Artikeln und Manuskripten - noch nicht veröffentlicht worden ist sowie, dass ich eine Veröffentlichung der Dissertation vor Abschluss der Promotion nicht ohne Genehmigung des Promotionsausschusses vornehmen werde. Die Bestimmungen dieser Ordnung sind mir bekannt. Darüber hinaus erkläre ich hiermit, dass ich die Ordnung zur Sicherung guter wissenschaftlicher Praxis und zum Umgang mit wissenschaftlichem Fehlverhalten der Universität zu Köln gelesen und sie bei der Durchführung der Dissertation zugrundeliegenden Arbeiten und der schriftlich verfassten Dissertation beachtet habe und verpflichte mich hiermit, die dort genannten Vorgaben bei allen wissenschaftlichen Tätigkeiten zu beachten und umzusetzen. Ich versichere, dass die eingereichte elektronische Fassung der eingereichten Druckfassung vollständig entspricht.

Teilpublikationen:

Gierens, R., Kneifel, S., Shupe, M. D., Ebell, K., Maturilli, M., Löhnert, U. (2020). Low-level mixed-phase clouds in a complex Arctic environment. Atmos. Chem. Phys. 20, 3459–3481. https://doi.org/10.5194/acp-20-3459-2020

Köln, September 2020

Rosa Gierens